CRANFIELD UNIVERSITY

ELOISE EIMER

INTEGRATION OF SUBSTRATE IN ALUMINIUM WIRE AND ARC ADDITIVE MANUFACTURING

SCHOOL OF AEROSPACE, TRANSPORT AND MANUFACTURING
Welding Engineering and Laser Processing Centre

PhD thesis
Academic Year: 2019

Primary Supervisor: Prof. S. Williams
Secondary Supervisor: Dr. J. Ding
April 2019

CRANFIELD UNIVERSITY

SCHOOL OF AEROSPACE, TRANSPORT AND MANUFACTURING
Welding Engineering and Laser Processing Centre

PhD thesis

Academic Year: 2019

ELOISE EIMER

Integration of substrate in aluminium Wire and Arc Additive Manufacturing

Primary Supervisor: Prof. S. Williams
Secondary Supervisor: Dr. J. Ding
April 2019

© Cranfield University 2019. All rights reserved. No part of this publication may be reproduced without the written permission of the copyright owner.

Contents

Table of Contents **v**

List of Figures **ix**

List of Tables **xvii**

Abstract **xix**

List of Abbreviations **xxi**

Acknowledgements **xxiii**

1 Introduction **1**
1.1 Context and research gap 1
1.2 Aim and objectives 5
1.3 Thesis structure 6

2 Literature review **9**
2.1 Aluminium alloys 9
2.1.1 Applications 9
2.1.2 Metallurgy of high strength aluminium alloys 11
2.1.3 Strain hardening alloys 18
2.2 Additive manufacturing 19
2.2.1 Principle 19
2.2.2 Wire + Arc Additive Manufacturing 22
2.2.3 Aluminium alloys in AM 27
2.3 Fusion welding 44
2.3.1 Fusion welding of aluminium alloys 44
2.3.2 Hybrid laser + arc welding 48

3 Methodology **51**
3.1 Sample manufacturing set up 51
3.1.1 GMA deposition 51

3.1.2 Laser assisted WAAM . . . 59
3.2 Microstructure study . . . 62
3.2.1 Samples preparation . . . 62
3.2.2 Interface samples and terminology . . . 62
3.2.3 Micro hardness measurements . . . 63
3.2.4 Optical microscope . . . 65
3.2.5 SEM . . . 66
3.2.6 Tensile test . . . 67
3.2.7 Digital image correlation (DIC) along tensile tests . . . 67
3.3 Materials . . . 72

4 Mechanical properties of a WAAM Al-Cu-Mg alloy - Effect of deposition process, inter-pass cold work and post-deposition heat treatment 75
4.1 Introduction . . . 75
4.2 Methodology . . . 76
4.3 Results . . . 79
4.3.1 Macro and microstructure . . . 79
4.3.2 Porosity . . . 91
4.3.3 Chemical composition . . . 92
4.3.4 Micro hardness . . . 93
4.3.5 Tensile tests results . . . 94
4.3.6 Fractography . . . 97
4.4 Discussion . . . 106
4.4.1 Chemical composition . . . 106
4.4.2 Effect of deposition process on as-deposited microstructure and mechanical properties . . . 107
4.4.3 Effect of inter-pass rolling on the microstructure and mechanical properties . . . 108
4.4.4 Effect of heat treatment on the microstructure and mechanical properties . . . 112
4.5 Conclusion . . . 115

5 Potential and issues in depositing Aluminium zinc alloys 117
5.1 Introduction . . . 117
5.2 Methodology . . . 118
5.2.1 GMA process . . . 118
5.2.2 Laser-assisted WAAM . . . 120
5.2.3 Zinc addition using laser-assisted WAAM . . . 122
5.3 Results . . . 125
5.3.1 Laser-assisted WAAM . . . 125
5.3.2 Zinc addition using laser-assisted WAAM . . . 133
5.4 Discussion . . . 142

5.4.1 Laser-assisted WAAM 142
5.4.2 Zinc addition using laser-assisted WAAM 146
5.5 Conclusions and further work 148

6 Phenomena and issues at the interface between the substrate and WAAM deposited material 151
6.1 Introduction 151
6.2 Methodology 153
6.3 Results 156
6.3.1 Aluminium zinc and aluminium lithium substrates 156
6.3.2 Aluminium copper wires and substrates 159
6.3.3 Aluminium magnesium-silicon alloy substrates 166
6.3.4 Aluminium magnesium deposited material and rapidly solidified substrates 172
6.4 Discussion 180
6.4.1 Use of aluminium zinc and aluminium lithium substrate 180
6.4.2 Use of aluminium copper as-deposited material and substrate . . . 181
6.4.3 Use of aluminium magnesium and silicon alloy as substrate . . . 183
6.4.4 Use of aluminium magnesium as deposit material 183
6.5 Conclusions 185

7 Effect of inter-pass rolling and heat treatment on the interface between the substrate and WAAM deposited material 187
7.1 Introduction 187
7.2 Methodology 189
7.3 Results 189
7.3.1 Aluminium zinc and aluminium lithium substrates 189
7.3.2 Aluminium copper wire and substrates 198
7.3.3 Aluminium-magnesium-silicon substrates 211
7.4 Discussion 217
7.4.1 Use of aluminium zinc and aluminium lithium substrate 217
7.4.2 Use of aluminium copper as-deposited material and substrate . . . 217
7.4.3 Aluminium-magnesium-silicon substrates 221
7.5 Conclusion 222

8 Discussion 225
8.1 Finding summary 225
8.1.1 Chapter 4 225
8.1.2 Chapter 5 227
8.1.3 Chapters 6 and 7 228
8.2 Discussion and future work 231
8.2.1 Effect of bead geometry and inter-pass rolled material properties . 231

8.2.2 Interface between the substrate and deposited material and component design strategies 233

9 Conclusions **237**

A Matlab code for the post treatment of tensile tests **261**

B Matlab code for the post treatment of DIC test **269**

List of Figures

1.1 Research team of the Welding Engineering and Laser Processing Centre carrying the largest additively manufactured metallic part 2
1.2 Manufacturing step of an aluminium spar: deposition of the very first layer (a), followed by the next layers in (b) and (c), and a close view of the final part in (d) 2
1.3 Simplified wing component 4
1.4 Research strategy 6

2.1 Diagram of the aluminium part used in aircraft 10
2.2 Principle of precipitation hardening: Phase diagram (a), Strength evolution curve (b) and diagram of crystal structure (c) 15
2.3 AM Titanium implants for the skull (left) and pelvis (right) manufactured by Direct Metal Laser Sintering [1] 20
2.4 Tungsten gas arc deposition of titanium [2] 22
2.5 Example of titanium near-net-shape WAAM part [2] 23
2.6 Example of a wing rib building strategies detailed by Locket et al. [3]: picture (a) shows the wing rib diagram and the building strategies which could be used to manufacture it are shown in pictures (b), (c), (d), and (e) 26
2.7 Illustration of the effect of scanning speed on the porosity level in an PBF part [4] 28
2.8 Illustration of the effect of the hatch spacing (distance between parallel passes) on PBF material density [4] 29
2.9 Effect of inter-pass rolling and heat treatment on porosity level of 2319 deposited with a AC GMA process: optical images of the (a) as-deposited, (b) as heat treated, (c), (d) and (e) as rolled with a respective rolling load of 15, 30, and 45 kN and (f) rolled with a rolling load of 45 then heat treated material [5] 30
2.10 Optical image of (a) 7075 and (b) 50% 7075 - 50% AlSi10Mg manufactured by a laser powder bed fusion process [6] 32
2.11 Stress-strain curve obtained during the test of SLM material [7] 33
2.12 Photograph of AlCuMg alloy deposited with WAAM: (a) Al-Cu3.71-Mg1.73 and (b) Al-Cu4.08-Mg1.62. 34

2.13 Double GMA system developed and used by Qi et al. to deposit aluminium copper magnesium alloys [8] 43
2.14 Diagram of the different areas affected by a weld in fusion welding 44
2.15 Schematic of a hybrid keyhole welding set up [9] 49
2.16 Effect of power density on the penetration depth in conduction, transition and keyhole modes on aluminium [10] 50

3.1 GMA set up used to deposit material on the substrate surface 52
3.2 GMA set up used to deposit material on the edge of the substrate to produce the interface samples for tensile testing in Chapters 6 and 7 52
3.3 Rolling rig set up [11] 53
3.4 Schematic of the inter-pass rolling process and its effect on the deposited bead geometry 54
3.5 Waveform of CMT (a), CMT-Pulse (b), CMT-Advanced (c), and CMT-Pulse-Advanced (d) [12] 55
3.6 Diagram of first deposited beads using CMT pulse advanced and CMT pulse process 56
3.7 Schematic of the heat flux during the first and further layer deposition . . 57
3.8 Laser assisted WAAM set-up: general view of the set-up (on the right) with a closer view on the torch, wire-feeder, and substrate (on the left) . . 60
3.9 Schematic of the set up showing (a) the angle between the leading torch and the laser beam, (b) the angle between the substrate and the zinc wire feeder, and (c) the Arc-zinc and Arc-laser distances 61
3.10 Diagram of the different zone found at the interface between the deposited material and substrate 63
3.11 Diagram of the micro hardness measurement across the interface between the substrate and deposited material. 64
3.12 Hardness profile measured at the interface between the deposited material and substrate for the two geometry shown in Figure 3.11 65
3.13 Painted sample for DIC testing. 67
3.14 Example of images used for the calibration of the double camera system (extract from the equipment manual [13] 68
3.15 Example of a strain map provided by the Istra4D software after the video post treatment 69
3.16 Example of three stress-strain curves and YS determination using local strain data 70
3.17 YS map calculated with a constant Young's modulus of 69, 71 and 73 MPa 71

4.1 Diagram of the different conditions tested 77
4.2 Four wall deposited with two deposition processes and with or without inter-pass rolling 78
4.3 Samples position in each wall and tensile specimen dimensions 78

4.4 Illustration of the metrics used to characterise (a) the wall geometry and (b) the re-melting zone 79
4.5 Schematic of the effect of inter-pass rolling on the wall geometry 81
4.6 Illustration of the metrics used to characterise the wall geometry 82
4.7 Optical images of as-deposited , heat treated , as-rolled, and as-rolled then heat treated samples deposited with CMT-P-Adv process 84
4.8 SEM images of the inter-pass rolled wall deposited with CMT-P-Adv process (a) and (b) in as rolled condition, and (c) and (d) in rolled and heat treated condition 85
4.9 High magnification SEM images of CMT-P-Adv (a) as-deposited, (b) heat treated, (c) as-rolled, and (d) as rolled then heat treated; and CMT-P (e) as-deposited, (f) heat treated, (g) as-rolled and (h) as rolled then heat treated 86
4.10 Optical images of as-deposited, as heat treated, as-rolled, and rolled then heat treated samples deposited with CMT-P process 89
4.11 SEM images of the edge of the wall deposited with CMT-P process, in as-deposited(a) and as heat treated (b) condition 90
4.12 SEM image of typical defects observed in (a) the as-deposited CMT-P and (b) as-rolled samples 90
4.13 Number of pores per 100 mm^2 measured for each condition 91
4.14 Relationship between total deformation and micro hardness for inter-pass rolled 2319 [11], 5087 [14], and 2024 alloys 94
4.15 Ruptures surfaces of specimens taken from material deposited with CMT-P-Adv process 98
4.16 Ruptures surfaces of specimens taken from material deposited with CMT-P process 99
4.17 Rupture surface of a vertical specimen made of inter-pass rolled then heat treated material, deposited with CMT-P-Adv process 101
4.18 Micro-cracks founded in the rupture surface of the rolled CMT-P specimen tested in the vertical direction 103
4.19 Optical images of longitudinal cut of vertical tensile specimens taken from (a) as-deposited material, (b) heat treated, (c) as-rolled, and (d) rolled then heat treated deposited with CMT-P-Adv process 104
4.20 Optical images of longitudinal cut of vertical tensile specimens taken from (a) as-deposited material, (b) heat treated, (c) as-rolled, and (d) rolled then heat treated deposited with CMT-P process 105

5.1 Electric arc characteristics in CMT-P mode 119
5.2 Metrics used to characterise (a) the bead geometry and (b) melt pool length 120
5.3 Schematic of a bead deposited using two different laser power 121
5.4 Schematic of the set up and the laser-arc and zinc-arc distances 122
5.5 Melt pool shape (a) without laser, and (b) with 4kW laser power 126

5.6 Effect of laser power on melt pool length - The laser power used is 0.2, 1, and 1.5 kW in picture (a), (b) and (c) respectively . . . 126
5.7 Effect of laser power on melt pool length . . . 127
5.8 Effect of laser power on arc voltage and current . . . 128
5.9 Macrograph of bead cross-section, (a), (b) and (c) shows the bead geometry obtained for a laser power of 200W, 1kW, and 4 kW respectively . . . 128
5.10 Effect of laser power on bead geometry . . . 129
5.11 Effect of laser-arc distance on melt pool shape for a laser-arc distance of (a) 5mm and (b) 10 mm . . . 131
5.12 Diagram of the melt pool with (a) and (c) views from the top and (b) and (d) side for a laser-arc distance of 5 and 10 mm . . . 131
5.13 Effect of laser-arc distance on (a) and (b) arc voltage and (c) and (d) arc current for the laser-arc distance of 5 mm (a) and (b) and 10 mm (b) and (d) 132
5.14 Effect of laser on arc stability: (a) and (b) example of the voltage and current profiles with a laser power of 0.2 kW, and (c) and (d) with a laser power of 4 kw. . . . 133
5.15 Optical images of longitudinal layer cut deposited with a zinc-arc distance of (b) 5 mm, (c) 10 mm, and (d)15 mm. Image (a) shows a reference microstructure without any zinc addition. . . . 134
5.16 Microstructure of aluminium zinc bead on plate. (a), (b), (c), (d), (e), (f), (g), (h), (i), and (j) shows the cross-section of sample A_1, B_1, C_1, D_1, E_1, F_1, G_1, A_3, F_3, and G_3 respectively. The process parameters are given in table 5.1 . . . 137
5.17 Longitudinal section of three-layer-high wall: (a) A_3, (b) F_3, and (c) G_3 . 139
5.18 Element mapping generated by SEM from the top of sample W_3. Picture (a) is the SEM image of the area, and (b), (c), and (d) are the maps of Al, Zn and Cu respectively . . . 140
5.19 Effect of Laser power on bead geometry for aluminium zinc deposition with different laser power and AlCu WFS . . . 142

6.1 Tensile specimen geometries (a) used to determine the properties of all interfaces but the combination 2139 & 2319 which was tested using the specimen shown in (b) . . . 154
6.2 Longitudinal section of as-deposited interface between 2050 & 2319 (a), and 7449 & 2319 (b) . . . 157
6.3 Vertical hardness profile of as-deposited interface between (a) 7445 & 2319, and (b) 2050 & 2319, and (c) 2050 & 2024 . . . 158
6.4 Composition measurement at the 7449 & 2319 interface . . . 159
6.5 cross-section of the as-deposited 2139 & 2319 interface . . . 160
6.6 cross-section of as-deposited interface between (a) 2219 & 2319, (b) 2024 & 2319, and (c) 2139 & 2319 . . . 160

6.7 Partially Melted Zone (PMZ) of the (a) 2219 & 2319 and (b) 2139 & 2319 interfaces. The arrow gives an idea of the size of the area affected by liquation 161
6.8 Hardness profile of as-deposited (a) 2219 & 2319, (b) 2024 & 2319, (c) 2139 & 2319, and (d) 2024 & 2024 interfaces 162
6.9 Composition and hardness profile at the interface of the 2024 & 2319 combination 163
6.10 SEM images of the rupture surface of tensile specimen from 2219 & 2319 and 2024 & 2319 combinations 164
6.11 Optical images of ruptured tensile specimens taken from (a) 2219 & 2319 and (b) 2024 & 2319 combinations 165
6.12 interface 2139 & 2319: (a) rupture profile, (b) maximum strain map, and (c) yield strength map 166
6.13 cross-section of as-deposited interface between (a) 6061_{Rolled} & 2319, and (b) 6061_{RSP} & 2319 167
6.14 PMZ of the interfaces (a) 6061_{Rolled} & 2319 and (b) 6061_{RSP} & 2319 . . 167
6.15 Vertical hardness profile of as-deposited interface between 6061_{RSP} & 2319 and 6061_{Rolled} & 2319 168
6.16 SEM images of rupture surface of representative specimens of the (a) 6061_{Rolled} & 2319 and (b) 6061_{RSP} & 2319 combinations 169
6.17 (a) Tensile specimen microstructure after rupture, (b) maximum strain map, and (c) yield strength map of the interface 6061_{RSP} & 2319 170
6.18 Tensile specimen microstructure after rupture (a), maximum strain map (b), and yield strength map (c) of the interface 6061_{Rolled} & 2319 171
6.19 YS profile across the 6061_{RSP} & 2319 combination 171
6.20 cross-section of the as-deposited (a) 905 & 5556 and (b) 501 & 5556 interfaces 172
6.21 SEM images of the boundary between fusion zone and substrate of the (a) 501 & 5556 and (b) 905 & 5556 combinations 173
6.22 Vertical hardness profile of as-deposited interface between 501 & 5556 and 905 & 5556 174
6.23 Chemical composition profile across the 501 & 5556 interface 175
6.24 Interface 501 & 5556 :(a) tensile specimen microstructure after rupture, (b) maximum strain map, and (c) yield strength map 177
6.25 Ruptured tensile specimen illustrating the two different tensile properties measured during the test of the 501 & 5556 combination 178
6.26 (a) Tensile specimen microstructure after rupture at the boundary between the substrate and the FZ, (b) maximum strain map , and (c) yield strength map of the interface 905 & 5556 178
6.27 (a) Tensile specimen microstructure after rupture in the first deposited layer, (b) maximum strain map, and (c) yield strength map of the interface 905 & 5556 179

6.28 Fracture surface of representative specimen of the 501 & 5556 (a) and 905 & 5556 (b) combination 180
6.29 Effect of scandium content on grain size in the fusion zone of a 7000 series welded join [15] 184

7.1 Micro hardness profile across the inter-pass rolled 7449 &2319 interface . 190
7.2 Optical images of ruptured tensile specimen of the inter-pass rolled 7449 & 2319 combination 192
7.3 SEM image of the rupture surface of the inter-pass rolled 7449 & 2319 combination 192
7.4 Hardness profile of interface using 2050 alloy substrate 194
7.5 Optical image of a cross-section taken from inter-pass rolled 2050 & 2024 combination 196
7.6 Optical images of ruptured tensile specimen cross-section of the 2050 & 2319 and 2050 & 2024 inter-pass rolled combination 197
7.7 Photograph and SEM images of the rupture surface of the (a) 2050 & 2319 and (b) 2050 & 2024 combination 198
7.8 optical images of the PMZs before and after heat treatment of the combination 2219 & 2319 in pictures (a) and (b), 2024 & 2319 in pictures (c) and (d), and 2139 & 2319 in pictures (e) and (f) 199
7.9 Effect of heat treatment and inter-pass rolling on the hardness profile of the combination 2219 & 2319 201
7.10 Effect of heat treatment and inter-pass rolling on the hardness profile of the combination 2024 & 2024 202
7.11 Effect of heat treatment and inter-pass rolling on the hardness profile of graded interfaces. 204
7.12 Effect of heat treatment (a), inter-pass rolling (b) and heat treatment on inter-pass rolled material (c) on the rupture area of the interface 2219 & 2319207
7.13 Effect of (a) heat treatment, (b) inter-pass rolling, and (c) heat treatment on inter-pass rolled material on the rupture surface of the interface 2219 & 2319 207
7.14 Effect of heat treatment and inter-pass rolling on the rupture surface of the interface 2024&2024 209
7.15 Optical images of ruptured tensile specimen of the 2024 & 2024 combination in (a) inter-pass rolled and (b) inter-pass rolled and heat treated conditions 209
7.16 SEM images of the rupture surface of 2024 & 2024 combination in (a) inter-pass rolled and (b) inter-pass rolled and heat treated conditions . . . 210
7.17 Optical image the cross-section of an inter-pass rolled 2024 & 2319 ruptured tensile specimen 211
7.18 SEM image of the rupture surface of a tensile coupon representative of the inter-pass rolled 2024 & 2319 combination 211

7.19 cross-section of the interfaces between (a) 6061_{Rolled} & 2319 and (b) 6061_{RSP} & 2319 after heat treatment 212
7.20 Vertical hardness profile of the as-deposited interface between 6061_{RSP} & 2319 and 6061 & 2319 213
7.21 (a) Microstructure of a ruptured tensile specimen of the heat treated 6061_{rolled} & 2319 combination along with (b) the map of the maximum strain obtained during the tensile test, and (c) the evaluated yield stress map 215
7.22 (a) Microstructure of a ruptured tensile specimen of the heat treated 6061_{rolled} & 2319 combination along with (b) the map of the maximum strain obtained during the tensile test, and (c) the evaluated yield stress map 216
7.23 Fractopgraphs of (a) 6061_{rolled} & 2319 at low and (c) (d) at higher magnification, and (b) 6061_{RSP} & 2319 at low and (e) (f) at higher magnification216

8.1 Example of potential building strategies to manufacture the part shown in (a): (b) and (c) for the deposition on the substrate surface, and (d) and (e) for the deposition on the edge of the substrate. 235

List of Tables

2.1 Mechanical properties achieved by AM aluminium magnesium and silicon alloys . . . 38
2.2 Mechanical properties achieved by AM aluminium zinc alloys . . . 39
2.3 Mechanical properties achieved by AM aluminium copper alloys . . . 40

3.1 Deposition parameters used to manufacture the 2024 samples used in Chapter 4 . . . 58
3.2 Deposition parameters used to deposit the interface study samples . . . 59
3.3 Material composition defined by the aluminium alloys classification [16] and composition measurement for the 2024 alloy wire . . . 73

4.1 Characterisation of wall geometry . . . 80
4.2 Chemical composition of the wire and deposited material determined by EDS . . . 92
4.3 Micro hardness values . . . 93
4.4 Tensile test results for CMT-P-Adv process . . . 95
4.5 Tensile test results for CMT-P process . . . 97
4.6 Example of tensile properties achieved by 2024 wrought and WAAM products . . . 114

5.1 Experimental parameters used for the deposition of bead on plate and 3 layer high wall aluminium zinc structure . . . 125
5.2 Effect of wire feed speed on bead geometry . . . 130
5.3 Arc and laser heat input during the deposition of single aluminium zinc bead . . . 135
5.4 EDS measurements in wt% of different points and areas shown in Figure 5.18 (a) . . . 138

6.1 Mechanical properties of the as-deposited interface between various alloy combination . . . 164
6.2 Mechanical properties of the as-deposited interface between various alloy combination . . . 169

6.3 Mechanical properties of the as-deposited interface between various alloy combination 176

7.1 Mechanical properties of the inter-pass rolled interfaces integrating 7449 substrates 191
7.2 Mechanical properties of the inter-pass rolled interfaces integrating 7449 and 2050 substrates 195
7.3 Mechanical properties of the interface between various alloy combination, with inter-pass rolling or/and heat treatment 206
7.4 Mechanical properties of the interface between various alloy combination, with inter-pass rolling or/and heat treatment 208
7.5 Mechanical properties of the interface between various alloy combination, with inter-pass rolling or/and heat treatment 210
7.6 Mechanical properties of the interface between various alloy combination, with inter-pass rolling or/and heat treatment 214

Abstract

Integrating wrought alloys into a wire and arc additively manufactured component is very beneficial in order to reduce the duration and cost of deposition. However the microstructure and therefore mechanical properties of the wrought and deposited materials will be different. This thesis reports on a study of the properties of integral parts made of a combination of wrought alloy and material deposited by Wire and Additive Manufacture. The study was divided into two parts. Firstly, high strength aluminium alloys were additively manufactured and studied. Secondly, the interface between additive manufactured material and wrought alloys was examined.

Aluminium copper magnesium alloy was deposited by wire and arc, and its microstructure and mechanical properties were characterised using optical microscopy, scanning electron microscopy, and tensile tests in as-deposited, inter-pass rolled and heat treated conditions. In the as-deposited condition, the mechanical properties achieved were significantly lower than those of wrought material, with a yield strength up to 150 MPA lower than this achieved by heat treated wrought alloy. After heat treatment to the T6 temper, the inter-pass rolled WAAM material properties in the horizontal direction were similar to these of wrought products but with a high anisotropy.

An investigation into depositing aluminium zinc alloys using the novel process of laser-assisted wire and arc. The process was studied using a video camera and a device measuring the electric arc characteristics. Optical and scanning electron microscopy were

used to analyse the deposited material quality. The potential of the laser-assisted wire and arc process for deposition of zinc alloys was successfully demonstrated by depositing some three layer high structure in aluminium zinc with a very high zinc content.

To examine the properties of the interface between deposited and wrought material, a large number of alloys from different aluminium alloy families, were used as substrates and wires. The microstructures of the interfaces were characterised using optical and scanning electron microscopy. The mechanical properties were evaluated using micro hardness, tensile test and digital image correlation.

Combinations including aluminium lithium and aluminium zinc wrought alloys resulted in specific issues at the interface, such as porosity or hot cracking. However in general the interface did not have a detrimental effect on the interface yield strength which was the same as the yield of the deposited material. In the as-deposited condition, the maximum tensile properties were limited only by the deposited material or by the heat affected zone which depended on the substrate.

Heat treatment made possible the partial or total recovery of the properties in the heat affected zone in the substrate. The mechanical properties of the deposited material were also drastically improved, resulting in a heat treated interface with higher mechanical properties than in the as-deposited condition.

Inter-pass rolling reduced the level of porosity in the deposited material and could reduce the formation of cracks in between the first and second layer. However, the rolling of the first layer were an issue because of the proximity of the substrate and the resulting change in bead geometry. This can lead to lower mechanical properties in this area and could be detrimental to the properties of the interface.

This project was funded by Constellium Technology Center.

List of Abbreviations

AM	Additive Manufacturing
WAAM	Wire + Arc Additive Manufacturing
GP	guinier preston
LPBF	Laser Powder Bed Fusion
EPBF	Electron beam Powder Bed Fusion
PBF	Powder Bed Fusion
DED	Direct Energy Deposition
GMA	Gas Metal Arc
GTA	Gas Tungsten Arc
PTA	Plasma Transfer Arc
TS	Travel speed
WFS	Wire Feed Speed
SEM	Scanning Electron Microscope
UTS	Ultimatum Tensile Strength
YS	Yield Strength
AD	As-Deposited
IR	Inter-pass rolled
HT	Heat Treated
FZ	Fusion Zone

PMZ	Partially melted zone
HAZ	Heat Affected Zone
CMT	Cold Metal Transfer
CMT-P	Cold Metal Transfer - Pulse
Adv	Advanced
ESEM	Environmental scanning electron microscope
EDS	Energy Dispersive X-Ray Spectroscopy
DIC	Digital Image Correlation
HI	Heat Input

Acknowledgements

First, I would like to thank my two supervisors, Stewart Williams and Jialuo Ding for their support and guidance along these years of research. Stewart, thank you so much for giving me enough space to take my own decisions and make my own mistakes while making sure I keep my objectives in mind and stay on the right path. Jialuo, thanks a lot for your help in the lab, your technical support and cheerfulness all along this project. Thanks a lot to you two for reviewing my written work and helping me to improve!

I would like to also thank my subject advisor, Supriyo Ganguly, for his support on all metallurgical aspects of my work. Thank you for your enthusiasm and detailed comments on every piece of work you have reviewed for me.

I would also like to thank Adrian Addison, without whom this journey may not have started. Adrian, just before leaving Cranfield University, you took the time of registering me as a student. Thank you for encouraging me to start this PhD.

I am very grateful to all the technical staff who helped me during my experimental work: Flemming, Nisar, and Jonathan your help and good moods were priceless and it was a pleasure to work with you. Steve, Tracey, Jarryd, Christine, and Xianwei: your help was precious to me, and I felt blessed to receive constant advice and suggestions from you all. Steve and Tracey, thank you for making metalb work an enjoyable time !

This project could not have been possible without the financial and technical support of Constellium Technology Center. I would like to thanks Bechir Chehab and Ravi Sha-

hani who supported this research project as well as Vincent Duhoux, Annabelle Bigot, the modelling team in Voreppe, and the extrusion shop team in Issoire, who gave me the chance to learn so many things during my first year of work experience. Without this short journey at Constellium, I would have never got the opportunity of doing a PhD in Cranfield University.

I want to thank my friends: Guilhem (who drove from Luxembourg for an English breakfast, life would not be the same without you jumeau!), Camille, Benoit, Charlie, PEB, Pierre, Sofien, JB, Geoffrey, Florient, Alain, Aline and Marine; thanks a lot for being here for me despite the distance. Thanks to my new friends whom I met in Cranfield playing handball (Alejandro, Campoos, Lucille, Meike, and Emmanouela), to my previous housemates Jamie and Pepe, and to Olivier, for feeding me so well with food from back home.

Thanks a lot to the WELPC family, it was a fantastic experience and a lot of fun to work with such a diverse and brilliant team. Sergio and Lucia, thank you so much for your kindness; Clement, I missed my gym partner a lot during the last year of my PhD !! Sonia, Goncalo, Florent, Marjorie, Jan, Deborah, Daniel, Leonor, Wojciech, Anthony, Gianrocco, Kwasi, Xiangfang, Julio, Zsolt, Filo, and Pawel, I had great fun during and after work with you all, thanks for making this PhD journey everything but a lonely road. Many thanks to all the others for being such great co-workers.

I am grateful to my family who supported me at all time: special thanks to Mathieu, Christine, Francis, Fabienne, Isabelle, Alain, Martine, Jean-Luc and Francoise who were there for me during my PhD, but also, and most importantly, who were there during rough times in the past. I would like to thank my parents, for their love and respect. Life is full of opportunities and it is thanks to them that I can see and go for them.

Junny, thank you for your support, especially during the long writing period... Thank you so much for putting up with my gloominess and believing in me at all time. I am sure

this would have been more challenging without you by my side. It will be soon your turn to write your own PhD thesis and I am sure you will be a great doctor sooner than you realise. I will do my best to love you and support you as much as you cared for me.

Finally, I want to express my gratitude to my country. After meeting so many people from different origins, I can appreciate to what extent I was lucky to grow and learn so much from amazing teachers in France in state schools and university. I will always feel indebted to the French educational system for this.

A mes grand-parents,

Monique & Emile Claudepierre

et Jeanine & Michel Eimer

Chapter 1

Introduction

1.1 Context and research gap

Additive Manufacturing (AM) development has been on the rise in the past decades because of its advantages compared with subtractive and more conventional manufacturing methods: AM consist in adding material to produce a component, while subtractive methods consist in using a large block of material and machining off part of it to create a component. Wire + Arc Additive Manufacture (WAAM) is an AM process using a wire as the feed material and an electric arc as the heat source to deposit large scale 3-dimensional components. WAAM benefits from a large reduction of material wastage and lead-time compared to subtractive processes. Contrary to powder-based processes, WAAM does not deal with the issues generated by powder use, such as powder manufacture, quality, transportation, manipulation and recycling. WAAM does not require vacuum or a controlled atmosphere and can reach high deposition rates up to a few kilograms per hour. Therefore, WAAM has the potential of building very large-scale components. The largest additive manufactured component ever built, a 6-meter long aluminium spar was carried by the research team at Cranfield University in Figure 1.1 demonstrate this potential.



Figure 1.1: Research team of the Welding Engineering and Laser Processing Centre carrying the largest additively manufactured metallic part

Figure 1.2 shows the different stages of the building of this aluminium spar: the first bead is deposited on a substrate, as illustrated by picture (a) and (b). Then the next layers are deposited to gradually build a 3-dimensional structure, as shown in (c). Picture (d) shows the final deposited feature. All parts require a substrate to start their build.

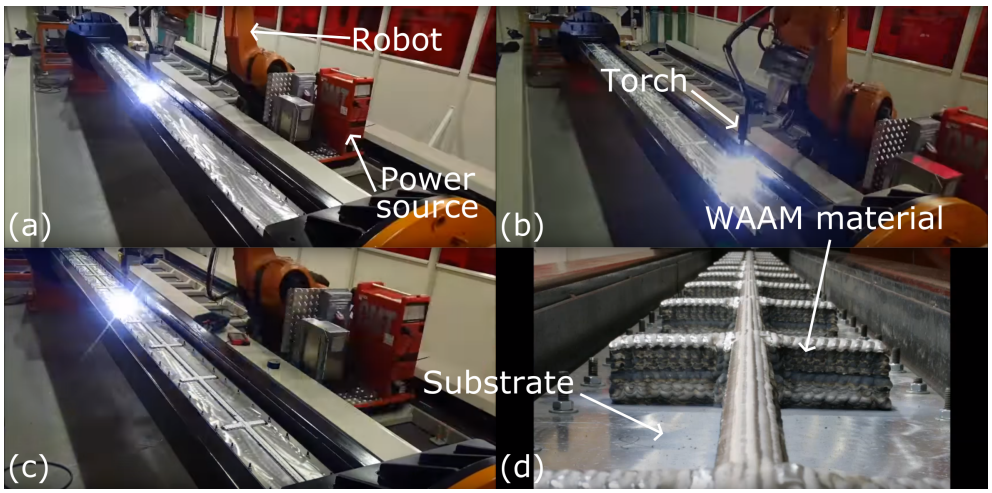


Figure 1.2: Manufacturing step of an aluminium spar: deposition of the very first layer (a), followed by the next layers in (b) and (c), and a close view of the final part in (d)

Two building strategies can be adopted: the substrate can be removed from the final part at the end of the manufacture, or the substrate can be kept and integrated into the final design. Keeping the substrate has excellent advantages: it reduces the amount of

wasted material, it can decrease the deposition time and filler wire consumption, and it could permit taking advantage of high and well-known mechanical properties of wrought products. Many part designs have been developed with the idea of integrating the substrate in the final component. That is the case of the aluminium spar, shown in Figure 1.1 and 1.2. This component is a perfect example of designs where the substrate is part of the final component.

Also, it is important to highlight that different mechanical properties can be required in different component areas: a very simple illustration is given in Figure 1.3. The anti-bulking parts, in red, need to be made of a stiff material, and the blue parts need to be resistant to crack propagation. The mechanical properties of the central part of the component, in grey, are determined by the working load and design requirement. The subtractive method of building such a component is to manufacture a large block of material and then machine it. In this case, only one material is used to manufacture the whole part, and this material needs to fulfil all the requirements listed above. As it is difficult to obtain such a wide range of properties with only one alloy, the component is often bulkier than it could be using an adapted alloy combination. Nonetheless, using WAAM could decrease the amount of wasted material, but also it could make possible the deposition of a multi-graded alloy by depositing one or two different alloys on a substrate made of another alloy itself. For instance, to manufacture the component in Figure 1.3, two alloys could be deposited on a substrate made of a third alloy, using one alloy for each coloured area. This strategy would allow the use of suitable alloys, overall higher mechanical properties, and lighter design.

Evidently, the interface between the substrate and WAAM deposited material is critical to produce a reliable and high mechanical properties component. Most of the wrought alloys used in aerospace, our industrial sector of interest, achieve very high strengths and damage tolerance. In order to make relevant the combination of wrought and WAAM

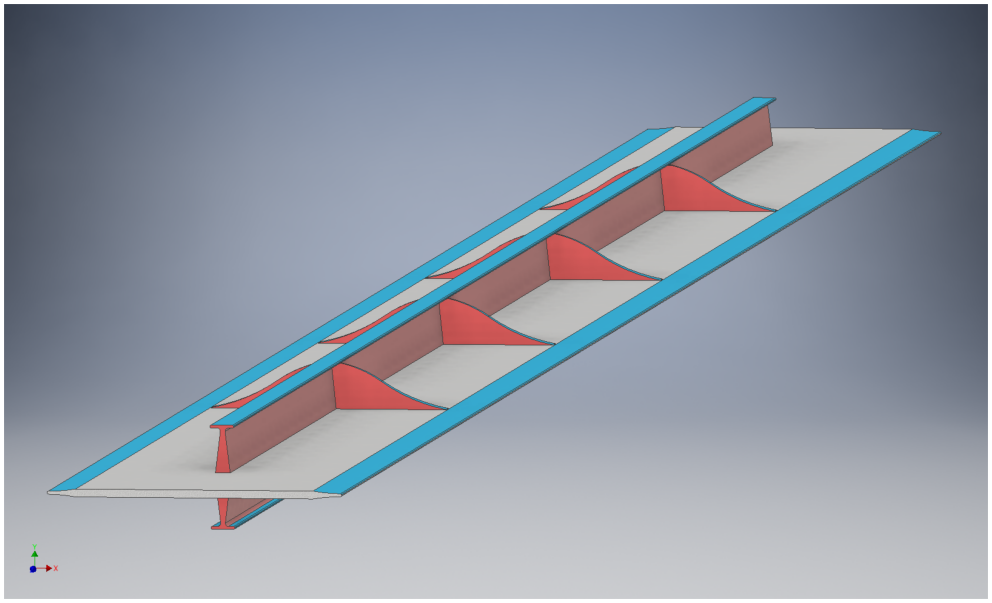


Figure 1.3: Simplified wing component

material, the need to reach a property level close to wrought and conventional alloys. Thus, to integrate the substrate to a final WAAM component, two main requirements must be considered: the properties of the WAAM material need to be comparable to those of wrought products, and the interface between the substrate and deposited material should not be detrimental to the component performances.

Numerous studies have been carried out on the WAAM deposition of aluminium, but so far two main alloy families widely used in aerospace have been partially left aside. First, aluminium copper magnesium alloys well-known for their high strength and very high damage tolerance, have been investigated and proven suitable for WAAM. However, their properties have not been fully characterised. Second, aluminium zinc alloys are broadly considered inappropriate for WAAM, and even for AM in general: their solidification behaviour is favourable to defect formation and their zinc content leads to porosity excess and is prone to depletion. Nonetheless, the very high strength achieved by wrought aluminium zinc alloys makes these worthy of consideration for WAAM development.

No study has been reported on the interface between the substrate and WAAM deposited material. Nevertheless, a very wide range of investigation has been carried out on fusion welding of aluminium, including the effect of alloys, process, and post joining procedure. As the interface between the substrate and WAAM material, and between the parent metal and weld bead are similar, the literature on fusion welding can be used, as a base, in the study of the interface between the substrate and WAAM material. However, it is imperative to investigate the microstructure and mechanical properties of the interface between the substrate and WAAM material because of the potential differences between welding and AM, such as residual stress, geometry, and process parameters.

1.2 Aim and objectives

The aim of this research project is to investigate the possibility to produce integral high strength aluminium alloy components incorporating wrought material using Wire + Arc Additive Manufacture.

The objectives are the following:

- Establish the property level achievable by WAAM for aluminium copper magnesium alloys, including cold work and heat treatment.
- Assess the potential and issues in depositing aluminium zinc alloys.
- Evaluate the properties of the interface between a wrought substrate and the deposited WAAM material for a range of alloy combinations.
- Investigate whether these properties at the interface can be influenced through the use of cold work and/or heat treatment.

1.3 Thesis structure

Chapter 2 gives a critical review of the literature underpinning this research project. The literature review is divided into three sections: aluminium alloys, additive manufacturing, and fusion welding. The first section provides a presentation of aluminium alloy applications and some metallurgy basis. The second section introduces AM technologies, with a more detailed presentation of the WAAM process as well as a review of challenges and mechanical properties of aluminium AM. Finally, the section on fusion welding is divided into two parts. The first one introduces the welding metallurgy of aluminium alloys, largely used as a base for the study of the interface between the substrate and deposited material. The second part, on laser – assisted welding is focused on the process. Chapter 3 gathers the methodology used for the different conducted experiments. Set up descriptions, material composition, process parameters, and material characterisation procedure are described in this Chapter.

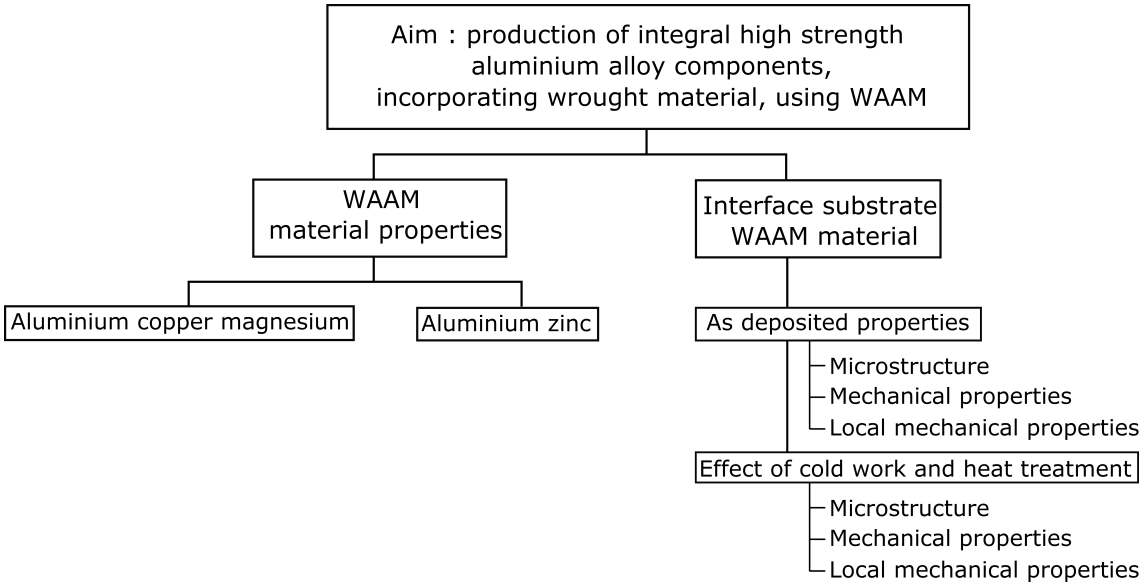


Figure 1.4: Research strategy

The structure of the core Chapters, 4, 5, 6, and 7, is based the research strategy illustrated in Figure 1.4. Each of them contains an introduction, methodology, results, discussion, and conclusion section. As most of the methodology is introduced in Chapter 3, only specific procedures and details are provided in each core Chapter. Chapter 4 deals with the characterisation of the mechanical properties of 2024 alloy deposited by WAAM, and how these are affected by process parameters and post – deposition heat treatment. Chapter 5 looks into the potentials and issues in depositing aluminium zinc alloys by WAAM. Chapter 6 and 7 are focused on the study of the interface between the substrate and deposited material: Chapter 6 gives an overview of the as – deposited mechanical properties achievable at the interface for a wide range of alloy combinations. Then, Chapter 7 investigates the effect of inter-pass cold work and post – deposition heat treatment on the microstructure and mechanical properties of the interface.

All four conclusions are brought together and discussed in Chapter 8. In this discussion Chapter, the findings are considered in respect of the aim and objectives provided in section 1.2. Finally, Chapter 9 gives the conclusions and suggestions for future work.

Chapter 2

Literature review

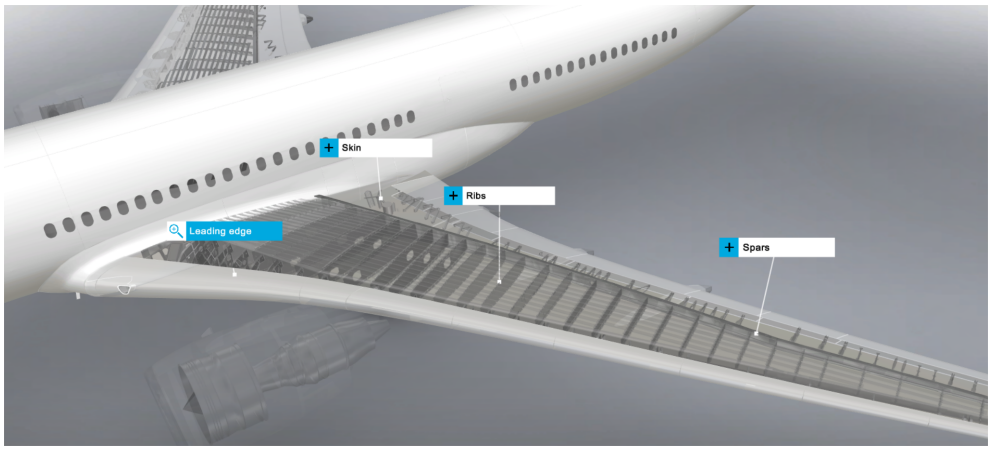
2.1 Aluminium alloys

2.1.1 Applications

Aluminium alloys are widely used in various industrial sectors such as automotive, transport, packaging and aerospace. Choosing a material is a crucial step in any new design development, especially in the aerospace sector: all the material properties are evaluated against their density as the ultimate goal is to reduce the weight of the components, without compromising their properties and integrity. Aluminium alloys have been used in the primary structure of aircraft for over 80 years due to their high strength to density ratio [17, 18, 19, 20, 21, 22]. An exploded view of the aluminium components in an aircraft is given in Figure 2.1a [23]. Recently, composite materials have been used more and more, but the impact resistance, damage identification, repair, joints and recycling of these materials remain great challenges and give aluminium alloys many more years of use before composites can replace them [20].



(a) Aircraft exploded view



(b) Outer wing diagram

Figure 2.1: Diagram of the aluminium part used in aircraft

Starke et al. [17] published a review of the aluminium alloys used in aircraft manufacturing: even though this paper is relatively old (1996) for a field where new alloys are patented every year, the detailed list of the properties required in the different parts of the aircraft is still very much topical. For instance, the structure of the wing includes top and bottom covers (made of skin and stringers), spars and ribs as shown in Figure 2.1b. The top cover is mostly in compression during flight and in tension during taxeing, with the opposite for the lower cover: therefore, the aluminium alloys used to manufacture the component of these two covers are different. Ideally, the components which connect the top and bottom covers should have graded functional properties between the two covers

properties on each of their end [17]. This is not possible to achieve with current manufacturing technologies, and results in bulky spars and ribs of homogeneous mechanical properties. The possibility of producing functionality graded components, using AM, for the aircraft manufacturing industry could radically change these designs obstacles and offer new disruptive solutions.

2.1.2 Metallurgy of high strength aluminium alloys

Several methods can be used to increase the strength of aluminium alloys

- Solid-solution hardening
- Grain-size strengthening
- Work or strain hardening
- Precipitation hardening

Solid Solution

Solid solution hardening is due to the presence of other elemental atoms solutionised in the matrix and the lattice distortions they generate slow down the movement of dislocations. The size of the distortion generated and the number of solutionised atoms depends on the size of the atoms and their solubility in the parent lattice. Only copper and magnesium can have a significant effect on aluminium strength once solutionised in the matrix [24].

Grain size strengthening

The Hall-Petch equation describes grain size strengthening :

$$\sigma_y = \sigma_0 + \frac{k}{\sqrt{d}} \tag{2.1}$$

with σ_y the yield stress, σ_0 the frictional stress of the alloy, k a constant characterising how difficult it is for slips to go across a grain boundary in this alloy, and d the average grain size [24]. For aluminium alloys, the value of the coefficient k is relatively low compared to ferrous alloys: so grain-size strengthening is not very strong for aluminium alloys, except when it comes to very small grain size.

Solid solution is the primary methods used to increase the strength of aluminium magnesium alloys but these alloys are not the one achieving the highest properties of all aluminium alloys. Aluminium alloys are divided into two main families: the precipitation hardened and strain hardened alloys [24]. Precipitation hardening achieves the highest mechanical properties [25] of all aluminium alloys and is, therefore, the focus of the experimental work detailed in the next Chapters. A large part of the following section deals with precipitation hardening alloys, but a small sub-section introduced strain hardening alloys: these are of interest for AM applications as they do not require a post deposition heat treatment.

2.1.2.1 Precipitation hardening

Aluminium copper, aluminium zinc and aluminium silicon magnesium alloys, designated as 2000, 7000 and 6000 series, are the precipitation hardening alloys. They can be binary or tertiary alloys, but their strength is based on the same phenomena. Al-6.3Cu alloy is often used to illustrate precipitation hardening because of its simple phase diagram. As it is also weldable by fusion, used in the space industry and compatible with WAAM, it is

the best example to use here.

Principle

The strength of a precipitation hardening material lies in small and homogeneously distributed precipitates which prevents dislocation movements. In most cases, it is required to carry out heat treatment after the shaping process and before machining, to activate these precipitates.

The precipitates are generated from a super-saturated solution at room or a higher temperature - usually from 150 to 250°C; they can be found in different forms [26]. Figure 2.2 (a) shows the phase diagram of the AlCu system with the metastable solvus curves for Guinier-Preston (GP) zones, θ" and θ' phases [26], (b) the effect of these phases on the material strength and (c) the intersection between the aluminium lattice structure and these phases [26].

- The first structures to form are the GP zones; they are disk-shaped monolayers of copper. These disks, lying on the faces of the face-centred cubic aluminium unit cell are less than 15 nm in diameter and are coherent with the aluminium matrix [27]. They do not have any significant effect on the material properties but are required to enable the formation of the next phases, which are beneficial for the material properties.

- θ" form from the GP zones. They are similar to the GP zone in shape but have a larger diameter (up to 50 nm) and thickness. These phases are semi-coherent (see Figure 2.2 (c)) with the aluminium matrix. θ" are the phases providing the highest strength to the material [27].

- θ' are semi-coherent with the aluminium matrix and much larger than the GP zones and θ" phases: they can reach a 100 to 1000 nm diameter and a 15 nm thickness

[27]. These phases are not beneficial for the material properties, and can even be detrimental to its resistance toward crack propagation. They are not related to GP or θ", and can nucleate heterogeneously and on dislocations [26].

- The stable version of all these phases are the θ phases, Al_2Cu in the aluminium copper system. These phases can be very large and are incoherent with the matrix.

When the material undergoes one or several thermal cycles, these precipitates, especially GP zone and θ" can disappear: this is called reversion [27]. The precipitation hardening of aluminium copper magnesium alloys is very similar: the precipitates grow from GP to S" and S'(semi coherent Al_2CuMg phase precursor) and S (Al_2CuMg) phases nucleate heterogeneously [28, 26].

In order to generate a homogeneously distributed network of precipitates, it is required to start with a supersaturated solution.

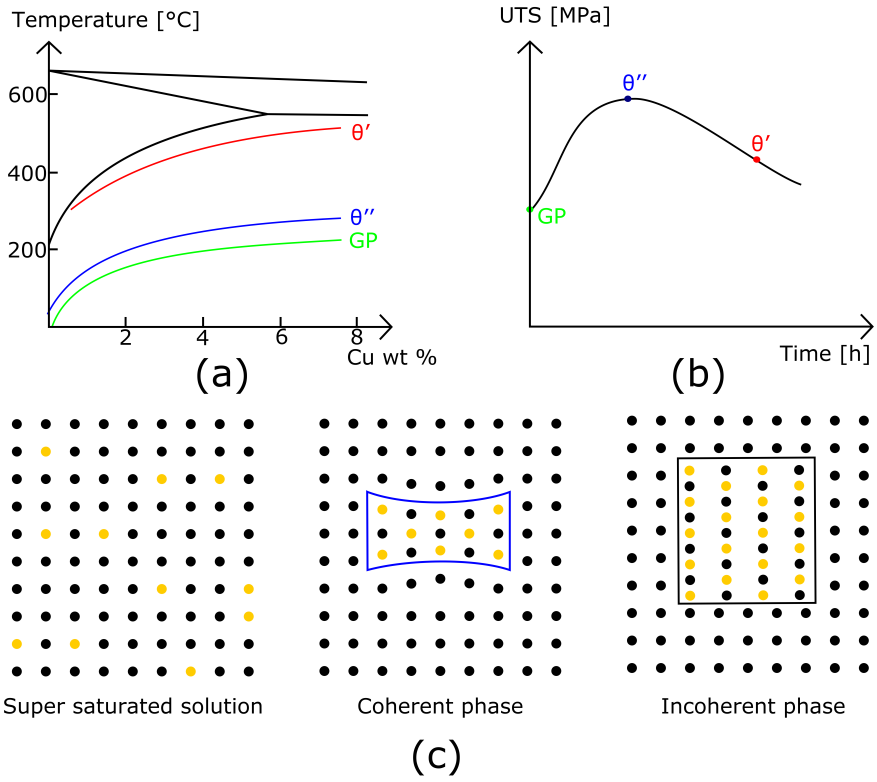


Figure 2.2: Principle of precipitation hardening: Phase diagram (a), Strength evolution curve (b) and diagram of crystal structure (c)

Solidification

During the solidification of the Al-6.3Cu alloy, the compositions of the solid and the liquid are not constant because the copper solubility in the liquid is higher than in the solid as shown in the phase diagram in Figure 2.2 (a). If the solidification rate is low, the liquid is enriched in copper, resulting in copper rich area in the solidified material. If the solidification rate is high enough, this copper segregation in the liquid does not have time to occur, and the solidified material is homogeneous in copper content.

Heat treatment

During most alloying processes, the solidification rate is too low and segregation occurs. The precipitates are too large and incoherent with the matrix (θ phases), not homoge-

neously distributed, and they do not have any beneficial effect on the material because of this copper segregation,. In order to generate small and homogeneously distributed precipitates, heat treatment needs to be carried out. This is commonly done after the shaping process of the part but before machining.

Heat treatments can include four steps: solution treatment, quench, cold work and ageing [24].

- The solution treatment consists in soaking the material at a high temperature, just below the eutectic point, which is 542°C for Al-6.3Cu. At this temperature, the alloying element diffusivity is higher than at room temperature, and this enables a homogenisation of the material. When the material is homogeneous, it is called a supersaturated solid solution.

- This solid solution is not thermodynamically stable at room temperature: in order to freeze this homogeneous material, it needs to be quenched. By quickly cooling the solid solution, it is possible to produce a homogeneous super saturated solution at room temperature.

- After the quench, it is common to apply cold work to the part in wrought alloy semi-finished product production. Firstly, cold work induces dislocations in the material, and these can lead to a more homogeneously distributed network of small precipitates. Secondly, this cold work process can help to reduce the residual stresses and distortions generated during the quench. It is interesting to note here that this cold work step cannot be easily carried out on complex shaped components.

- The last step is ageing, which can be natural at room temperature, or artificial at temperatures below 200°C. The role of this step is to promote the growth of precipitates.

Heat treatment procedures classified as tempers, include solution treatment and quench. Cold work is not always carried out, and the ageing can be done naturally or artificially depending on the targeted properties: the procedure can be different in order to achieve an intricate balance between strength, fatigue and corrosion properties [24].

Manufacturing steps: conventional versus AM

The manufacture of wrought products can be divided into five steps:

- Shaping process: this can be done by rolling or extrusion for instance. Usually the geometry obtained after this stage is simpler and bulkier than the final component shape. This is done to avoid the multiplication of semi-finished product shapes and shape tooling (extrusion die for instance).
- Solution treatment
- Cold work: this is usually done by traction
- Ageing. After ageing, the component is a semi-finished product.
- Machining: the shape of semi-finished product are usually very simple and extensive machining is required to achieve the final component shape. In aerospace, it is not unusual to remove up to 90 % of the semi-finished product mass to produce the final component shape [29].

To produce a part with a near net shape AM process, such as WAAM, the steps need to be adapted:

- Deposition of the material: contrary to conventional manufacturing process, the geometry of the part produce at the stage would be very close to the shape of the final component. The step of manufacture could also include some cold or hot work.

- Solution treatment
- Cold work: it would be difficult to apply cold work to a complex near net shape component. This step is not practical and alternatives should be developed to avoid it.
- Ageing
- Machining: very little material should be machined in order to reduce the manufacturing cost as much as possible [30].

The issue of precipitation hardening material is the requirement for heat treatment after the deposition. Firstly, it would be difficult to heat treat, especially quench, a complex component and obtained homogeneous mechanical properties. Also, the distortions and residual stresses generated during the quench of the near-net shape component could be detrimental to the final machining step. Finally, as stated above, some alloys require cold work in between the solution treatment and ageing. It would be difficult to generate plastic deformation in a complex part. This is why strain hardening alloys are of interest for AM applications: they do not need heat treatment, and cold work could be applied to them in situ using an inter layer cold work process.

2.1.3 Strain hardening alloys

Pure aluminium (1000), aluminium manganese (3000), aluminium magnesium (5000) and aluminium iron and silicon (8000) are the four strain hardening alloy families. The 5000 alloys are the one with the highest magnesium content, and they can reach the highest mechanical properties among these four series.

Strain hardening consists in changing the material structure by plastic deformation in order to increase both Yield Strength (YS) and Ultimate Tensile Strength (UTS), often

at the expense of the material ductility. During plastic deformation, a large quantity of energy is lost in heat, but some is stored in the material as dislocations [31]: this leads to an increase of mechanical properties.

If the material is overworked it can become very fragile. Heat treatment can be carried out to recover part of the ductility lost during the strain hardening. At high temperature, the aluminium structure is rearranged first with reduction and rearrangement of dislocations: this is the recovery. In a second heat treatment step called annealing, the grain size drastically increases and the deformation texture can be erased [24, 31, 32].

2.2 Additive manufacturing

2.2.1 Principle

AM consists in depositing material layer by layer to build a 3D component. For several decades, the development of AM processes has been increasing because of their numerous advantages compared to conventional manufacturing processes: the use of AM can drastically decrease material wastage and lead times while allowing more complex shape design [1, 33, 34, 35]. AM processes allow the manufacture of customisable parts without the need for expensive tooling: this leads to the possibility of manufacturing unique, or small series of parts, quickly and at low cost. This is why AM is widely used in medical applications and prototyping, as these two sectors require a very high customisation level and low lead times: Figure 2.3 shows an example of titanium implants made with AM. Nowadays, AM applications are becoming more extensive with the production of end-parts for various industrial fields such as aerospace [34, 35, 36, 37], rail [38], shipbuilding [39], and energy [40]. AM processes can be divided into different families, according to their heat source and raw material [41].



Figure 2.3: AM Titanium implants for the skull (left) and pelvis (right) manufactured by Direct Metal Laser Sintering [1]

2.2.1.1 Powder-based processes

The majority of commercialised AM machines are based on the use of powder as raw material [42], and the vast majority of the research on AM is focused on these processes. These processes can be divided into two main families: Firstly, where the powder is pre-placed, powder bed fusion, using either a laser (LPBF) or electron beam (EPBF) as the energy source; Secondly, where the powder is directed towards the moving energy source, are categorised as Direct Energy Deposition (DED) [41]. Regardless of what family a process belongs to, any heat sources such as laser beam, electron beam, or plasma arc can be used.

Powder-based processes benefits lie in allowing very complex shapes to be produced and the new design possibilities they offer [1]. However, this building accuracy is at the expense of the building rate, reaching a maximum of 300 mm^3/h for DED [43], and 150 cm^3/h for Powder Bed Fusion (PBF) using multiple lasers [44]. Also, as powder needs to be used in an un-contaminated closed atmosphere, these processes are conducted in a controlled working environment. Therefore, the maximum component size achievable by PBF, at the moment, is less than 400 by 400 by 400 mm^3 and can reach 900 by 1500 by 900 mm^3 with powder DED [45].

Another problem related to the use of powder is the amount of powder required to build a part. In PBF processes, the whole bed needs to be filled with powder regardless of the size of the component. In powder DED, the deposition efficiency is relatively low. The deposition efficiency is the ratio between the weight of the final port over the total weight of powder used to build this components[46]. For instance, a deposition efficiency of 14% have been reported by Unocic et al. for Laser Engineered Net Shaping Process [47]. Usually, the deposition efficiency varies from 10 to 90% [29]. The powder can be recycled after being used but it needs to be sifted to avoid contamination [47], and this can be a difficult step to handle safely. This combined with the high powder cost compared to wire cost [48] makes the use of powder as raw material for building large 3-dimensional part expensive. Therefore, powder-based processes are suitable to build small and complex net shape parts, but they cannot be used to build large components.

2.2.1.2 Wire-based processes

Wire-based AM is based on DED processes; they use various heat sources such as a laser, electron beam, and electric arc. The use of wire instead of powder overcomes most of the issues mentioned in the section 2.2.1.1. The cost of metallic wire is considerably lower than powder and wire is much easier and safer to use and stock. In order to build large component at an attractive cost, a sufficient building rate needs to be achieved: according to Sciaky INC, a machine manufacturer, it is possible to deposit more than 10 kg/h using these technologies [45].

Another critical factor limiting the maximum part size reachable is the size of the workspace. The use of an electron beam as heat source requires a vacuum chamber: the size of this chamber limits the final component size. When using a laser beam or an electric arc as the heat source, it is possible to build very large scale component as neither

an inert atmosphere nor vacuum is required to deposit the material.

2.2.2 Wire + Arc Additive Manufacturing

2.2.2.1 Principle

Wire + Arc Additive Manufacturing is a DED process that uses an electric arc as the heat source and wire as raw material; it has the potential to build very large scale near-net-shape components [33]. Figure 2.4 shows a photograph taken during the tungsten gas arc deposition deposition of titanium and illustrates how the process works [2]. WAAM was first patented in 1925 [49] as a process intended to build ornamental items. Nowadays, this process is developed in order to manufacture end parts for diverse industrial applications. To build a component, a manipulator, a power source, and equipment such as torch and wire feeder, and a wire are required.

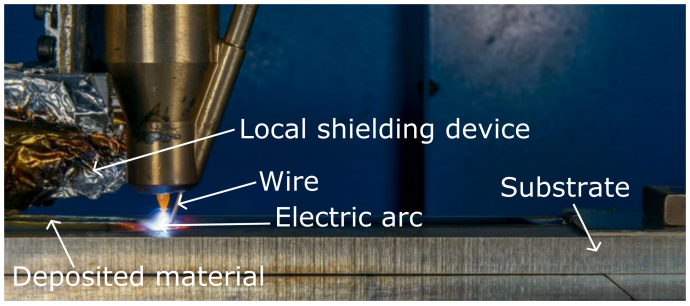


Figure 2.4: Tungsten gas arc deposition of titanium [2]

2.2.2.2 Large parts manufacture

The possibility of building very large scale part relies on a high deposition rate and the size of the working area: it is possible to deposit up to 4 kg/h of Steel with WAAM, and even 10kg/h is achievable, but at the expense of the building precision [33]. Most materials do not require an extensive shielding and the local shielding provided by the

torch is enough for specific materials such as Aluminium [12, 50], and for more reactive materials, local shielding, especially designed for WAAM can be used [51]. Therefore, the final part dimensions are limited only by the manipulator movement.

WAAM process is not suitable for building very complex and small-scale shapes. However, the use of WAAM can be very beneficial to build near-net-shape large parts which are currently made by subtractive methods. Nowadays, to build a large component, a cast, extruded or rolled product of basic geometry is machined down to the final geometry: this generates a large amount of scrap which, even if it can be recycled increases the total production cost. The buy-to-fly ratio is the ratio between the final part mass to the total material mass used to manufacture it. It is often used to quantify the material waste generated during the manufacturing process. In subtractive manufacturing, it reaches values of 10 to 20 easily [29]. WAAM has the possibility of manufacturing these same parts, but with a buy-to-fly ratio closer to 1. Figure 2.5 shows a part deposited with WAAM: currently machined from solid, the buy-to-fly ratio of this part is 12, and it could be reduced to 2.3 using WAAM [2].

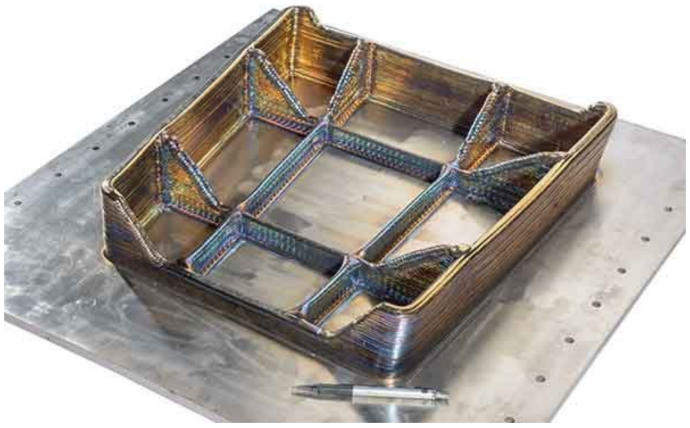


Figure 2.5: Example of titanium near-net-shape WAAM part [2]

2.2.2.3 Material and processes

A wide range of material can be deposited with WAAM, including titanium [46, 52, 53], Inconel [54], steel [39, 55], copper [56], magnesium [57], and various aluminium alloys [11, 14, 58, 59, 60]. Different heat sources can be used: Gas Metal Arc (GMA) is often preferred because the wire is coaxial to the torch in this process, and it facilitates the tool path planning [33]. Numerous studies in the literature focus on the development of GMA based processes [12, 50, 61, 62] or are based on the use of GMA processes [5, 11, 63, 64, 65, 66]. Gas Tungsten Arc (GTA) [52, 59, 67, 68] and Plasma Transferred Arc (PTA) [46, 55, 64] can also be used.

WAAM is a process easy to work on because a whole set up can be made of Commercial Off The Shelf equipment such as arc power sources, wire feed units, and manipulator such as robots. Some studies focus on the capability of the WAAM process without using any hardware or software upgrade [66], but numerous research projects, detailed in the literature alo focus on the in-depth development of niche process components. For instance, a local shielding device has been developed at Cranfield University in order to deposit highly reactive material such as titanium [51] without working in a controlled atmosphere enclosure.

When depositing with an electric arc synergic power source, the arc current and voltage polarities are very often pre-determined by the power source manufacturer. Many different working modes are available [12], but it is not easy to modify them extensively because of the interdependence between Travel Speed (TS), Wire Feed Speed (WFS), and the different waveform phases [69]. This is why recent studies were conducted on the development of waveform specifically for WAAM [64, 68].

2.2.2.4 Residual stresses

Residual stresses and distortion are commons issues in AM due to the numerous thermal cycles the material undergoes. Inter-pass rolling can be used to limit both residual stresses and distortion during titanium [70, 71], steel [72] and aluminium [73] deposition. Not only does inter-pass rolling reduce residual stresses and distortion, but it also improves the microstructure and the mechanical properties of titanium [74] and aluminium [5, 11, 14] deposited material.

2.2.2.5 Design strategies

The development of a process like WAAM benefits from other fields, such as process modelling [75] tool path software [76] and new design strategies [3] are also investigated. Regarding design strategies, WAAM allows the possibility of producing mixed part made of wrought and WAAM deposited alloy. Lockett et al. [3] introduced a procedure to determine when it is relevant to use WAAM to manufacture a component and what can and cannot be done in term of part design using this process. In their paper, the authors evaluate different building strategy for some components. One of the example they used is details in this section. Figure 2.6 (a) shows the drawing of the component, and Figure 2.6 (b), (c), (d), and (e) propose different building strategies to manufacture this component. In these 4 diagrams, the dark grey colour is used for the WAAM deposited material and the substrate is coloured in light blue. The authors determined that the option in picture (e) is the best one due to the low deposited material mass, the low waste material from the substrate, the good symmetry and the small number of build operations compared with the other options [3]. All building strategies, apart from the one shown in Figure 2.6 (c), include the substrate in the final component, showing the importance of the properties of the interface between the substrate and WAAM material.

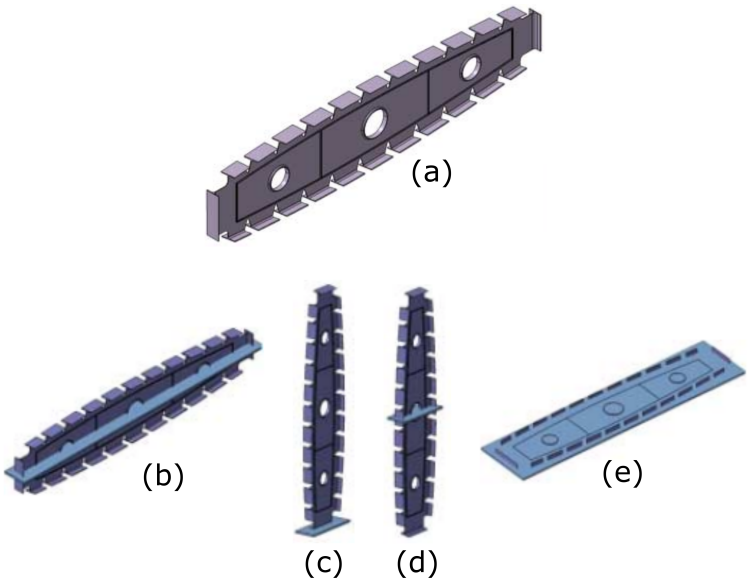


Figure 2.6: Example of a wing rib building strategies detailed by Locket et al. [3]: picture (a) shows the wing rib diagram and the building strategies which could be used to manufacture it are shown in pictures (b), (c), (d), and (e)

However, if this building strategy makes perfect sense in a design and manufacturing process point of view, further investigation would need to be carried out on the final properties of a component of this type, especially at the interface between the substrate and the WAAM material. So far, only a few data have been published on the matter: Zhang et al. studied crack propagation in samples made of wrought and WAAM Ti6Al4V [77]. The authors show that the cracks most often propagate in the substrate, as this has a higher crack growth rate than the WAAM material. However, it needs to be highlighted that residual stresses, local microstructure and load direction have a great effect on crack growth and could impact significantly on the fatigue properties of a graded component. Also, Akuno shows the possibility of depositing an aluminium copper on an aluminium zinc substrate [78]. This material design freedom has not been thoroughly investigated yet.

2.2.3 Aluminium alloys in AM

Aluminium alloys are widely used in aerospace because of their high strength to density ratio, and this is one reason among others why many research projects have been carried out on the use of AM with aluminium alloys.

This section gives an overview of the challenges that AM has to tackle to produce aluminium parts and the current mechanical properties achieved in aluminium AM.

2.2.3.1 Porosity

A widespread issue in fusion welding of aluminium is porosity: this issue is also a major problem in AM. Hydrogen solubility in aluminium is much higher at liquid (0.69 cm^3/100g) than solid state (0.036 cm^3/100g) [79]. At liquid state, hydrogen from the atmosphere and wire and substrate surface contamination is dissolved into the melt pool. During solidification, the solubility of hydrogen drops and gas pores are formed: as aluminium solidify very quickly, most of these pores are trapped in the material. These pores are called gas or bulk pores. Another type of porosity can also be found: during solidification shrinkage, gas can be entrapped between dendrite arms. These pores are called interdendritic pores [80, p. 260].

Powder-based processes

Porosity in Powder Bed Fusion (PBF) is part of the broader problem of low-density material. For instance, Aboulkhair et al. studied the effect of process parameters on the porosity of AlSi10Mg parts and showed that porosity is drastically affected by parameters such as the scanning speed, the overlap between parallel layers and the laser power [4], as illustrated by Figure 2.7. Figures 2.8 illustrate the effect of the distance between passes on density and the scanning speed on the porosity level.

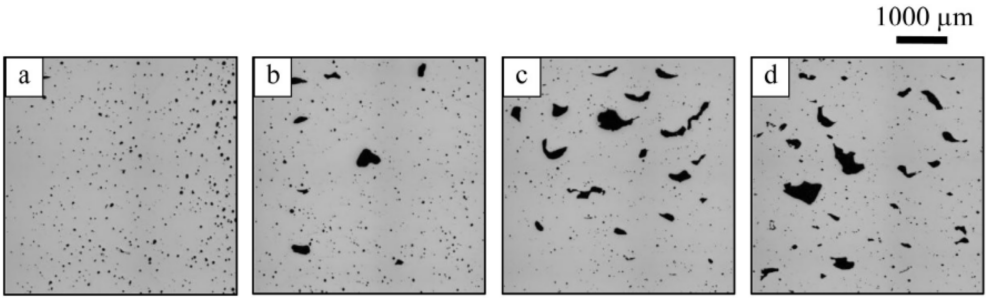


Figure 2.7: Illustration of the effect of scanning speed on the porosity level in an PBF part [4]

However, these parameters affect the melt pool shape which can cause lack of fusion. In the latest study, the pockets of non-molten powder were removed during the grinding of the sample and the void then generated were counted as pores during the porosity analysis. This shows how difficult it is to study gas porosity in a material produced by a powder bed process. Similar studies all showed that it is challenging to build high-density aluminium component using powder bed system and that the powder quality and process parameters have a drastic effect on the metal density [81, 82].

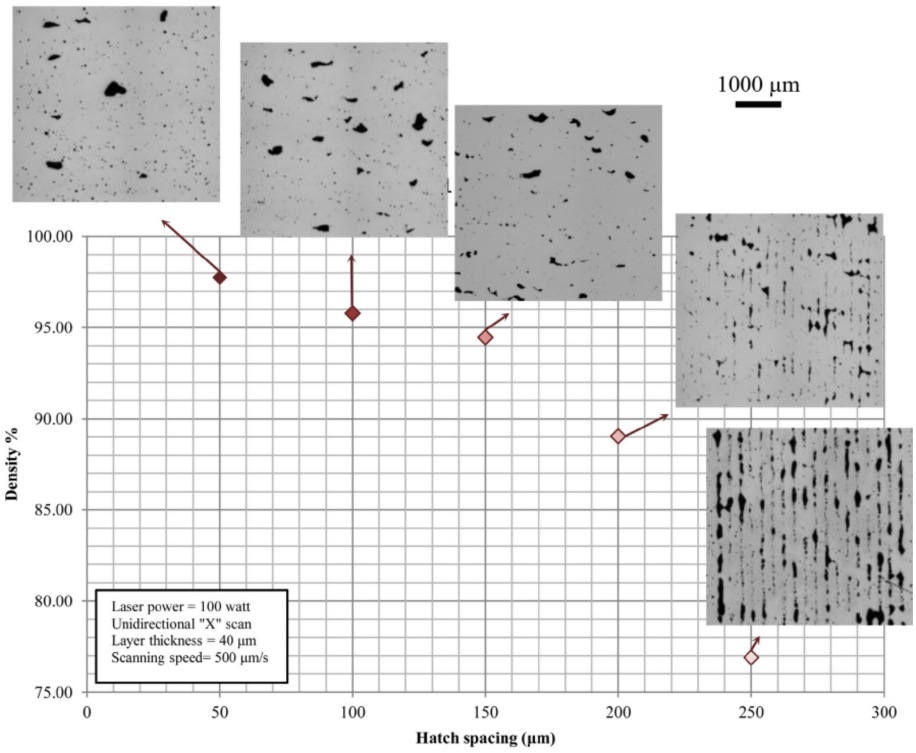


Figure 2.8: Illustration of the effect of the hatch spacing (distance between parallel passes) on PBF material density [4]

WAAM

Cong et al. showed the deposition process could play a key role in the porosity level: the use of low heat input and alternating current and voltage can drastically reduce the number of pores on 2319 alloy deposited with GMA processes [12]. Similar conclusion on the positive effect of alternative current was observed during the deposition of 5556 alloys with a GTA process [68]. However, no significant effect of alternating current was observed in Ryan et al.' work on GMA deposition of 2319 alloy [65]. Instead, this latest work showed a high dependence between wire and deposition quality; the surface quality of the wire seems to play a critical role in the deposition quality, at least when a GMA process is used. The correlation between wire quality and porosity level in the deposit has also been observed during GMA deposition by Gu et al. and Pinter [64, 83]. No

extensive study has been published on the matter, but Pinter showed the use of AC PTA could drastically reduce the porosity level compared to GMA process, even for a poor wire quality.

Inter-pass rolling has been successfully applied to reduce the porosity level by Gu et al. in WAAM 2319 and 5087 alloys [5]. Figure 2.9 shows optical images of material as-deposited, rolled at different rolling load, and after heat treatment. The authors suggested that the porosity level was reduced due to the increase in dislocation density, well known for being a hydrogen trapping site.

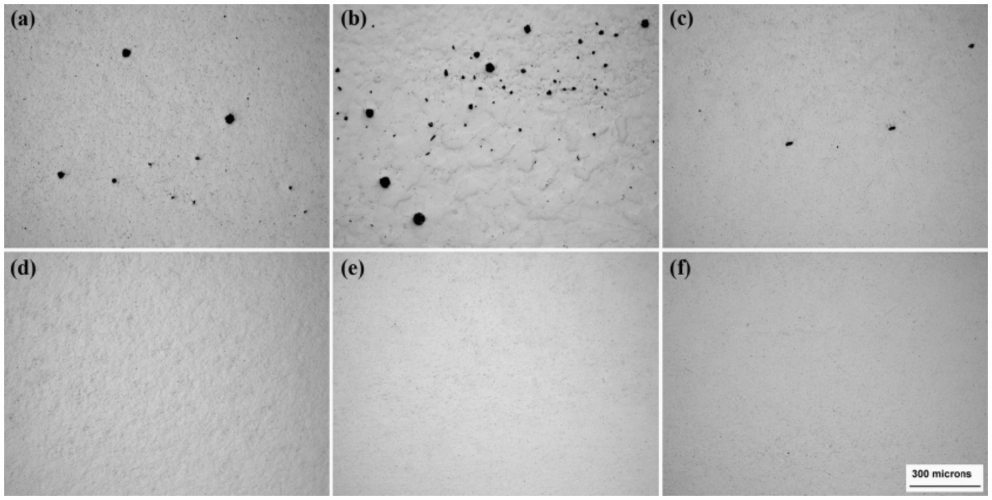


Figure 2.9: Effect of inter-pass rolling and heat treatment on porosity level of 2319 deposited with a AC GMA process: optical images of the (a) as-deposited, (b) as heat treated, (c), (d) and (e) as rolled with a respective rolling load of 15, 30, and 45 kN and (f) rolled with a rolling load of 45 then heat treated material [5]

Many aluminium alloys require heat treatment after being deposited to reach their highest mechanical properties. Unfortunately, the exposure to high temperature is detrimental to the porosity level in aluminium alloys [84], and this effect has been observed in WAAM material [5, 85] and shown in Figures 2.9 (a), (b), and (f). As illustrated in Figure 2.9, when inter-pass rolling is carried out, Gu et al. showed that the porosity level remains low, even after post-deposition heat treatment [5].

2.2.3.2 Solidification cracking

One of the main reasons why a limited number of aluminium alloys are available as raw material for AM, other than porosity, is their inappropriate solidification behaviour which makes them very sensitive towards hot cracking [86].

Most of the papers published on aluminium AM use Aluminium silicon alloys [83, 59, 60, 66], or aluminium silicon magnesium alloys [82, 87, 88, 4]: these two families, classified as 4000 and 6000 series respectively, are widely used in casting and welding because most of their alloys have favourable solidification behaviour.

However, these alloys are not the most interesting ones in term of mechanical properties. For this reason, many studies focus on the solidification sensitivity of aluminium alloys, and how process parameters and alloy composition can be modified in order to make high strength aluminium alloys suitable for AM.

Powder bed processes

Mauduit et al. [89] used aluminium powder of various alloys to check the compatibility between these alloys and the PBF process. Un-surprisingly, samples made of 2017A, 2219, 7075, 7020, 6061 and 5083 alloys contained cracks. The authors also confirmed that the cracks were caused by the fast solidification rate for 2017A and 7075 alloys [89]. Numerous hot cracks were also observed in 7075 PBF material manufactured by Kaufmann et al, and their attempt of reducing the number of these cracks by preheating the part to 200°C in order to reduce the solidification rate was not successful [90]. Aversa et al. and Martin et al. also used 7075 powder to manufacture samples with a laser PBF machine: when using a commercially available powder, numerous cracks were observed in the material [6, 7].

However, the authors of the two latest studies tried to manufacture samples using a generic powder, and they also changed the chemical composition of this powder in order to deposit a modified crack-free aluminium zinc alloy. Aversa et al. mixed the 7075 powder with an AlSi10Mg powder to reduce the solidification range, in order to improve the fluidity of the melt pool and reduce the thermal expansion coefficient of the material. As shown in Figure 2.10, using a 50/50% mix made possible the production of a crack-free material. In this study, the material manufactured had a very different composition compared to the original alloy studied (7075): this had detrimental consequences on the final material properties [6].

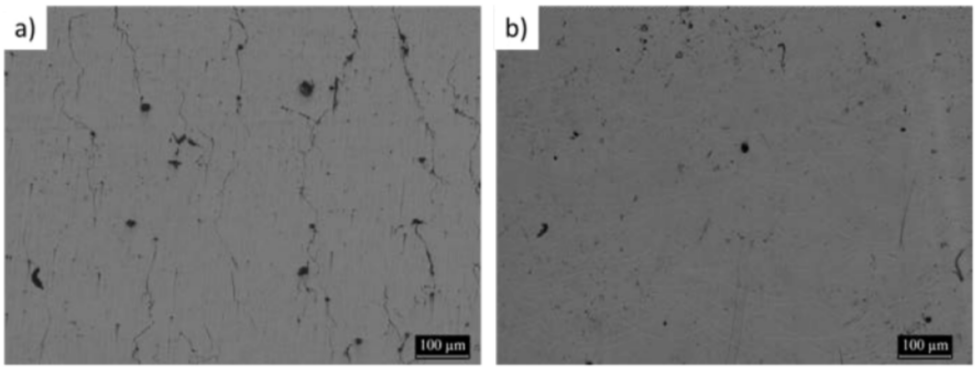


Figure 2.10: Optical image of (a) 7075 and (b) 50% 7075 - 50% AlSi10Mg manufactured by a laser powder bed fusion process [6]

Martin et al. realised a much more subtle change in composition: in their study, the 7075 powder was coated with 1 vol% hydrogen- stabilised zirconium nucleants using an electrostatic assembly technique. This addition of zirconium was made in order to add a high-density of Al_3Zr nucleant phases in the material during solidification. These phases changed the solidification behaviour of the material: they prevented the formation of large columnar grains during the solidification and promoted the formation of small dendritic grains. This way, the authors manage to deposit crack-free, slightly modified 7075 alloys [7]. Figure 2.11 shows the tensile test results reported by the authors and

illustrates the drastic improvement realised thanks to this small zirconium addition. Zhang et al. [91] mixed pure zirconium powder to an aluminium copper magnesium powder and manufactured sample using PBF. Similar results than those obtained by Martin et al. were achieved: the addition of zirconium drastically reduces the crack sensitivity of the alloy [91].

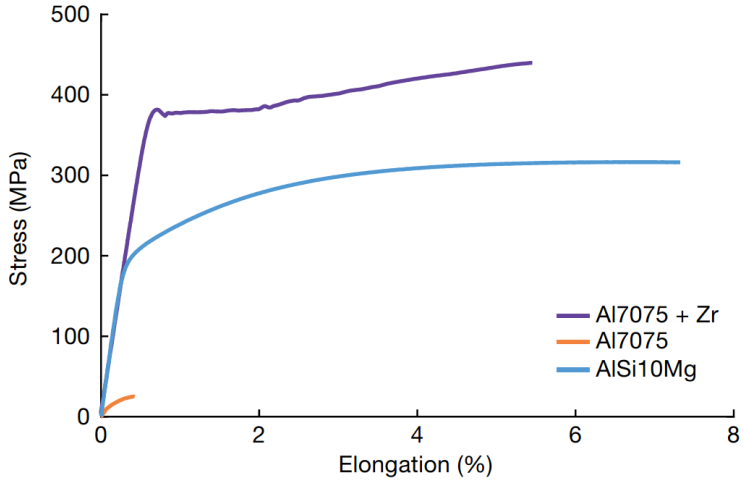


Figure 2.11: Stress-strain curve obtained during the test of SLM material [7]

WAAM

Few studies have been conducted on crack sensitive alloy and their suitability for WAAM processes. Fortunately, the solidification rate in WAAM is lower than in powder bed processes, and this reduces the likelihood of generating hot cracking during the solidification. If most of the studies on solidification cracking in PBF of aluminium alloys are focused on aluminium zinc alloys, the few studies conducted on solidification cracking in aluminium WAAM focus on aluminium magnesium alloy. Aluminium zinc alloys have not been investigated in WAAM mainly because of the behaviour of zinc in electric arcs and melt pools (see section 2.2.3.3).

Gu et al. used a tandem GMA system in order to deposit various composition of

aluminium copper magnesium alloy by mixing two alloys among AlCu10, 2319, 5087 and 5554. Some compositions could not be successfully deposited without cracks, as illustrated in Figure 2.12. However, the authors showed that alloys containing between 4.2 to 6.3 %wt of copper and 0.8 to 1.5% of Mg could be deposited without any cracks visible during Scanning Electron Microscopy (SEM) imaging [58].

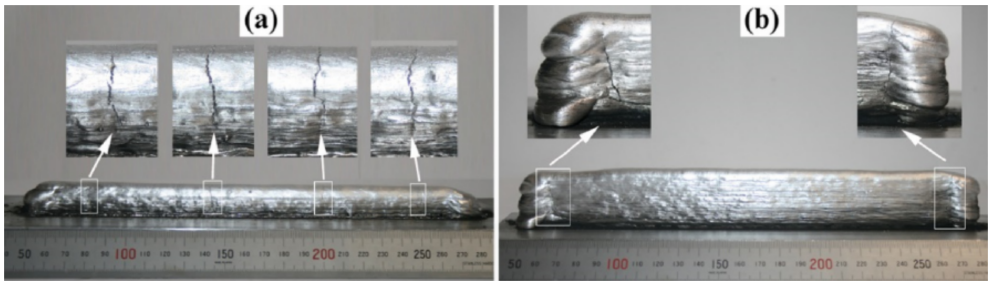


Figure 2.12: Photograph of AlCuMg alloy deposited with WAAM: (a) Al-Cu3.71-Mg1.73 and (b) Al-Cu4.08-Mg1.62.

Fixter et al. used a numerical model to predict hot crack susceptibility and showed that the 2024 alloy could be deposited by WAAM, despite being widely considered as un-weldable by fusion. There are no 2024 wires available on the market, and therefore a customised wire was made to confirm the results of the numerical model, and the authors were able to deposit crack-free 2024 alloy [92]. Qi et al.also managed to deposit 2024 alloy by WAAM using a GTA tandem system to mix 2319 with 5087 wires [93].

2.2.3.3 Management of volatile elements

High strength aluminium alloys have very complex compositions which include elements such as magnesium, zinc and lithium. Magnesium and zinc have a low boiling point, 1091°C and 907°C respectively, compared to aluminium melting and boiling points (660 °C and 2470°C). At liquid state, the temperature of the molten pool can be higher than these boiling points. Therefore, magnesium and zinc can vaporise during deposition, leading to a loss of these elements in the material after solidification.

Powder bed process

Martin et al. measured a zinc and magnesium loss of about 25 and 32% respectively during their manufacture of 7075+Zr by SLM [7], and Mauduit et al. measured a magnesium loss from 17 to 57% during the deposition of various aluminium alloys by PBF, and a zinc loss up to 33% during the manufacture of 7075 alloy [89]. This reduction in alloying elements will have a drastic impact on the mechanical properties of the material produced because the precipitate size and distribution depend on the amount of alloying element in the matrix. This reduction in alloying element will need to be counterbalanced, probably by adding more of these elements in the raw material. In addition, vaporisation of elements and its impact on melt pool behaviour has been investigated in fusion welding. This has not been addressed specifically in powder bed AM yet, but it is highly probable that the metal vapours impact on the process stability and the deposition quality.

WAAM

The reason why there are only a few studies on the deposition of aluminium zinc alloys is the very low boiling point of this element. In fusion welding, it has been demonstrated that it is challenging to use a filler wire which contains zinc: for instance, Woods [94] described the droplet transfer in GMA welding with various aluminium wires. The author observed explosion inside metal droplets in the electric arc, and these explosions were more severe when the magnesium content of the wire was high. The most unstable droplet transfer and almost systematic explosions were observed when a binary aluminium - zinc (5%) wire was used [94]. The use of aluminium zinc with a GMA process seems therefore impossible for welding and WAAM.

The vaporisation of magnesium has been observed by all studies focused on aluminium magnesium or aluminium copper magnesium alloys. Gu et al. measured a loss of about 1.2% during the GMA deposition of 5087 alloy (Wire Mg content of 5.05%) [14]

and a loss up to 24% when depositing aluminium copper magnesium alloys using a GMA tandem system [58]. These values, considerably lower than those measured in powder bed studies, seems to be very sensitive to the deposition process: the heat input during the deposition of 5087 alloy (177.9 J/mm) was considerably lower than the heat input in the tandem study (up to 250 J/mm). In the latest study, the heat input varied with the different Wire Feed Speed (WFS) used, and the author noticed that the magnesium loss was higher when the heat input was increased. In their study, Brice et al. deposited 2139 and measured a magnesium loss up to 80%, but managed to counterbalance this loss by using a higher magnesium content in their wire [95].

2.2.3.4 Mechanical properties

Tables 2.1, 2.3, and 2.2 show the mechanical properties published in the papers used as references in the previous sections. In most cases, the authors carried out tensile tests only in the horizontal direction (parallel to the deposition direction), but some studies also provide tensile properties in the vertical directions [11, 63, 78] (perpendicular to the deposition direction). For the latest studies, the tensile properties are reported in the table under the form of multi-rows, with the properties in the horizontal direction on top of those measured in the vertical direction.

The table 2.1 does not give a complete overview of what has been achieved, especially for powder bed systems with AlMgSi alloys. This is because, in this study, powder bed methods were not investigated, and these properties are just given as a benchmark. AlMgSi is also not studied with WAAM due to the general low properties that are obtained compared with other alloy systems.

Regarding aluminium magnesium alloy, the highest properties were achieved by Akuna et al. with the rolled Safra66 alloy, with a UTS of 390 MPa and an elongation above 23%

in the horizontal directions, with slightly lower properties in the vertical direction.

Regarding the mechanical properties of aluminium zinc alloys, all data found in the literature is reported in Table 2.2. The only data published before the beginning of the work reported in this thesis were obtained during the test of material built by microdroplet deposition manufacturing by Zuo et al.. The authors obtained acceptable properties, but much smaller to these of heat treated wrought 7075 alloy. Unfortunately, no heat treatment was carried out in this study, and the tensile properties show considerable variability with process parameters [97], showing a lack of process maturity.

In parallel of the work detailed in Chapter 5, two studies on LPBF manufacture of 7075 alloy were published in 2018. Other studies investigated the feasibility of manufacture aluminium zinc alloys by AM, but none of them includes mechanical properties results. This shows the beginning of interest these alloys recently received. However, the maximum properties achieved by 7075 AM were, after T6 heat treatment, a YS, UTS and an elongation at rupture of 349 MPa, 400 MPa, and 9% respectively. This is lower than the minimum required by the ASTM standard for a T6 heat treated 7075 plate (YS= 372 MPa, UTS=462 MPa and El=3%), and much lower than properties usually reported for this alloy, such as a YS from 372 to 469 MPa, a UTS from 462 to 538 MPa, and an elongation at rupture from 3 to 9% [7]. There is a large gap between the properties of AM and wrought zinc alloys.

Recently, many research projects have focused on the AM of aluminium copper alloys. However, no mechanical properties were found before 2015, and numerous studies were published in the last three years. Inter-pass rolling and heat treatment make possible the manufacture of 2319 with higher properties than wrought alloys by WAAM [5]. However, without rolling or heat treatment, the properties of this alloy remain low. The deposition of aluminium copper magnesium alloys have slightly higher as-deposited mechanical properties, reaching a YS of 178 MPa and a UTS of 284 MPa with 2024 alloy, very similar

Table 2.1: Mechanical properties achieved by AM aluminium magnesium and silicon alloys

Alloy	Process	State	Hardness [HV]	YS [MPa]	UTS [MPa]	El* [%]	Ref year
5087	WAAM						
		AD[1]	77	142	291	22.4	[14]
		IR[2]	107	240	344	20.1	2018
Safra 66	WAAM						
		AD	83	147	322	23.7	
				152	317	20.5	[78]
		IR	117	275	390	20.0	2017
				255	341	14.6	
5556	WAAM	AD	79	146	302	28.4	[68] 2017
AL6Mg	WAAM	AD	-	-	314	-	[62]
					289		2018
5346	WAAM	AD	-	108	230	10	[66] 2016
5059	WAAM	AD	-	124	273	34	[96]
				124	273	34	2016
AlSi10Mg	PBF	AD	127	-	391	5.5	[88]
				-	396	3.5	2012
4043	WAAM	AD	-	61	141	17	[66] 2016
4943	WAAM	AD	-	85	193	15	
4047	WAAM	AD	-	88	180	15	

*Elongation

[1]As Deposited

[2]Inter-pass Rolled

Table 2.2: Mechanical properties achieved by AM aluminium zinc alloys

Alloy	Process	State	Hardness [HV]	YS [MPa]	UTS [MPa]	El [%]	Ref year
7075							
	PBF	AD	-	-	25	0.4	[7]
+ Zr	PBF	T6[1]	-	349	400	4.6	2017
	MDDM	AD	-	-	373	9.95	[97] 2015
7075 + AlSi10Mg							
	PBF	AD	136	315	387	2.7	[6] 2018
		3h 170°C	150	315	370	2.1	
		6h 160°C	153	250	362	3.3	

[1] Solution treated and aged at peak age

to Al-4.4Cu-1.5Mg properties. These alloys have been only investigated recently due to the development of in-situ alloying technique relying on the use of multiple wires. No properties in the vertical direction were found in the literature, and only a preliminary study was published on inter-pass rolling of 2024 alloy [92].

Table 2.3: Mechanical properties achieved by AM aluminium copper alloys

Alloy	Process	State	Hardness [HV]	YS [MPa]	UTS [MPa]	El [%]	Ref year
2024							
	WAAM	AD	-	173	288	12.1	[92] 2017
		IR	-	278	379	7.4	
		ST+NA	-	334	469	15.2	
		T4	-	409	501	8.2	
		T6	-	408	493	10.4	
		AD	95	178	284	6.0	[93] 2018
		ST(485°C) +NA	133	294	423	9.0	
		ST(498°C) +NA	138	310	456	12.7	
		ST(503°C) +NA	143	328	495	15.9	
Al 3.6Cu2.2Mg	WAAM	AD	86	157	280	8.2	[8] 2018
				155	279	8.9	
Al 4Cu1.8Mg	WAAM	AD	90	158	279	7.5	
				154	276	7.5	
Al 4.4Cu1.5Mg	WAAM	AD	95	176	285	6.0	
				176	280	5.5	
2319							
	WAAM	AD	68	133	261	18.4	[11] 2016
				130	258	15.6	
		IR	102	249	320	8.5	
				244	310	7.3	
		T6	144	332	463	14.1	
				308	454	13.6	
		IR+T6	142	318	459	17.1	
				306	454	16.2	
		AD	-	108	250	10.7	[67] 2015
				108	237	10.5	
ZL205A							
	WAAM	AD	66	110	248	20.7	[78] 2017
				105	253	18.8	
		T6	152	405	483	11.5	
				402	478	11.8	

Comparison

Comparing properties given by Table 2.1, 2.2, and 2.3, it is clear that chemical composition and process development affect the mechanical properties of deposited alloy: post-deposition heat treatment [93] or inter-pass rolling [11] also have a drastic impact on the final properties.

In Table 2.3 it is possible to see the results obtained with different process, in as-deposited, heat treated and inter-pass rolled conditions for the 2024 alloy. In as deposited condition the properties achieved are very similar, whether the material was deposited with GMA [92] of tandem GTA [93]. However, the elongation reported by Gu et al. (12.1 %) is considerably higher than this reported by Qi et al. (6.0 %). Similar observation can be made on 2319 deposited with GTA or GMA by different research centres, and achieving relatively similar properties [11, 67], apart from the elongation. This suggests that deposition parameters do not affect the mechanical properties of the material, for a given alloy, but impact drastically on the level of defect in the deposited material.

This suggests that in order to increase the properties of AM aluminium alloys, not only the development of cold work or heat treatment techniques are required, but it is also crucial to introduce new alloys, developed explicitly for AM, to compete with wrought aluminium product mechanical properties.

2.2.3.5 Alloy development

Aluminium alloy compositions are designed to achieve the specific properties, such as tensile strength, toughness, and corrosion resistance, required by the final part specifications. However, the compositions are also dependent on the manufacturing process used: for instance, silicon is commonly added to cast alloys in order to improve fluidity and their solidification behaviour. It is therefore natural to think that most wrought aluminium

alloys are not adapted to AM processes. As detailed in section 2.2.3.2, alloy modification can be carried out to adapt common alloys to AM processes.

Powder bed processes

A few selections of powder are available on the market: to deposit a new alloy it is possible to manufacture a customised power, but this takes time and is expensive. An obvious route of new powder development is to mix powder of different alloy in order to produce powders of various compositions. This route has been chosen in various studies [6, 91, 98, 99], but it is not always easy to produce a good quality powder. Commercialised powders have all different characteristic and mixing powders of un-even particle size or flowability can be an issue. Martin et al. used another approach by coating their powder with 1 vol% hydrogen stabilised zirconium nucleants [7].

WAAM

As for powders, the manufacture of customised wire composition is very time and money consuming, and not all composition can be drawn. In order to produce a various range of compositions, it is required to use existing wires. Pickin et al. show the possibility of using a tandem system with aluminium magnesium and aluminium copper wires to produce a weld with a customised composition. Even a third wire was used to feed copper into the melt pool away from the arc [100, 101].

In 2018, Gu et al. used the same strategy to deposit aluminium copper magnesium by WAAM [58] with a tandem GMA process. In parallel, Qi et al. deposited aluminium copper magnesium alloys with a tandem GTA system, shown in Figure 2.13 [8]. None of this studies included the deposition of aluminium zinc alloys.

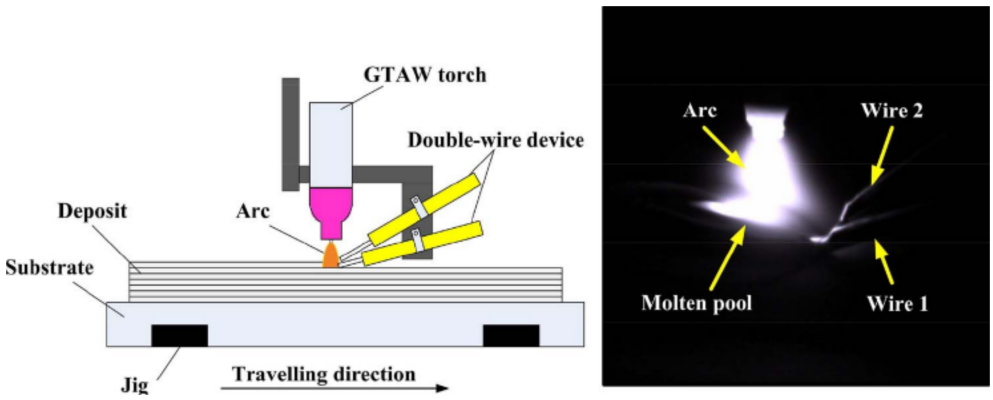


Figure 2.13: Double GMA system developed and used by Qi et al. to deposit aluminium copper magnesium alloys [8]

2.2.3.6 Summary

The additive manufacture of aluminium components has been widely investigated, and some challenges such as porosity, hot cracking and loss of volatile elements are contributing to make the use of AM processes difficult. However, in the last two to three years, the number of studies published is increasing, showing the growing interest in AM technologies to build aluminium parts.

Despite the very recent interest in aluminium magnesium copper and magnesium zinc alloys, very little data is available on these series. In most cases, there are considered unsuitable because of all the trouble they give to the welding industry. However, the few studies published in the past two years show it is possible to use these alloys, which can achieve the very high mechanical properties as wrought material [6, 7, 8, 14, 58, 92, 97, 93].

Another missing part in the literature of aluminium AM is the study of the interface between the substrate and deposited material where no report have been found. This topic is of interest primarily for WAAM process, as the integration of the substrate can reduce drastically the amount of material deposited as well as the buy-to-fly ratio, and could enable the production of functionally graded components, as mentioned in section 2.2.2.5.

2.3 Fusion welding

2.3.1 Fusion welding of aluminium alloys

WAAM uses equipment similar to that of welding and is similar to arc welding in many aspects. As mentioned in section 2.2.2.5, WAAM could enable the production of functionality graded component by integrating the substrate into the part design. However, very little research has been done on the interface between the substrate and WAAM deposited material. Nevertheless, the interface between the base material and weld bead has been extensively studied in arc welding of high strength aluminium alloy. The following section is focused on the microstructure and the properties of fusion welded aluminium alloys.

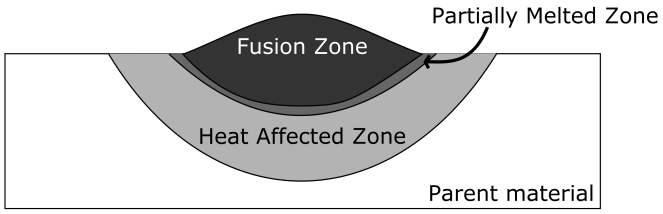


Figure 2.14: Diagram of the different areas affected by a weld in fusion welding

Figure 2.14 shows the different zones of the interface between the weld and based material [79]:

- The Fusion Zone (FZ) is the area where the metal is fully melted during the process. If a wire filler is used, the composition of this zone is different from the substrate: it is a mix between the composition of the wire filler and the substrate.

- The partially Melted Zone (PMZ) is the area where only a small part of the metal is melted during the process.

- The Heat Affected Zone (HAZ) is the area which remains in solid state during the weld, but the heat involved in the process changes the material microstructure.

The properties of these areas depend on numerous parameters such as the power source, process parameters (WFS, TS, shielding gas), geometry (thickness of the base plates, edge preparation), base plate (alloy, temper) and wire (quality, alloy) [27, 102, 103]. That being said, some phenomena often occur in fusion welding of aluminium, regardless of those parameters, and can not be completely eliminated.

2.3.1.1 Cracking

Fusion Zone

At the end of the solidification, solidification shrinkage and thermal contraction induced tensile stresses around the melt pool: the liquid yet to be solidified in between grain or dendrites can be un-sufficient to accommodate these tensile stresses, leading to solidification cracking [104]. Rolling can be used to reduce the tensile stress in the melt pool [105], and few strategies can be used to reduce the sensitivity of an alloy toward hot cracking. The first and most common one is to use a suitable wire filler of a different composition in order to change the solidification behaviour of the melt pool [106, 107]. Lists of parent material / wire filler pairs are available in the literature [79], and for unusual cases, Pickin et al. showed the possibility of using multiple wire filler to control the weld composition and avoid hot cracking [100, 101]. However, changing the composition of the weld bead can have drastic effects on its properties such as corrosion and strength.

Partially Melted Zone

In the PMZ, where only a small fraction of metal melts and then solidifies, the local microstructure is changed due to liquation. Liquation consists in the segregation of alloying elements between solid and liquid material, due to the different solubility of these

elements at liquid and solid states [108]. Liquation cracking occurs in the PMZ mainly at the grain boundary, but also at large second phases [109]. There are different liquation mechanisms, and these can be greatly affected by local composition, heat treatment history of the parent material and thermal cycle [110]. If liquations are severe, they can lead to liquation cracking due to the local tensile stress applied to the melted material. During welding, the restraint and stress on the melt pool are much greater than during WAAM. This is due to the change in geometry: WAAM is similar to free space casting, therefore, solidification and liquation cracking is much less likely than during welding.

2.3.1.2 Porosity

Hydrogen bubbles tend to form during solidification because hydrogen solubility is much higher in liquid than solid aluminium, and as aluminium solidifies quickly, lots of those bubbles get trap in the metal [79]. Porosity, as all the other weld characteristics depend on many parameters, including the alloying element in the plate: for instance, lithium is well known for generating a large amount of porosity during fusion welding [111, 112]. It is essential to clean the wire and the base material before welding in order to reduce to a minimum the contamination on their surface, and variable polarity can be used to improve the in-situ cleaning of these two [26].

2.3.1.3 Mechanical properties reduction

Even if all precautions are taken to avoid solidification, liquation cracking, and porosity aluminium welds often suffer from high loss of mechanical properties.

Heat Affected Zone

The microstructure of the HAZ is modified by the heat involved during the process without any change of state. As detailed in section 2.1.2.1 (page 12) most high strength

aluminium alloys are heat treatable and their high strength is the result of precipitation hardening. To reach specific properties, thermo-mechanical treatments specifically designed for each alloy chemical composition are used. During welding, the material near the join undergoes a thermal cycle which changes its microstructure and can neutralise all the benefits of the pre-welding thermo-mechanical treatment. The effect of this thermal cycle on the material depends on its maximum temperature and cooling rate [113]: for instance, Yang et al. reported a study on the effect of different thermal cycle on 2024 plates [114]. The microstructure of the material can be affected in different way: grain growth and recrystallisation for work hardened alloys [115] and ageing, over ageing or reversion for heat treatable alloys [115]. Numerous studies have been published on the heat affected zone properties and the effect of post weld heat treatment to improve them. For instance, Dumolt et al. showed the effect of the base material temper on the mechanical properties of the HAZ [27]: because the precipitates in the base material are not the same if the material is under-aged (GP), at peak age (θ") or over-aged (θ' and θ), the effect of the heat on them is not the same. This results in HAZ of different mechanical properties. Post weld solution treatment is not a common process because it is often complicated to quench joined components. However artificial ageing can be performed on a weld to recover the properties in the HAZ. Kou [115] detailed the effect of different heat treatments on few precipitation system showing that the HAZ properties cannot be completely recovered by ageing. The author also reported the effect of welding process and show the dependence between the welding process heat input and the width of the HAZ.

The properties of the HAZ are often measured using micro hardness profile along the weld [115, 116, 117] because it enables local measurements. Also, Bai et al. and Acar et al. [116, 118] used digital image correlation along tensile test to measure the local yield strength of the different areas of the heat affected zone. This technique is introduced and

detailed further in section 3.2.7.

Partially Melted Zone

If liquations do not lead to liquation cracking in the PMZ, they still can be detrimental to the joint mechanical properties. They induce in-homogeneous mechanical properties and reduces the ductility of the joint drastically [119].

2.3.2 Hybrid laser + arc welding

WAAM usually includes one heat source only but could include more in order to achieve better control of the bead geometry, heating and cooling rate. The use of a laser could permit to produce an elongated melt-pool in order to feed a cold wire in the melt pool, without disturbing the arc. The following section gives a brief overview of hybrid laser + arc welding processes.

2.3.2.1 Keyhole welding

The vast majority of studies on hybrid or laser assisted arc welding deals with keyhole welding; it consists in combining the high penetration, low heat input and controllability of the laser with the high gap bridging ability, independence toward material reflection and high electrical efficiency of arc welding [9]. This makes possible to achieve very high penetration depth without having to use multi-pass welding, usually time-consuming and causing high residual stresses and distortions. Figure 2.15 shows a diagram of a keyhole welding set up.

During keyhole hybrid welding, the coupling between the two processes is considerable: laser keyhole generates a plume of vaporised metal, which can disturb or stabilise the electric arc [120, 121, 122]. Also, the process usually requires a short distance between the laser and the arc: the heat input brought by the laser beam can disturb the metal

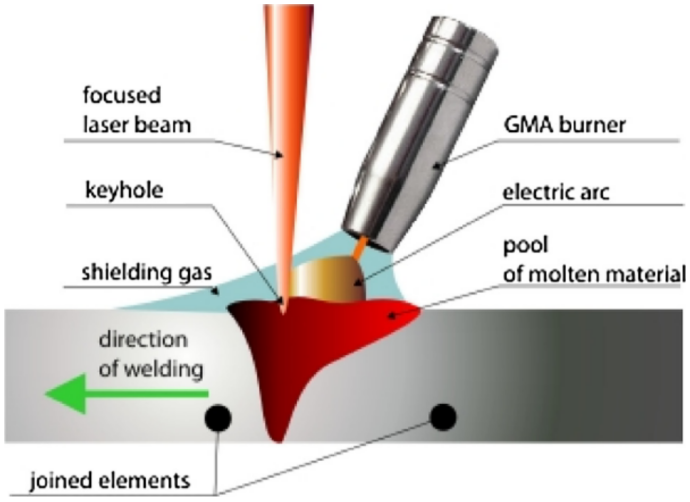


Figure 2.15: Schematic of a hybrid keyhole welding set up [9]

transfer of the arc process [121, 123] and the arc can absorb and defocus the laser beam, reducing its effects [122].

Keyhole welding has been extensively studied, but a keyhole weld is fundamentally different from what needs to be achieved in AM. The objective in AM is to add material layer by layer, and the higher the penetration depth is, the lower the efficiency of the process. Conduction mode should be preferred over Keyhole mode for AM application.

2.3.2.2 Conduction welding

The depth-to-width ratio of the weld determines the transition between keyhole and conduction welding: if this ratio is below 0.4, the welding mode is either conduction or transition, and if it is higher than 0.4, then the welding mode is keyhole. The value of 0.4 can be modified if the beam diameter and travel speed are changed [124]. Also, the transfer from conduction to keyhole mode is not very sharp, and depend on the material thermal properties [10]. Assuncao et al. showed that the value of power density (laser power to beam spot area ratio) usually used to distinguish laser welding mode, $10^6 W/cm^2$, should not be independent of the welded material. Figure 2.16 shows the profile of the penetra-

tion depth over the power density: the boundary between transition and conduction mode is a power density of 5 x $10^5 W/cm^2$.

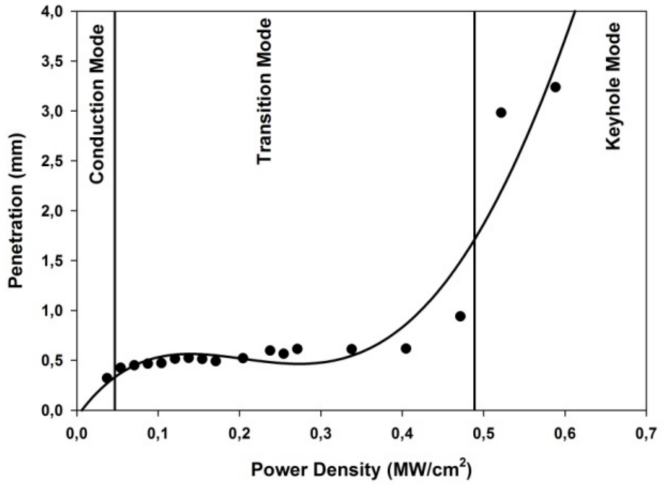


Figure 2.16: Effect of power density on the penetration depth in conduction, transition and keyhole modes on aluminium [10]

Regarding bead shape, Ayoola et al. [125] showed the great dependence between interaction time (ratio of the TS to the spot beam diameter) and penetration depth, as well as the effect of power density on this metric. Also, as long as the beam diameter is large enough to compensate the heat loss in the material, the beam diameter does not affect the penetration depth but impact the bead width, which is very close to the beam diameter.

A few studies on hybrid conduction welding are available as most of the research projects focus on keyhole welding. As mentioned in the previous sections, interactions between laser and arc are common in hybrid keyhole welding, but these interactions depend mainly on the metal vapour induced by the keyhole welding. It is difficult to evaluate the interaction between arc and laser in conduction mode. However, for material like aluminium, with high reflexivity and high thermal conduction, the laser adsorption is much improved in case of hybrid welding: the melt pool generated by the arc has a much higher absorption coefficient than at solid state.

Chapter 3

Methodology

3.1 Sample manufacturing set up

3.1.1 GMA deposition

3.1.1.1 Set up

Figure 3.1 shows a photograph of the set up used to deposit the samples used in Chapters 4, 6, and 7. An ABB robot was used to deposit the material on a fixed bed with a Fronius CMT Advanced 4000R power source. For the interface samples, two configurations were used : some samples were deposited on the face of the substrate, and some were deposited on its edge to be able to carry out tensile test across the interface, as shown in Figure 3.2.

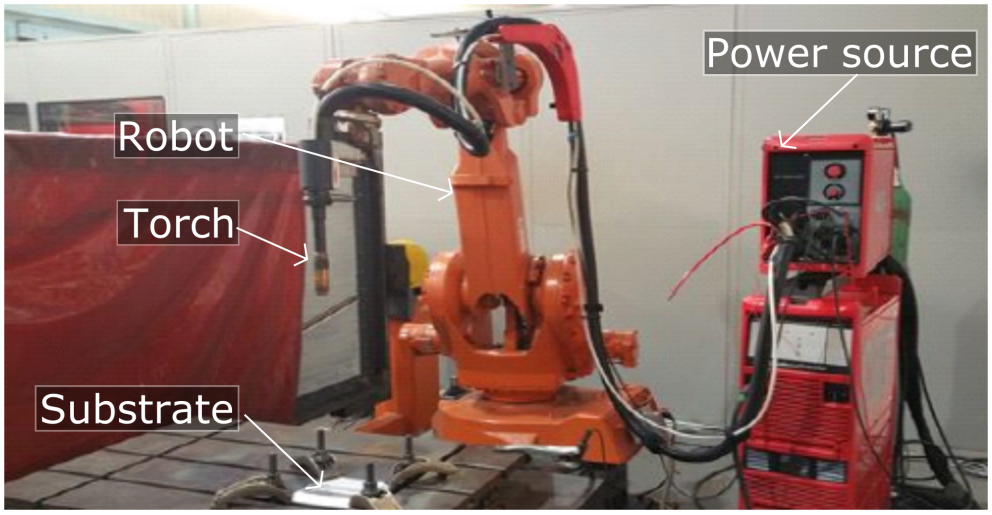


Figure 3.1: GMA set up used to deposit material on the substrate surface

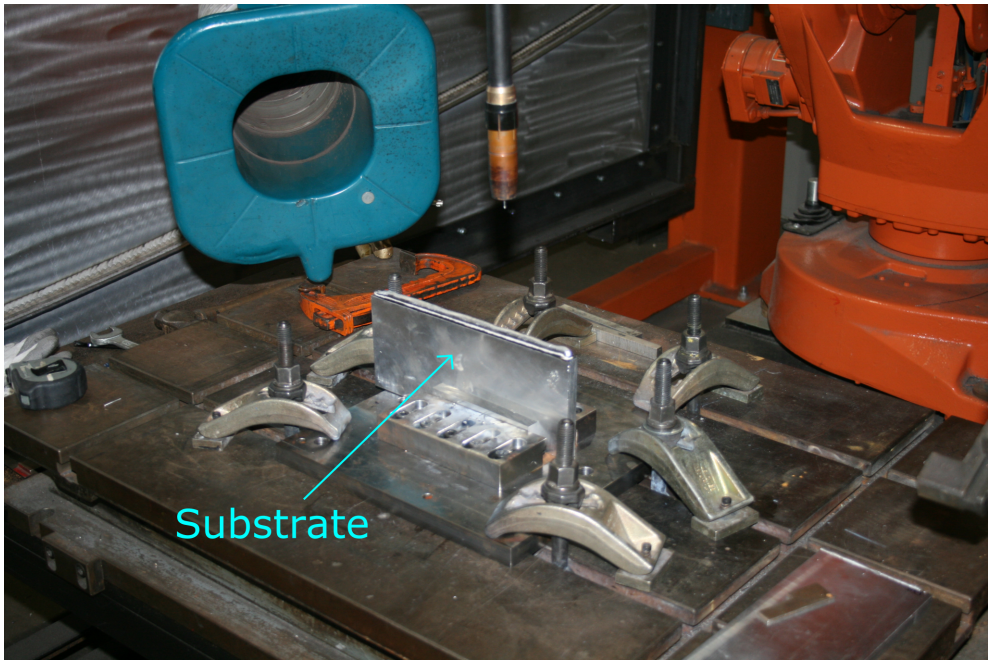


Figure 3.2: GMA set up used to deposit material on the edge of the substrate to produce the interface samples for tensile testing in Chapters 6 and 7

Inter-pass rolling

Inter-pass rolling consisted in applying compressive pressure to the top layer, in between each layer, by a hydraulic cylinder through a roller of 100 mm diameter. The rolling set

up is shown in Figure 3.3 The set-up and parameters used were very similar to the one described by Gu et al. [11, 14], the only difference being the use of the ABB robot to control the torch position instead of fixing it to the rolling rig. A rolling load of 45 kN was used in all cases to be able to compare the results with the literature.

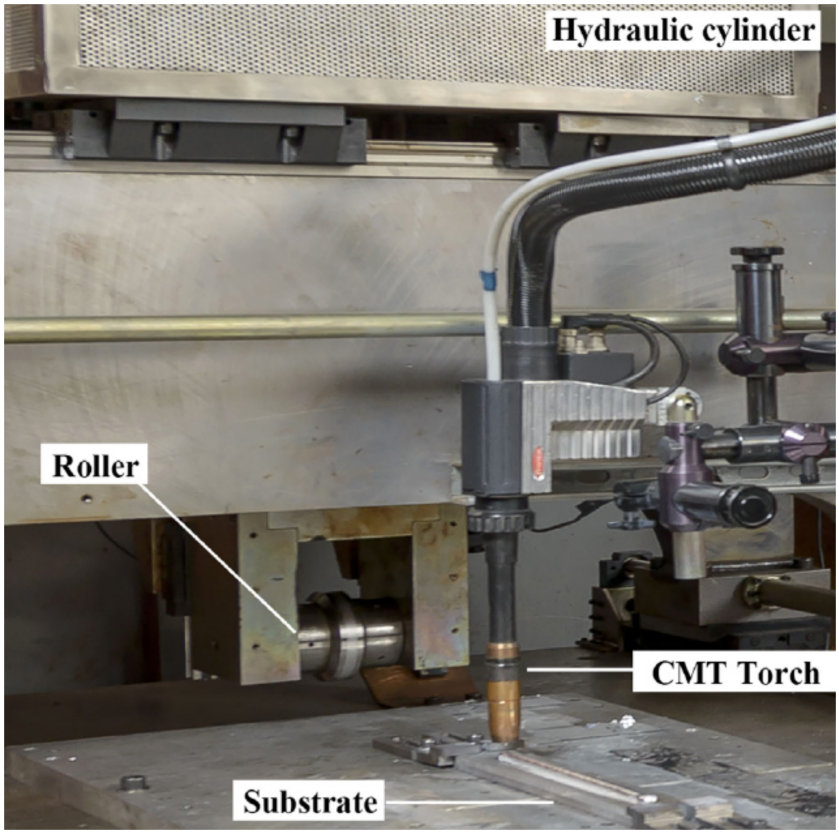


Figure 3.3: Rolling rig set up [11]

Figure 3.4 provides a schematic of the set up as well as the contact area between the roller and the material: this contact area is used to calculate the contact pressure. The contact surface, contact pressure and percentage of deformation are calculated using the following equations:

$$L = \sqrt{R^2 - (R - \Delta H)^2} \tag{3.1}$$

$$\Delta H = LH_{un\,rolled} - LH_{rolled} \tag{3.2}$$

$$Contact\ surface = \frac{W \times L}{2} \tag{3.3}$$

$$P = \frac{Rolling\ load}{Contact\ pressure} \tag{3.4}$$

$$Percentage\ of\ deformation = \frac{\Delta H}{LH_{un\,rolled}} \times 100\% \tag{3.5}$$

With R the roller radius, $LH_{unrolled}$ the layer height of the as-deposited layer, LH_{rolled} the height of the layer after rolling, W the width of the rolled layer and L the contact length between the WAAM material and the roller. These variable are shown in Figure 3.4

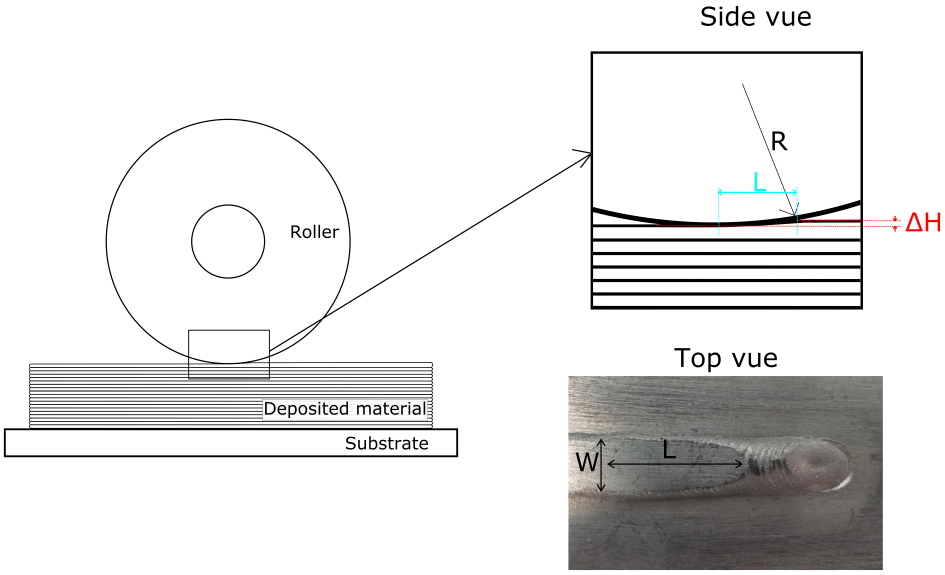


Figure 3.4: Schematic of the inter-pass rolling process and its effect on the deposited bead geometry

3.1.1.2 GMA deposition modes and deposition parameters

Cold Metal Transfer (CMT) was used to deposit the samples made of 2024 alloy in Chapter 4, and all the interface samples in Chapters 6 and 7. There are different CMT deposition modes, including CMT, CMT-pulse, CMT-Pulse-Advanced, and CMT-Advanced; the waveform of each mode is shown in Figure 3.5. The waveform show the complexity of the process with short circuit phases - when the voltage is equal to zero - pulse phases - when the voltage and current oscillate - and positive and negative phases. Advanced processes consist in alternating the polarity of the arc: according to the literature, this alternative current and voltage enables in-situ cleaning of the wire, leading to a lower porosity level in the deposit [12, 126]: CMT-pulse-advanced (CMT-P-Adv) is commonly used to deposit aluminium alloys [5, 12, 50, 63, 64, 65, 126], and was therefore chosen to deposit most of the materials in these studies.

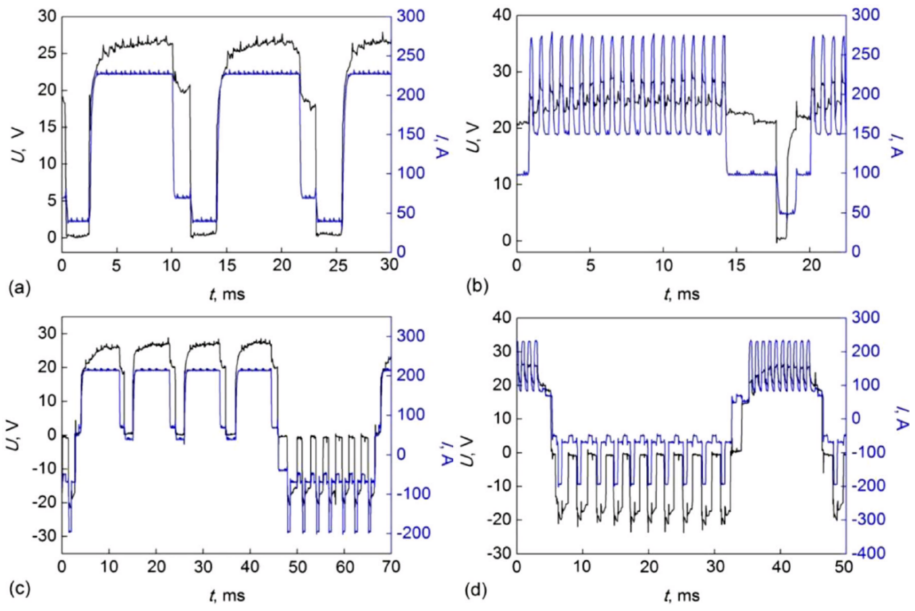


Figure 3.5: Waveform of CMT (a), CMT-Pulse (b), CMT-Advanced (c), and CMT-Pulse-Advanced (d) [12]

However, CMT pulse advanced can generate issues, especially if it is used for the

first layer deposition, because of its low heat input: Figure 3.6 shows the geometry of the first layer deposited with CMT-P-Adv and CMT Pulse (CMT-P) processes. If CMT Pulse Advanced process is used, the contact angle between the bead and the substrate is higher than 90°, and the join between the WAAM material and substrate is limited. If CMT pulse is used instead, the contact angle is reduced, and the connection between the WAAM material and substrate is acceptable.

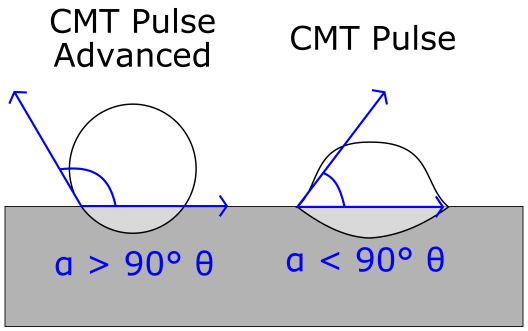


Figure 3.6: Diagram of first deposited beads using CMT pulse advanced and CMT pulse process

Deposition parameters used for the manufacture of 2024 samples used in Chapters 4

As shown by Figure 3.7 (a) and (c), the heat flux is extracted from the weld pool in all directions in the substrate, which acts as a heat sink. When subsequent beads are deposited, the heat flow is restricted to the previously deposited layers, and the distance to the substrate heat sink is larger, as shown in figure 3.7 (b) and (d). This is why a relatively high heat input process, such as CMT Pulse, should be used to deposit the first layer and a lower heat input process then used to deposit the subsequent layers.

Two deposition processes were used to manufacture the 2024 samples. CMT-P-Adv was used because of its low heat input and alternative waveform leading to a low porosity level when used to deposit other aluminium alloys. Also, many published studies on alu-

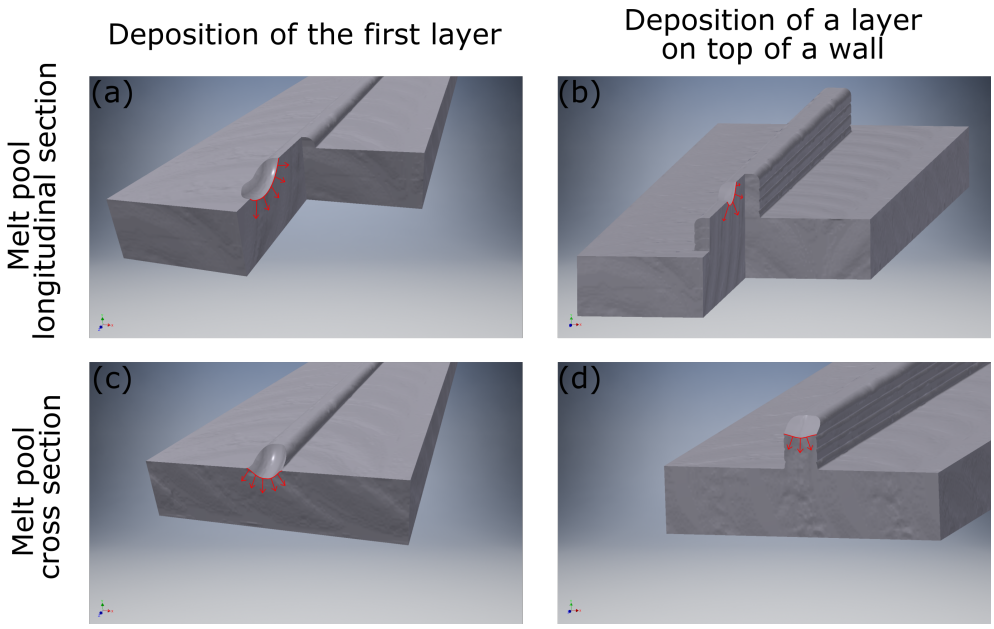


Figure 3.7: Schematic of the heat flux during the first and further layer deposition

minium WAAM focus on the use of this process, making possible a comparison between the work carried out in Chapter 4 and the literature.

However, an un-published preliminary study, conducted by Jianglong Gu, a former PhD student in the centre, shows issues in the vertical direction of WAAM 2024 when CMT pulse advanced was used, and this was even more severe after rolling. 2024 was therefore also deposited with CMT-P, considering the hypothesis that the bead shape generated with this waveform would be more suited for inter-pass rolling.

The deposition parameters were progressively changed during the deposition of the first layers to compensate the heat sink effect of the substrate. Table 3.1 provides the process and the WFS used during the manufacture of the samples. Argon was used as shielding gas, at a flow rate of 25 L/min, the travel speed and the work-piece contact tip distance were kept constant at 10 mm/s and 11 mm respectively.

Table 3.1: Deposition parameters used to manufacture the 2024 samples used in Chapter 4

	CMT pulse advanced samples		CMT pulse samples	
Layer	Wire Feed Speed [m/min]	Process	Wire Feed Speed [m/min]	Process
1	7	CMT Pulse	7	CMT Pulse
2	9	CMT Pulse Advanced	7	
3	9		6.5	
4	7		6.5	
5	7		6	
6-...	6		6	

Deposition parameters used for the manufacture of interfaces samples used in Chapters 6 and 7

Table 3.2 gives the deposition parameters used to deposit interface samples, including 2219, 2024, 2139, 2050, and 7449 substrates, described in Chapters 6 and 7. The progressive reduction of WFS was applied to reduce step by step the heat input as the distance between the deposited layer to the substrate increased. The final deposition parameters (for layer 6 and onward) were the same than these used by Gu et al. [11]. For the sample containing 6061_{RSP}, 6061_{Rolled}, RSP 905, and RSP 501 substrates, the process parameters, also shown in Table 3.2 were adapted because of the small substrate thickness. The travel speed was kept constant at 10 mm/s, 99% Argon gas was used at a gas flow rate of 25 L/min for shielding, and the distance between the work-piece and contact tip of the torch of 11 mm was used.

Table 3.2: Deposition parameters used to deposit the interface study samples

<table>
<tr><td></td><td colspan="2">Deposition on 2219, 2139, 2024, 2050, and 7449</td><td colspan="2">Deposition on 6061_{RSP}, 6061_{Rolled}, 501_{RSP}, and 905_{RSP}</td></tr>
<tr><td>Layer</td><td>Wire Feed Speed [m/min]</td><td>Process</td><td>Wire Feed Speed [m/min]</td><td>Process</td></tr>
<tr><td>1</td><td>7</td><td>CMT Pulse</td><td>5.5</td><td rowspan="2">CMT Pulse</td></tr>
<tr><td>2</td><td>9</td><td rowspan="4">CMT Pulse Advanced</td><td>5.5</td></tr>
<tr><td>3</td><td>9</td><td>7</td><td rowspan="4">CMT Pulse Advanced</td></tr>
<tr><td>4</td><td>7</td><td>7</td></tr>
<tr><td>5</td><td>7</td><td>5</td></tr>
<tr><td>6-...</td><td>6</td><td>6-6...</td></tr>
</table>

GMA Heat input calculation

The heat input was calculated using the following equation:

$$HI = \eta \times \frac{U \times I}{TS} \tag{3.6}$$

with U the voltage, I the current, η the efficiency (a value of 0.84 was used [127]) and TS the travel speed. The calculation was carried out point by point, and the average value was evaluated during the steady state of the deposition.

3.1.2 Laser assisted WAAM

A hybrid laser GMA set up was used to deposit aluminium samples shown in Chapter 5. An IPGYLR-8000 continuous wave fibre laser was used in out of focus position in order to achieve a beam diameter of about 10 mm and a very low power density, below 10 kW/cm^2, to avoid keyhole effects. A Fronius CMT Advanced 4000R power source was used to generate the melt pool using pulse and CMT-pulse processes with a 1.2 mm diameter 2319 filler wire. This alloy was chosen because of its simple binary aluminium copper

composition, and the good understanding of WAAM of 2319 from the literature review. 2219 substrates were used for all experiments. A pure zinc 1.6 mm diameter wire was used, with a push KT4 Megatronic wire feeder.

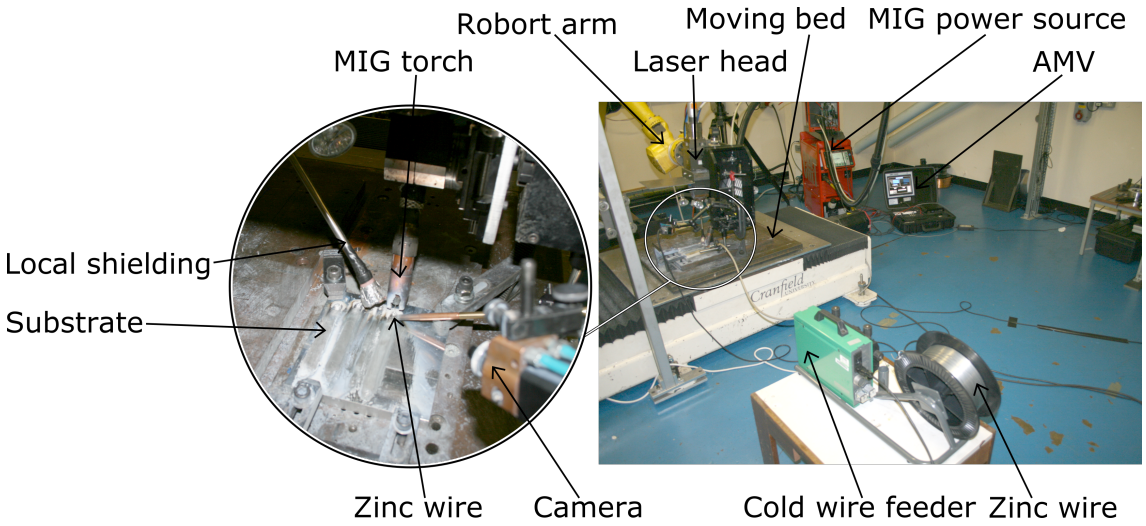


Figure 3.8: Laser assisted WAAM set-up: general view of the set-up (on the right) with a closer view on the torch, wire-feeder, and substrate (on the left)

The set up used is shown in Figure 3.8, and the schematic in Figure 3.9 provides a view of the relative position of the torch, laser beam and cold wire. The GMA process is leading, followed by the laser beam at an angle of 5° in order to avoid back reflection, as shown in Figure 3.9 (a). The GMA torch was inclined by a 60° angle to allow the laser beam to reach the melt pool; a triangular gap was machined in the shroud of the torch to prevent any shadowing of the laser beam. A local gas shielding was positioned on the side of the torch, to protect the melt pool from contamination using 100% argon gas at a flow of 20L/min. The distance between the torch and the work-piece was kept constant at 8 mm. The travel speed was kept constant in all experiment at 10 mm/s. Two distances of interest, which are the distance between the arc and the laser beam and the distance between the arc and the zinc wire, are pictured in Figure 3.9 (c).

All bead depositions were recorded using a Redman MC500 camera; in order to re-

duce the impact of arc brightness on the video, two lights bulbs were used to increase the overall luminosity. During deposition, the electric arc characteristics were measured and recorded by an AMV5000 from Triton Electronics.

All of the laser head, GMA torch, cold wire, local shield, camera and lightening system were fixed to the robot head. The whole system was moved horizontally between each bead deposition. However, during deposition, the robot arm was immobile and the moving bed was used to move the substrate below the set up. Different sets of experiments were conducted using different parameters and each of them is detailed in the methodology section of Chapter 5.

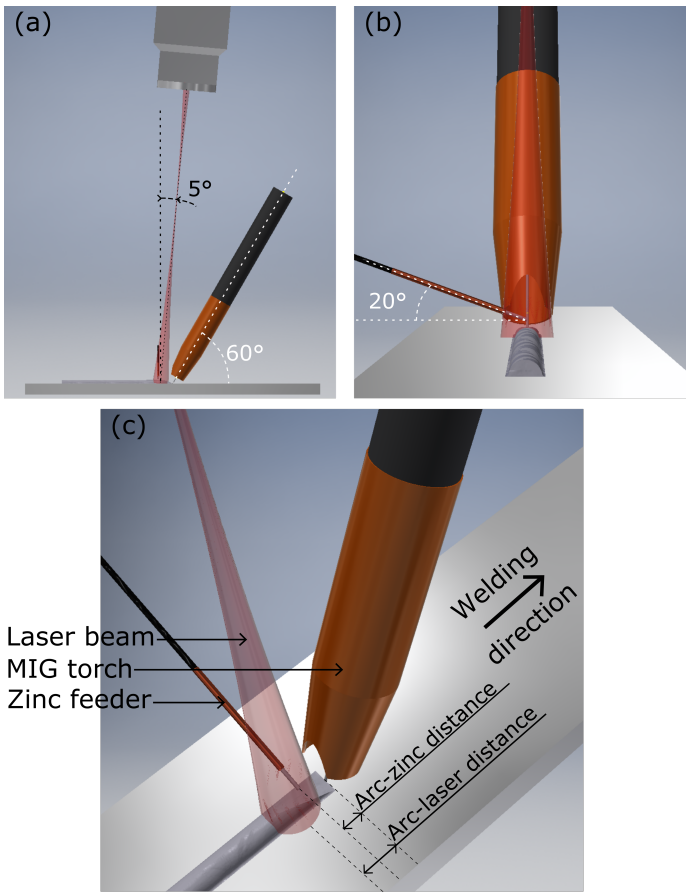


Figure 3.9: Schematic of the set up showing (a) the angle between the leading torch and the laser beam, (b) the angle between the substrate and the zinc wire feeder, and (c) the Arc-zinc and Arc-laser distances

3.2 Microstructure study

3.2.1 Samples preparation

Samples were cut using an automatic saw either in the longitudinal or the transversal direction. The latter was only used for porosity analysis, as detailed below. Samples were then mounted in cold epoxy resin, apart from Chapter 5 samples which were hot mounted using a hot press Opal 410.

After at least 24 hours of rest (for the cold mounted samples), the samples were ground and polished on automatic machines using successively 240, 1200, and 2400 grit SiC papers under flowing water, and 6 μm then 3μm diamond paste were used to polish the samples, followed by alumina alpha 0.3 μm and colloidal silica 0.05 μm suspension to achieve a mirror finish.

For some aluminium zinc samples shown in Chapter 5, it was necessary to clean the samples in an ultrasonic bath in between the grinding and polishing steps. This was done in order to reduce to a minimum the amount of small particles stuck in pores and cracks. These would otherwise generate numerous scratches on the sample surfaces.

Etching with Keller's etchant was carried out before optical microstructure observations.

3.2.2 Interface samples and terminology

In Chapters 6 and 7, the samples include the interface between the deposit and substrate, and therefore, contain different zones of interest. These zones are the Heat Affected Zone (HAZ), Partially Melted Zone (PMZ) and Fusion Zone (FZ) as in fusion welding, as well as the deposit zone: Figure 3.10 shows these zone of interest. These terms are widely used in both Chapters 6 and 7. Micro hardness measurement were carried out to determine the

width of the HAZ, SEM was used to study the PMZ and FZ microstructure, and an optical microscope was used to observe the grain structure in each of these areas.

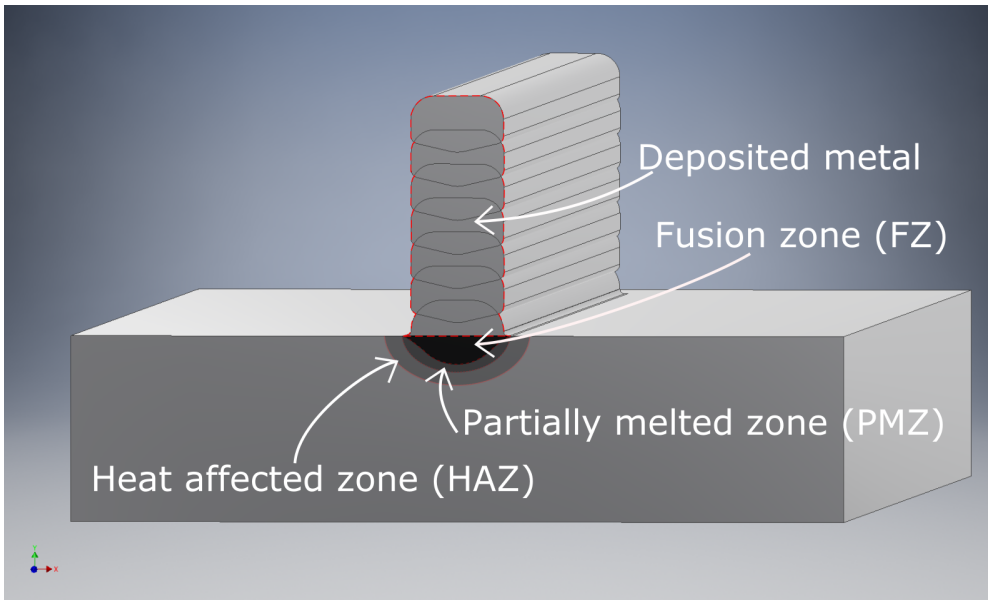


Figure 3.10: Diagram of the different zone found at the interface between the deposited material and substrate

3.2.3 Micro hardness measurements

Micro hardness measurements were carried out with an Auto-C.A.M.S. machine from Zwick Roell manufacturer with a load of 100 g for a duration of 15 s. Figure 3.11 shows how the measurements were carried out: indentations were situated in the centre line of the specimen, with a measurement density higher near the interface. The material was deposited on the edge of the substrate when tensile tests were to be carried out on the material.

In both configurations, the deposition parameters were identical, as detailed in section 3.1.1.2. However, the thermal cycle in the substrate was different if the deposition was done on its surface or edge because of the different geometry. Figure 3.12 shows the

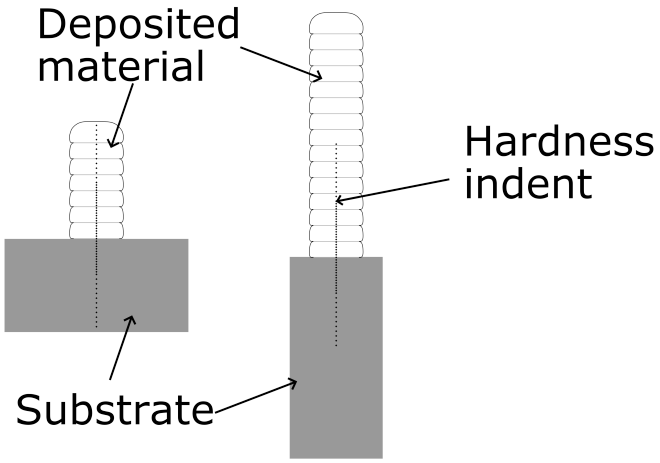


Figure 3.11: Diagram of the micro hardness measurement across the interface between the substrate and deposited material.

difference of hardness profile by the two geometries: the heat affected zone is considerably larger when the material is deposited on the substrate edge. However, the phenomena occurring in the material are the same. In Chapters 6 and 7, the same geometry configurations are compared with each other in most cases, and it is brought to the attention of the reader when two profiles obtained with two different geometries are studied together.

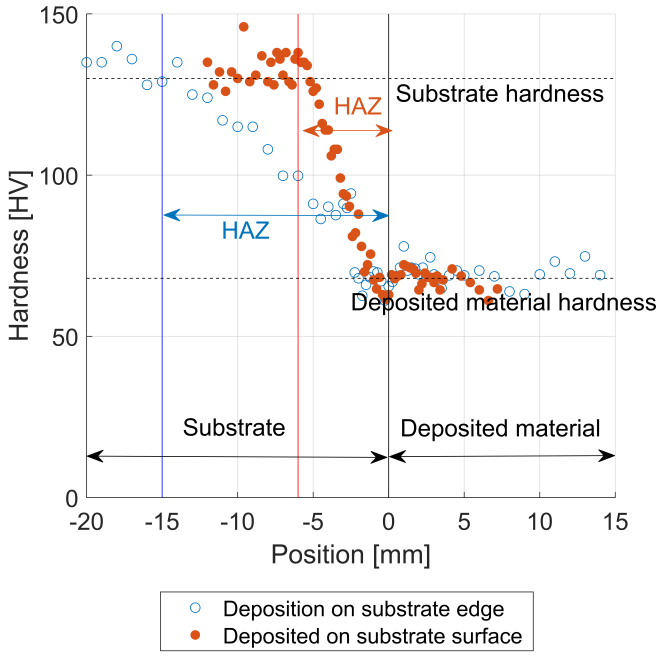


Figure 3.12: Hardness profile measured at the interface between the deposited material and substrate for the two geometry shown in Figure 3.11

3.2.4 Optical microscope

3.2.4.1 Imaging

Nikon Optiphot Microscopes were used to observe the microstructure, after etching, of the material. A low magnification (x2.5) was used to take a grid of photographs which were then stitched together to generate macrographs. The software AxioVision was used to measure geometrical characteristics from these images. Higher magnifications, up to x40, were used to take pictures to illustrate microstructural features.

3.2.4.2 Porosity measurement

A porosity study was conducted in Chapter 4 to evaluate the effect of the deposition process, inter-pass rolling and heat treatment on the porosity level of WAAM 2024 alloy.

For this purpose, four types of pictures were taken: cross and longitudinal sections

were used, and for each case, magnifications of 5 and 20 were used to measure the porosity density of pores with a diameter above 50 μm and 10μ respectively. The area analysed was around 10 mm^2 for the images taken with x20 magnification and 100 mm^2 when x5 magnification was used.

The software ImageJ was used to carry out the pore size measurement and counting. The software provided a list of pore areas which was then converted in a list of pore diameters, considering pores spherical and using the following equation:

$$Diameter = \sqrt{\frac{4 \times Area}{\pi}} \tag{3.7}$$

In order to compare samples with each other, the number of pores was divided by the studied area, and porosity level was compared based on the number of pores per 100 mm^2.

3.2.5 SEM

An XL30 ESEM machine with an X-MAX^N detector was used under ESEM mode to observe cold mounted sample, while the rupture surfaces of tensile specimens were observed under Hivac mode. In both cases, the backscatter detector was used as well as a working distance of 10.5 mm, a spotsize of 6 mm and a voltage of 20 kV.

For the fracture surfaces, the ruptured tensile specimen ends were cut with a handsaw, and the cut ends of the samples were polished by hand using a 1200 grit SiC paper in order to ensure good contact, hence a good conductivity, between the sample and the machine base.

3.2.6 Tensile test

Tensile tests were carried out with an electro-mechanical machine with a displacement rate of 1 mm/min. The tensile specimen dimensions are provided in the methodology section of Chapters 4 and 6. The tensile specimens were coated with graphite, to prevent reflection, and a reflective tape was placed on the specimen to mark out the gauge length. A laser extensometer was used to measure the gauge length during the tensile test.

In order to ensure a consistent analysis of the data, a code was developed with Matlab was used to determine the YS, UTS, and elongation from the load and displacement data. This Matlab code is provided in Appendix A.

3.2.7 Digital image correlation (DIC) along tensile tests

Tensile tests only provide global tensile properties, but, for the interface samples in Chapters 6 and 7, digital image correlation was used with the tensile test in order to determine the local mechanical properties. Jarryd Braithwaite, a trained technician, carried out the sample preparation, set up and calibration, and the tests and post-treatment were conducted by both the technician and student.

3.2.7.1 Set-up

The machine used for the tensile test was the same as described above, with a displacement rate of 1mm/min as well. Specimen were sprayed with white and then black paint in order to generate a pattern on their surfaces as shown in Figure 3.13.



Figure 3.13: Painted sample for DIC testing.

A system of two cameras was placed in front of the specimen; a powerful lighting device was used to ensure a good image. In order to calibrate the camera, a target ($Gl-06-WMB_9x9$) was used to take five pictures in random orientations, and positions. Figure 3.14 shows an example of images taken by a two camera system during its calibration.

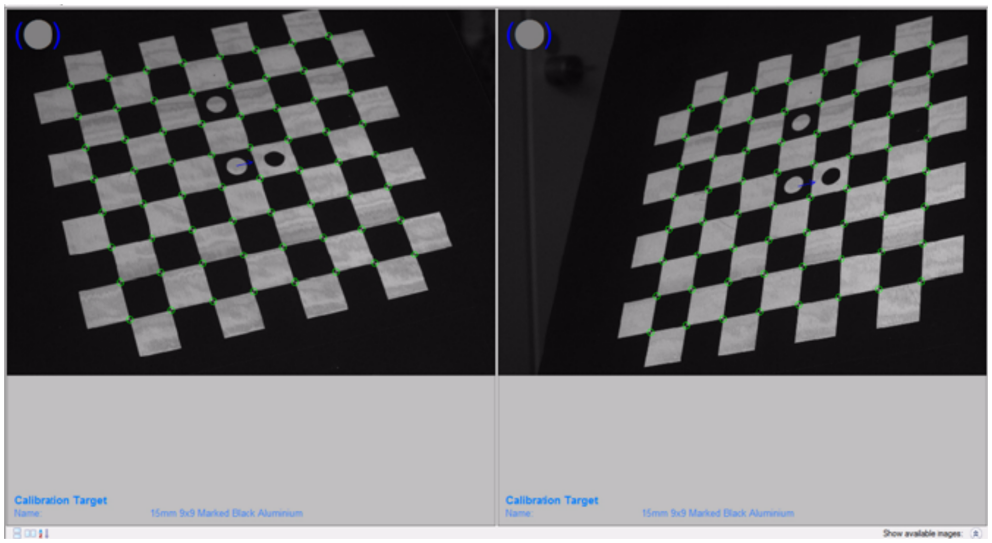


Figure 3.14: Example of images used for the calibration of the double camera system (extract from the equipment manual [13]

During the test, the two cameras recorded the distortions of the painted mesh as if followed the surface of the tested specimen. The frequency of the recording was set to 2 Hz and a resolution of 150 by 100 pixels was used.

3.2.7.2 Yield Strength mapping

Istra 4D software was used to analyse the video and to determine the local strain during the tensile tests: Figure 3.15 shows an example of a strain map provided by the software. However, the built-in analysis tools do not enable the determination of the local yield strength of the material, and only a limited number of data points can be extracted and

analysed manually in a feasible way. A code was therefore developed with Matlab to extract the data and analyse it: the code is provided in the Appendix B.

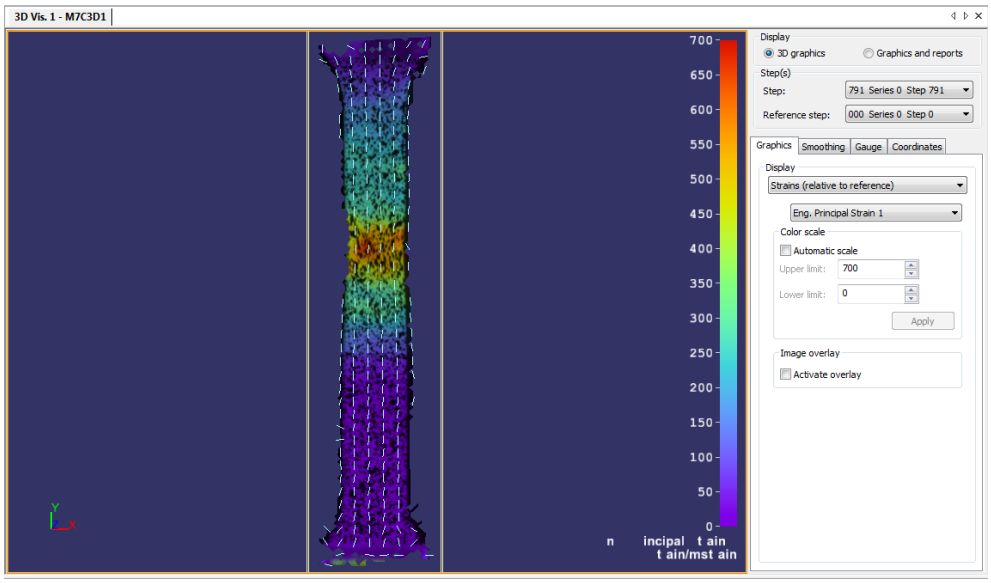


Figure 3.15: Example of a strain map provided by the Istra4D software after the video post treatment

An ASCII file was generated for each recorded step, and the Matlab code extracted the coordinates and principal engineering strain. Stress-strain curves were then generated and the YS was automatically determined for each point. Figure 3.16 shows the principle of the code used and how it generated the YS map shown in Chapter 6 and 7.

It was not possible to evaluate the local Young's modulus of the material because of the high variability of the strain, especially in the low strained: a constant young modulus of 71 MPa was therefore used. Figure 3.17 shows that the strain map is not affected by the Young's modulus: the use of a constant Young's modulus for the YS mapping is therefore not an issue.

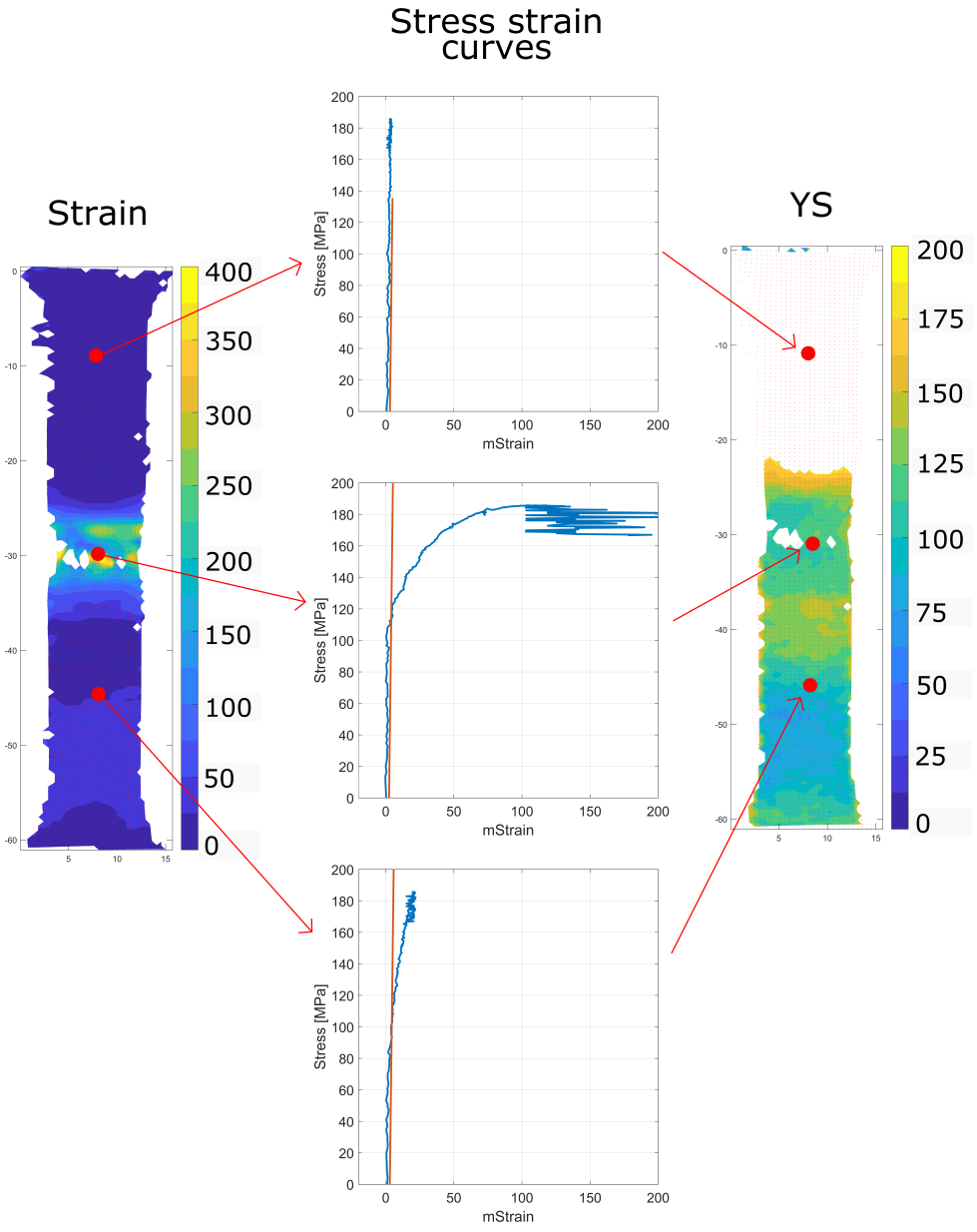


Figure 3.16: Example of three stress-strain curves and YS determination using local strain data

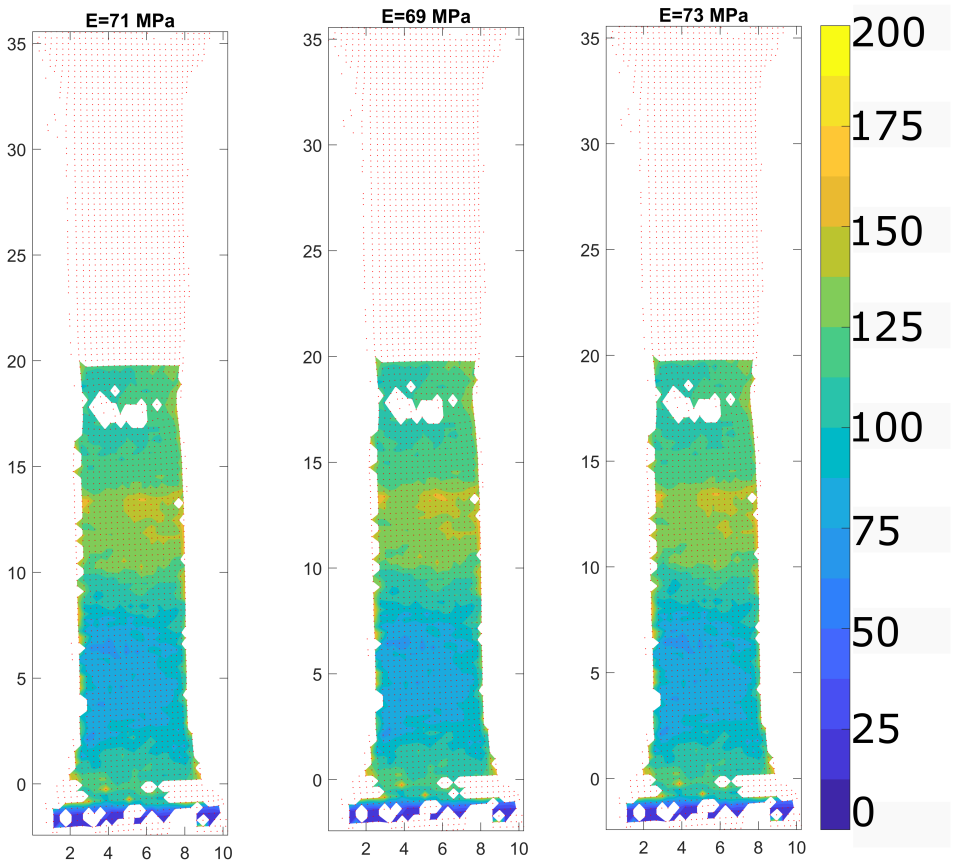


Figure 3.17: YS map calculated with a constant Young's modulus of 69, 71 and 73 MPa

3.3 Materials

Table 3.3 provides the chemical composition of the alloys used in this study. All compositions are indicated in weight percent.

905 and 501 are rapidly cooled alloys with unusual compositions which do not fit with the other alloys in Table 3.3. 905 alloying elements are Fe 2.5, Ni 5, Cu 2.5, Mn 1, Mo 0.8, and Zr 0.8 ; 501 contains Mg 5, Mn 1, Sc 0.8,and Zr 0.4.

Alloy	Form (temper)	Cu	Mg	Mn	Ag	Li	Fe	Si	Zn	Ti
2219	Plate(T8)	5.8-6.8	0.20-0.40	0.20-0.40	...	...	0.30	0.20	0.10	0.02-0.10
2319	Wire	5.8-6.8	0.02	0.20-0.40	...	...	0.30	0.20	0.10	0.10-0.20
2024	Plate(T3)	3.8-4.9	1.2-1.8	0.30-0.9	...	...	0.50	0.50	0.25	0.15
2024*	Wire	4.3	1.16	0.61	...	...	0.25	0.4	0.22	0.1
2139	Plate(T3)	4.5-5.5	0.20-0.8	0.20-0.6	0.15-0.6	...	0.15	0.10	0.25	0.15
2050	Plate(T3)	3.2-3.9	0.20-0.6	0.20-0.50	0.20-0.7	0.7-1.3	0.10	0.08	0.25	0.10
7449	Plate(T7)	1.4-2.1	1.8-2.7	0.20	...	...	0.15	0.12	7.5-8.7	...
6061	Plate(T3)	0.15-0.40	0.8-1.2	0.15	...	...	0.7	0.40-0.8	0.25	0.15

*Measured by EDS

Table 3.3: Material composition defined by the aluminium alloys classification [16] and composition measurement for the 2024 alloy wire

Chapter 4

Mechanical properties of a WAAM Al-Cu-Mg alloy - Effect of deposition process, inter-pass cold work and post-deposition heat treatment

4.1 Introduction

The compatibility between AM and aluminium alloys have been tested for a various range of composition and numerous AM processes. As shown in Chapter 2 2.2.3.4 aluminium silicon, aluminium magnesium and few aluminium copper alloys have been investigated in depth, but aluminium copper magnesium alloys have not. However, some investigations have been reported on these alloys which shows the possibility of depositing these alloy by WAAM (see page 41). 2024 is a well-known alloy from this family and is widely used as aircraft structural alloy as fuselage clad sheets. This alloy is widely considered as unweldable due to its unfavourable solidification behaviour when welded by fusion with

common wire filler alloy. However, this alloy composition has been proven weldable by fusion when using a wire filler of similar composition and suitable for WAAM deposition. Nevertheless, little data can be found in the literature regarding its mechanical properties when deposited. The aim of this study was to report the characteristic mechanical properties of component built by WAAM and correlate to microstructural features of 2024 WAAM.

According to similar research projects on other aluminium alloys, the as-deposited microstructure can be significantly affected by the deposition process. The first objective of this chapter was to evaluate the effect of the deposition process on the bead shape, microstructure, and mechanical properties; the CMT-P and CMT-P-Adv processes described page 55 were used.

2024 is a precipitation hardening alloy, its mechanical properties are therefore affected by the thermal history of the material, the type of microstructure and level of segregation, and can be improved by post-deposition heat treatment. The second objective of this study was to evaluate the potential of heat treatment to improve the mechanical properties of deposited 2024.

Finally, previous work [11, 14] showed the excellent capability of inter-pass rolling to improve the mechanical properties of aluminium copper and aluminium magnesium alloys. The third and last objective of this study was to evaluate the effect of inter-pass rolling on the bead shape, microstructure and mechanical properties of 2024 deposited by WAAM.

4.2 Methodology

The two deposition processes, CMT-P and CMT-P-Adv were introduced in the methodology chapter, as well as the calculation used to determine their respective heat input.

Four 400 mm long wall were deposited using CMT-P and CMT-P-Adv with or without inter-pass rolling on 2024 substrates. A wire feed speed of 6 m/min and a travel speed of 10 mm/s were used with a contact tip to work-piece distance of 11 mm and a local shielding, provided by the power source, of 25 L/min of pure argon. Figure 4.1 shows the diagram of the different conditions tested. For the rolled walls, the roller travel speed was 10 mm/s, and for both rolled and un-rolled walls, the waiting time between layers was two minutes. Figure 4.2 gives photographs of each wall: each wall was divided into two parts, the first one was tested in as-deposited or as inter-pass rolled condition, depending on whether the wall was inter-pass rolled or not, while the sample taken from the second part of the wall were heat treated. As illustrated in Figure 4.3, four tensile specimens were tested in the horizontal and vertical directions, and some material in the centre of the wall was kept for the microstructural study.

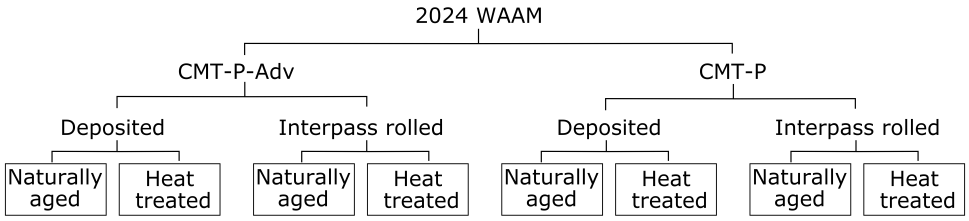


Figure 4.1: Diagram of the different conditions tested

To avoid quench cracking due to the high surface waviness that rolling introduces (see in Figure 4.6). Rectangular blocks of material were cut and pre-machined to a thickness of 5 mm before heat treatment. These blocks were heat treated to T6 conditions before they were further machined to the final dimensions of the tensile specimens. A two-step heat treatment was used : the material was first solution treated at 498°C for 90 minutes and quenched in room temperature water; then, ageing was carried out for 10 hours at 177°C. The set up and deposition parameters, rolling and tensile testing procedure as well as the microstructure study was carried out following the methodology detailed in the sections

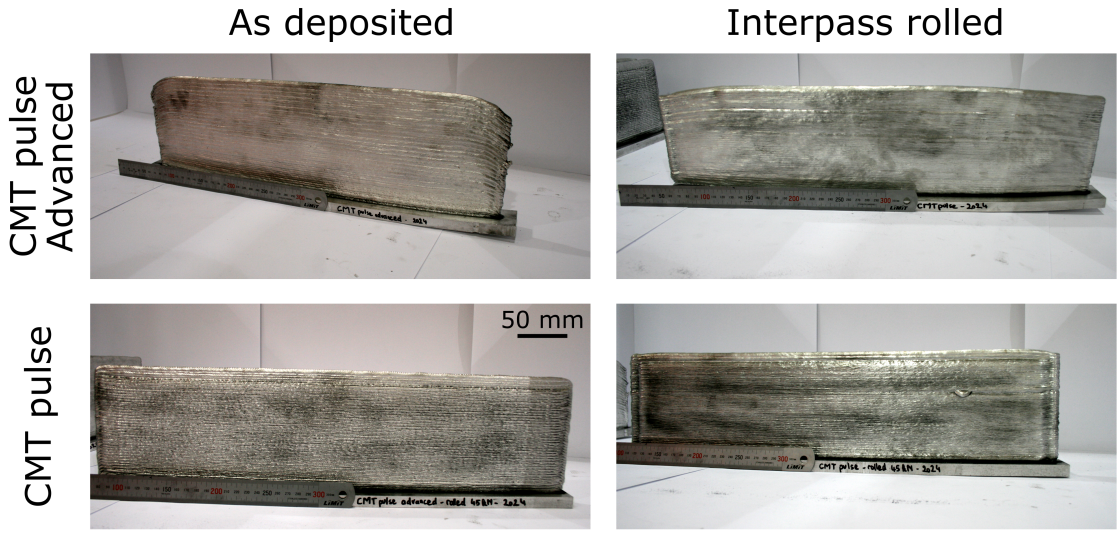


Figure 4.2: Four wall deposited with two deposition processes and with or without inter-pass rolling

3.1.1.1, 3.2.6 and 3.2 of Chapter 3.

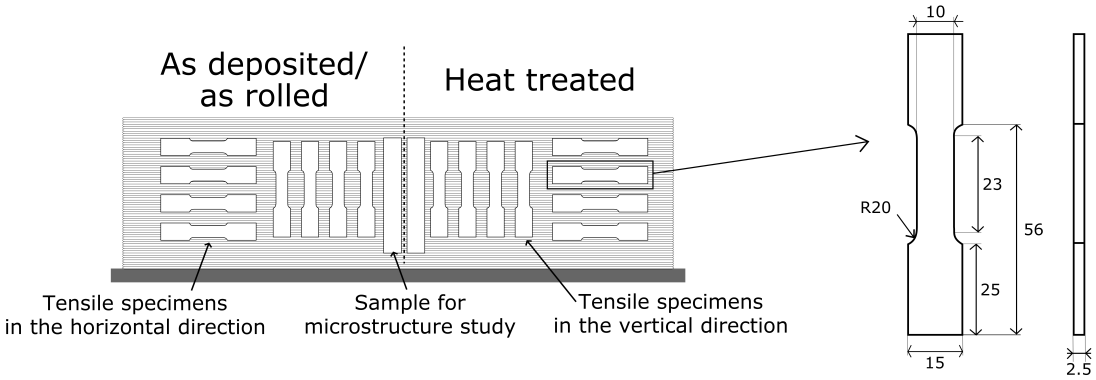


Figure 4.3: Samples position in each wall and tensile specimen dimensions

4.3 Results

4.3.1 Macro and microstructure

4.3.1.1 Geometry

Deposition process and rolling have a significant effect on the bead shape. Table 4.1 provides the bead geometry characteristics for each condition. The measurements of the Total Wall Width (TWW), Effective wall width (EWW) and Surface Waviness (SW) are shown in Figure 4.4 (a). The SW, provided in Table 4.1, was determined by the following equation:

$$SW = \frac{TWW - EWW}{2} \tag{4.1}$$

The re-melting depth of the as-deposited material was determined by subtracting the average layer height from the top layer height, as shown in Figure 4.4 (b). The re-melting depths of the rolled samples were measured at the top of the walls.

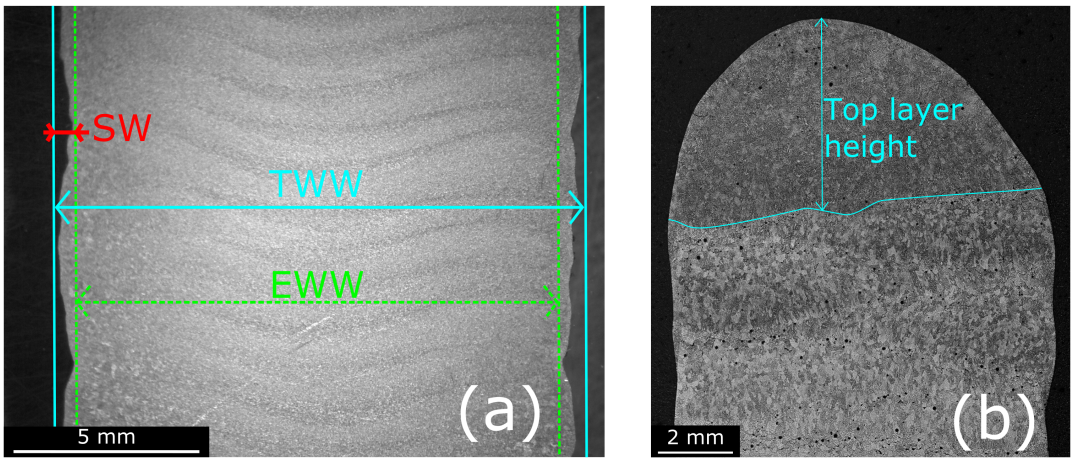


Figure 4.4: Illustration of the metrics used to characterise (a) the wall geometry and (b) the re-melting zone

Table 4.1: Characterisation of wall geometry

		TWW [mm]	EWW [mm]	SW [mm]	LH [mm]	Re-melting depth [mm]	% deformation
CMT-P Advanced							
	Un-rolled	6.0	4.2	0.9	2.53	2	
	Rolled	10.6	8.5	1.1	1.35	1.3	47 %
CMT-P							
	Un-rolled	10.3	8.9	0.7	1.29	3.7	
	Rolled	13.3	12.2	0.5	0.93	1.8	28 %

In as-deposited condition, the layer width and re-melting depth are smaller, and the layer height is higher if CMT-P-Adv is used when compared with CMT-P. This is due to the lower heat input of CMT-P-Adv process as compared to CMT-P (120 against 234 J/mm): as shown by Martin et al.[128] in titanium deposition, heat input drastically impacts the bead shape in WAAM deposition. The surface waviness of the CMT-P wall is lower than that of CMT-P-Adv, showing the former deposition process generates a more regular wall geometry. This is mainly due to the higher bead width to bead height ratio of the CMT-P process.

Inter-pass rolling reduces the layer height, leading to a percentage of deformation of 47 % and 36 % for the wall deposited with CMT-P-Adv and CMT-P respectively. However the rolling pressures calculated using the equations 3.1.1.1 and detailed in Chapter 3, are 501 and 832 MPa for the CMT-P-Adv wall and the CMT-P deposited wall, respectively. It is important to highlight here that these pressures were calculated based on the last rolled bead geometry and a slight change in layer height or rolling width measurement have a drastic impact on these values. For instance, a measurement error of $\pm$ 0.05 mm in the layer height leads to an error of $\pm$ 100 MPa in rolling pressure. Therefore these values of rolling pressure need to be considered carefully.

Despite this high variability of measurement, it seems that the material undergoing the highest total deformation is not the one rolled at the highest pressure: this shows that the initial bead geometry plays a crucial role in the reduction of layer height. Figure 4.5 shows a schematic of the top of the wall, before and after the rolling of the top layer. These diagrams show that inter-pass rolling affects the top bead but also the previous layer, themselves being inter-pass rolled. Also, the remelting depth is lower than the LH when CMT-P-Adv process is used, but considerably larger than the LH when the CMT-P process is used.

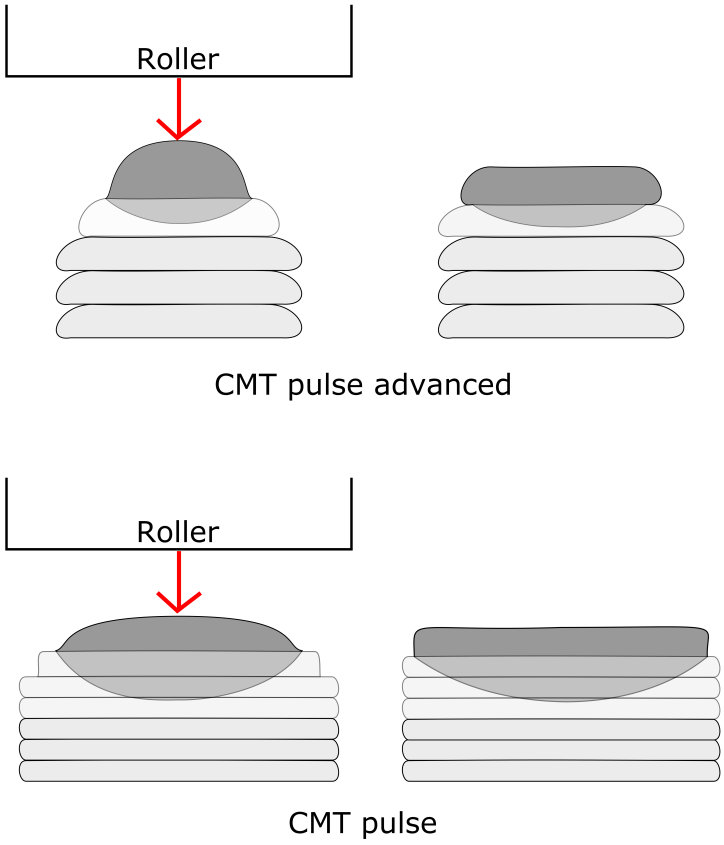


Figure 4.5: Schematic of the effect of inter-pass rolling on the wall geometry

Figure 4.6 shows that micro-crack can be seen in between layers, on the side of the wall deposited with CMT-P-Adv process. In line with the crack, shown in the high mag-

nification image, numerous micropores can be observed. No cracks of this nature were observed in the CMT-P wall.

When CMT-P-Adv is used, the SW increases with rolling because of rolling generates bulges on the edges of the wall. However, when CMT-P is used, the SW is reduced by rolling. In both cases, the TW is increased by inter-pass rolling, and therefore, the effective wall width is increased by 50% for the samples deposited by CMT-P-Adv and by 38% for the samples deposited with CMT-P.

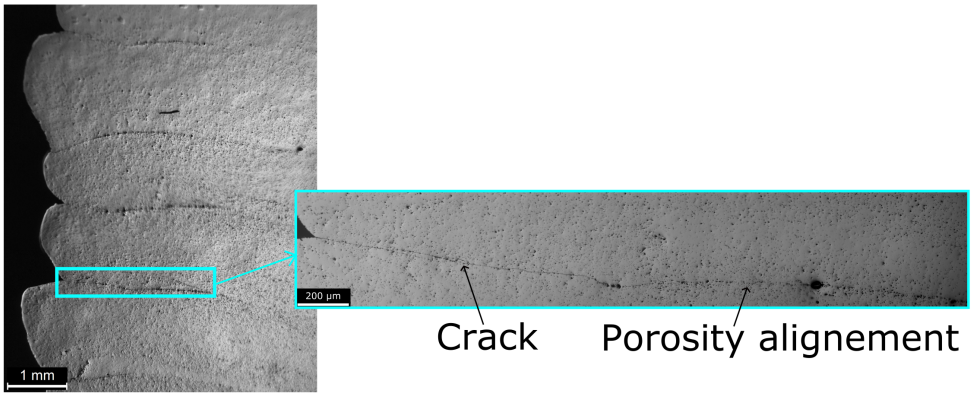


Figure 4.6: Illustration of the metrics used to characterise the wall geometry

4.3.1.2 Microstructure

CMT-P-Adv samples

Figure 4.7 shows the microstructures of the material deposited with CMT-P-Adv process. The microstructures of the as-deposited sample mainly consist of dendritic equiaxed grains, and columnar grains can be seen at the boundaries between layers. After heat treatment, the grain merge and form coarse grains, but no significant grain growth was visible. In both as-deposited and as heat treated conditions, some micro-cracks can be seen at grain boundaries.

This microstructure was drastically changed by inter-layer rolling. The microstructure

of the rolled CMT-P-Adv specimen is non-homogeneous: a clear line of coarse equiaxed grains can be seen between layers, and across the whole wall width. This line becomes wider on the side of the wall. The rest of the microstructure is composed of small equiaxed grain, much smaller than the as-deposited sample. After heat treatment, the microstructure is more homogeneous mainly because of partial recrystallisation. It is still possible to observe coarse grain alignment between layers and on the side of the wall.

The SEM images provided in Figure 4.8 (a) show a microcrack at the edge of the wall, similarly to what was shown in Figure 4.6. In line with this crack, it is possible to see a white line going across the wall in picture (b). This copper-rich line could have a detrimental effect regarding tensile properties in the vertical direction. After heat treatment, there is a risk of propagating these cracks because of the high-stress concentration points at the notches generated by rolling and the high thermal stress applied to the material during the quench. Picture 4.8 (c) gives an example of a crack propagated by heat treatment. In the alignment of this crack, it is still possible to observe a alignment of second phases, not totally solutionised during the solution treatment.

Figure 4.9 provides high magnification SEM images of the four conditions in pictures (a), (b), (c), and (d). The as-deposited sample, in picture (a) contains large and coarse copper-rich particles. After heat treatment, a large quantity of this copper-rich network is solutionised in the matrix: as shown in picture (b), there are much less copper rich particles, and this even after ageing. Picture (c) shows that inter-pass rolling affected the distribution of the copper-rich areas: they are fractured and elongated by the rolling load. After the heat treatment of the rolled sample, most of the eutectic compound is solutionised (picture (d)), or form precipitates invisible at this magnification, and the copper-rich particles left are smaller than the one observed in the un-rolled heat treated sample (picture (b)).

These observations are very similar to the observations made by Gu et al. [11] on

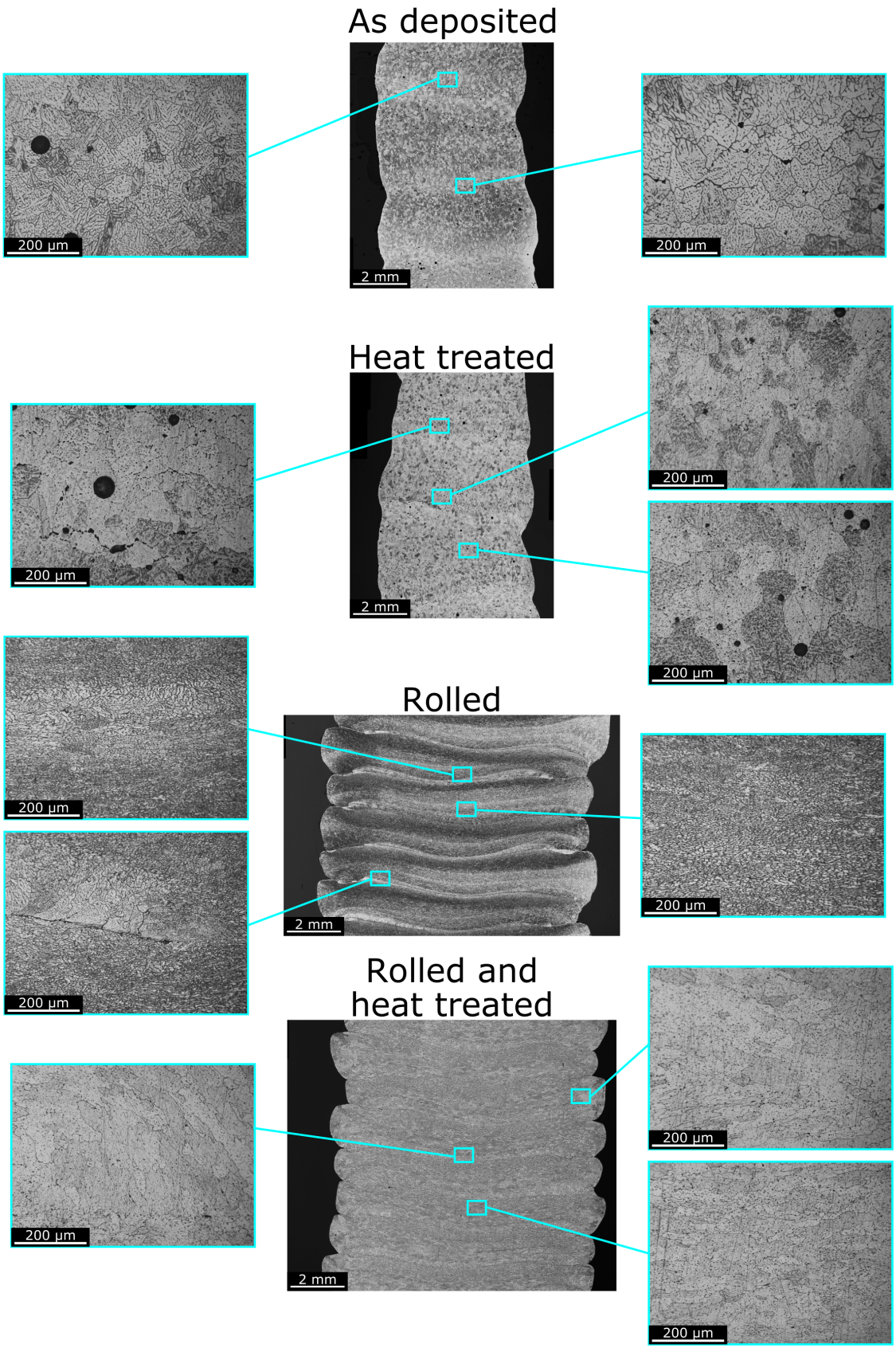


Figure 4.7: Optical images of as-deposited , heat treated , as-rolled, and as-rolled then heat treated samples deposited with CMT-P-Adv process

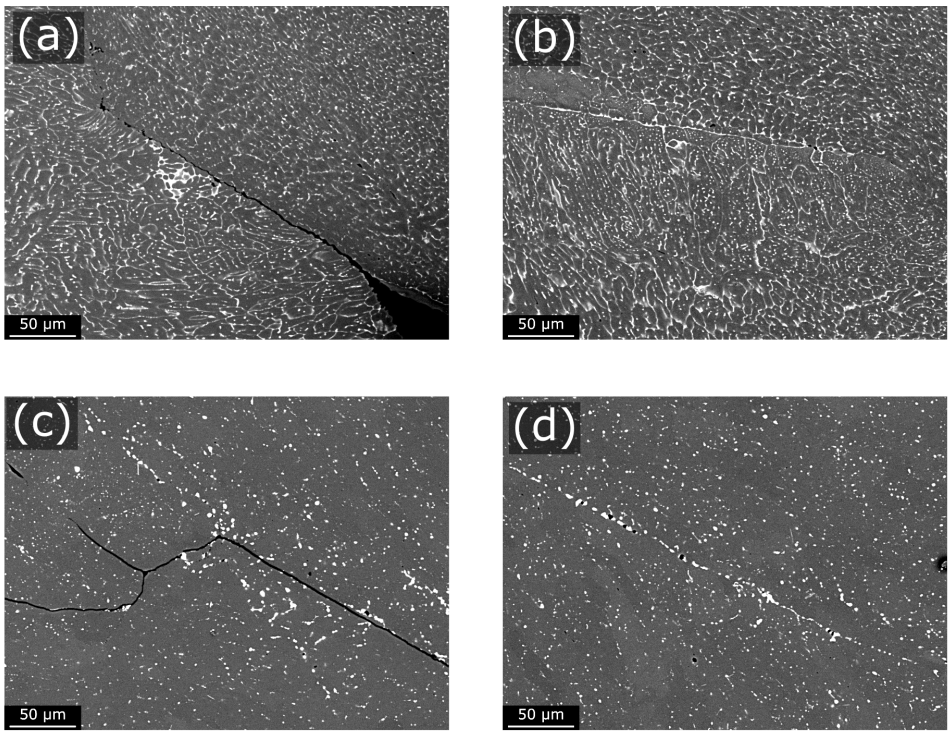


Figure 4.8: SEM images of the inter-pass rolled wall deposited with CMT-P-Adv process (a) and (b) in as rolled condition, and (c) and (d) in rolled and heat treated condition

2319 deposition. The amount and the distribution of copper-rich phases largely depend on the solidification behaviour, and the subsequent thermal cycle applied to the material. The solidification rate in WAAM is not high enough to avoid the formation of these areas during deposition. Furthermore, during the deposition of the subsequent layers, numerous phase of re-melting, re-heating, and cooling are applied to the material, leading to coarser copper-rich areas. During rolling, these particles are fractured into small and elongated areas: these particles are then easier to solutionised. Also, solutionising is faster in presence of dislocations and other lattice imperfections: the dislocation generated by inter-pass rolling facilitate the solutionising of the copper rich particles.

It is important to highlight here that a significant amount of un-solutionised copper can be observed, even after heat treatment. This was observed and expected in the case of

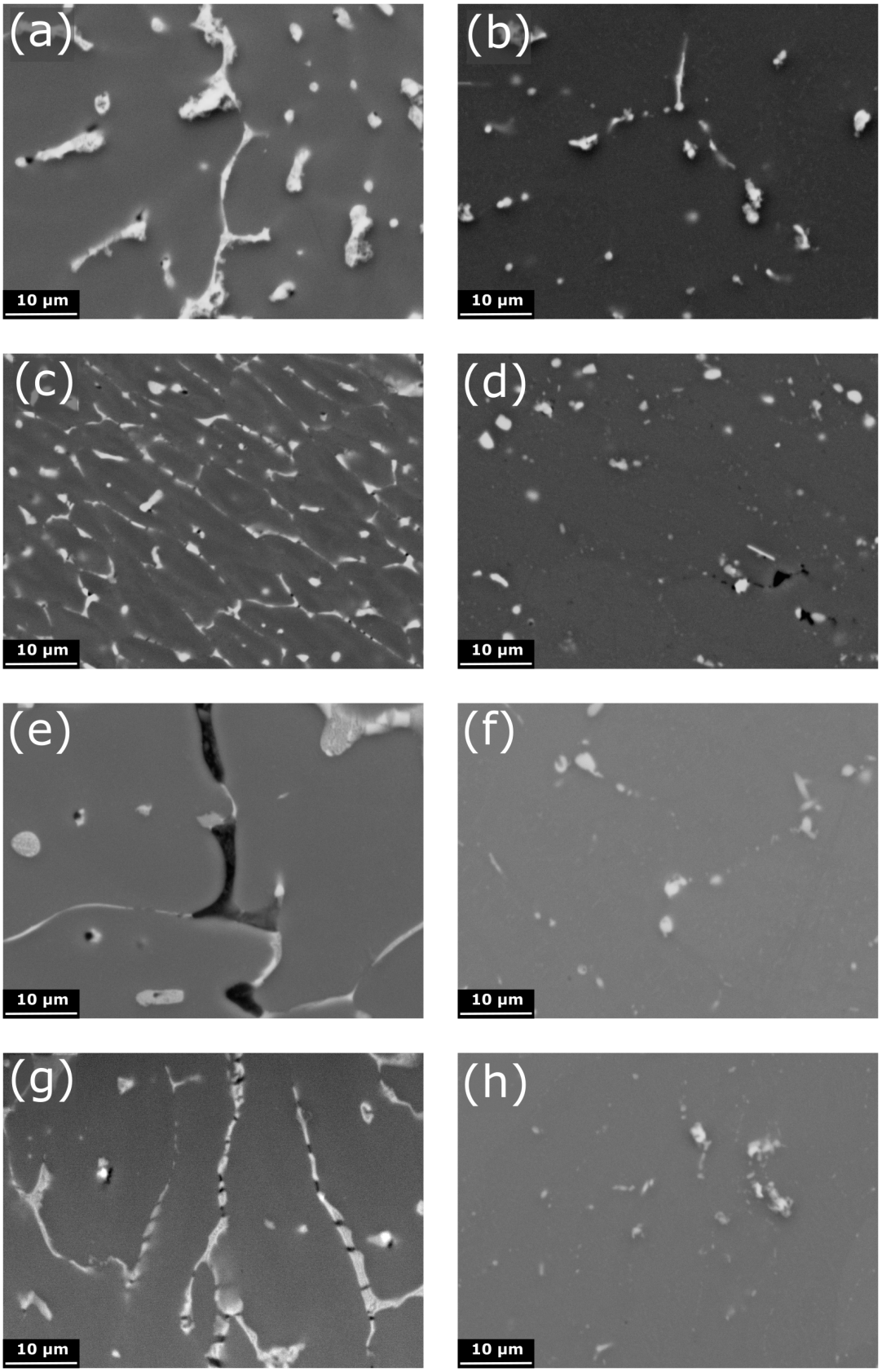


Figure 4.9: High magnification SEM images of CMT-P-Adv (a) as-deposited, (b) heat treated, (c) as-rolled, and (d) as rolled then heat treated; and CMT-P (e) as-deposited, (f) heat treated, (g) as-rolled and (h) as rolled then heat treated

heat treated WAAM 2319 [11] because 2319 is a saturated alloy: the maximum solubility of copper in solid aluminium is 5.75 wt% at 548°C and the copper content of 2319 is between 5.8 and 6.8 wt%. However, the copper content in 2024 is 4.5 wt%: the copper solubility in the aluminium matrix does not prevent a full solutionising. The amount of second phases left after heat treatment could be due to a solution treatment too short or too low in temperature. This means the properties of this material after heat treatment could probably be optimised by using a different heat treatment than the one carried out in this study.

CMT-P samples

Figure 4.10 shows the microstructures of samples deposited with CMT-P process. The as-deposited microstructure is mainly made of dendritic grains, with some small columnar grains and pore alignments between layers. After heat treatment, the dendritic grains are transformed into coarse grains and large areas are covered by small columnar grains. At the edge of the wall, some small areas covered with much smaller equiaxed grain than the grains observed in the rest of the sample. The SEM images in Figure 4.11 shows the effect of heat treatment on these areas. In the as-deposited conditions, picture (a) shows that numerous voids can be seen in these dendritic regions. This type of micro voids can also be observed in the rest of the sample: as shown in Figure 4.11 (a), some can be observed in between layers. These are segregation voids due to the solidification shrinkage. Due to the low mechanical constrains around the melt pool during deposition, these micro voids did not lead to hot cracking. Heat treatment seems to be beneficial regarding these micro-voids: Figure 4.11 picture (b) shows that they can be recovered especially at the edges of the wall. This recovery could be due to the diffusion of alloying elements from the copper rich zones.

When inter-pass rolling is carried out, the microstructure becomes much thinner: tiny

equiaxed grain can be observed in the middle of the sample. The change in colour visible in the low magnification image is due to the slight change in grain size and nature, from equiaxed to dendritic, occurring in between, but also inside the layer. It is difficult to say if these lines are situated at the layer boundary or not, because of the considerable re-melting occurring during the deposition of this sample. The grains are larger on the edge of the sample. As shown in Figure 4.12 picture (b), pores are crushed during rolling, and the amount of micro void observed was drastically reduced.

Heat treatment increases the grain size, and leads to a more uniform microstructure. However, some horizontal lines can still be observed: they seem to be caused by a change of grain orientation. The grain size increases from the centre to the edge of the deposit.

Figure 4.9 shows high magnification SEM images of (e) as-deposited, (f) heat treated, (g) as-rolled, and (h) rolled then heat treated material. Image (e) shows a good example of the numerous micro-voids observed in the as-deposited condition. Large second phases can also be observed; these are similar to the one observed in the CMT-P-Adv as-deposited sample in image (a). After heat treatment, the number of micro voids was reduced, and a large part of the copper-rich areas was solutionised in the aluminium matrix. Inter-pass rolling reduces drastically the micro-void density but, unlike what was observed for the CMT-P-Adv rolled sample, inter-pass rolling does not affect the size of the copper-rich particles. Nevertheless, inter-pass rolling elongates and severed the copper-rich phases. After heat treatment, the microstructure of the rolled sample is very similar to that of the heat treated unrolled specimen.

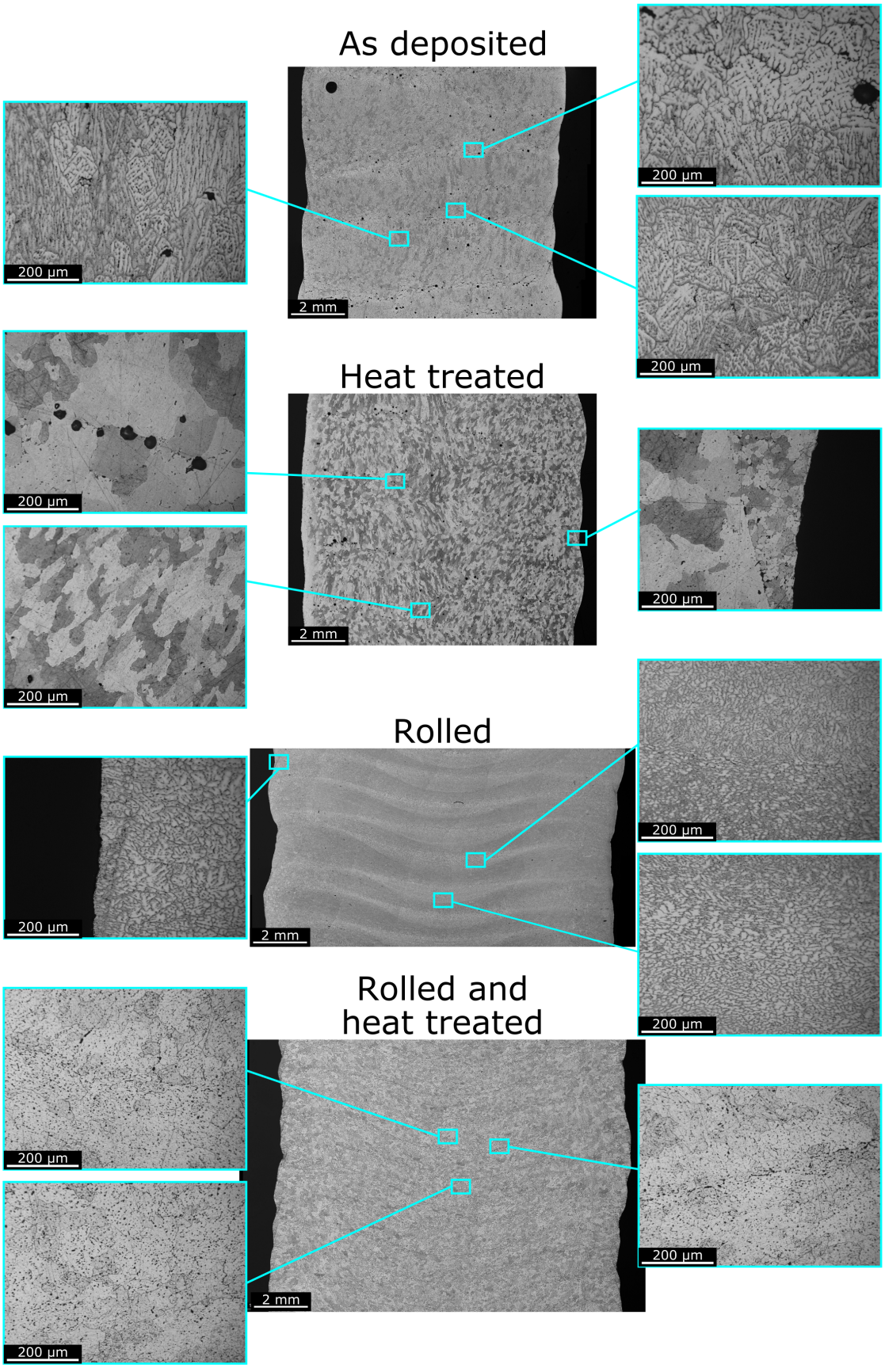


Figure 4.10: Optical images of as-deposited, as heat treated, as-rolled, and rolled then heat treated samples deposited with CMT-P process

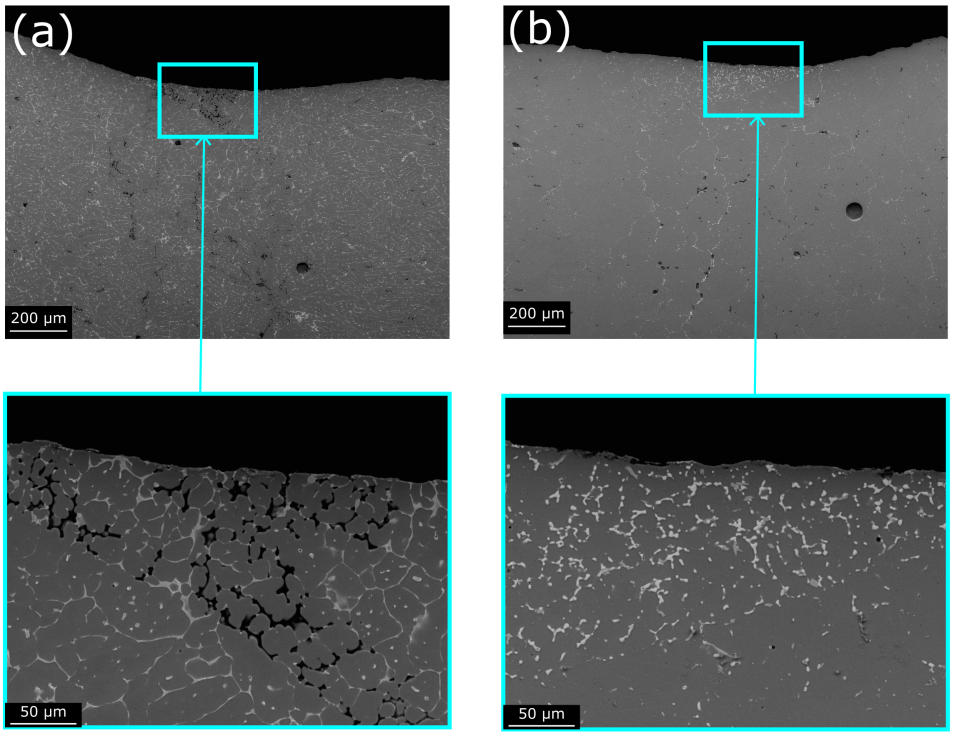


Figure 4.11: SEM images of the edge of the wall deposited with CMT-P process, in as-deposited(a) and as heat treated (b) condition

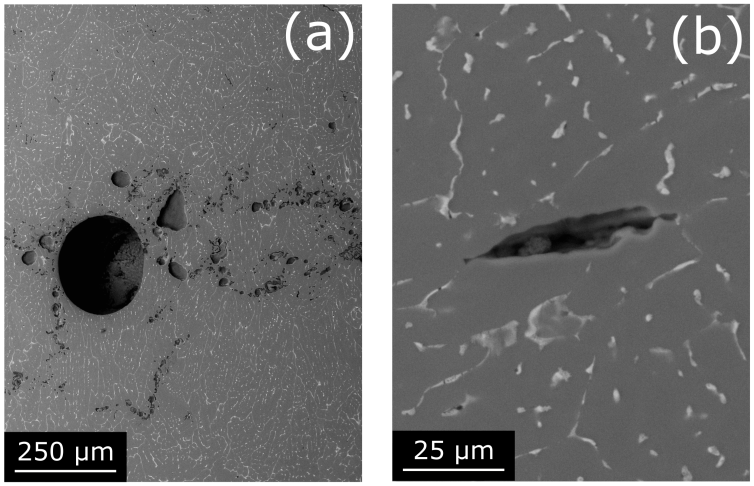


Figure 4.12: SEM image of typical defects observed in (a) the as-deposited CMT-P and (b) as-rolled samples

4.3.2 Porosity

Figure 4.13 provides the results of the porosity analysis. For the CMT-P-Adv samples, it shows a drastic reduction of pores of all sizes when inter-pass rolling is applied; however, porosity was not eliminated. An increase by more than 55 % of the number of small pores occurred in both un-rolled and rolled samples during heat treatment. However, there was no significant change in the number of large pores after heat treatment. The drastic reduction of porosity due to inter-pass rolling was already shown on 2319 and 5087 alloys by Gu et al.[5]. Heat treatment does not significantly affect the number of small pore for the CMT-P material, but increases the number of large ones.

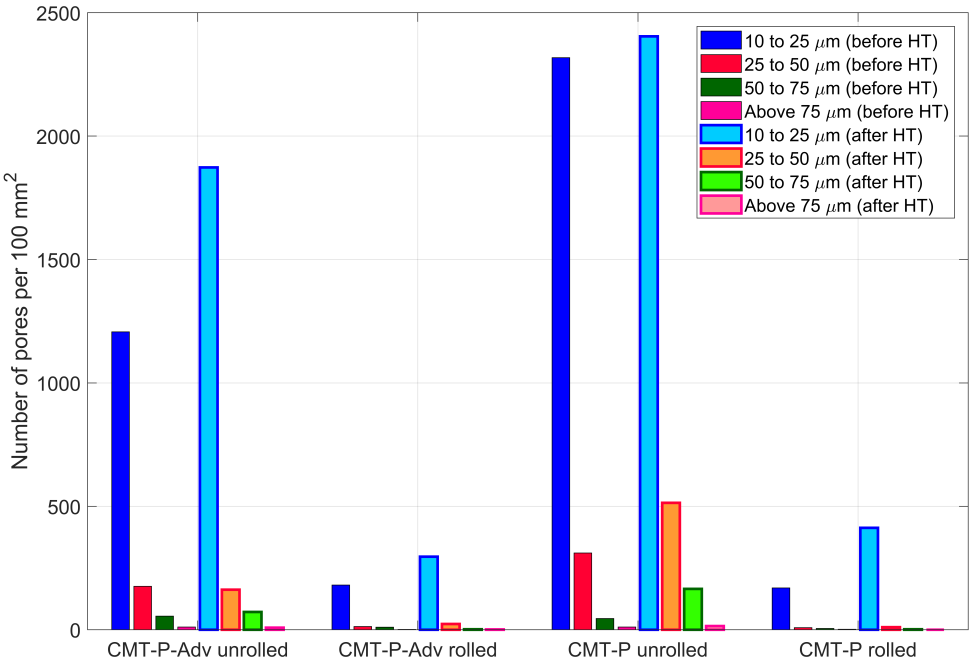


Figure 4.13: Number of pores per 100 mm^2 measured for each condition

In a similar manner, inter-pass rolling drastically decreases pore number, and this for all pore sizes for the samples deposited with CMT-P process. In the as-deposited condition, the pores density is higher than that for the CMT-P-Adv sample. This is due to the use of alternative current during CMT-P-Adv, known for its beneficial wire cleaning and porosity reduction [12, 68].

4.3.3 Chemical composition

Table 4.2 shows the composition of the wire and deposited material. The composition in Ti an Mn seems to be not affected by the deposition regardless of the process used. No zinc concentration was measured in the deposited material whereas the wire composition analysis shows a low level of this element. This can be explained by the low vaporisation point of this element, leading to its loss during the deposition. The level of silicon and iron is also considerably reduced during the deposition. The concentration of magnesium is slightly higher in the deposited material than in the wire. This is due to the loss of the other elements which increases the concentration of magnesium.

No significant effect of the deposition process can be observed regarding the measured composition.

Table 4.2: Chemical composition of the wire and deposited material determined by EDS

	Mg	Cu	Ti	Mn	Si	Zn	Fe
Wire	1.16	4.33	0.11	0.61	0.41	0.22	0.25
CMT-P as deposited	1.23	4.41	0.10	0.63	0.15	-	0.09
CMT-P rolled	1.34	4.50	0.07	064	0.08	-	0.06
CMT-P-Avd as deposited	1.32	4.63	0.10	0.66	0.11	0.01	0.09
CMT-P-Avd rolled	1.23	4.38	0.06	0.65	0.08	-	0.06

4.3.4 Micro hardness

Table 4.3 provides the micro hardness measured on each cross section. Apart from the as-rolled configuration, there is no significant effect of the process on the micro hardness. Heat treatment increases the hardness from 100 HV to about 140 HV when applied to as-deposited material or rolled samples, regardless of the deposition process used.

Rolling does not have any significant effect on the samples built with CMT-P process. This is due to the depth of the re-melting zone: all the dislocations generated by inter-pass rolling and which strengthened the material are dissolved during the considerable re-melting occurring during the deposition of the subsequent layer.

However, inter-layer rolling drastically increases the hardness of the samples built with CMT-P-Adv process, up to the value of 128 HV. Gu et al. showed that there is a linear relationship between hardness and percentage of deformation increase for inter-pass rolled 2319 [11] and Al-Mg4.5Mn [14]; the values from these papers are reported in the plot in Figure 4.14. This graph shows that the increase rate in hardness is very similar for these three alloys: the strengthening effect seems to be independent of the alloy composition.

Table 4.3: Micro hardness values

		Before heat treatment	After heat treatment
CMT-P-Adv			
	Un-rolled	103 ± 7	140 ± 5
	Rolled	128 ± 5	141 ± 6
CMT-P			
	Un-rolled	100 ± 11	132 ± 13
	Rolled	105 ± 5	142 ± 6

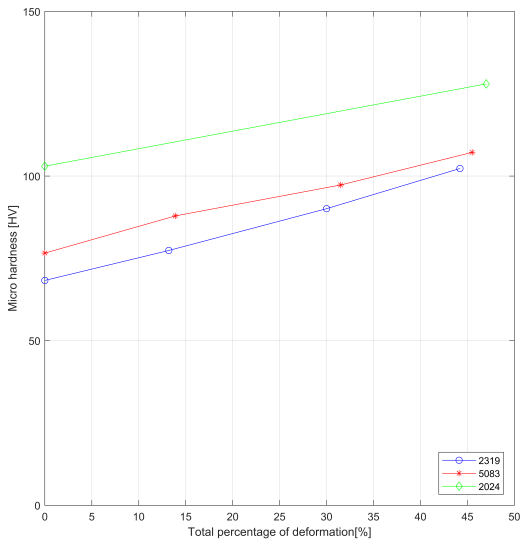


Figure 4.14: Relationship between total deformation and micro hardness for inter-pass rolled 2319 [11], 5087 [14], and 2024 alloys

4.3.5 Tensile tests results

Tables 4.4 and 4.5 provide the mechanical properties obtained for each configuration with specimen built using CMT-P-Adv and CMT-P process respectively.

4.3.5.1 CMT-P advance results

In as-deposited condition, the UTS and elongation in the vertical direction are much lower than in the horizontal direction, but the YS is not significantly different.

In the horizontal direction, rolling increases the YS and UTS but has no effect on the elongation. In the vertical direction, rolling drastically improves the YS but has no significant effect on the UTS; it drastically reduces the samples ductility leading to a very poor elongation. According to Gu et al., when inter-layer rolling is carried out on 2319 WAAM, the elongation is considerably reduced in both directions: it goes from 19 % to 9 % in the horizontal direction [11]. However, inter-layer rolling does not drastically

Table 4.4: Tensile test results for CMT-P-Adv process

CMT-P Advanced		As-deposited	as-rolled	Heat treated	Rolled and heat treated
YS [MPa]					
	Horizontal	204 ± 2	308 ± 7	262 ± 8	283 ± 10
	Vertical	186 ± 12	273 ± 16	259 ± 9	284 ± 2
UTS [MPa]					
	Horizontal	324 ± 5	394 ± 7	429 ± 2	467 ± 5
	Vertical	267 ± 1	280 ± 22.0	340 ± 12	411 ± 35
Elongation [%]					
	Horizontal	7.7 ± 1.4	7.3 ± 1.0	10.7 ± 1.4	22.6 ± 2.0
	Vertical	2.4 ± 0.1	0.5 ± 0.2	2.6 ± 0.6	6.0 ± 2.0

affect the elongation of horizontal specimen made of Al-Mg4.5Mn alloy (22.4 % for as-deposited material, and 20.1% for the as-rolled material) [14]. According to the authors, the reason why rolling can increase the material strength without affecting its plasticity is the high grain refinement induced by rolling. If the grain size is not a critical factor regarding the mechanical properties of precipitation hardening alloys such as 2319, it plays a key role in strain hardening material, such as aluminium magnesium alloys. In this present study, the absence of ductility loss in the horizontal direction when inter-layer rolling is carried out could be due to a reduction of grain size and a drastic reduction of defects, which compensates the material ductility loss.

Heat treatment applied on as-deposited samples improves the YS in both directions which remain the same. However, the difference in UTS and elongation between both directions is still high, and the elongation in the vertical direction is low.

When heat treatment is applied on rolled samples, the YS are the same in both directions and slightly higher than the YS measured in the case of heat treatment of un-rolled specimens. Both UTS and elongation of this material are also significantly higher than those reached by heat treated material. Finally, rolling also decreases the anisotropy: in

as heat treated condition, the UTS in the vertical direction reaches 79% of the horizontal direction against 88 % if inter-pass rolling is carried out before heat treatment.

4.3.5.2 CMT-P results

In all configurations, the YS in the vertical direction is not significantly lower in the vertical direction compared with the horizontal direction.

The UTS and elongation of the as-deposited configuration are much lower than the one obtained for the samples built with CMT-P-Adv process.

Inter-pass rolling improves all YS, UTS and elongation and reduces the anisotropy: the UTS measured in the vertical direction is 95% of the horizontal one, against 80 % in the as-deposited condition.

When heat treatment is carried out on as-deposited samples, there is a significant increase of YS and UTS, but the elongation is not changed and stays low. As in the as-rolled condition, the gap of UTS between horizontal and vertical direction is relatively low (vertical UTS = 95 % horizontal UTS).

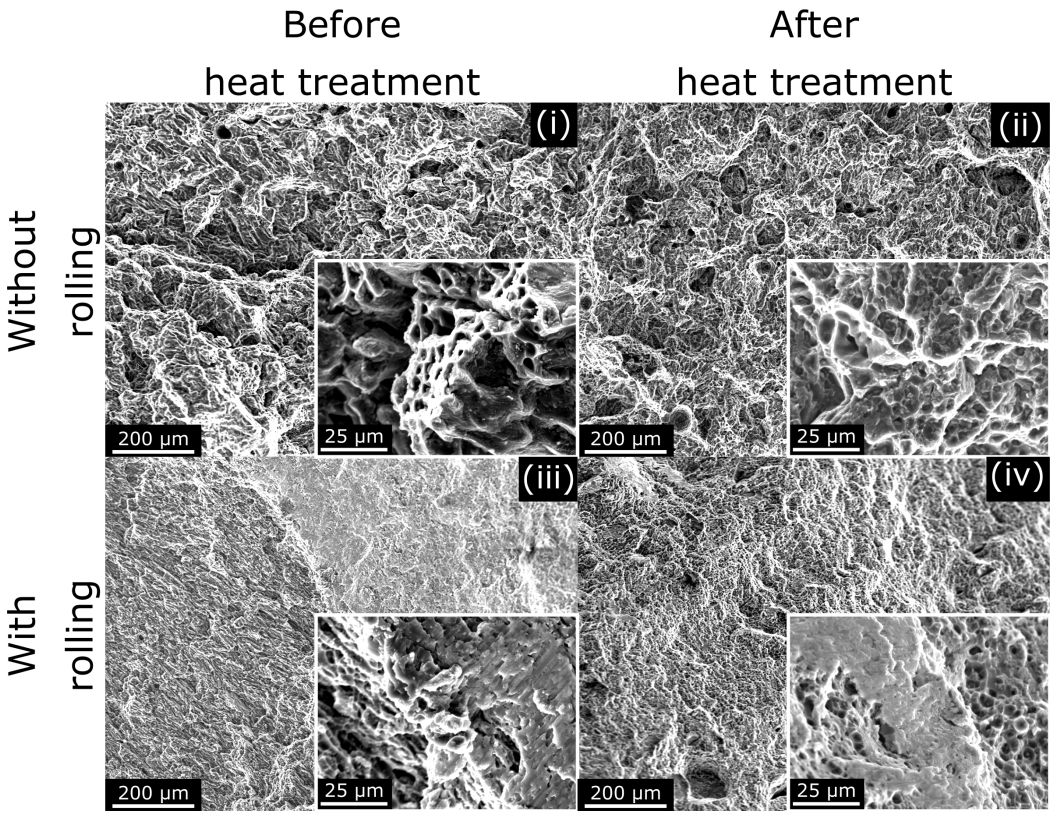
The rolled and heat treated samples achieve a slightly higher YS and a much greater UTS and elongation compared with un-rolled heat treated samples, with an improvement in elongation of 1000 % and UTS of 40 % in the horizontal direction. As for the CMT-P-Adv deposited material, carrying out inter-pass rolling before heat treatment reduces the material anisotropy.

Table 4.5: Tensile test results for CMT-P process

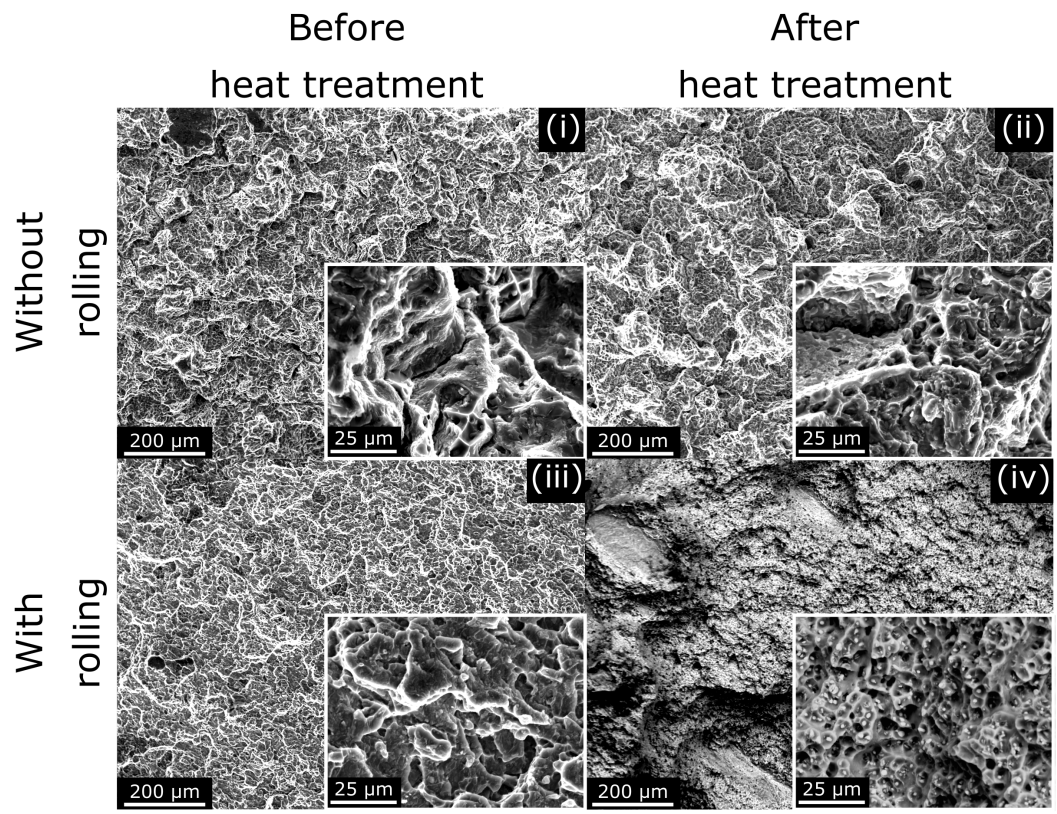
CMT-P		As-deposited	As-rolled	Heat treated	Rolled and heat treated
YS [MPa]					
	Horizontal	178 ± 9	221 ± 6	263 ± 5	301 ± 7
	Vertical	163 ± 12	210 ± 5	261 ± 20	290 ± 6
UTS [MPa]					
	Horizontal	260 ± 10	328 ± 4	328 ± 23	468 ± 10
	Vertical	210 ± 16.0	313 ± 4	314 ± 12	444 ± 4
Elongation [%]					
	Horizontal	2.9 ± 0.4	12.4 ± 0.2	2.6 ± 0.8	20.6 ± 2.0
	Vertical	1.4 ± 0.5	6.2 ± 0.8	1.6 ± 0.1	9.8 ± 0.7

4.3.6 Fractography

Figures 4.15 and 4.16 provide SEM images of tensile specimen rupture surfaces for CMT-P-Adv and CMT-P deposition respectively. Both figures are divided into two sub-figures depending on the tested direction, and each sub-figure shows the rupture of an (i) as-deposited, (ii) as heat treated, (iii) as-rolled and (iv) as-rolled then heat treated specimen.

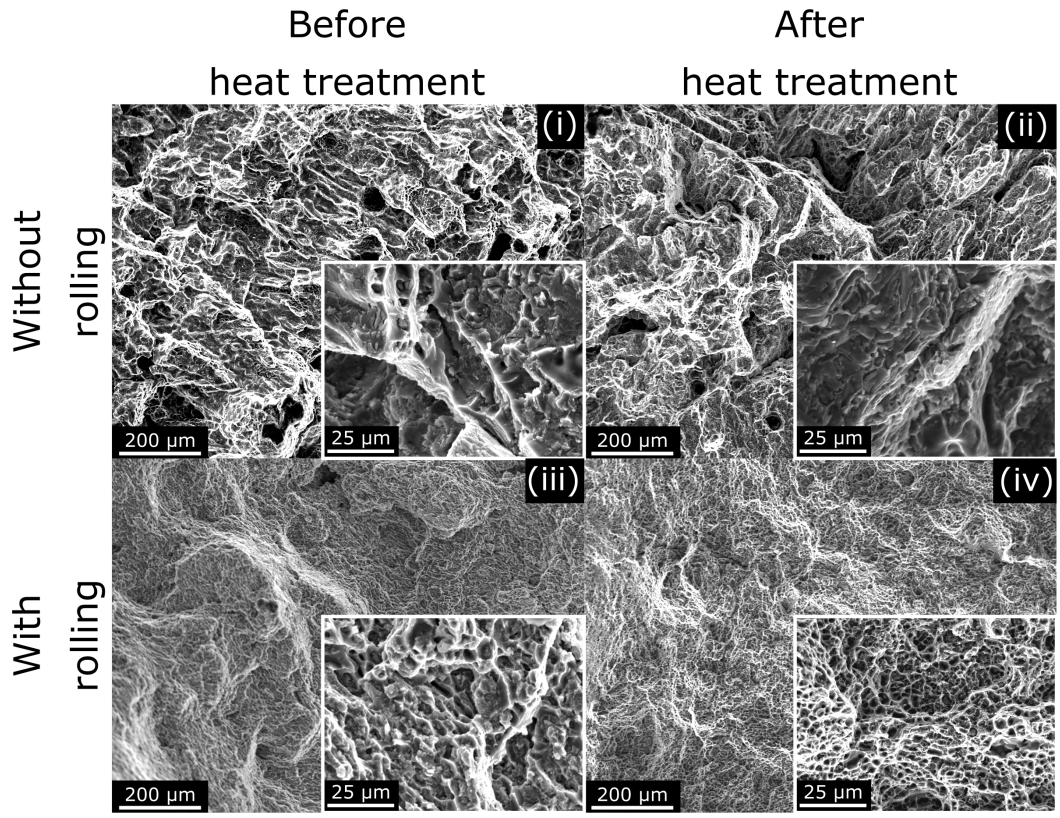


(a) Horizontal direction

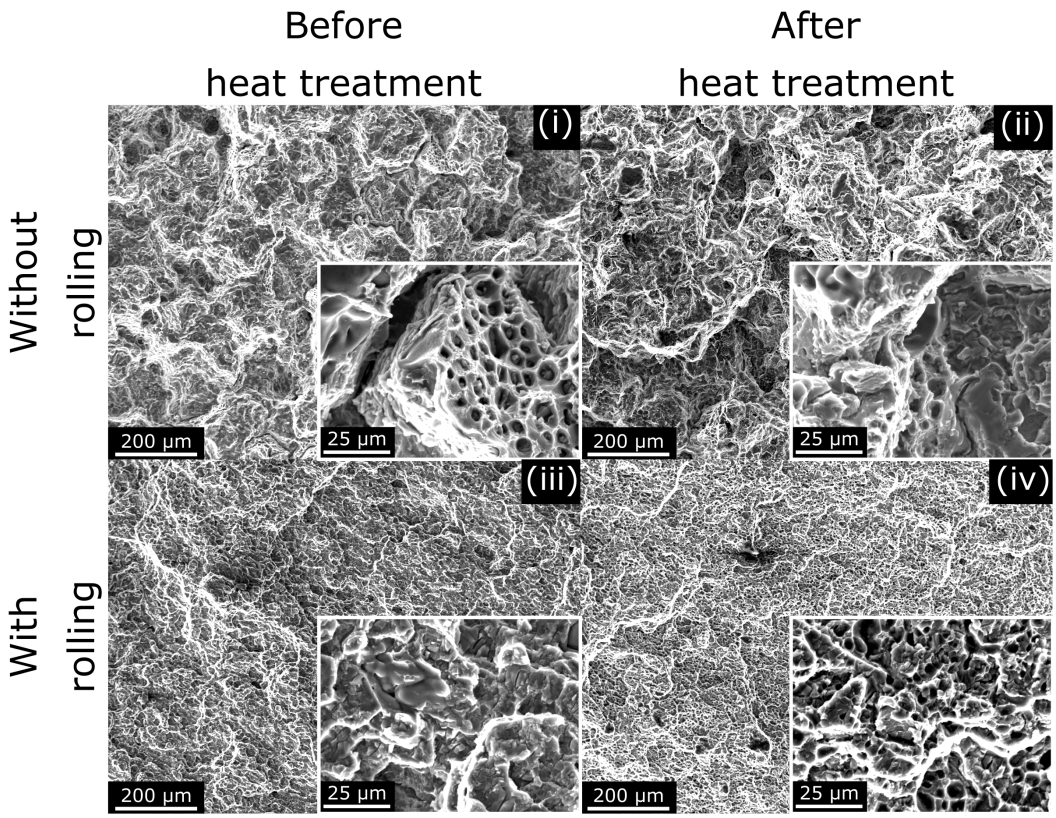


(b) Vertical direction

Figure 4.15: Ruptures surfaces of specimens taken from material deposited with CMT-P-Adv process



(a) Horizontal direction



(b) Vertical direction

Figure 4.16: Ruptures surfaces of specimens taken from material deposited with CMT-P process

4.3.6.1 CMT-P-Adv specimens

Horizontal direction

Figure 4.15a shows the rupture surfaces of specimens manufactured using CMT-P-Adv process and tested in the horizontal direction.

Picture (i) shows the as-deposited specimen: the rupture surface is heterogeneous, with very ductile areas covered with dimples, and large zones showing a moderate work of the material against crack propagation. Few pores can also be observed.

After heat treatment, the small areas covered with dimples disappeared, and the surface is more homogeneous than it is before heat treatment. The absence of dimples shows that the rupture is not very ductile; however, signs of material resistance toward crack propagation can be observed (see picture 4.15a (ii)).

After inter-pass rolling, the rupture surface in picture (iii) is very heterogeneous. Part of it shows a material deformation due to crack propagation resistance, but some large and smooth features show that the crack propagated very easily in some parts of the specimen.

When heat treatment is carried out on the rolled material, most of the rupture surface is covered with dimples or coarser features, demonstrating a resistance toward crack propagation. Some smooth areas, similar to those observed in picture (iii) can be observed, but these are much smaller than the one observed in as-rolled condition.

Vertical direction

Figure 4.15b provides the SEM image of the rupture surface of specimens tested in the vertical direction and built with CMT-P-Adv. Comparing with the horizontal direction, fewer areas covered with dimples can be observed on the as-deposited specimen rupture surface in picture (i). The rupture surface is also smoother, showing less crack propagation resistance than in the horizontal direction. Finally, some micro-cracks can be observed.

After heat treatment, some coarse features typical of brittle rupture can be seen. The rest of the surface is similar to this of the horizontal specimen in Figure 4.15a picture (ii). Picture (iii) shows a very brittle rupture surface for the as-rolled specimen, with no evidence of material resistance toward crack propagation. However, after heat treatment, the rupture is much more ductile despite being coarser than in the horizontal direction, as shown by pictures (iv) in Figures 4.15a and 4.15b. Some very smooth areas can be observed in the rupture surface: Figure 4.17 shows the rupture surface of a vertical specimen which broke at a relatively low elongation (3.7%). Numerous pores can be observed, and the largest of these is a 570 μm long and 220 μm large ellipse. The very smooth surface of this defect suggests that this ellipse is the results of a un-closed pore during rolling which offer no resistance toward crack propagation.

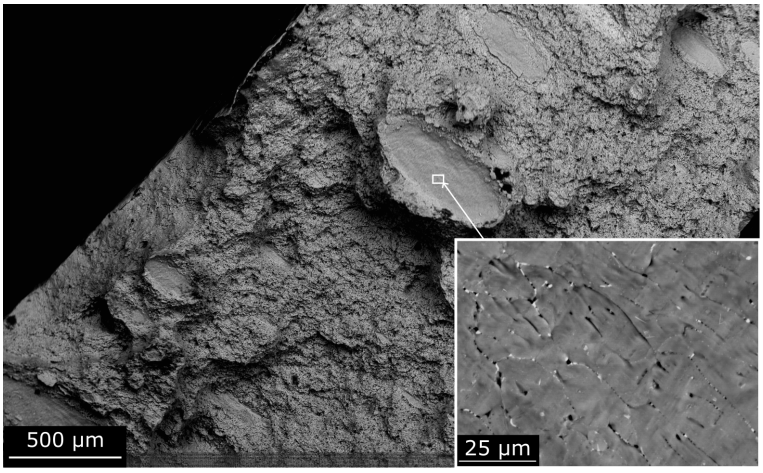


Figure 4.17: Rupture surface of a vertical specimen made of inter-pass rolled then heat treated material, deposited with CMT-P-Adv process

4.3.6.2 CMT-P specimens

Horizontal direction

Figure 4.16a Picture (i) shows that, in the as-deposited condition, few areas are covered by dimples in a similar manner to what was observed in picture (i) of Figure 4.15a. The rest of the surface shows a moderate work of the material against crack propagation but also contains pores and very smooth zones where the crack propagated without any difficulties in the material.

Picture (ii) shows that after heat treatment the small areas covered by dimples disappear. The rupture surface is heterogeneous, many areas are typical of brittle rupture, and the rest of it demonstrates a moderate deformation against crack propagation.

Picture (iii) shows that the rupture surface of the rolled specimen is much more homogeneous than the as-deposited or heat treated one. The features are small and demonstrate a good resistance toward crack propagation.

The rupture surface of the rolled then heat treated specimen, in picture (iv) is very homogeneous and covered with small dimples, typical of a ductile fracture.

Vertical direction

Figure 4.16b Picture (i) shows that the rupture surface of the rolled specimen is heterogeneous, with small areas covered by coarse dimples. In the high magnification images, it is possible to see second phases in the centre of these dimples. The rest of the surface is well deformed, showing a moderate resistance to crack propagation. Smooth features showing no resistance toward crack propagation can also be observed. The rolled then heat treated specimen shown in picture (ii) has a similar rupture surface but without the small areas covered by dimples.

The rupture surface of the rolled specimen in picture (iii) is much more homogeneous

than the as-deposited or as heat treated ones. The features found on the rupture surface are small, and in the high magnification image (in picture (iii) and Figure 4.18), it is possible to see numerous microcracks. After heat treatment on the rolled specimen, the features founded on the rupture surface are smaller and show a high material deformation to prevent crack growth.

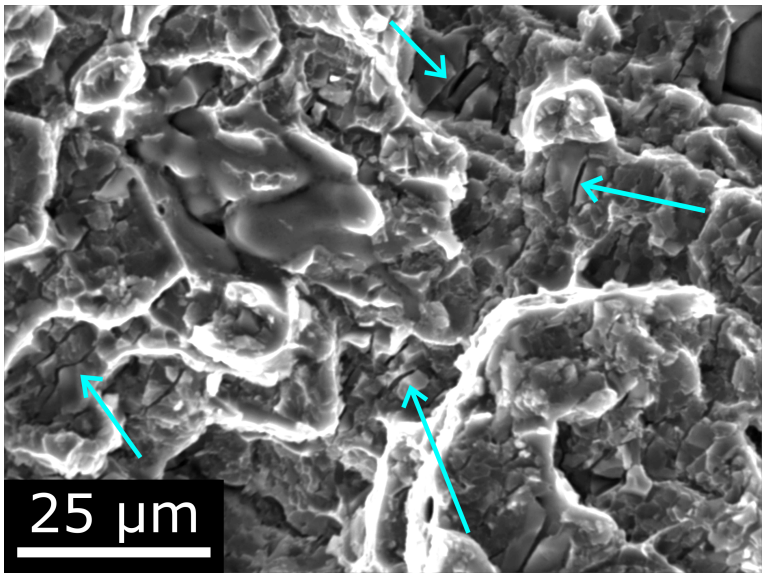


Figure 4.18: Micro-cracks founded in the rupture surface of the rolled CMT-P specimen tested in the vertical direction

4.3.6.3 Tensile specimen cross sections

In addition to the rupture surface observed by SEM, tensile specimen longitudinal sections were observed with an optical microscope. Figure 4.19 and 4.20 show broken vertical tensile specimens deposited with CMT-P-Adv and CMT-P respectively. In all cases but one, the rupture occurred at the boundary between two layers. This is probably due to the higher concentration of defect at the interlayer area. The case for which the rupture occurred inside a layer is the as-rolled CMT-P-Adv samples: the rupture seemed to occur in an area where the grains were larger than at the inter-layer region.

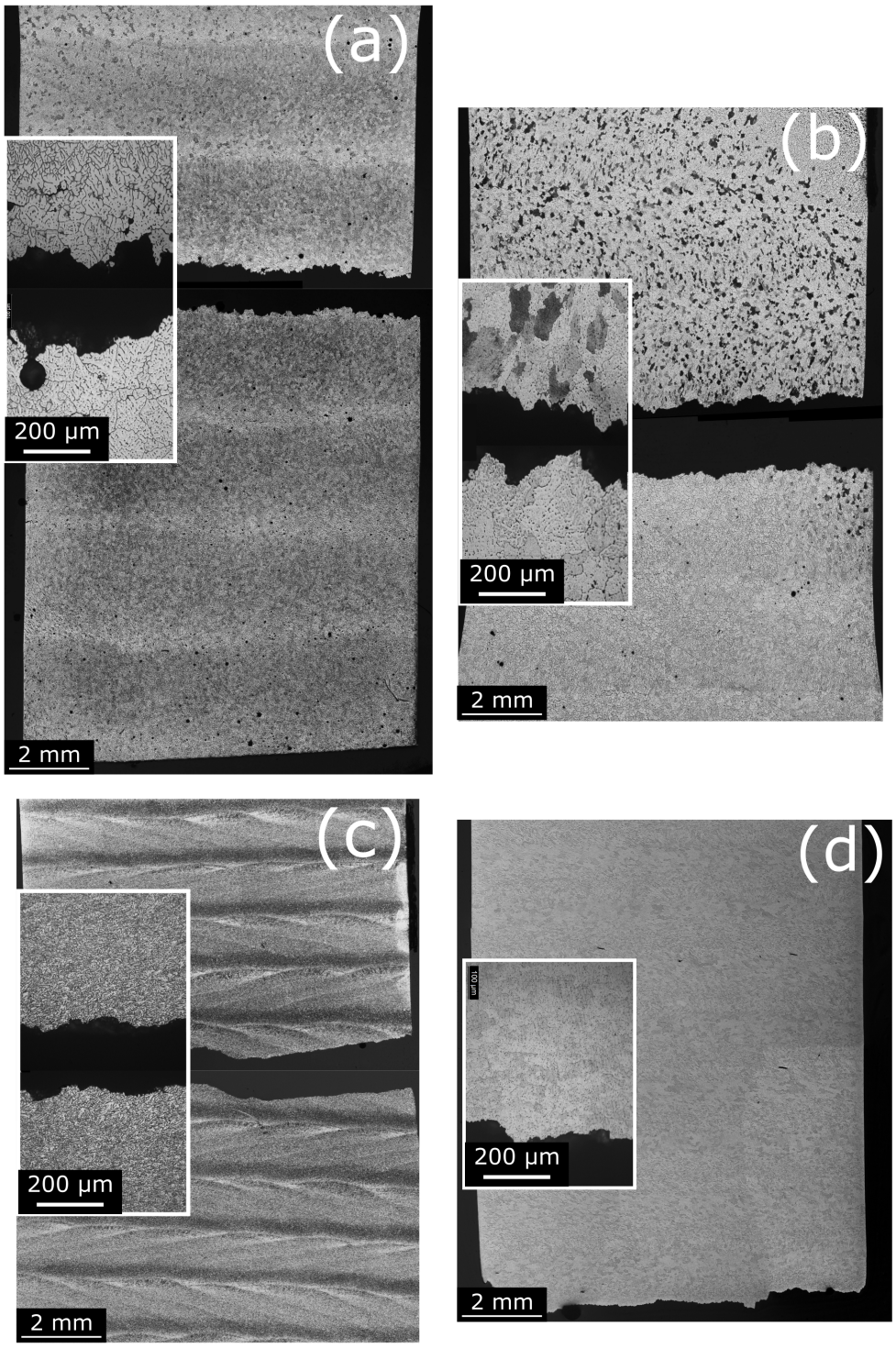


Figure 4.19: Optical images of longitudinal cut of vertical tensile specimens taken from (a) as-deposited material, (b) heat treated, (c) as-rolled, and (d) rolled then heat treated deposited with CMT-P-Adv process

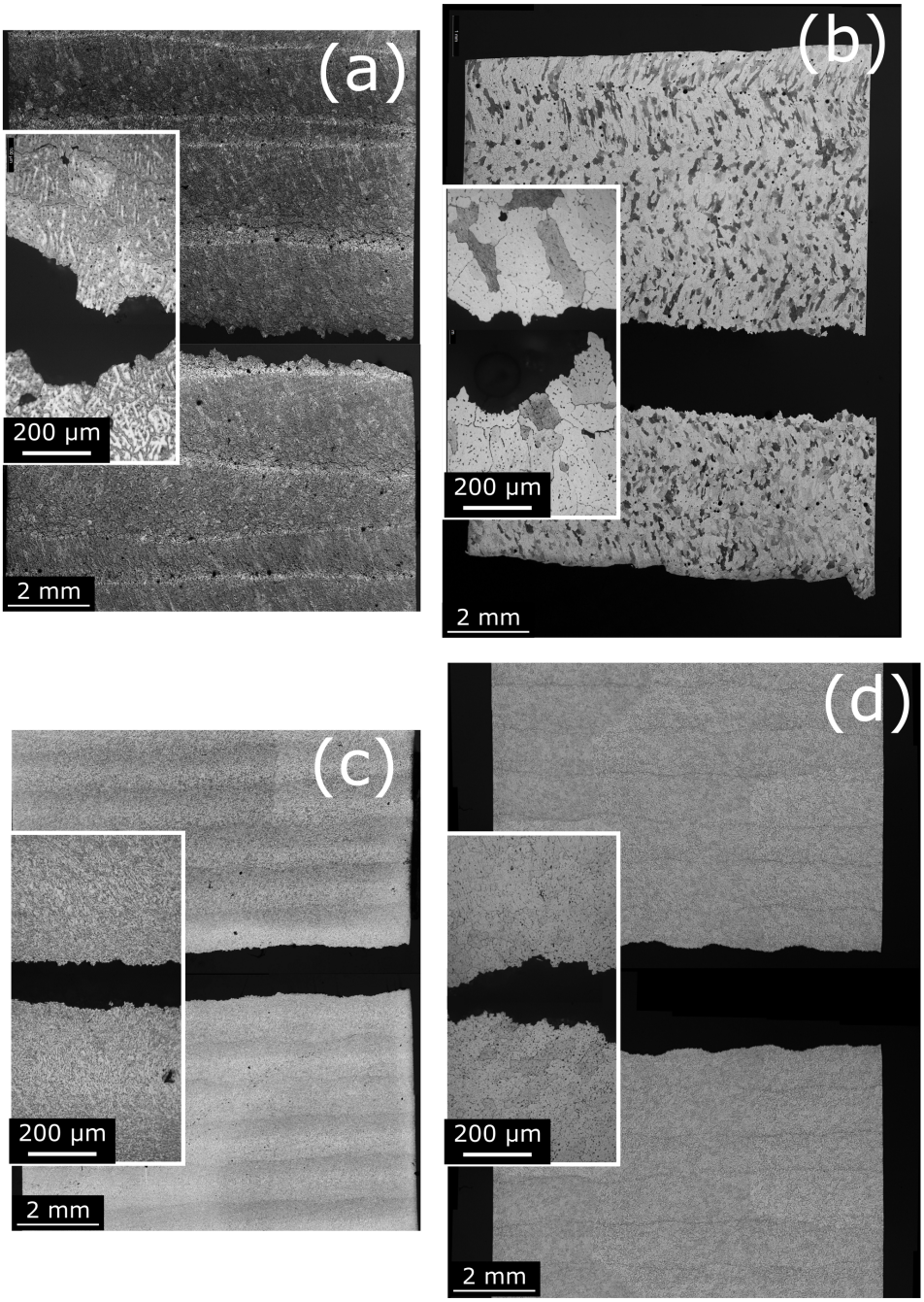


Figure 4.20: Optical images of longitudinal cut of vertical tensile specimens taken from (a) as-deposited material, (b) heat treated, (c) as-rolled, and (d) rolled then heat treated deposited with CMT-P process

4.4 Discussion

All the data introduced in the previous section show the drastic effect of the deposition process, inter-pass rolling and heat treatment has on the microstructure and mechanical properties of 2024 WAAM.

4.4.1 Chemical composition

The EDS measurement results for the wire and the different deposited material do not show any effect of the process on element losses. However, for all the deposited material, a loss of zinc, and reduction of iron and silicon content were measured. The loss of zinc can easily be explained by the low vaporisation point of this element. The reduction of iron and silicon is less obvious: it could be due to the formation of weld smut on the surface of the bead. However, no data are available on the depletion of iron and silicon during additive manufacturing or welding of aluminium alloys. An in-depth study, based on a more accurate chemical composition analysis technique, would be required to assess if this elements loss is effective and if it affects the WAAM material properties.

Many authors reported a consequent loss of magnesium during the additive manufacture of aluminium alloys [7, 14, 58, 89, 95]. However, it is not possible to assess the effect of the deposition process on the magnesium level in the WAAM material because of the loss of other elements.

4.4.2 Effect of deposition process on as-deposited microstructure and mechanical properties

CMT-P-Adv process leads to a better deposition quality than CMT-P process, with fewer gas pores and less inter-dendritic voids. This lower porosity can be attributed to the alternating current and voltage profiles, typical of CMT advanced processes, which are well known for their wire cleaning role, leading to a lower porosity level in the deposited material [12].

CMT-P generates more micro voids in between dendrites than CMT-P-Adv process: the fact that the material deposited with CMT-P process endures numerous partial re-melting and re-heating cycles, because of the smaller LH, could partly cause these phenomena. These micro voids generated during the solidification of wide freezing-range alloys and formed under specific solidification paths, depend on the heat input, among many other parameters. In multi pass welding, it has been shown that successive remelting and low cooling rate can lead to the formation of these dendritics voids due to the segregation of alloying elements [108]. The micro voids observed in the material are distributed in horizontal lines, parallel to the solidification front showing that they are generated by a specific thermal cycle. In fusion welding, a standard recommendation to reduce the micro-void of material in the dendritic regions is to use a lower heat input. The higher heat input of the CMT-P process and the numerous re-melting and re-heating phases are probably the reason why numerous micro voids can be observed in as-deposited condition while none were observed in the as-deposited CMT-P-Adv sample.

The as-deposited hardness does not depend on the process, but the tensile properties of the material deposited by CMT-P-Adv are significantly higher than those of CMT-P material. This is due to the gas pores and solidification voids present at a much higher level in the CMT-P material, which drastically reduce the UTS and elongation and slightly

decrease the YS in both horizontal and vertical directions.

Regardless of the deposition process used, the tensile properties in the vertical direction are significantly lower than in the horizontal direction. The optical images of the tensile specimens in the vertical direction show that the ruptures occurr at the boundary between two layers and the ruptured surfaces of the vertical specimen observed by SEM also show a lower resistance to crack propagation and more defects than in the horizontal direction. The inter-boundary layers are hardened and source of defects due to additional segregation: this can explain the anisotropy observed in as-deposited condition.

The properties achieved are much lower when compared with any 2024 semi-finished products conventionally manufactured (UTS $>$ 400 MPa, YS $>$ 260 MPa and elongation $>$ 4% according to BS EN 755-2:2016). The horizontal properties of the material deposited with CMT-P-Adv are very close to the properties of 2024 deposited by a tandem GTA system (see table 4.6 [93]). This confirms the very low dependence between deposition process and mechanical properties mentioned in Chapter 2.

4.4.3 Effect of inter-pass rolling on the microstructure and mechanical properties

Regardless of the deposition process used, inter-pass rolling increases the TWW and EWW. However, the SW of the walls increases when CMT-P-Adv is used and decreases if the CMT-P process is used. This increase in SW means that, in the case of the manufacture of a part a large amount of material would need to be machined away to get the final smooth surface finish. Moreover, the residual stress concentration points in between the bulges at the edges of the wall could behave as crack initiation sites under load or during the quench. The layer height and the total deformation also depend on the deposition process used despite the use of the same rolling load.

The micro hardness measurements show no hardness increase for the material deposited with CMT-P and a drastic improvement of the wall deposited using CMT-P-Adv and indicate the relationship between properties and rolling load or total deformation cannot be investigated without taking into account the process used to deposit the material.

4.4.3.1 Material deposited with CMT-P process

Macro-structure, microstructure and micro hardness measurement suggested that rolling does not have any strengthening effect on the material deposited by the CMT-P process. This is believed to be due to the considerable remelting occurring during the deposition. However, rolling drastically reduced gas and dendritic porosity in the material. This fact by itself leads to greater tensile properties as well as a much lower anisotropy than these of as-deposited material.

The effect of rolling on porosity has been shown for numerous alloys such as 2319 [5], Safra66, and ZL205A [78]. In these papers, the explanation of porosity reduction by rolling is that the rolling strain generates dislocations, and these dislocations are well known hydrogen trapping sites. Therefore, while the pores are closed by compressive strain, the hydrogen they contain is re-distributed in the numerous formed dislocations. However, this explanation alone is not sufficient to justify the drastic porosity reduction in the case of CMT-P 2024 deposited and rolled: if the hydrogen were stored in the dislocation, in this case, it would re-form gas pore during the re-melting of the material. If the porosity level decrease, in this case, could be due to a combination of these three phenomena:

- The shallow melt pool and the high heat input could be beneficial for porosity reduction: the gas pores in the liquid could have enough time to escape from the melt pool during the deposition process because of a slower solidification rate and a high

bead width to layer height ratio.

- Toda et al. [129] suggested that, in addition of having great storage capability, dislocations can also provide hydrogen with high dislocation-pipe diffusion paths. After the top layer of the wall has been deposited and rolled, the dislocation-pipes generated by the rolling strain could allow a large part of the hydrogen to diffuse to the material surface and escape. This would explain why, even after remelting occurring during the deposition of the next layer, the porosity does not increase drastically. It would also explain why porosity does not drastically increase during heat treatment. This theory of dislocation-pipe diffusion path was also mentioned by Gu et al. as one explanation of the effect of inter-pass rolling on porosity reduction [5].

- Grain boundaries are also a trapping site for hydrogen. Most studies on the effect of deformation on the porosity of aluminium alloys were conducted on cast alloys, which are mainly composed of large grains. During these studies, grain boundaries were often considered as a trapping site capable of storing only 10 to 100 time less hydrogen than dislocations [130]. However, WAAM material is composed of much smaller grain, especially when inter-pas rolling is carried out. This means that there are many more grain boundaries in rolled WAAM material than in wrought alloys: grain boundary areas could play a key role in hydrogen storing.

4.4.3.2 Material deposited with CMT-P-Adv process

Inter-pass rolling drastically increased the hardness and the YS of the material deposited with CMT-P-Adv. The elongation in the horizontal direction was not affected by rolling, but it was drastically reduced in the vertical direction. The fact that the elongation in the horizontal direction was not affected does not allow to conclude on the change of ductility

of the material: the reduction of ductility caused by rolling added to the drastic drop of the porosity level probably caused this constant elongation.

It is possible to compare 2024 with 5087 and 2319: Gu et al. [14] showed that inter-pass rolling of 5087 increases both YS and UTS without affecting the elongation in the horizontal direction. Unfortunately, no data in the vertical direction were published on 5087 [14]. When 2319 is rolled, both YS and UTS increase, but the ductility decreases in both horizontal and vertical direction, but the elongation of the horizontal specimens is not very different from this of the vertical direction (8.5 % against 7%). [11]. According to the authors, the principal mechanism of strengthening was the formation of high-density dislocation and by grain refinement for 5087 alloy.

2024 is a precipitation hardening alloy, and as shown by the hardness measurement and its tensile properties, it seems to behave in a similar way than 2319. However, it has been shown that plastic deformations can have a drastic effect on the mechanical properties of 2024 alloys by altering its precipitation behaviour after rolling. Zhao et al. [28] show the complex relationship between tensile properties of 2024 and its thermochemical history. Three types of precipitates play a key role in the strength of 2024 alloys: Al_2Cu, Al_2CuMg and Ω. The Ω phases are very sensitive to strain and are more thermally stable than Al_2Cu and Al_2CuMg precipitates. Also, precipitates might form on specific crystallographic planes. It is possible that in addition to generating dislocations inter-pass rolling also change the precipitation behaviour of this alloy leading to an improvement of the mechanical properties. An observation of the material with a TEM would be necessary to conclude this matter.

Regarding the very low ductility in the vertical direction, it can be explained by long eutectic line crossing the wall from one edge to the other. These areas behave like crack propagation preferential path and offer very poor resistance toward crack propagation. Also, the microstructure observed by SEM also shows an effect of the eutectic rich net-

work, which is elongated in the horizontal direction. Then, the hardness and the YS, measured in both directions, are very high and show that some regions of the material have been overworked, leading to the formation of brittle areas, areas parallel to the rolling direction.

4.4.4 Effect of heat treatment on the microstructure and mechanical properties

Only one heat treatment was carried out in this study and as mentioned before, the solution treatment may have not been optimum (see page87). As shown by [93] the properties of 2024 manufactured by WAAM can be improved by heat treatment, and the temperature of the solution treatment is a key factor regarding the maximum properties achievable. The work conducted here is therefore not conclusive on the highest mechanical properties achievable with this alloy after heat treatment. However, the effect of heat treatment can be observed, as well as the effect of the deposition process and inter-pass rolling on the heat treated mechanical properties.

4.4.4.1 Heat treatment of un-rolled material

As for the effect of inter-pass rolling, the effect of heat treatment is different if it is carried out on CMT-P-Adv or CMT-P deposited material. When carried out on CMT-P-Adv material, it has a great effect on YS and UTS and increases the elongation slightly . The anisotropy can be explained by the alignment of pores in the inter-layer boundary, pores which are more numerous than in as-deposited condition due to the heat treatment. The effect of heat treatment is more mitigated when carried out on CMT-P material. This is due to the higher concentration of defect on the as-deposited material. Also, the grain size of the heat treated CMT-P-Adv material is smaller than this of CMT-P material, which

could contribute to the difference in tensile properties between the two material in the as heat treated condition.

4.4.4.2 Heat treatment of rolled material

CMT-P-Adv

When heat treatment is carried out on the rolled CMT-P-Adv material, it does not affect considerably the YS, but the UTS and the elongation drastically increase. The material is still anisotropic despite a massive increase of ductility in the vertical direction. This significant improvement suggests again that the very low ductility in the vertical direction under as-rolled condition was caused by some over-worked horizontal regions which have been recovered during the solution treatment. Also, as shown by the SEM observations, a significant amount of the copper-rich lines were solutionised during the heat treatment. However, the presence of un-closed pores in the inter-layer boundary have a drastic effect on the rupture behaviour of the vertical specimens, as shown by the fractographs in Figure 4.15b (iiii) and considerably affect the UTS and elongation measured in the vertical direction. Finally, some sharp change in the grain size and orientation can be observed in between layers (see Figure 4.14). This sharp change could behave as a preferential crack propagation path during tensile test, especially in the vertical direction for which the change in grain size is perpendicular to the stress direction, resulting in a lower elongation in the vertical direction.

CMT-P

Interpass rolled then heat treated 2024 deposited with CMT-P process reaches the highest mechanical properties of all the conditions evaluated in this study, with a slightly higher YS than the material deposited with CMT-P-Adv. The anisotropy of this material is also slightly lower than this of CMT-P-Adv material, but the elongation in the vertical direction

remains low, below 10%.

Table 4.6 shows few mechanical properties provided by standards for wrought products and reported in the literature for WAAM material. The properties indicated in the standards are minimum properties for wrought products of similar thickness to the this of the WAAM material and different temper.

Table 4.6: Example of tensile properties achieved by 2024 wrought and WAAM products

	YS [MPa]	UTS [MPa]	Elongation [%]
T3 2024 bare [131]	290	395	12
T351 plates (up to 12.5 mm thick) [25]	290	440	12
T6 plates (up to 12.5 mm thick) [25]	345	440	5
WAAM 2024 [93] ST 498 + NA (horizontal direction)	300	450	12.5
WAAM 2024 [93] ST 503 + NA (horizontal direction)	330	497	16
WAAM 2024 CMT-P inter-pass rolled and heat treated (horizontal direction)	301	468	20.6
CMT-P inter-pass rolled and heat treated (vertical direction)	290	444	9.8

As shown by Table 4.6, the mechanical properties of 2024 alloys depend on the manufacturing process used to produce it. The properties of the material made in this study (in CMT-P inter-pass rolled and heat treated condition) are close to these of T6 plates, but the YS is significantly lower than 345 MPa. When compared with T3 2024 bar properties, the properties achieved by the CMT-P inter-pass rolled after T6 heat treatment are considerably higher. Also, the properties of T3 plates (solution treatment followed by natural ageing) are relatively close to those obtained in this study: these properties are almost reached by WAAM material in both directions, and only the low elongation in the vertical

direction is below these limits.

After solution treatment at the same temperature than in this study (498°C) and natural ageing, Qi et al. obtained similar tensile properties but a considerably lower elongation of 12.5 % [93] compared with the horizontal properties obtained in this study. The higher ductility of the aged material is coherent with the result published by Zhao et al. [28], showing a possibility of increasing the ductility of 2024 alloy by using a longer ageing time in order to reach a second strengthening peak. Qi et a. showed higher mechanical properties can be achieved using a solution treatment temperature of 503°C. Also, the elongation obtained in this study is considerably higher than the elongation achieve by Qi et al. [93] and heat treated wrought products. This shows that properties achieved after heat treatment in this present study could have even been higher if a different heat treatment temperature and duration would have been applied to the inter-pass rolled material.

4.5 Conclusion

Despite being widely considered as un-weldable by fusion, this study is one of the few showing the potential of 2024 for AM application. If in as-deposited or as-rolled conditions, the measured properties were relatively low, the tensile properties achieved with inter-pass rolled and heat treated material were able to compete with these of semi finished products made of 2024 alloy, despite a lower yield strength achieved by the WAAM material.

Few interesting points were highlighted in this study:

- The deposition process has a drastic effect on the bead and wall geometry, and this effect is considerable even if inter-pass rolling is carried out after deposition.The inter-pass rolling strengthening effect can be observed only if the re-melting occurring during deposition remains low compared with the layer high.

- Even in the case for which the re-melting is larger than the layer height, a beneficial effect of rolling can be observed: it drastically reduces the porosity level. This shows that the presence of dislocations only is not a sufficient phenomenon to explain how inter-pass rolling reduces the porosity level in WAAM material. Other mechanisms such as the formation of high diffusivity hydrogen paths or the existence of weld pool shape more favourable to gas pore release could also play a key role in porosity reduction.

Further investigations need to be carried out on the effect of as-deposited bead shape on the inter-pass rolled material geometry, deposition quality and mechanical properties. In order to do so, independent control of bead shape (layer height, bead width and re-melting depth) and heat input is required. It seems very difficult to achieve an independent control of these metrics using a GMA process because of the link between WFS, bead shape, and heat input. A new process, such as PTA, GTA or a combination of several heat sources could be the solution control appropriately the bead geometry, allowing a better understanding of how inter-pass rolling can affect the material properties and quality.

In the manufacture of aluminium products, a meticulous balance between strength, fatigue properties and corrosion resistance is chosen depending on the design requirements. It is possible to use different heat treatment to achieve a various range of properties with the same alloy. In this study, only the tensile properties were evaluated and further investigation on toughness and fatigue properties would be required to fully characterise this WAAM alloy.

Chapter 5

Potential and issues in depositing Aluminium zinc alloys

5.1 Introduction

Relatively few studies about deposition of aluminium zinc alloys have been published because of the numerous issues already mentioned in the literature review in section 2.2.3. However, aluminium zinc alloys are of interest because of their very high mechanical properties. This chapter explores the possibility of depositing aluminium zinc alloys by WAAM. One of the main issues reported in the literature in aluminium zinc welding is the behaviour of zinc in the arc: because of its low boiling point, zinc vaporise in the arc and thus generates high instabilities. To overcome this problem, the approach chosen here was to generate a melt pool of aluminium copper with a GMA process and add zinc outside the arc using a cold wire.

Aluminium solidifies quickly because of its high conductivity, causing the melt pool to be small and mainly below the electric arc. In order to have space to feed a zinc wire into the melt pool without disturbing the arc, an elongated melt pool is needed. The

strategy chosen in this chapter was to use a laser beam behind the arc in order to create an elongated melt pool that elongates after the electric arc. This process is further referred to as laser-assisted WAAM.

The aim of this study was to assess the possibility of depositing an aluminium zinc alloy using laser-assisted WAAM. The first objective was to determine if the laser-assisted WAAM process could be used to achieve an elongated and stable melt pool: the effect of laser power, wire feed speed, and distance between laser and arc on the deposition behaviour, process stability, and bead geometry were investigated. The second objective was to assess the possibility of depositing an aluminium zinc alloy using laser-assisted WAAM. Firstly, the effect of zinc addition on process stability and microstructure was evaluated. Secondly, single beads were deposited using a fixed set up, but with varying WFS and laser power, to produce a homogeneous aluminium copper zinc matrix. Finally, the best parameters were used to deposit three-layer-high walls, to prove the possibility of depositing three-dimensional structures in aluminium zinc.

5.2 Methodology

The set up and material used are described in Chapter 3.

5.2.1 GMA process

A GMA process was used to form an aluminium copper melt pool with a 2319 wire. It was selected for its great stability, even when the torch is not perpendicular to the work piece, and because the wire is directly fed into the arc. Using PTA or GTA instead would have required the use of two cold wires (a AlCu wire in front of the arc, and the zinc wire behind). GMA was therefore the easiest option to implement.

There are many GMA processes, and one commonly used in aluminium WAAM is CMT-P. It is a pulsed GMA process which includes short circuit phases: during deposition, droplets are deposited in spray mode, and regularly, the distance between the wire and the work piece is reduced to zero, and a droplet of material is deposited in short circuit mode. Figure 5.1 shows the voltage and current profiles during the deposition, illustrating the two mode of droplet transfers. The frequency of short circuit depends on the WFS: it decreases when the WFS increases. As this process is, in general, considered more stable than Pulse mode alone, it was used during the first experiments for the study of the effect of laser power on bead geometry and the effect of zinc-arc distance on microstructure and process stability. The frequency of short circuit was low (18 sprayed droplets for one short circuit), and was therefore not very different from Pulse mode. Also, during preliminary trials, CMT-P did not show any great advantages in term of stability compared with Pulse mode. As Pulse mode has a higher heat input, more advantageous to generate a large and hot melt pool, it was preferred for the rest of the experimental work.

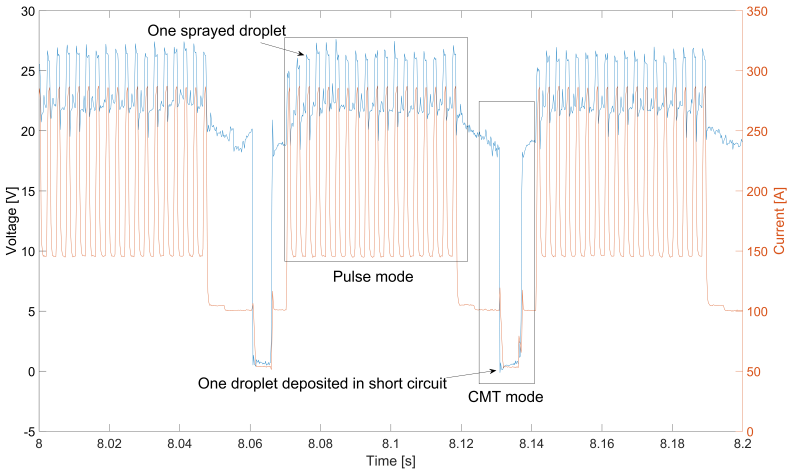


Figure 5.1: Electric arc characteristics in CMT-P mode

For each sub-study, the process parameters used are detailed in the following sections.

5.2.2 Laser-assisted WAAM

5.2.2.1 Effect of laser power on melt pool and bead shape

This experiment was conducted without any zinc addition and consisted of depositing single beads using different laser power, from 0.2 to 5kW. CMT-P process was used, with a WFS of 7 m/min and a TS of 10 mm/s. For the laser, a beam diameter of 10.5 mm on the substrate top surface, with a laser-arc distance of 10 mm was used. Three cross-sections of each bead were prepared following the procedure described in section 3.2 of Chapter 3 to produce the optical images used to characterise the bead geometry. Figure 5.2 (a) shows the measurements carried out. The length of the melt pool was measured at the solidification point as shown in 5.2 (b).

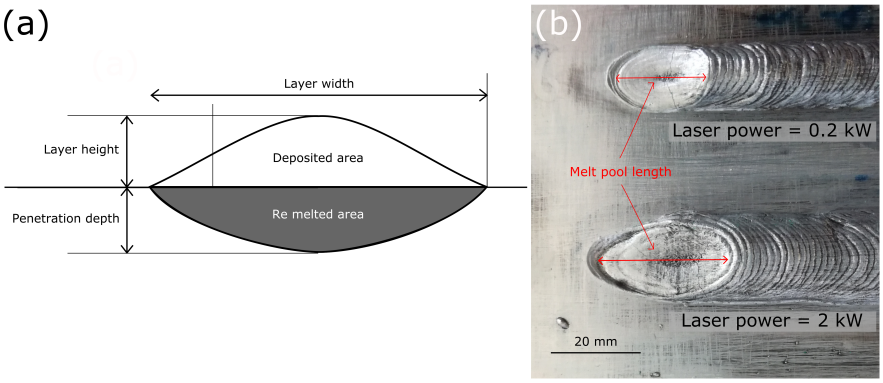


Figure 5.2: Metrics used to characterise (a) the bead geometry and (b) melt pool length

5.2.2.2 Effect of Wire feed speed on bead shape

Two beads were deposited to investigate the effect of WFS on bead geometry. As illustrated in Figure 5.3, the first half of each bead was deposited using a laser power of 0.2 kW, and the second half length with a laser power of 4 kW. A laser-arc distance of 5

mm and a Travel Speed (TS) of 10 mm/s were used. In this section, Pulse process and a laser spot diameter of 9.5 mm on the substrate top surface were constantly used. The bead geometry was characterised by the measurements shown in Figure 5.2. Two cross-sections were measured for each condition, and the average arc heat input was calculated as indicated in Chapter 3.

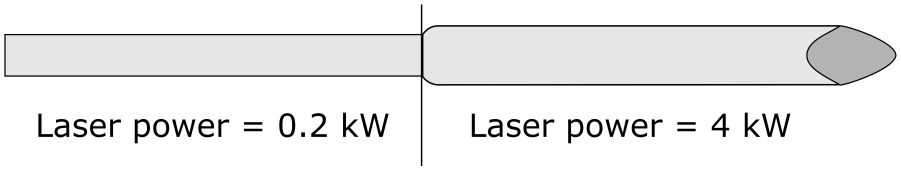


Figure 5.3: Schematic of a bead deposited using two different laser power

5.2.2.3 Effect of laser on process stability

Effect of laser on arc stability

To show the effect of the laser on process stability, two beads were deposited with a low laser power of 0.2 kW, and one bead was deposited using a high laser power of 4 kW. A WFS of 7 m/min, a laser-arc distance of 10 mm, and a TS of 10 mm/s were used. Electric arc current and voltage are used to illustrate the process stability.

Effect of laser-arc distance on process stability

To show the effect of laser-arc distance on process stability, two beads were deposited using a WFS of 7 m/min and a TS of 10 mm/s. The first half length of the bead was deposited using a laser power of 0.2kW, and 4 kW was used for the second half length (see Figure 5.3). Video recording and arc characteristic were used to assess the process stability.

5.2.3 Zinc addition using laser-assisted WAAM

5.2.3.1 Effect of distance between zinc wire and electric arc on process stability and deposited material microstructure

During this stage of the study, all deposition parameters were kept constant apart from the zinc wire-arc distance. This distance was measured as indicated in Figure 5.4 The CMT-P process was used with a WFS (further called AlCu WFS) and zinc WFS (Zn WFS) of 7 and 1.2 m/min respectively, a laser power of 5kW, a laser-arc distance of 5 mm, and a TS of 10 mm/s. To check the effect of zinc addition on the microstructure, longitudinal sections were prepared as outlined in section 3.2.

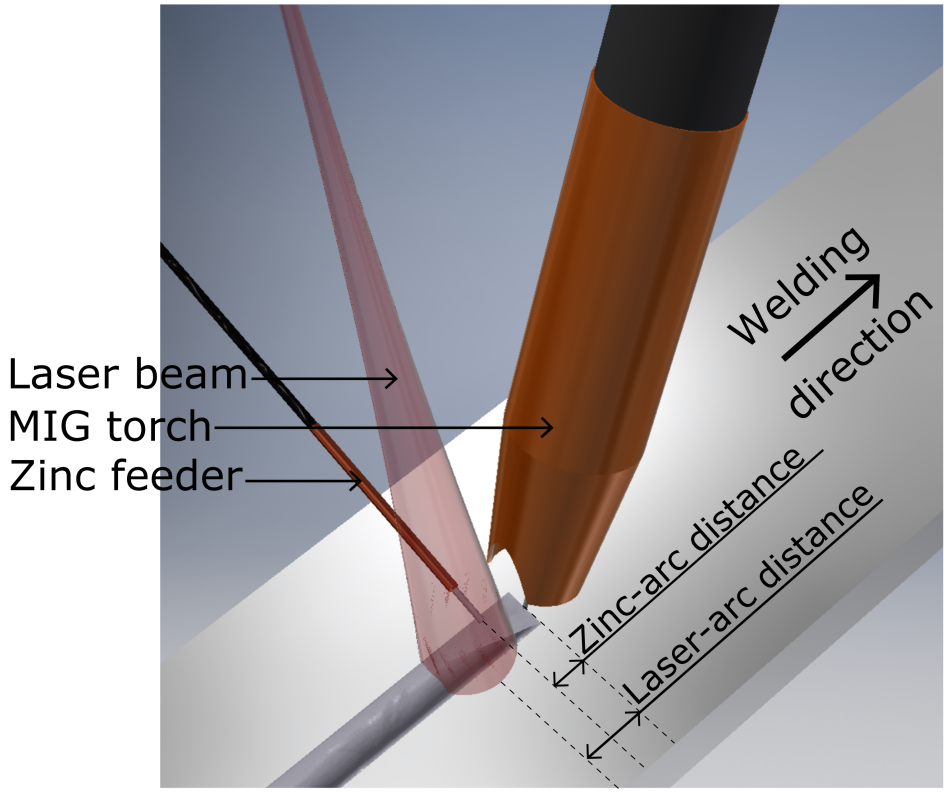


Figure 5.4: Schematic of the set up and the laser-arc and zinc-arc distances

5.2.3.2 Effect of laser power and wire feed speeds on deposited material microstructure

For this section, the set up was fixed using the best parameters found during the preliminary studies introduced above. Laser-arc and zinc-arc distances were kept constant at 7 and 10 mm respectively, the pulse process and a TS of 10 mm/s were used. Laser power, AlCu WFS, and Zn WFS were changed : the list of parameters used is given in table 5.1 as well as the expected composition, in weight percent, of the deposited material. The composition were calculated without considering any loss of element during the process using the following set of equations:

$$M_{Zn} = \frac{\pi \times {d_{Zn}}^2}{4} \times WFS_{Zn} \times \rho_{Zn} \tag{5.1}$$

$$M_{Cu} = \frac{\pi \times {d_{AlCu}}^2}{4} \times WFS_{AlCu} \times \rho_{Cu} \times C_{Cu} \tag{5.2}$$

$$M_{Al} = \frac{\pi \times {d_{AlCu}}^2}{4} \times WFS_{AlCu} \times \rho_{Al} \times C_{Al} \tag{5.3}$$

$$W_{Zn} = \frac{M_{Zn}}{M_{Zn} + M_{Cu} + M_{Al}} \tag{5.4}$$

$$W_{Cu} = \frac{M_{Cu}}{M_{Zn} + M_{Cu} + M_{Al}} \tag{5.5}$$

$$W_{Al} = \frac{M_{Al}}{M_{Zn} + M_{Cu} + M_{Al}} \tag{5.6}$$

with M_x, ρ_x, C_x the mass per unit length of deposit, the density, and the concentration

in the wire of element X; d_{Zn} and d_{AlCu} the diameters of the Zn and AlCu wire; and WFS_{Zn} and WFS_{AlCu} the WFS of the Zn and AlCu wires. For the calculation, the AlCu wire was considered as a binary-alloy with a concentration of 6% copper and 94% aluminium. The WFS used were selected in order to achieve a stable deposition process. Unfortunately these WFS led to a very high expected zinc composition in the deposited material. The arc heat input was calculated using the equation 3.6, and the laser heat input using the following equation :

$$HI = \frac{\rho \times LaserPower}{TS} \tag{5.7}$$

with ρ the absorption coefficient. This value was difficult to determine because the absorption coefficient of aluminium depends on many parameters. Firstly it is drastically higher at liquid than solid state and, in this study, the amount of liquid and solid aluminium below the laser beam depended on the process parameters such as the laser beam spot diameter, the laser-arc distance, the WFS and the laser power. Secondly, the melt pool absorption depend on the amount of oxide layer floating on its surface. Therefore, it was not possible to determine precisely the absorption coefficient and a constant value of 0.3 was used.

After a microstructural observation of beads on plates, three parameter combinations were chosen to deposit three-layer-high walls.

Table 5.1: Experimental parameters used for the deposition of bead on plate and 3 layer high wall aluminium zinc structure

Samples	Laser power [kW]	AlCu WFS [m/min]	Zn WFS [m/min]	Expected comp. [weight %]		
				Zn	Cu	Al
A_1	2	8	1.2	37	4	59
B_1 & B_3*	2	9	1.2	37	4	59
C_1	3	9	1.2	50	3	47
D_1	3	9	2	37	4	59
E_1	3	6	1.2	47	3	50
F_1 & F_3*	5	6	1.2	47	3	50
G_1 & G_3*	3	10	2	50	3	47

*3 layer-high walls

5.3 Results

5.3.1 Laser-assisted WAAM

5.3.1.1 Effect of laser power on bead shape

Figure 5.5 provides images of the melt pool without the laser and with a laser power of 4 kW. It can be seen that the melt pool is longer when the laser is used. Figure 5.6 shows that the effect of laser on melt pool length occurs even at a power lower than 1.5 kW. Figure 5.7 is a plot of the melt pool length measured at the solidification point of each bead. It confirms that the addition of the laser beam fulfils the objective of increasing the length of the melt pool by more than a factor of 2.

Figure 5.7 provide schematic of the melt pool to illustrates its change in geometry with the laser power. In each drawing, the melt pool observed for a laser power of 0.2 kW is drawn in black, and the melt pool generated at higher laser power is drawn in blue. Below 2 kW, the melt pool is elongated only in the opposite direction of deposition. Above 2kW, a slight increase in length can be seen in front of the melt-pool. However, the melt pool

was mainly elongated in the opposite direction to the travel direction. It can be seen that the surface of melt-pool below the laser power drastically increases when the laser power was higher than 2 kW. This had a great impact on the amount of laser power absorbed by the metal, as the absorption coefficient of liquid aluminium is much higher than this of at solid state.

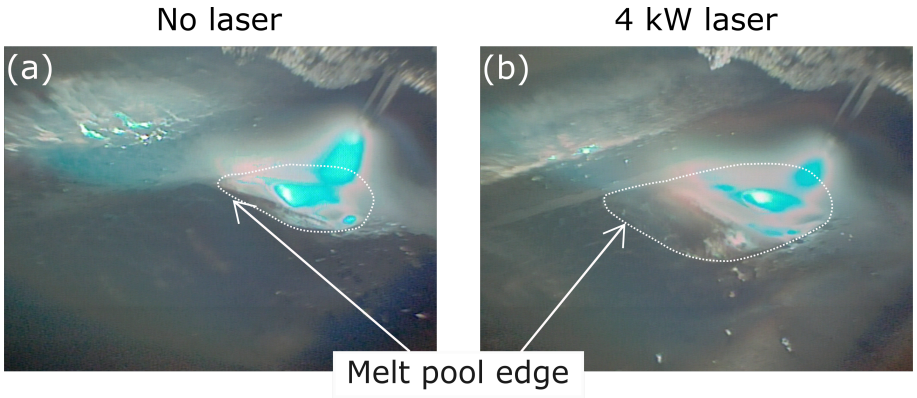


Figure 5.5: Melt pool shape (a) without laser, and (b) with 4kW laser power

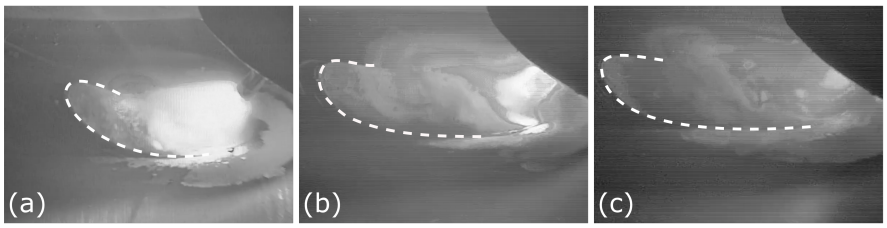


Figure 5.6: Effect of laser power on melt pool length - The laser power used is 0.2, 1, and 1.5 kW in picture (a), (b) and (c) respectively

Figure 5.8 shows the arc voltage and current for a laser power of 0.2 and 4 kW. Both voltage and current profiles are the same regardless of laser power. This shows that laser power has here no effect on the arc behaviour.

To illustrate the effect of the laser power on the bead shape, examples of cross-section are given in Figure 5.9. Figure 5.10 gives the geometry measurement relative to each laser power. The plot in Figure 5.10 (a) shows the deposited and re-melted area as well as the

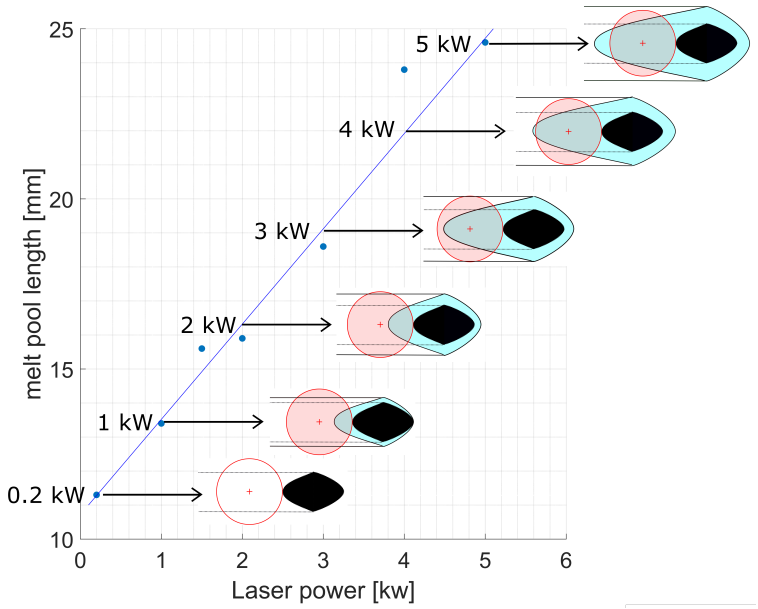


Figure 5.7: Effect of laser power on melt pool length

penetration depth. The deposited area is not affected by the change of laser power but the re-melted area and penetration depth are. Their profile are similar and can be divided into two zones:

- From 0 to about 2.5 kW, both re-melted area and penetration depth are stable
- Above about 2.5 kW, these both metrics regularly increase with the laser power

5.10 (b) is a plot of the bead width and layer height. Again, this plot can be divided into two areas:

- From 0 to about 2.5 kW, the layer height drastically decreases with the laser power while the bead width increases, also at a high rate.
- Above about 2.5 kW, the two measurement keep decreasing and increasing respectively, but at a reduced rate.

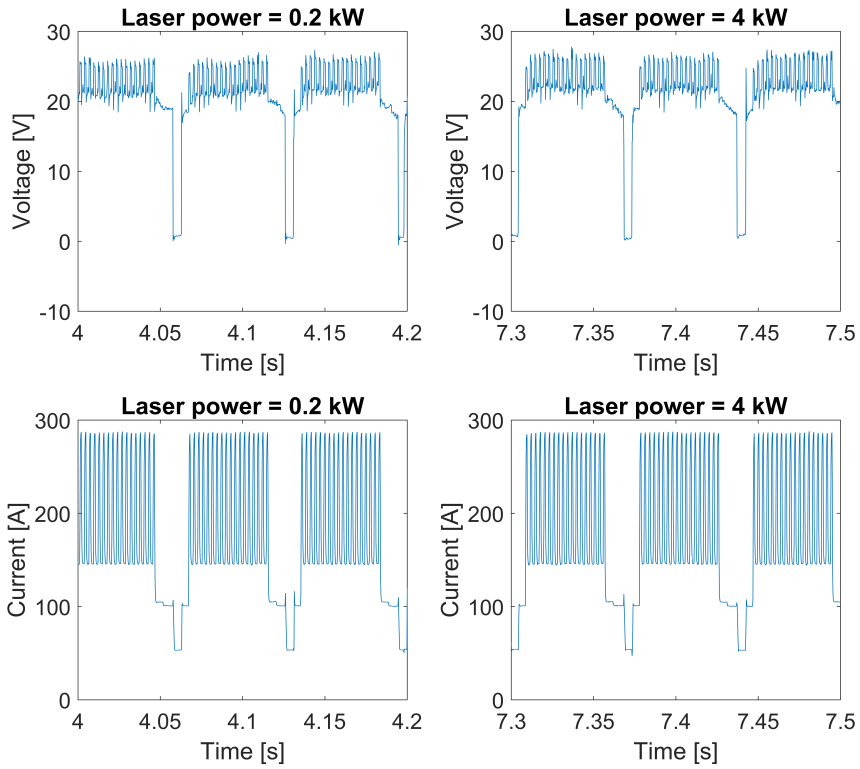


Figure 5.8: Effect of laser power on arc voltage and current

All measurements errors increase greatly with the laser power: thus, the melt pool shape is inconsistent when a high laser power is used

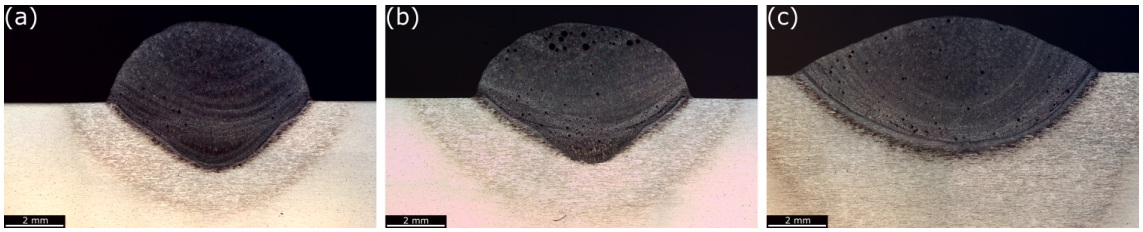


Figure 5.9: Macrograph of bead cross-section, (a), (b) and (c) shows the bead geometry obtained for a laser power of 200W, 1kW, and 4 kW respectively

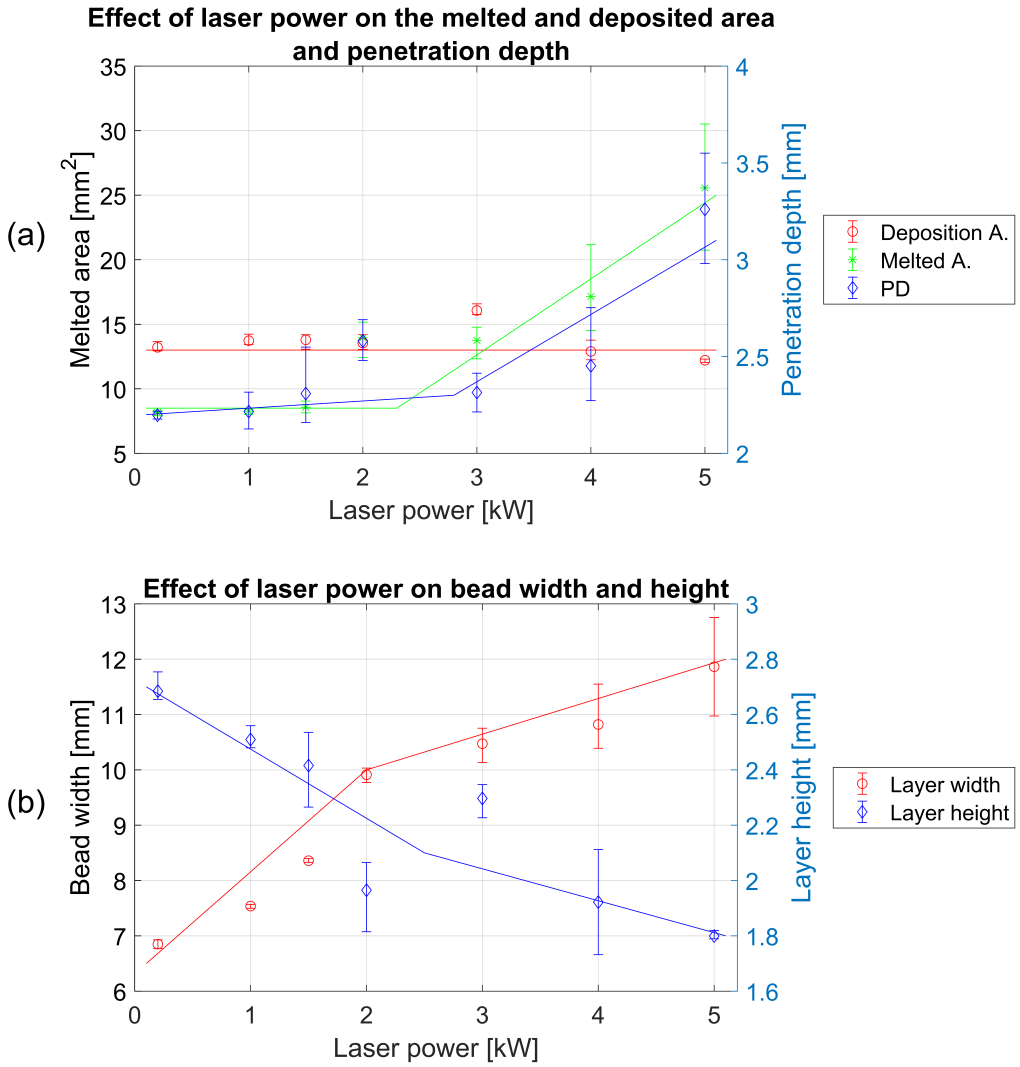


Figure 5.10: Effect of laser power on bead geometry

5.3.1.2 Effect of WFS on bead shape

Table 5.2 gives the geometry measurements and evaluated heat input for a AlCu WFS of 5 and 9 m/min, and a laser power of 0.2 and 4 kW. All geometric values are higher for a WFS of 9 m/min than for 5 m/min, apart from the layer height, which is constant. Regarding the arc heat input, it only depends on WFS and it is not affected by laser power. The errors indicated in the table are the measurement error.

Certain value such as the deposited area and layer height can vary along the bead width due to bead geometry irregularity. For instance, the deposited area of the sample deposited with a WFS of 5 m/min and a laser power of 0.2 kW is 10.7 mm^2 against 15.5 mm^2 with a laser power of 4 kW. However, there was no change in WFS between these two configuration, and these two values should be close to each over. This gap can be explained by the deposition irregularity but also by the different impact the two heat sources can have on the substrate: a higher heat input can generate a higher reinforcement caused by the thermal expansion of the material in the re-melted area.

Table 5.2: Effect of wire feed speed on bead geometry

	Laser power = 0.2 kW		Laser power = 4 kW	
WFS	5 m/min	9 m/min	5 m/min	9 m/min
Arc heat input [J/mm]	207	484	210	482
Deposited area [mm^2]	10.7 ± 0.7	18.7 ± 0.2	15.5 ± 0.6	20.8 ± 2.2
Re-melted area [mm^2]	3.4 ± 0.3	24.8 ± 0.9	15.6 ± 2.4	36.3 ± 2.6
Penetration depth [mm]	1.2 ± 0.1	4.4 ± 0.1	2.1 ± 0.2	4.0 ± 0.1
Bead width [mm]	5.8 ± 0.1	10.6 ± 0.7	11.3 ± 0.7	13.9 ± 0.7
Layer height [mm]	2.6 ± 0.2	2.4 ± 0.1	2.0 ± 0.1	2.2 ± 0.7

5.3.1.3 Effect of laser on process stability

Effect of laser-arc distance on process stability

Figure 5.11 provides a picture taken during the deposition of two beads, for a laser-arc distance of 5 mm (a) and for a laser-distance of 10mm (b), with a laser power of 4 kW. Picture 5.11 (a) shows a uniform melt pool with regular edges. But, when the laser-arc distance is increased to 10 mm as in picture (b), the melt pool becomes wider behind the arc and can be split into two parts, one below the arc, and one below the laser. Figure 5.12 show a schematic of the melt pool for the different configuration. This diagram was drawn using the dimension of the end of the bead as the shape of the melt pool. These schematics

show that the melt pool shape is affected by the laser-arc distance and, in the case of a 10 mm distance, the melt pool can be divided into two areas.

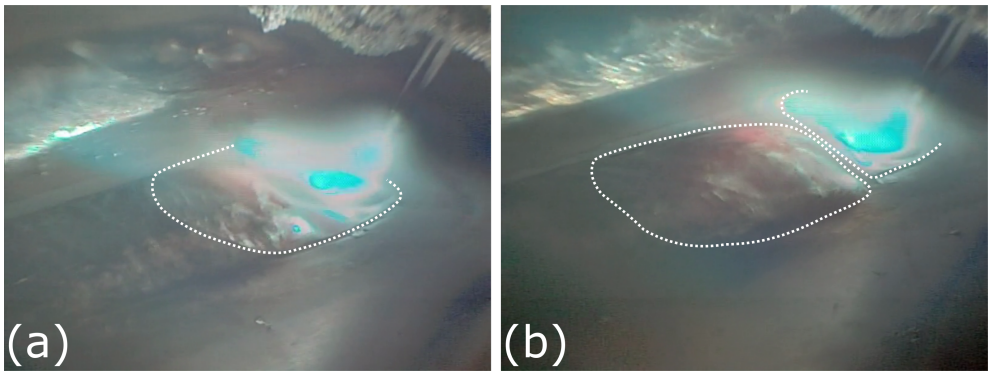


Figure 5.11: Effect of laser-arc distance on melt pool shape for a laser-arc distance of (a) 5mm and (b) 10 mm

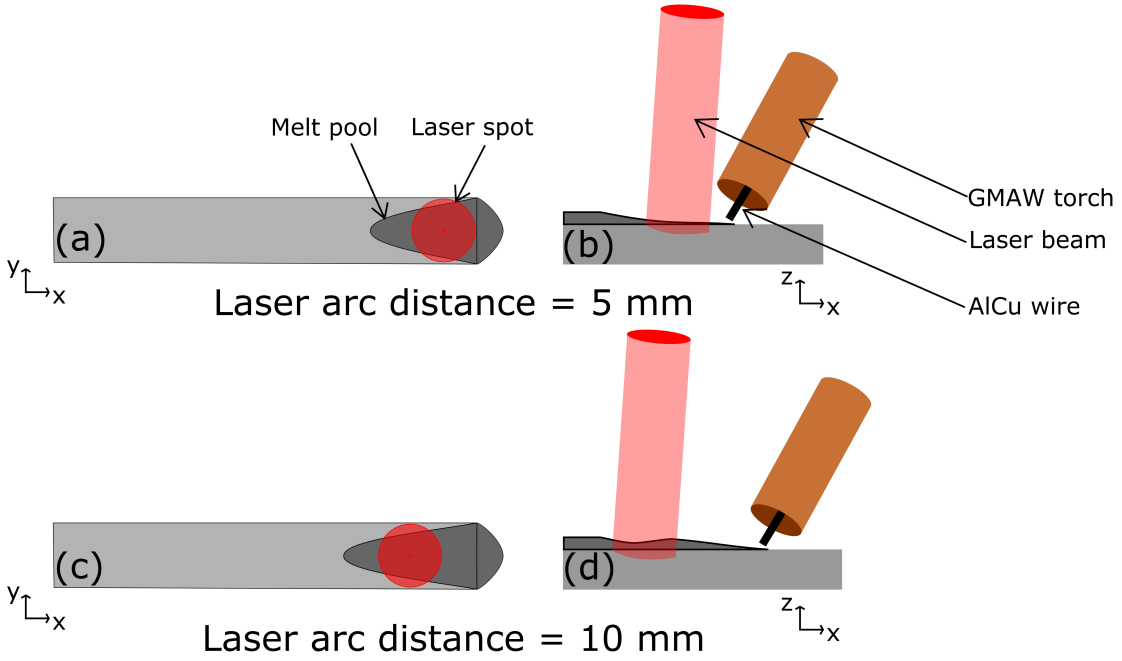


Figure 5.12: Diagram of the melt pool with (a) and (c) views from the top and (b) and (d) side for a laser-arc distance of 5 and 10 mm

Figure 5.13 shows the arc characteristics for both bead depositions. In the four plots, a vertical dash line is used to mark the time when the laser power goes from 0.2 to 4 kW.

Regarding the first deposition (laser-arc distance = 5 mm), the voltage is not affected by the laser power change, as shown in (a). However, for the laser-arc distance of 10 mm, the maximum voltage is reduced by about 1 volt, as shown in (b). Also, lots of voltage irregularities are detected between 10 and 14 seconds, when the laser power is 4 kW.

The current, shown in (c) and (d), does not change when the laser power is increased and the current profile is the same for both beads. Nevertheless, it is possible to see some irregularities at the end of the deposition of the second bead, in picture (d).

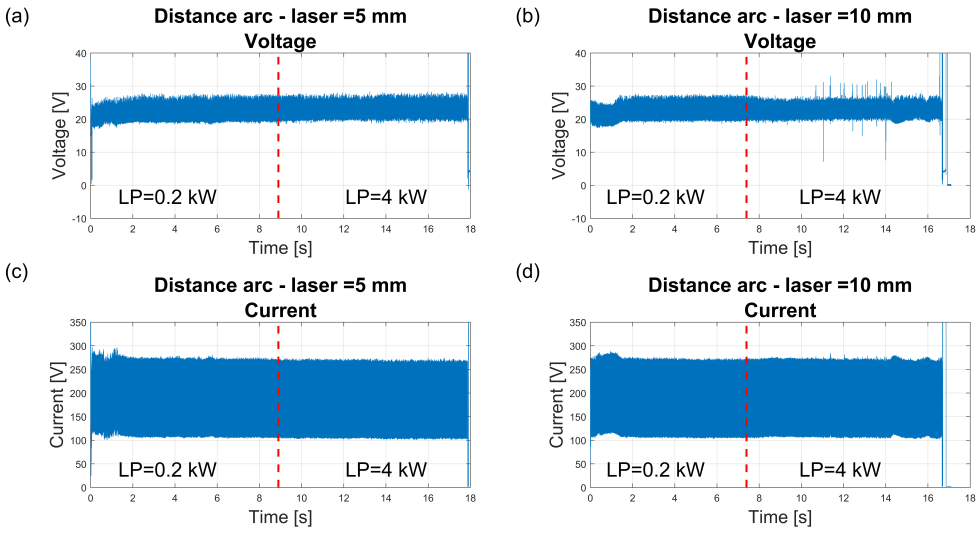


Figure 5.13: Effect of laser-arc distance on (a) and (b) arc voltage and (c) and (d) arc current for the laser-arc distance of 5 mm (a) and (b) and 10 mm (b) and (d)

Effect of laser on arc stability

Figure 5.14 shows the voltage and current profile measured during deposition. Both voltage and current show instabilities for a laser power of 0.2 kW. For the exact same configuration but with a laser power of 4 kW, there is no signs of instabilities. In the previous section it was shown that laser power did not have effect on the electric arc if CMT pulse process is used. But Figure 5.14 shows that, when Pulse process is used, the use of laser

can dramatically reduce instabilities if there are any.

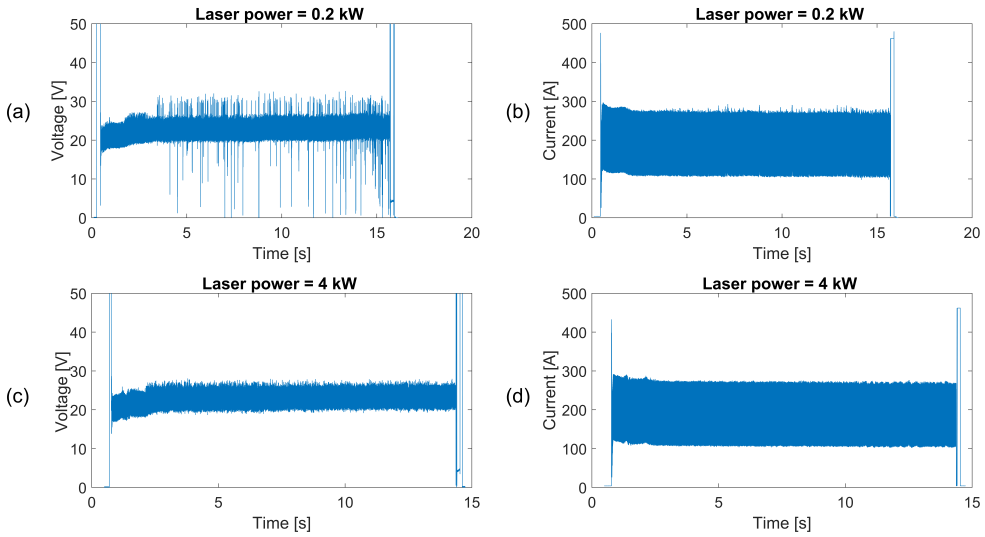


Figure 5.14: Effect of laser on arc stability: (a) and (b) example of the voltage and current profiles with a laser power of 0.2 kW, and (c) and (d) with a laser power of 4 kw.

5.3.2 Zinc addition using laser-assisted WAAM

5.3.2.1 Effect of zinc addition on process stability and microstructure

In Figure 5.15 (a) (c) (e) and (g) can be seen longitudinal section of bead deposited with different zinc-arc distance. The following observations can be drawn:

- When no zinc was added, the process was smooth and spatter free. The optical image in Figure 5.15 (a) shows a wrinkled bead profile and regular microstructure.
- When zinc was added 5 mm away from the arc, there was a large amount of spatter generated as zinc is melted and vaporised by the very high electric arc temperature. The bead profile is relatively smooth and no coarse zinc area can be seen (b). As part of the zinc is vaporised, it is not possible to say from this macrograph if there is actually zinc in the bead.

- When zinc was added 10 mm away from the arc, the process was spatter-less and stable. The bead profile is smooth but some zinc accumulation is exposed by etching in the bottom of the bead (c).

- When zinc was added 15 mm away from the arc, spatters were formed and the process was not stable: the wire position fluctuated because its end rubbed the bead during deposition. It resulted in an inhomogeneous addition of zinc which can be seen in (d); some very large zinc aggregation at the top of the bead can be found.

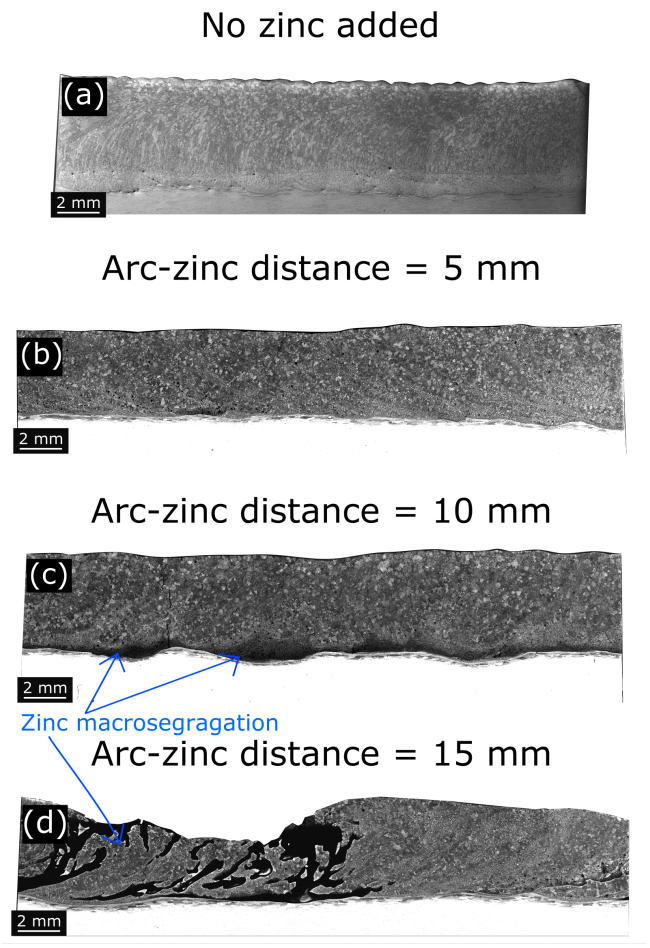


Figure 5.15: Optical images of longitudinal layer cut deposited with a zinc-arc distance of (b) 5 mm, (c) 10 mm, and (d)15 mm. Image (a) shows a reference microstructure without any zinc addition.

5.3.2.2 Effect of laser power and wire feed speeds on microstructure of deposited material

Table 5.3 provides the average heat input during the deposition of the single beads. As shown before, the laser power has no effect on the arc heat input, which increases with the AlCu WFS.

Table 5.3: Arc and laser heat input during the deposition of single aluminium zinc bead

	A_1	B_1	C_1	D_1	E_1	F_1	G_1
AlCu WFS [m/min]	8	9	9	9	6	6	10
Arc heat input [J/mm]	378	478	479	480	270	269	500
Laser heat input [J/mm]	60	60	90	90	90	150	90
Total heat input [J/mm]	438	538	569	570	360	419	590

Figure 5.16 gives the cross-section of all samples deposited for this part of the work. Pictures (a), (b), (c), (d), (e), (f), and (g) show the cross-section of the bead on plate A_1, B_1, C_1, D_1, E_1, F_1, and G_1 respectively; pictures (h), (i), and (j) show the cross-sections of the 3 layer-high wall B_3, F_3, and G_3. In pictures (a), (c), (d), and (e), it is possible to see high zinc concentrated areas, darker than the rest of the matrix, which clearly shows a insufficient mixing between the AlCu and zinc wires. In picture (e) can be seen, in a bright colour, part of the zinc wire not fully melted during the process.

The effect of WFS of both Al-Cu and zinc wires and laser power on microstructure is considerable. Figure 5.16 (e) shows that a certain heat input is required to melt the zinc wire. This heat input can be increased by either increasing the arc heat input or the laser power. In the latter case, increasing the laser power from 3 to 5 kW works but leads to zinc accumulation at the bottom of the bead (f). Increasing the arc heat input, by increasing the WFS from 6 to 9 m/min, allows a better melting and mixing of the zinc wire (b). This positive mixing effect can also be noticed when comparing pictures (a) with (b), and (c) with (g). Finally, the lack of mixing in sample C_1 (c) compared to B_1 (b) shows that, for

the same WFSs, increasing the laser power can reduce the mixing capability of the melt pool.

Pictures in (b), (f), and (g) show a relatively homogeneous microstructure, despite some small zinc accumulation at the bottom of the bead in (f) ; therefore the parameters used to deposit these three beads were used to deposit three-layer-high walls, whose microstructures are displayed in pictures (h), (i), and (j). The deposition of layers on top of each other did not leads to process instabilities despite the zinc content of the bottom layer and no the bead geometry obtained was regular. These cross-sections include cracks in the lower part of the wall. Picture (i) presents two very dark areas, one at the bottom of the wall, and a second one, which seems to follow the bottom of the second deposited layer. There is not such zinc concentrated area visible in picture (h) and (j). A large part of the microstructure, away from the substrate, was very uniform in all three samples.

Figure 5.17 gives the microstructure in a longitudinal section of samples A_3, F_3, and G_3, in picture (a), (b), and (c) respectively. Five pictures taken at higher magnification for each wall are provided in (a.1) to (a.5), (b.1) to (b.5), and (c.1) at (c.5). Dark areas, where zinc concentration is high, can be seen in all samples despite what was observed in Figure 5.16 (h) and (j). However, there are more of these areas in sample F_3 than in the other two, and sample A_3 seems to be the one where the mixing between AlCu and zinc wire is the best.

As noticed in Figure 5.16 (h), (i), and (j), there are numerous cracks in the lower part of the three walls, as shown in Figure 5.17 (a.5), (b.3), (b.5), and (c.4). (b.4), and (c.5) show that some cracks, generated in the bottom of the bead, tend to propagate in the wall. It is possible to see the lack of mixing between the two wires in picture (a.1), (a.4), (b.2), (b.5), (c.2), and (c.4). However, for all three samples, the microstructure on top of the wall is reasonably uniform, as shown by (a.3), (b.1), and (c.1). Pictures (a.2), (b.3) and (c.3) show the difference of grain structure in the lower part of the wall, with bigger grain

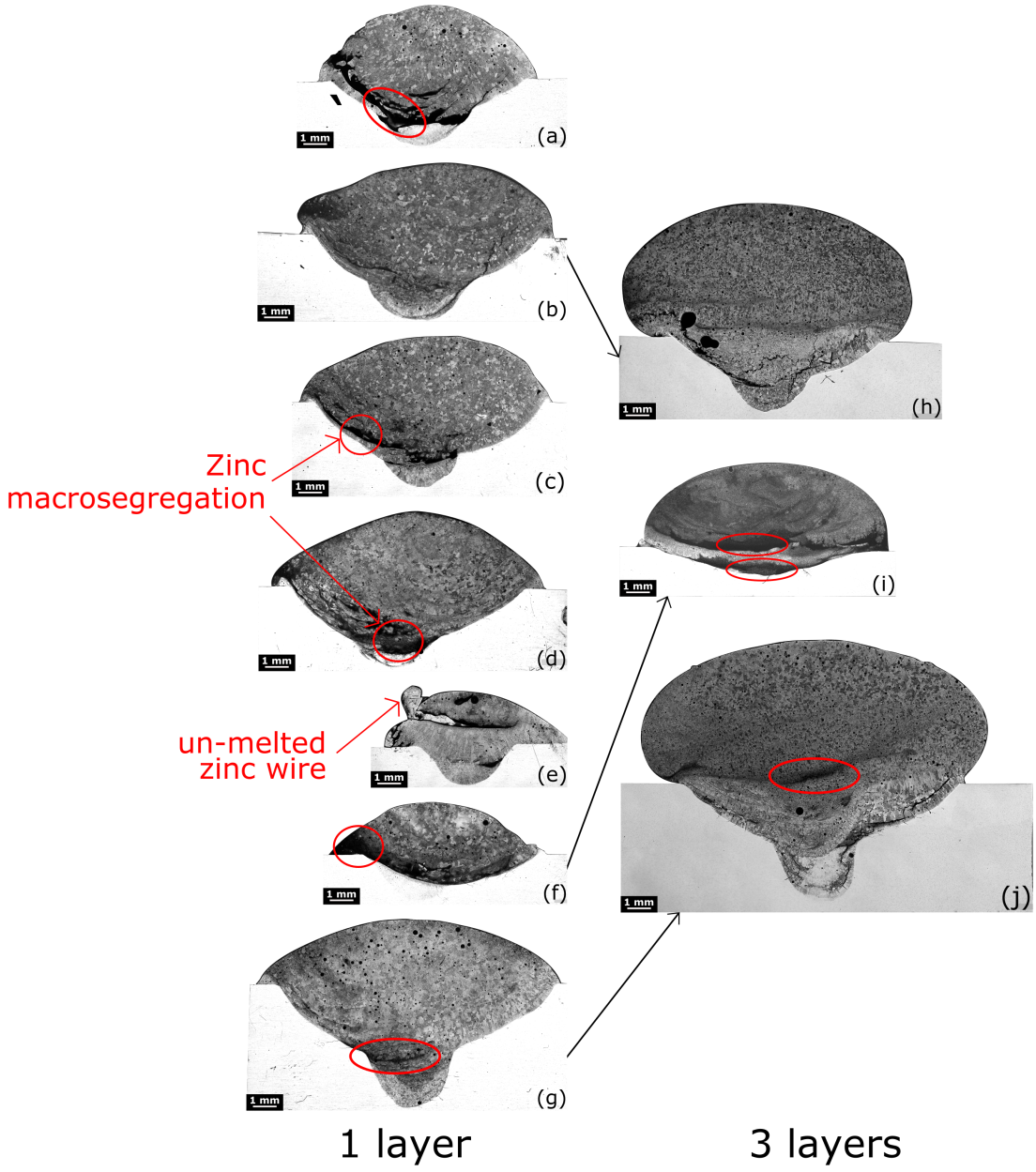


Figure 5.16: Microstructure of aluminium zinc bead on plate. (a), (b), (c), (d), (e), (f), (g), (h), (i), and (j) shows the cross-section of sample A_1, B_1, C_1, D_1, E_1, F_1, G_1, A_3, F_3, and G_3 respectively. The process parameters are given in table 5.1

than in the top of the wall.

Figure 5.18 shows the result of element mapping carried out on top of the sample A_3. EDX measurements, given in table 5.4, were carried out in the areas highlighted in Figure 5.18 (a). These elements prove that zinc was successfully mixed in the matrix. Some zinc micro segregations can be observed around the pore (spectrum 5, 9, and 10) and in the matrix (spectrum 2 and 3). Micro segregation of copper can also be observed and measured (spectrum 11).

Table 5.4: EDS measurements in wt% of different points and areas shown in Figure 5.18 (a)

Element	Spect. 1	Spect. 2	Spect. 3	Spect. 4	Spect. 5	Spect. 6
Al	74.6	43	65.3	65.3	33.1	37.6
Zn	23.9	51.4	32.4	31.9	36.1	54.6
Cu	1.3	4.9	1.7	2.2	30.5	6.3
Si	...	0.5	0.3	0.4	0.3	0.9
Mn	0.2	...	0.2	0.3	0.32	0.7

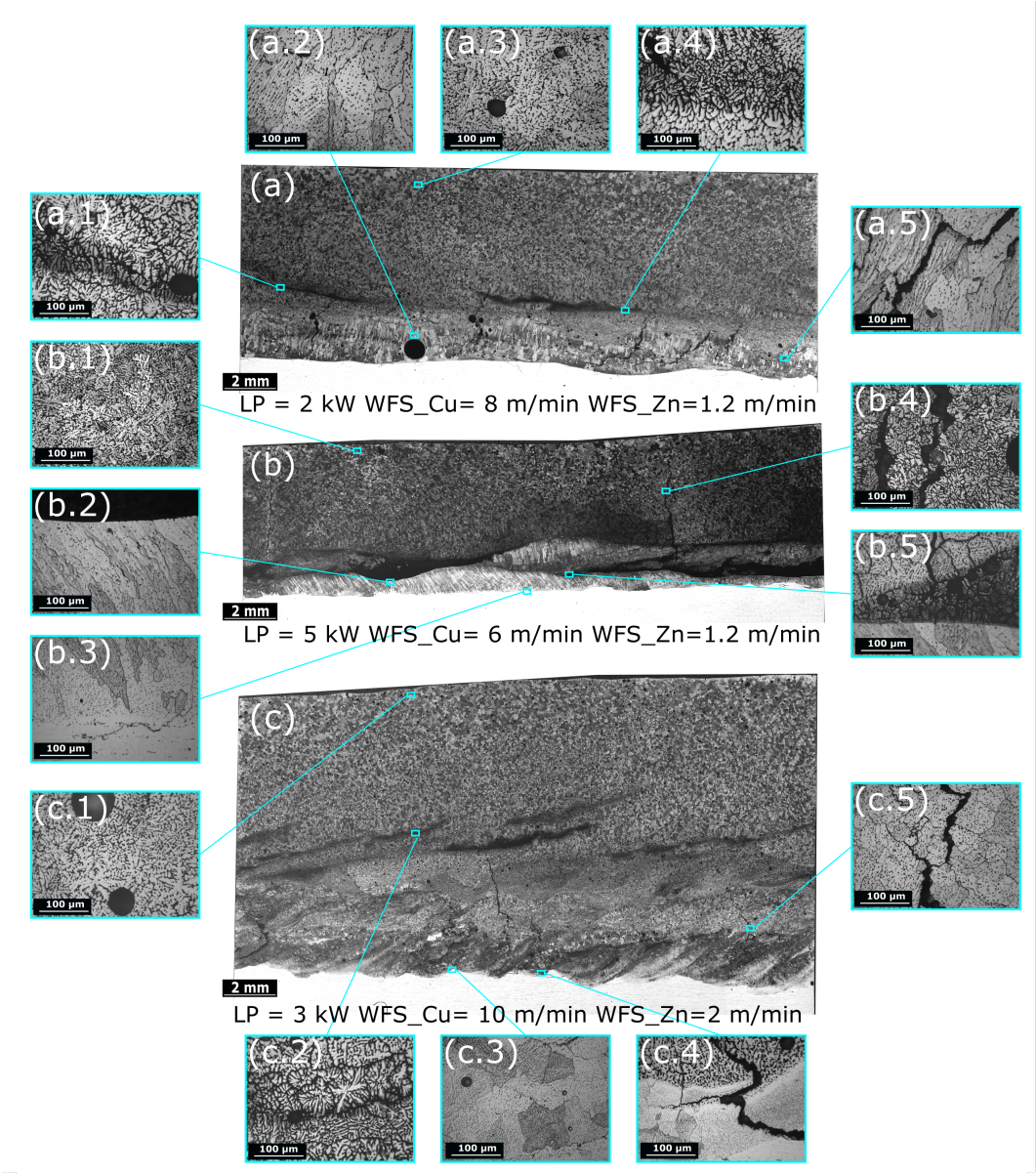


Figure 5.17: Longitudinal section of three-layer-high wall: (a) A_3, (b) F_3, and (c) G_3

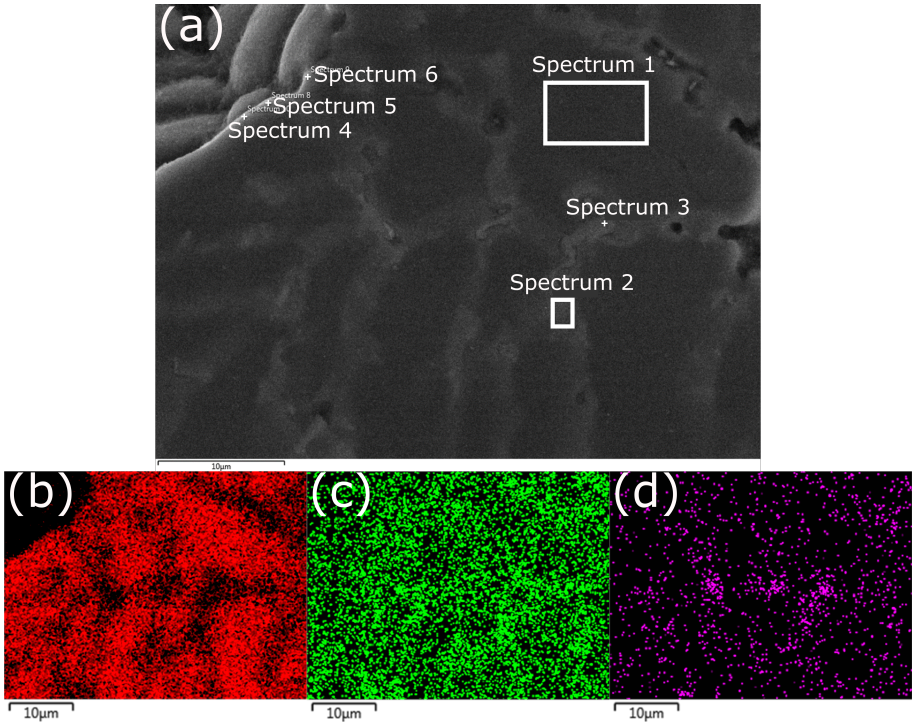


Figure 5.18: Element mapping generated by SEM from the top of sample W_3. Picture (a) is the SEM image of the area, and (b), (c), and (d) are the maps of Al, Zn and Cu respectively

5.3.2.3 Effect of deposition parameters on bead shape

Regarding bead geometry, AlCu WFS has a great impact on the bead shape, just as shown in the case of laser-assisted WAAM without any zinc addition in section 5.3.1.1. As for bead without zinc addition, the laser power has an effect on the bead geometry when zinc is added. Figure 5.19 provides the plot of penetration depth and layer height for samples B_1, C_1 (AlCu WFS = 9 m/min), E_1, and F_1 (AlCu WFS = 6 m/min), along the value measured in the case of no zinc addition.

The first plot shows that the penetration depth is higher for a AlCu WFS of 9 than 6 m/min, as shown for deposition without zinc addition in paragraph 5.4.1.2. The penetration depth of the bead deposited using a AlCu WFS of 6 m/min unexpectidly decreases with laser power. That can be explained by the drastic change in geometry, as shown by pictures (e) and (f) in Figure 5.16, probably due to the full melting of the zinc wire when a laser power of 5kW is used. The penetration depth of the bead deposited using a AlCu WFS does not change between 2 to 3 kW lase power. This follow the same pattern as the value measured for the deposition without zinc.

Regarding the layer height, the value reached by aluminium zinc deposition is higher than the one achieved by deposition without zinc: this is due to the extra material added with the zinc cold wire. More material is deposited without increasing the heat input, resulting in a higher layer height. The layer heights measured for the aluminium zinc bead follow the same trend than zinc-free deposit, with similar slopes in both AlCu WFS cases.

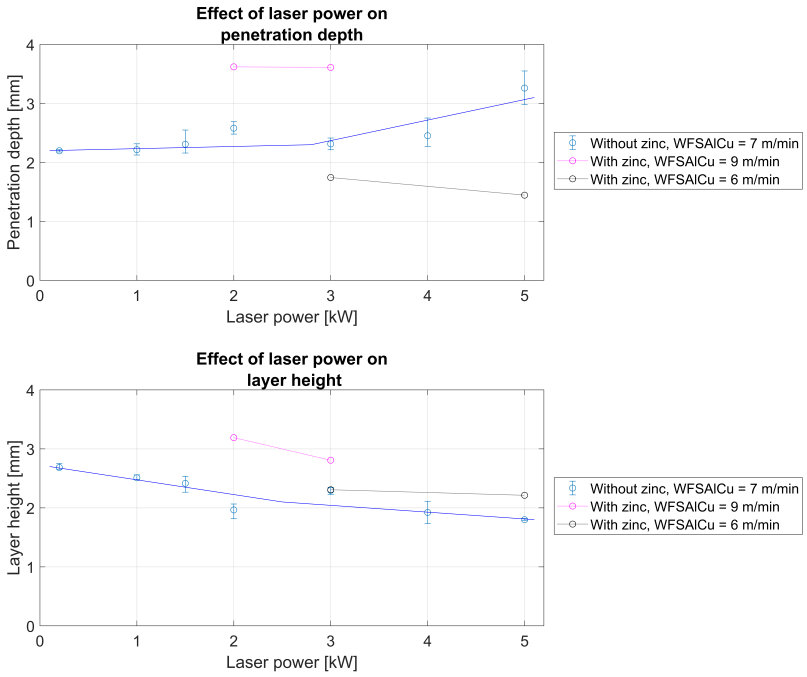


Figure 5.19: Effect of Laser power on bead geometry for aluminium zinc deposition with different laser power and AlCu WFS

5.4 Discussion

5.4.1 Laser-assisted WAAM

5.4.1.1 Effect of laser power on bead shape

According to Figure 5.8, the parameters chosen to study the effect of laser power on bead geometry do not lead to any of the interaction between laser and arc mentioned in the Literature review Chapter page 49. The laser has a visible effect on both melt pool shape, see Figure 5.5, and final bead geometry, see Figure 5.10.

Below a laser power of 1.5 kW, the laser has no effect on the melted or deposited area nor on the penetration depth. However, Figure 5.6 and 5.7 show that the melt pool is longer when laser power increases, while staying below 1.5 kW. This means that the

laser beam energy is not high enough to melt more material than the amount melted by the electric arc, but by compensating heat losses it elongated the melt pool.

Above a laser power of 2 kW the laser has a considerable effect on the bead shape. This means that not only does the laser melt the metal behind the arc, but it also contributes to the melting of more material. It can be seen in Figure 5.9 that the melted area shape changed from a V shape to a semi-circle one. The V shape is due to a non-uniform heat source with a higher power density in the middle of the arc. The semi-circle shape is typical in laser welding in conduction and transition mode [10, 125].

As the arc heat input is not affected by the laser beam the global heat input increases with the laser power. The increase in bead width and decrease in layer height with laser power is due to the increase in heat input, as observed by Martina during plasma deposition of Ti–6Al–4V [128] and by Ayarkwa during CMT [50] and GTA [68] deposition of aluminium. It is interesting to note that the change in slope when the laser power is above 2 kW: some energy goes into melting so the bead width keeps increasing, the layer height keeps decreasing, but at a lower rate than for laser powers below 2 kW. This suggests that below 2kW the laser power balances the heat loss and is only enough to contribute to the melting above 2 kW.

5.4.1.2 Effect of wire feed speed on bead shape

The WFS has a drastic effect on bead geometry. When the WFS increases, all bead width, penetration depth, melted area are increasing. The layer height is relatively stable. This is due to the much higher arc heat input during the deposition of high wire feed speed, as more heat is required to melt the material. Cong et al. [12] showed that the travel speed play a key role in bead geometry, and Ayarkwa et al. [50] demonstrated that the ratio between WFS and travel speed is the key factor to control bead geometry. It is hence

not surprising here to observe such drastic changes when the WFS varies. This inter dependence between WFS, heat input, and bead geometry makes GMA very difficult to control in term of bead shape.

For a laser power of 4kW, the arc heat input does not change: the global heat input (laser + arc) is, therefore, increasing by 400 J/mm. This explains the increase in melted area, depth of penetration and bead width. The change in geometry caused by the laser is greater for the bead deposited using a WFS of 5 m/min as the global heat input increased by 153% compared with an increase of 66% for the bead deposited with a WFS of 9 m/min. Especially when using low WFS, using a laser beam could be an option to control better the bead shape.

5.4.1.3 Effect of laser on process stability

Effect of laser on arc stability

The process is stabilised by the laser, as shown in Figure 5.14. Numerous studies showed the effect of laser on the electric arc in keyhole welding: it can change the droplet transfer [121, 123], increase the electron density and temperature in the arc [132, 133], leading to a better arc stability, and this even for low laser power.

In the case of this experiment, the process is stable if the laser power is 4kW. However, some fluctuation of the distance between the wire and the work piece generated excessive spatter when a low laser power was used. Despite the differences between the experimental set up used for this study and the one used in the literature (mainly involving much smaller beam diameter and thus higher power density, and a smaller distance between the arc and the laser beam, see page 49), it is possible to conclude that the laser has a stabilisation effect on the process. Due to the large laser-arc distance and beam diameter, it is unlikely that the laser is stabilising the arc itself. But it is possible that the laser

stabilises the melt pool and stabilises the electric arc by extension.

Effect of laser-arc distance on process stability

A negative effect of the laser can occur if the laser-arc distance is too large as shown in Figure 5.13. This seems to be due to two phenomena:

- The stabilisation effect occurring in keyhole welding explained above is probably considerably reduced in this case because of the large distance between the arc and the laser.

- As shown in Figure 5.11, it is possible to see that the melt pool is divided into two parts, below the arc and below the laser. Small variations of the arc lead to a disturbance of the front of the melt pool; as the laser absorption largely depends on the state of the material it reaches, these small disturbances could induce large changes in the second half of the melt pool. Hence, small instabilities in the arc melt pool can generate large instability of the full melt pool.

Therefore, the distance between arc and laser beam needs to be kept within a certain limit, in order to have a stable deposition process.

In conclusion, regarding laser-assisted WAAM, the use of laser allows an elongation of the melt pool, and both laser power and WFS play a key role in the bead shape. Also, if the distance between the arc and the laser beam is wisely chosen the laser can enhance the deposition process stability.

It is important to highlight here that instabilities during deposition with low laser power were not systematically observed during this research project. The reason why instabilities occurred here is in all likelihood the presence of spatters on the substrate surface, disturbing the arc and melt pool stability.

5.4.2 Zinc addition using laser-assisted WAAM

5.4.2.1 Effect of zinc addition on process stability and microstructure

The area where the zinc wire is fed plays a key role in process stability and microstructure. As observed by Pickin [134], it is not possible to feed a cold copper wire in the arc, or near it because it generates spatters and disturbs the arc. During GMA of aluminium zinc alloy, it has been shown that metal droplets explode during the process, because of high zinc vapour pressure, generating excessive spatter [135]. Here, a cold zinc wire cannot be fed in the arc without generating excessive spatters. However, it is possible to feed the wire behind the arc without disturbing the process stability.

5.4.2.2 Effect of laser power and wire feed speeds on microstructure of deposited material

Bead geometry

The analysis of the effect of WFS ad laser power conducted on laser-assisted WAAM trials, without zinc addition seems to be valid when zinc is added to the melt pool.

Zinc macrosegregation

WFS and laser power play a key role in zinc macrosegregation. The objective of this study was to prove the possibility of depositing aluminium zinc using laser-assisted WAAM, therefore, there are not enough experimental results to conclude on the specific effect of process parameters on zinc macrosegregation. However, by comparing the observation made in section 5.3.2.2 to the literature it is possible to draw some hypothesis. Kou presented the various driving force for fluid flow in the melt pool [135] and used these forces to explain some macrosegregation phenomena [136] in welding. During arc welding the electromagnetic forces tend to promote mixing in the melt pool, and according to

the fluid velocity calculated in [136], this mixing has time to occur before solidification. The buoyancy force and surface tension gradient together with the electromagnetic forces generate a convection pattern below the melt pool surface. Even if the convection pattern can prevent mixing, the droplets of filler material can gain some momentum from the arc plasma and gravity force, and a good mixing can be achieved [136]. However, in laser beam welding the convection is dominated by surface tension and the melt pool mixing can be poor. Finally, there is an area near the melt pool boundary where very little mixing occurs, even in arc welding.

Thus, in the case of this work, several phenomena can impact on macro segregation:

- At constant laser power, if the WFS increases, the electromagnetic forces also increase and could improve the mixing.

- At constant WFS, if the laser power increases the convection pattern at the melt pool surface is getting stronger. This can trap zinc at the bead top surface and prevent a good mixing.

- At constant WFS, if laser power increases, it could change the droplet transfer of the cold wire, leading to a better mixing due to droplet momentum.

- As zinc is much denser than aluminium, 7.14 against 2.7, the gravity force might be counter-productive as it might bring zinc in the bottom of the melt pool where very little mixing occurs.

A more detailed study is required to determine the optimum conditions for a good zinc mixing. It is very important to highlight that the ratio between AlCu and zinc WFS lead to a very high expected zinc content, as shown in Table 5.1. This has obviously a drastic effect on macro and micro segregation, on the material solidification behaviour and hot

cracking sensitivity would be very different if the zinc content was below 8%, as it is in most of aluminium zinc wrought alloys.

Nevertheless, some parameters used here led to a relatively homogeneous microstructure. The EDS measurements in Table 5.4 show some microsegregations of zinc and copper and Figure 5.17 shows numerous cracks. These are due to the solidification behaviour of the specific aluminium copper zinc mix, which follows complex phase diagrams described by the Aluminium development association [137]. Again, as no composition optimisation was intended during this work, these microsegregations and cracks, which highly depend on alloying element concentrations will not be discussed here. However, the element mapping and EDS measurements prove it is possible to generate a relatively homogeneous matrix composed of aluminium, copper and zinc using laser-assisted WAAM.

5.5 Conclusions and further work

This research project led to the following conclusions regarding laser-assisted WAAM and the possibility of depositing aluminium zinc by this process.

- Laser-assisted WAAM can be used to deposit aluminium and to produce an elongated melt pool with a stable process.

- The bead shape produced by laser-assisted WAAM largely depends on the main wire feed speed, but also on laser power.

- It is possible to add zinc in the deposited material using a cold wire by changing the melt pool shape with the laser beam. As the melt pool elongated behind the electric arc it was possible to cold feed zinc directly in the melt pool without impacting on

process stability. In some cases, the mixing between the two materials was successful and led to the deposition of an aluminium copper zinc matrix.The possibility of achieving this in situ alloy mixing was proved possible for a three-dimensional structure of three-layer height.

There is still plenty of work to do to build 3-dimensional high strength aluminium zinc component. The composition of the matrix will need to be optimised to minimise the risk of solidification cracking and increase the mechanical properties. In order to do so, a mixed aluminium zinc wire should be used as a cold wire instead of a pure zinc wire. The use of a smaller diameter cold wire would also give a wider working envelop in term of WFS and therefore composition. The effect of beam diameter, relative angle between the GMA torch and laser beam, and travel speed on mixing capability of the melt pool and solidification behaviour will also need to be characterised.

Moving away from the specific application of laser-assisted WAAM investigated in this study, this process also has great potentials in term of bead shape and microstructure control and alloy development.

Firstly, numerous studies have been conducted so far on the effect of process and deposition parameters on bead shape: this topic is critical for 3-dimensional component manufacture. In laser-assisted WAAM, parameters such as the relative angle between GMA torch and laser beam, travel speed, and laser beam diameter doubtlessly play a key role in bead shaping process and would require a dedicated research study to be brought to light. Secondly, solidification and cooling rate have a great effect on microstructure and mechanical properties: controlling these rates is another crucial part of WAAM development. Laser-assisted WAAM has the potential to adjust thermal cycle during deposition and could be subject to further investigations in this regard. Finally, in situ alloying is the only financially applicable solution for composition optimization in WAAM. This

is because the other path for composition optimization, the manufacture of customized composition wire is too expensive and time-consuming to be used during an optimisation by iteration method. Laser-assisted WAAM give the possibility of depositing a wide range of composition, even with volatile elements: this make possible affordable alloy development for WAAM application.

Chapter 6

Phenomena and issues at the interface between the substrate and WAAM deposited material

6.1 Introduction

In order to produce aluminium parts which integrate both WAAM material and wrought product, it is essential to evaluate the properties of the interface between the substrate and WAAM deposit. Most of the literature on aluminium WAAM focuses on the deposited material microstructure and mechanical properties and very few studies have been carried out on the interface between the substrate and deposit. The aim of this study is to investigate the phenomena occurring at the interface, which may be detrimental to the integrity and mechanical properties of the component.

Numerous studies of fusion welding of aluminium and of the interface between weld bead and parent material have been published as detailed in Chapter 2 section 2.3.1. This literature gives a strong base for the study of the WAAM material-substrate interface: it

explains how heat affects the parent material, with or without melting, and how welding parameters, wire and substrate alloys play a key role in weld microstructure and post-weld mechanical properties.

The first objective of this chapter was to assess the possibility of producing part with homogeneous mechanical properties when combining WAAM material and wrought product. The second objective was to assess the possibility of producing components with graded mechanical properties made of both WAAM deposit and wrought product. The idea behind this second objective was to check if it is possible to produce a part with different mechanical properties in the WAAM deposit and substrate, with an interface between them which is not detrimental to the part performance. The strategy chosen was to study a wide range of interfaces by depositing three alloys, 2319, 2024 and 5556 onto nine different substrates.

Both Results and Discussion sections are divided into four parts. The first part introduces the issues found at the interface between aluminium lithium and aluminium zinc alloys substrates. These substrate alloys are of interest because they can achieve very high mechanical properties. Also, aluminium lithium alloys are very expensive: they would greatly benefit from the very low buy-to-fly ratio a part made of both wrought and WAAM material could reach. Unfortunately, these two alloy families are widely considered as un-weldable because of their high solidification cracking sensitivity, and porosity level in the fusion zone: this is the reason why these alloys are treated together in this first section.

The second part deals with combinations of aluminium copper alloys both as substrate and wire. These alloys are widely used in aerospace because of their high mechanical properties, but most of them are considered un-weldable. In this part of the work, it was possible to manufacture samples made of one alloy by using the same alloy for the substrate and wire.

The third section focuses on using aluminium magnesium-silicon substrates and the effect of substrate microstructure on the interface. The substrate alloy used, 6061, is a very common aluminium alloy and is used when middle strength, high corrosion resistance, and good weldability is required. In this section two types of 6061 substrates are used, one rolled plate, referred as 6061_{Rolled} and one plate produced by melt spinning, referred as 6061_{RSP}. These two plates were chosen to investigate the effect of grain size on the interface microstructure and properties.

The fourth and last part is about the use of rapid melt spinning alloy as substrate and aluminium magnesium as deposit. These substrate alloys are very expensive compared with common rolled or extruded product, and therefore would not be used to manufacture large component with a high buy-to-fly ratio. That is why it would be interesting to use them as substrate to deposit on. The first alloy, 501, is an aluminium magnesium scandium alloy, and the second, 905, is an alloy usually used to manufacture optical mould but was selected here because of its high as extruded tensile properties. 5556 was used as wire.

To make the reading of these two chapters easier, the interface between a substrate of alloy XXXX with a WAAM deposit of alloy YYYY is further referred to XXXX & YYYY combination or XXXX & YYYY interface.

6.2 Methodology

The deposition parameters, material composition and the experimental procedures used to conduct the microstructural study and tensile tests, with and without Digital Image Correlation (DIC), are described in Chapter 3. Figure 6.1 shows the tensile specimen geometries used. Apart from the combination 2139 & 2319, all interfaces were tested using the geometry shown in Figure 6.1 (a); the specimen thickness and gauge length were 2.5 mm and 22 mm respectively. The combination 2139 & 2319 was tested with

considerably larger tensile coupons, shown in Figure 6.1 (b): this combination was the first one investigated and the tensile specimens were then downsized in order to reduce the manufacturing time and cost of the specimens. The specimen thickness and gauge length were 2.5 mm and 64 mm respectively.

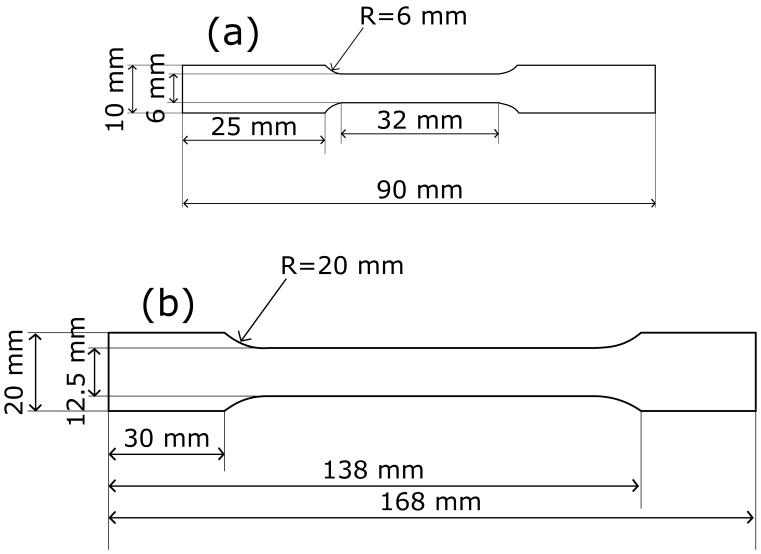


Figure 6.1: Tensile specimen geometries (a) used to determine the properties of all interfaces but the combination 2139 & 2319 which was tested using the specimen shown in (b)

Various alloys were used in this study; the following section aims to justify why these alloys were chosen.

- 2219 is an aluminium copper alloy, with a high copper level (between 5.8 to 6.8 wt%): it is often considered as a binary aluminium copper alloy. It is widely used in launcher vehicles cryogenic fuel tank manufacture at T8 temper because of its mechanical properties and its fusion weldability with 2319 [138, 139, 140]. This alloy is very close to 2319 in composition except for the addition of grain refinement elements (Ti, Va and Zr) in 2319 wire.

- 2024 is an aluminium copper magnesium alloy (Cu content between 3.8 % and 4.9 % and Mg content between 1.2 % and 1.8 %). It is used in the form of clad plates in aircraft fuselage [17, 140] but is considered as unweldable by fusion processes because of its high susceptibility to liquation and hot cracking due to its large freezing range, especially when mixed with other alloys [110, 141]. However, it has been proven that 2024 as a wire filler can be used to weld 2024 plates [101].

- 2050 is an aluminium lithium alloy (Cu: 3.2 % to 3.9 %; Mg: 0.2 % to 0.6 % Li: 0.7 % to 1.3 % ;and Ag: 0.2 % to 0.7%). It is considered a medium to high strength alloy with high damage tolerance and corrosion resistance. The use of lithium also significantly reduces density, e.g. the addition of 1% of lithium decreases the density by about 3% [111]. It can be used to replace 7000 series thick plates in aircraft internal structures [142]. However, to reach these high mechanical properties, it is required to apply cold work after solution treatment [143]. It might be a problem to carry out this cold work on complex near net shape parts and therefore to deposit aluminium lithium, but these alloys can be used as substrates.

- 2139 is an aluminium copper silver alloy (Cu: 4.5 % to 5.5 %); Mg: 0.2 % to 0.8 %; and Ag: 0.15 % to 0.6%), used in armoured vehicles manufacture [144]. In contrast to 2050, this alloy can reach high strength and damage tolerance without cold work. For this reason, the compatibility of this alloy with additive manufacturing was studied using electron beam free-form fabrication process [95].

- 7449 is an aluminium zinc alloy resulting from the optimisation of commonly used alloys such as 7055 and 7075. It is widely used in aircraft manufacture in compression dominated part. 7449 alloy components can be found in the upper wing skin, where damage resistance is not such a strong requirement as in the lower wing [20].

- 6061 is an aluminium magnesium silicon alloy widely used as structural alloy when medium strength is required. It is a weldable alloy with good corrosion resistance [145]

- RAS 905 is an alloy produced by melt spinning process. The very fine grain structure of this alloy is very beneficial for diamond turning optics and moulds: this alloy is commonly used in the manufacture of moulds for contact lenses [146]. For this project, this alloy was chosen for its high strength.

- RAS 501 is a melt spun scalmalloy (Aluminium magnesium scandium alloys). Scandium is a well known grain refiner meagrely used because of its extensive cost. Additive manufacturing and its low fly to buy ratio could enable the use of these expensive aluminium scandium alloys: this is why this alloy was used in this study.

6.3 Results

6.3.1 Aluminium zinc and aluminium lithium substrates

Figure 6.2 provides optical images of longitudinal sections of the 7449 & 2319 and 2050 & 2319 combinations. A large number of pores can be seen in the first layer deposited on the 7449 substrate as well as small cracks. Pores can be seen in the bottom of the first layer deposited on the 2050 substrate, at the boundary between fusion zone and substrate

Figure 6.3 gives the hardness profile across the interfaces between 7449 and 2050 substrates and 2319 and 2024 deposits. The hardness is always higher in the substrate (below the interface plane at 0 mm) than in the deposited material, as shown by the gap

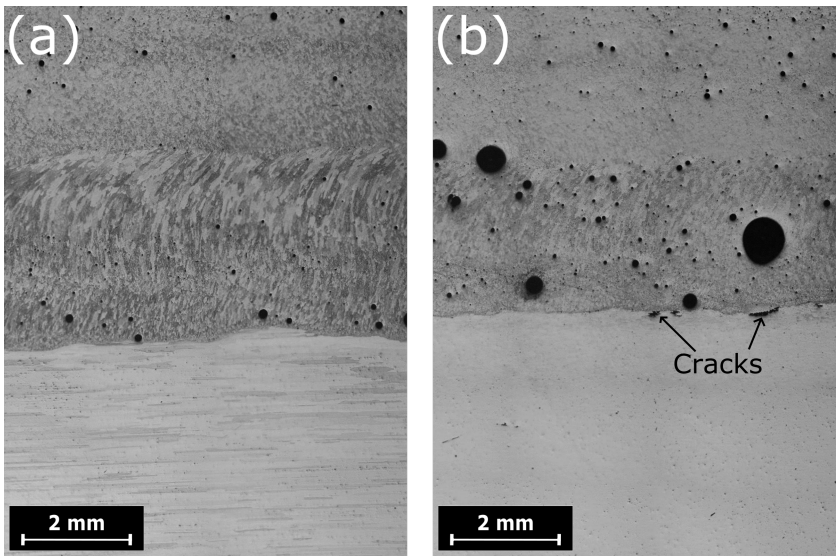


Figure 6.2: Longitudinal section of as-deposited interface between 2050 & 2319 (a), and 7449 & 2319 (b)

between the dash green and red lines representing the hardness of the substrate and deposited material respectively. In image (c), the hardness decreases above 7 mm: this is because the last layers of the wall have a lower hardness than the lower layers due to a different thermal history.

For the combination 7449 & 2319, a plateau of hardness can be observed between -1.8 and 1.5 mm. This is due to the change in composition across the interface: the 1^{st} layer has a different composition to the 2^{nd} layer and the rest of the deposit because of the melting of the substrate during the first layer deposition. This is confirmed by EDS measurement shown in figure 6.4: the concentration of zinc, magnesium and copper is different in the first layer than in the substrate or the rest of the deposit. The plot in Figure 6.4 shows a correlation between composition and micro hardness.

A HAZ can be observed in the 7449 substrate but no hardness variations can be seen in the 2050 substrates.

No tensile tests were carried out on the combination using 7449 and 2050 substrates

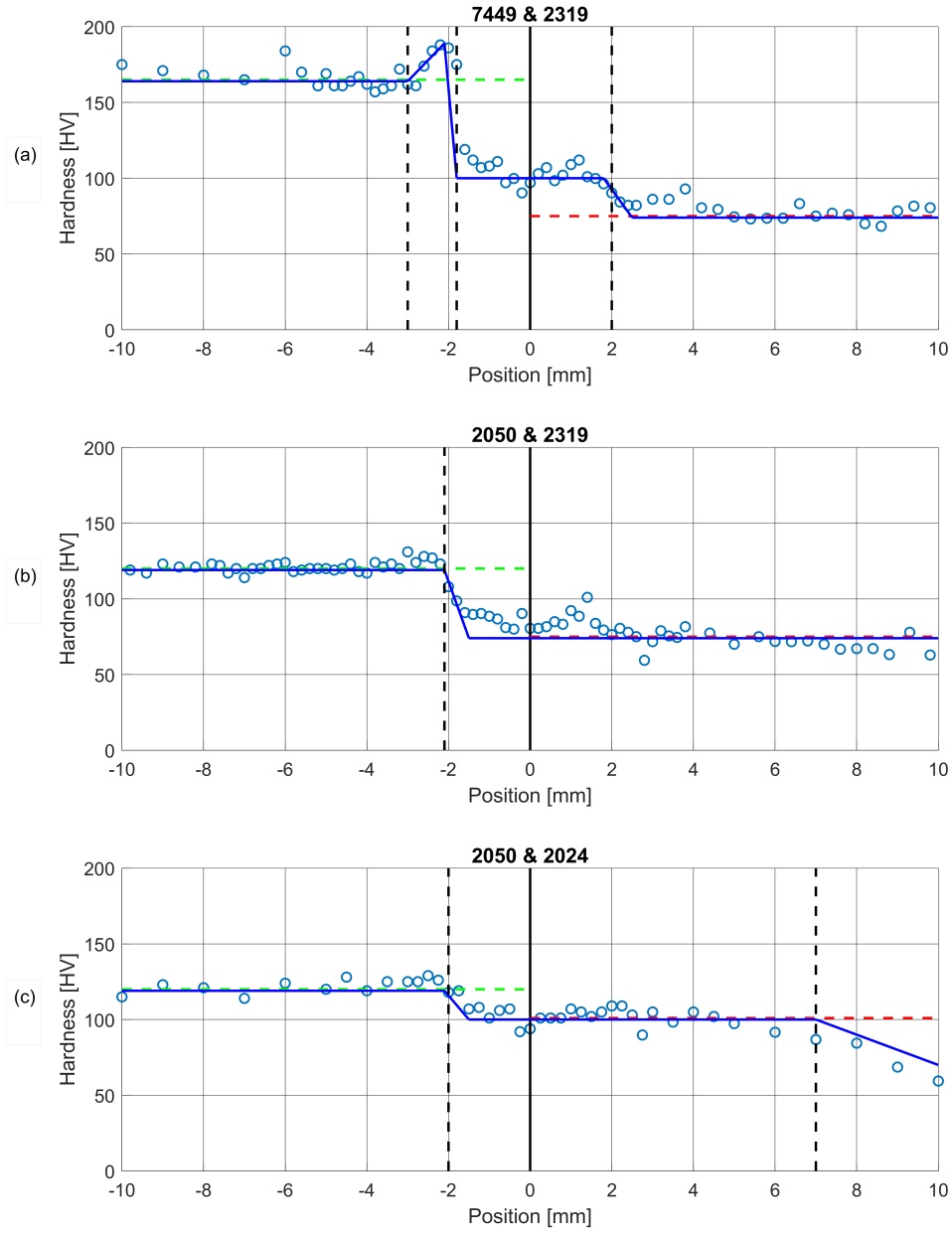


Figure 6.3: Vertical hardness profile of as-deposited interface between (a) 7445 & 2319, and (b) 2050 & 2319, and (c) 2050 & 2024

because of the high level of porosity in the first layer.

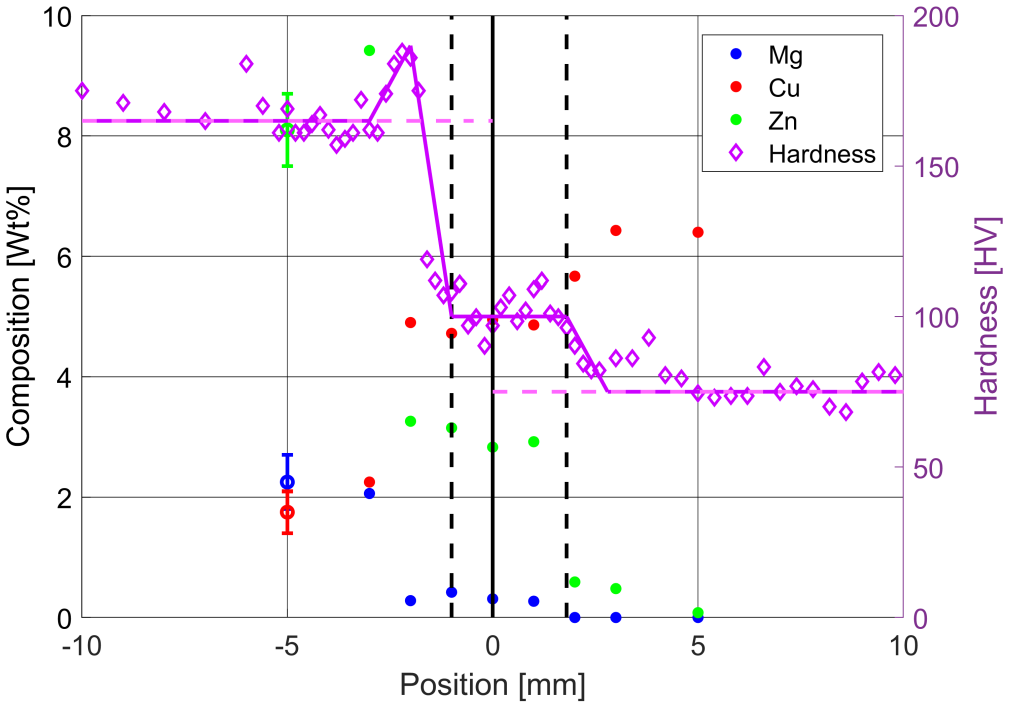


Figure 6.4: Composition measurement at the 7449 & 2319 interface

6.3.2 Aluminium copper wires and substrates

6.3.2.1 Microstructures

Figure 6.5 shows the change in microstructure at the interface with large grain in the substrate, typical of rolled plate, and small equiaxed and columnar grain in the deposited material.

Figure 6.6 shows the edge of 2319 deposit on 2219, 2024, and 2139 substrates. There is no specific issue of porosity in any of them. No cracks were found in the 2219 & 2319 and 2024 & 2319 interfaces. However, a micro-crack in the 2139 substrate was observed in picture (c) at the edge of the deposition.

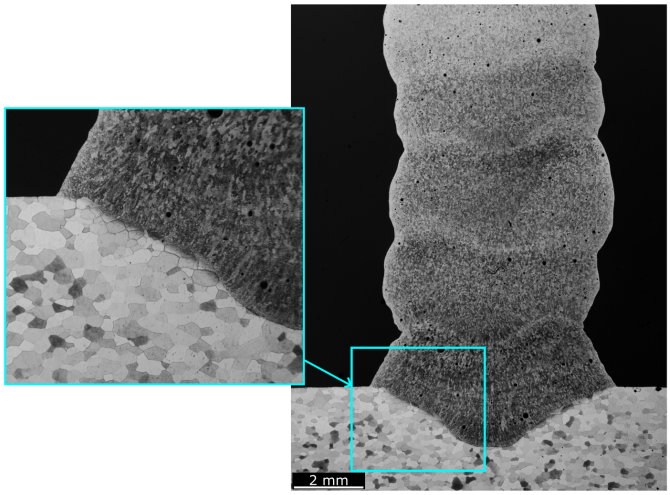


Figure 6.5: cross-section of the as-deposited 2139 & 2319 interface

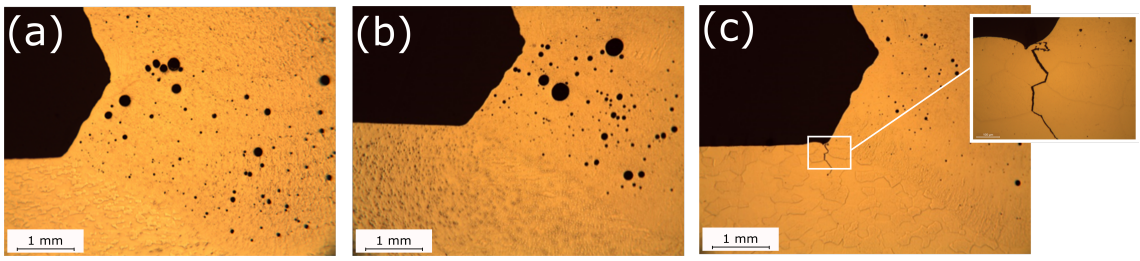


Figure 6.6: cross-section of as-deposited interface between (a) 2219 & 2319, (b) 2024 & 2319, and (c) 2139 & 2319

Figure 6.7 provided SEM images of two PMZ, in 2219 and 2139 substrate. Liquations can be observed in all three substrates. The area affected by liquation depend on the substrate: the width of the affected area is about 200 μm for the 2024 and 2219 substrate, but is 480 μm wide in the 2139 substrate.

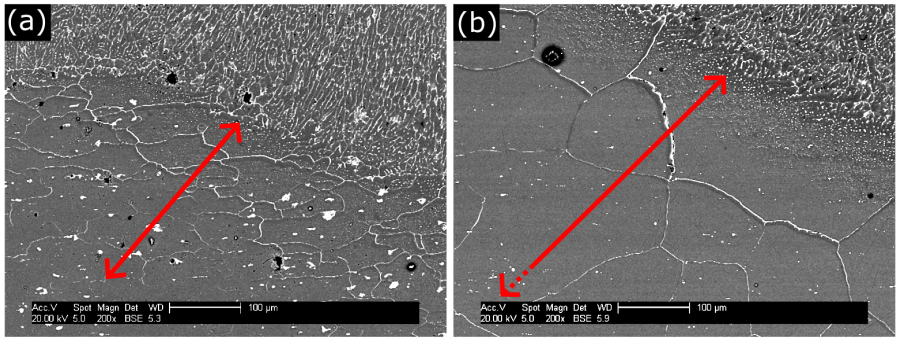


Figure 6.7: Partially Melted Zone (PMZ) of the (a) 2219 & 2319 and (b) 2139 & 2319 interfaces. The arrow gives an idea of the size of the area affected by liquation

6.3.2.2 Micro hardness

Figure 6.8 provides the hardness profile across various interfaces. A few observations can be drawn from these plots:

The hardness of the deposited material is lower than the substrate hardness for all alloy combinations. When the deposit and the substrate are made of the same alloy, the drop of hardness is relatively smooth (2219 & 2319 and 2024 & 2024 combinations). For the 2219 substrate, the HAZ consist in a smooth hardness decrease down to the FZ hardness value. For the 2024 substrates, a drop of hardness can be observed 6 mm under the interface plane. If the substrate and deposited alloys are not the same, a plateau of hardness can be observed in the first deposited layer. As previously shown in Figure 6.4 for the 7449 & 2319 combination, Figure 6.9 shows the correlation between hardness and magnesium content at the 2024 & 2319 interface.

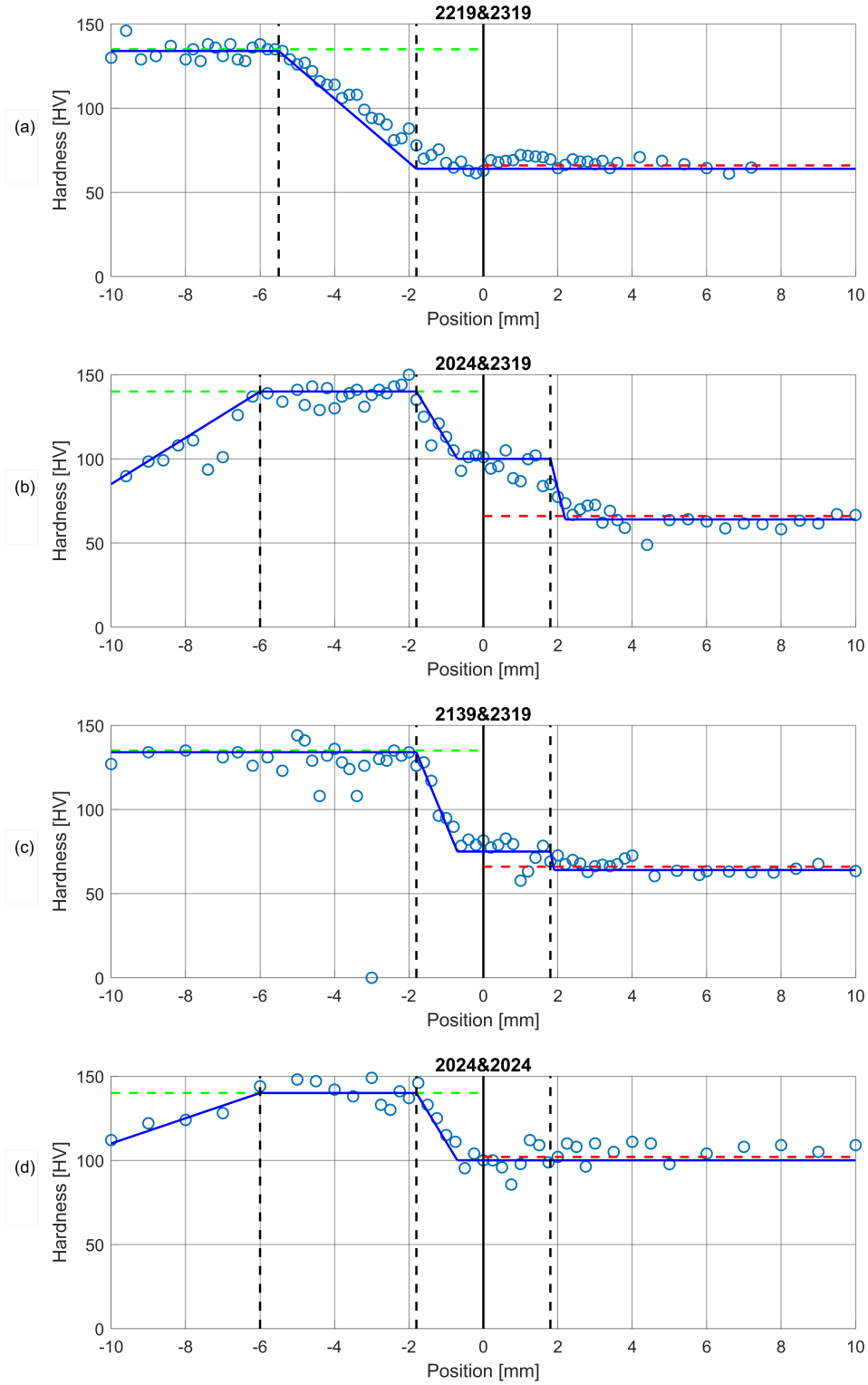


Figure 6.8: Hardness profile of as-deposited (a) 2219 & 2319, (b) 2024 & 2319, (c) 2139 & 2319, and (d) 2024 & 2024 interfaces

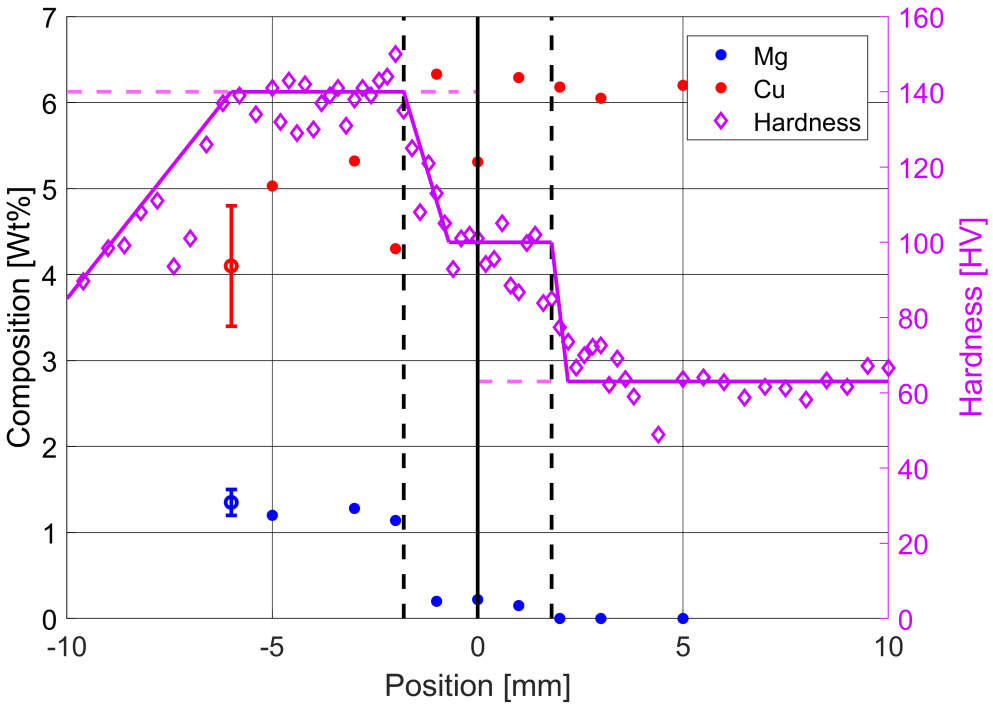


Figure 6.9: Composition and hardness profile at the interface of the 2024 & 2319 combination

6.3.2.3 Tensile test

Table 6.1 gives the results of the tensile tests carried out on the 2219 & 2319, 2024 & 2319 and 2139 & 2319 combinations

The YS and UTS achieved by the combination 2219 & 2319 are close to the properties of 2319 deposit reported in by Gu et al. [11]. However, the elongation reached by the combination 2219 & 2319 is much lower than the elongation of 15.5% reported by Gu et al. The tensile properties of the combination 2139 & 2319 are very close to these of the 2219 & 2319 combination. The properties of the 2024 & 2319 combination are different from the two others, with a higher YS, similar UTS, and a much lower elongation.

Figure 6.10 shows an SEM image of the rupture surface of two specimen representative of the 2219 & 2319 and 2024 & 2319 combinations. For the 2219 & 2319 com-

Table 6.1: Mechanical properties of the as-deposited interface between various alloy combination

Alloy combination	YS [MPa]	UTS [MPa]	Elongation [%]
2319 deposited on			
- 2219	118 ± 8	257 ± 13	8.5 ± 1.5
- 2024	147 ± 14	232 ± 12	2.8 ± 0.9
- 2139*	116 ± 1	248 ± 4	7.6 ± 0.5
2319 as deposited [11]	131	259	15.5
2024 (T3)	364	500	19
2219 (T8)	350	450	10
2139 (T3)	274	377	23

*Different coupon size

bination, most of the rupture surface consists of dimples, a sign of ductile rupture [147]. At higher magnification it is possible to see broken second phases inside these dimples. Numerous pores can also be observed.

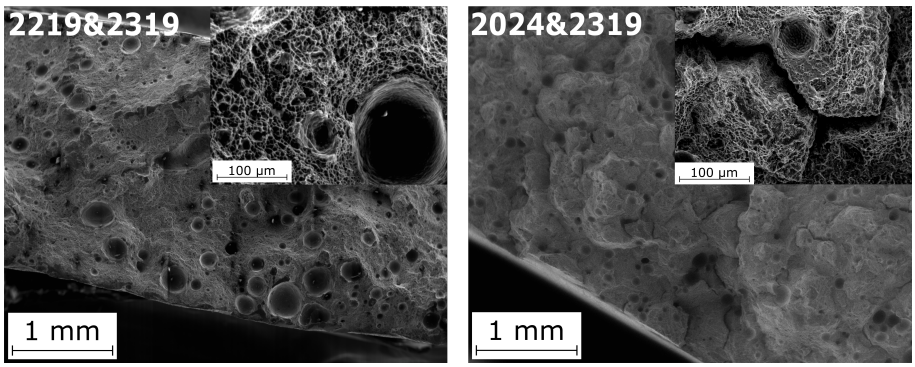


Figure 6.10: SEM images of the rupture surface of tensile specimen from 2219 & 2319 and 2024 & 2319 combinations

The rupture surface of the 2024 & 2319 combination is composed of numerous circular pores and dimples of similar size to those observed in 2219 & 2319 combination, but it also contains numerous inter-granular cracks.

Figure 6.11 gives the optical images of the cross-sections of two representative specimens of 2219 & 2319 and 2024 & 2319 combinations. As observed on the rupture surface

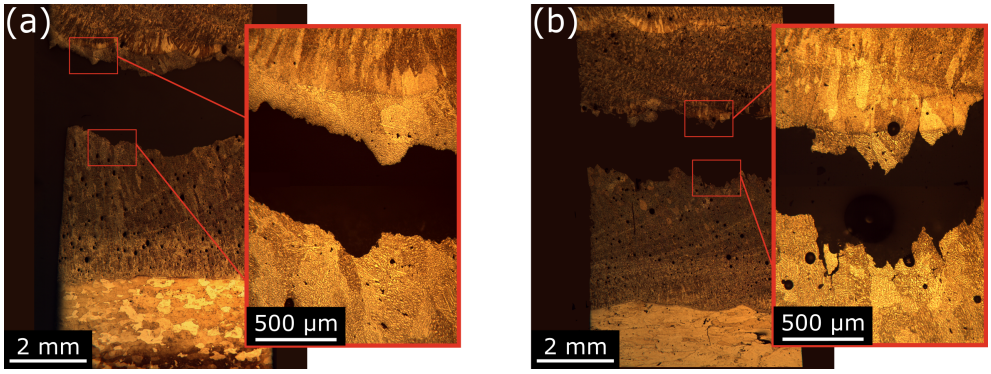


Figure 6.11: Optical images of ruptured tensile specimens taken from (a) 2219 & 2319 and (b) 2024 & 2319 combinations

in figure 6.10, there are inter-granular cracks in the rupture area of the 2024 & 2319 specimen, in picture (b). No inter-granular crack can be observed in picture (a) showing the 2219 & 2319 combination. Also, the rupture of the 2024 & 2319 specimen occurs at the boundary between the first and second layer, as shown in picture (b). It is worth mentioning here that all five 2024 & 2319 samples, not shown here, broke at this same layer boundary.

6.3.2.4 Digital Image Correlation (DIC)

Figure 6.12 shows (a) a picture of a ruptured tensile specimen representative of the 2139 & 2319 combination, (b) its strain map just before rupture, and (c) its YS map. The YS map was evaluated using the DIC data as described in Chapter 3 The picture (a) shows that the rupture took place away from the interface, and the strain map shows a strain concentration at the rupture area and no specific features at the interface. The strain map shows that the part of the specimen made of substrate material does not stretch during the test, as the maximum strain in the substrate does not exceed 5 millistrain.

The YS map does not provide any data on the substrate because the substrate material did not strain during the test, and therefore no calculation of the YS was possible. The

substrate YS value was evaluated at 344 MPa during a conventional tensile test. The YS is varying between 100 and 140 in the deposit. At the interface, the YS gradually decreases from the substrate value to the deposit value: it takes 6 mm for the YS to go from 200 to 130 HV.

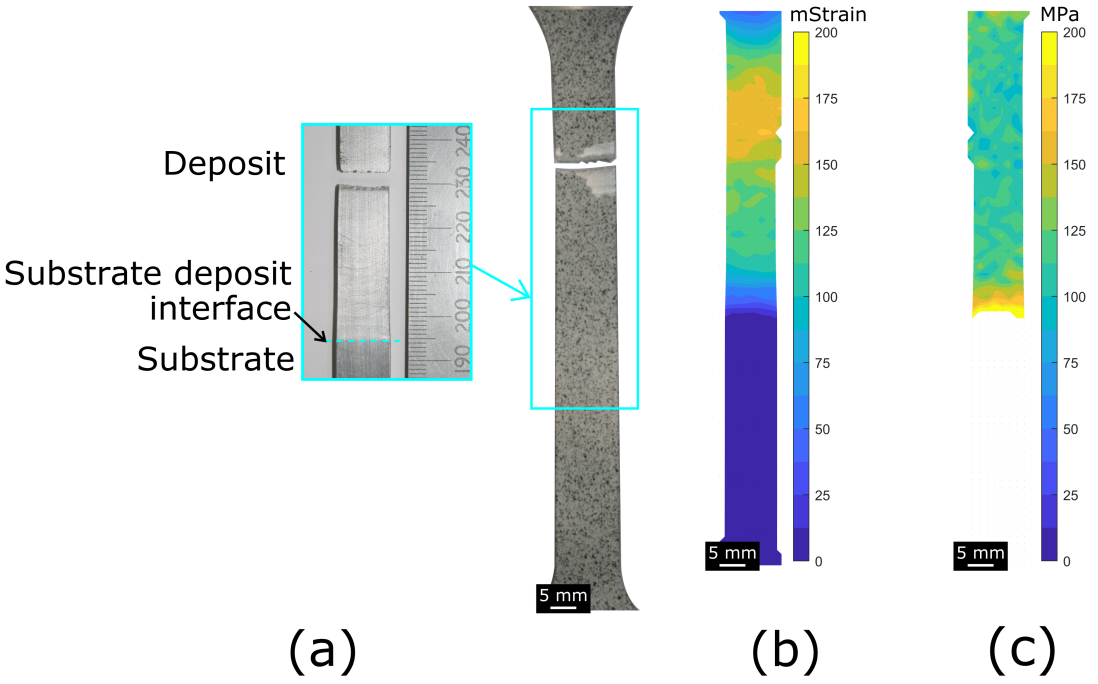


Figure 6.12: interface 2139 & 2319: (a) rupture profile, (b) maximum strain map, and (c) yield strength map

6.3.3 Aluminium magnesium-silicon alloy substrates

6.3.3.1 Microstructures

Figure 6.13 provides optical images of the sample cross-section used for the microstructure study and the micro hardness measurements in this part.

Figure 6.14 shows SEM images of the PMZ in both (a) 6061_{Rolled} and (b) 6061_{RSP} substrates. It is possible to see liquation at the grain boundary in the 6061_{Rolled} substrate,

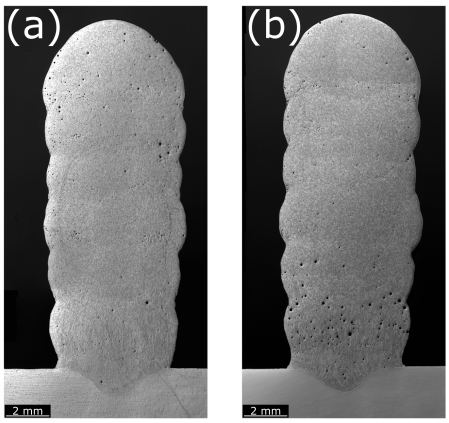


Figure 6.13: cross-section of as-deposited interface between (a) 6061_{Rolled} & 2319, and (b) 6061_{RSP} & 2319

but no liquations were observed in the 6061_{RSP} substrate.

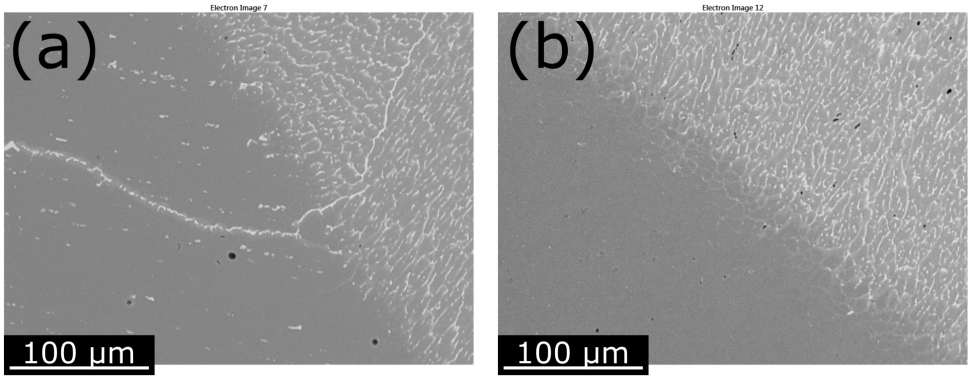


Figure 6.14: PMZ of the interfaces (a) 6061_{Rolled} & 2319 and (b) 6061_{RSP} & 2319

6.3.3.2 Micro hardness

Figure 6.15 gives the hardness profiles measured at both interfaces. The two profiles are very similar. The hardness drop in the substrate shows the HAZ and the slow decrease in hardness above the interface plane at 0 mm can be attributed to the change in composition in this area as shown for previous alloy combinations.

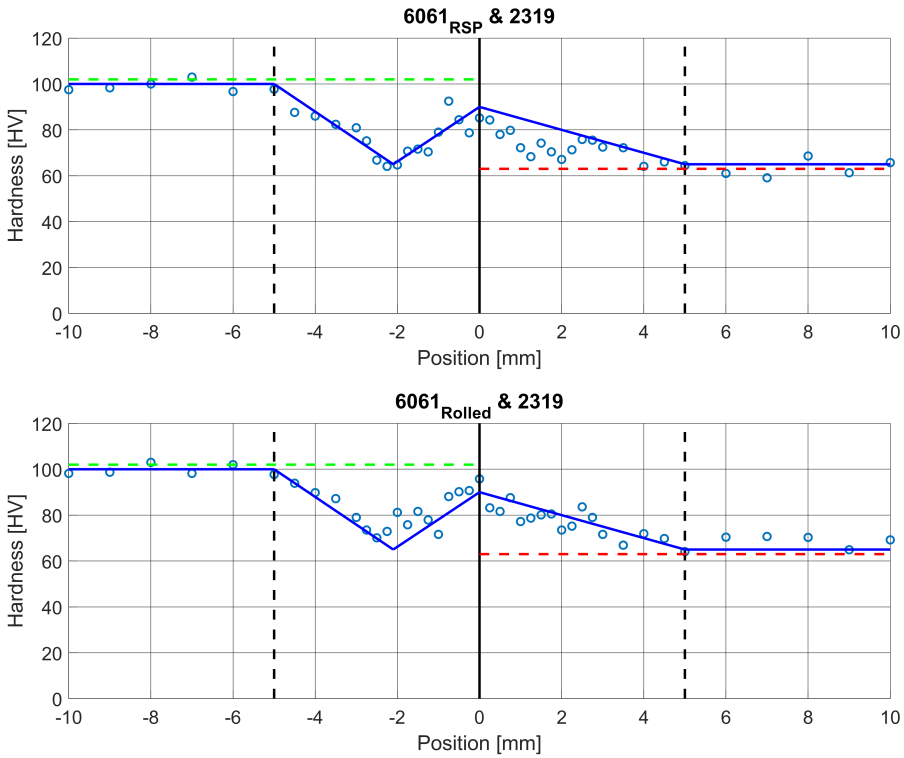


Figure 6.15: Vertical hardness profile of as-deposited interface between 6061_{RSP} & 2319 and 6061_{Rolled} & 2319

6.3.3.3 Tensile test

Table 6.2 gives the tensile properties measured for the two 6061 & 2319 combinations. The properties of the 6061_{RSP} & 2319 combination reach slightly higher properties than 6061_{Rolled} & 2319. But, in both cases the properties of the interfaces are lower than the properties of the substrates.

Figure 6.16 provides SEM images of the rupture surface of a representative specimen of the 6061_{RSP} & 2319 and 6061_{Rolled} & 2319 combinations. Picture (a) shows the rupture surface of the 6061_{Rolled} & 2319 specimen, which broke after necking, leading to a large cross-section reduction. In the higher magnification image, it is possible to see dimples with large second phases in their centre. Most of the dimples are typical of a void

Table 6.2: Mechanical properties of the as-deposited interface between various alloy combination

Alloy combination	YS [MPa]	UTS [MPa]	Elongation [%]
2319 deposited on			
- 6061_{RSP}	148 ± 18	225 ± 10	6.9 ± 0.2
- 6061	124 ± 21	208 ± 18	5.9 ± 2.6
2319 as deposited [11]	131	259	15.5
6061_{RSP} [148]	315	340	16
6061_{Rolled} [145]	276	310	14

coalescence by internal necking rupture, but it is also possible to distinguish some sheared dimple. Picture (b) shows the fracture of the 6061_{RSP} & 2319 combination specimen. Two zones can be distinguished in this rupture surface, the darker area, where dimples can be found, typical of shearing fracture, and the brighter area where dimples typical from void coalescence can be seen. This specimen rupture is a mix between ductile and shearing fracture. The gaps between the cross-section area in pictures (a) and (b) are due to the different rupture mode of the two specimens.

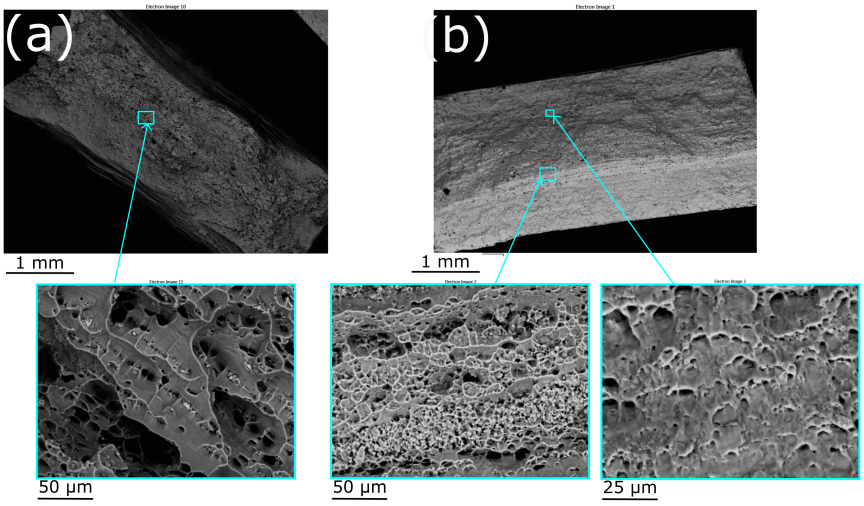


Figure 6.16: SEM images of rupture surface of representative specimens of the (a) 6061_{Rolled} & 2319 and (b) 6061_{RSP} & 2319 combinations

6.3.3.4 DIC

Figure 6.17 and 6.18 show the results of DIC trials for the 6061_{RSP} & 2319 and 6061_{Rolled} & 2319 respectively. These results are very similar regardless of the type of substrate that was used. Therefore, the 6061_{RSP} & 2319 combination DIC results are further analysed, and this analysis is also applicable to the 6061_{Rolled} & 2319 combination. The tensile specimen cross-section in Figure 6.17 (a) shows that the rupture took place in the substrate about 1.3 mm below the fusion line zone, where the strain map shows a strain concentration. This area matches with the HAZ highlighted in Figure 6.15.

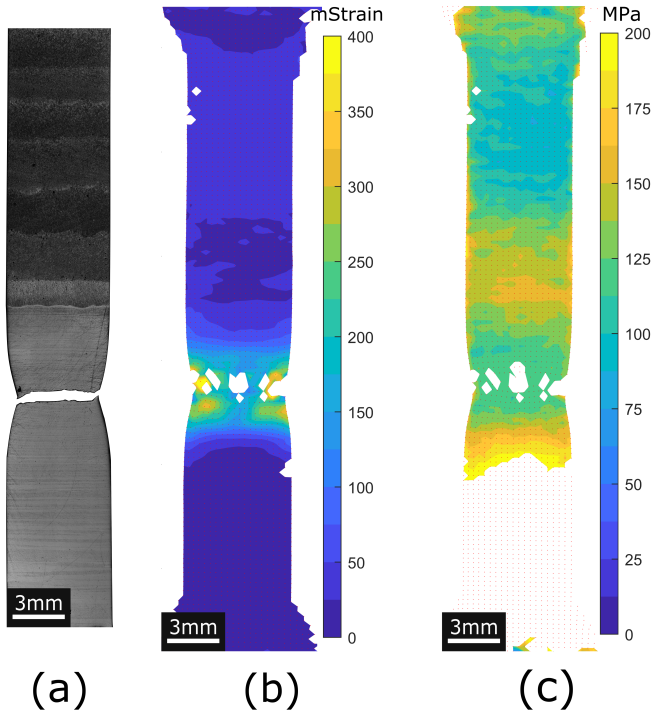


Figure 6.17: (a) Tensile specimen microstructure after rupture, (b) maximum strain map, and (c) yield strength map of the interface 6061_{RSP} & 2319

The YS map provides data for the deposit, FZ and HAZ, but not for the parent metal, as no calculation was possible in the parent material, due to the very low strain in this area. Figure 6.19 shows the YS profile extracted from Figure 6.17 picture (c). The YS

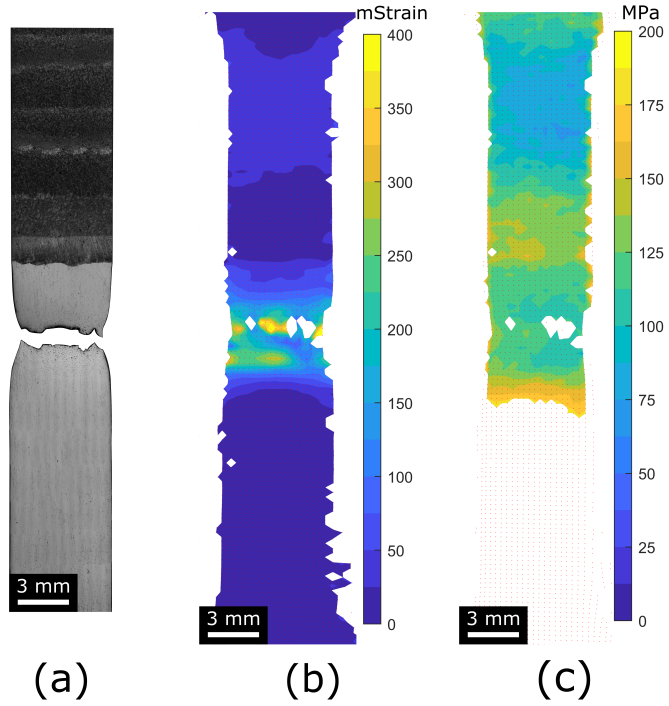


Figure 6.18: Tensile specimen microstructure after rupture (a), maximum strain map (b), and yield strength map (c) of the interface 6061_{Rolled} & 2319

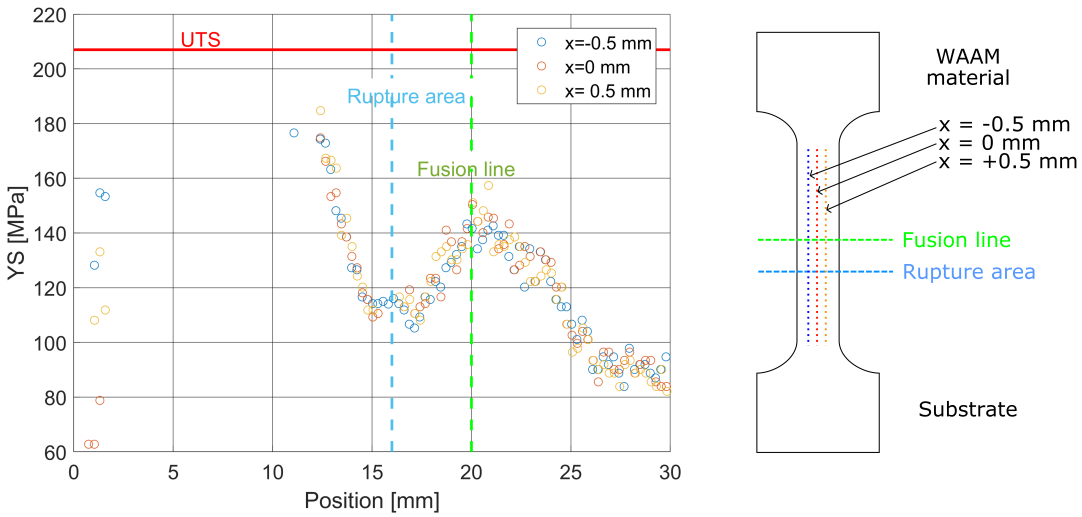


Figure 6.19: YS profile across the 6061_{RSP} & 2319 combination

profile was extracted and plotted along three vertical lines crossing the specimen from one end to the other, in the centre of the specimen, spaced out by 0.5 mm. The HAZ YS is much lower than the YS of the parent material (315 MPa according to the substrate supplier [148]). However, the YS of the deposited material is lower than the YS of the HAZ.

The YS profile coincide with the micro hardness profile in the first plot in Figure 6.15. It is interesting to note that the hardness in the HAZ is the same as in the deposit, but the YS evaluated in the HAZ is significantly higher than in the deposit.

6.3.4 Aluminium magnesium deposited material and rapidly solidified substrates

6.3.4.1 Microstructures

Figure 6.20 shows the cross-sections of the 905 & 5556 and 501 & 5556 combinations.

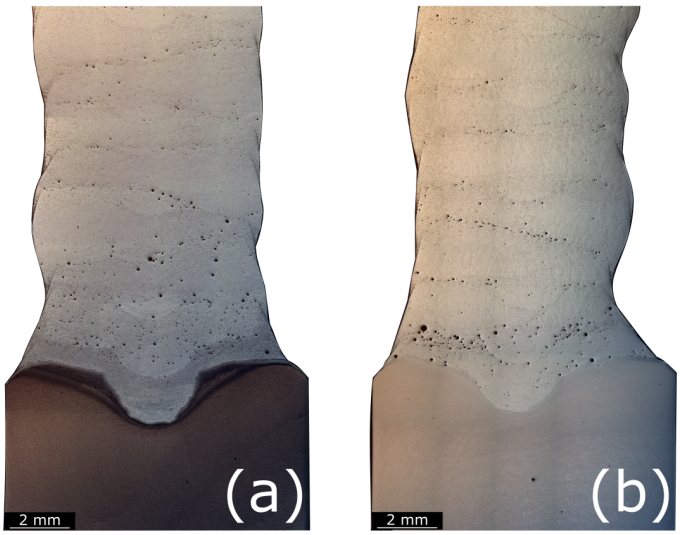


Figure 6.20: cross-section of the as-deposited (a) 905 & 5556 and (b) 501 & 5556 interfaces

Figure 6.21 provides SEM images of the interface between deposited material and

substrates for both combinations. Picture (a) shows the 501 & 5556 interface, where the boundary between deposit and substrate can easily be seen as the second phases in the deposit are bigger and less numerous than in the substrate. Also, in the substrate, at about 50 μm from the deposit, a line of large second phases can be observed. This line is shown in the higher magnification pictures. The transition between the substrate and deposited material is smoother when 905 substrate is used, as shown in picture (b).

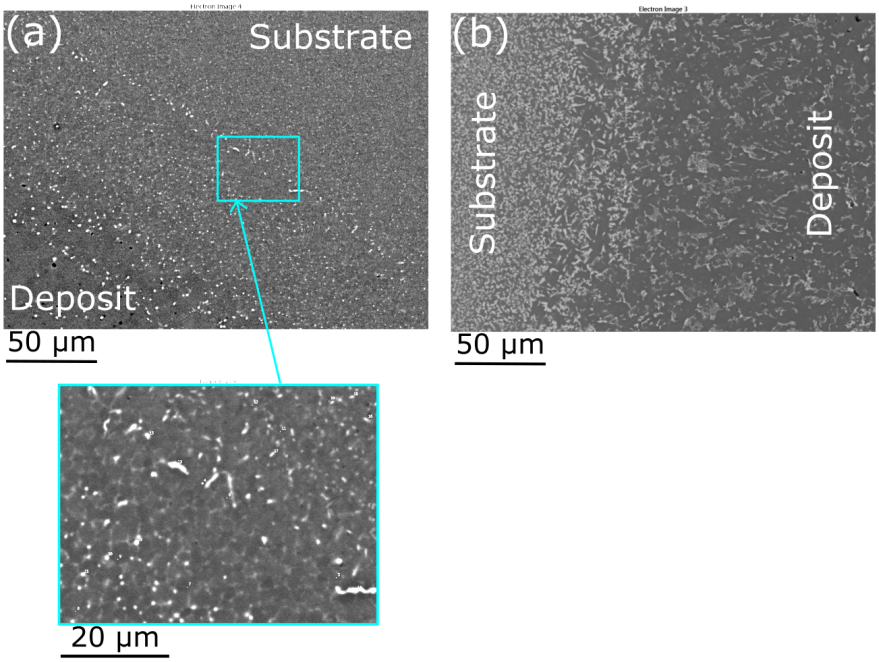


Figure 6.21: SEM images of the boundary between fusion zone and substrate of the (a) 501 & 5556 and (b) 905 & 5556 combinations

6.3.4.2 Micro hardness

Figure 6.22 provides the micro hardness profile across these two interfaces. In both cases, there is a steep drop of hardness between the parent material and the FZ. In the case of the 905 & 5556 combination, the composition of the two material are very different and this cause the steep drop.

Regarding the 501 & 5556 combination, the only difference between the two alloys is the scandium and zirconium content. As shown in Figure 6.23, the drop of these elements at the fusion zone (shown by the dashed line at -1.4 mm) can be correlated with the drop in hardness.

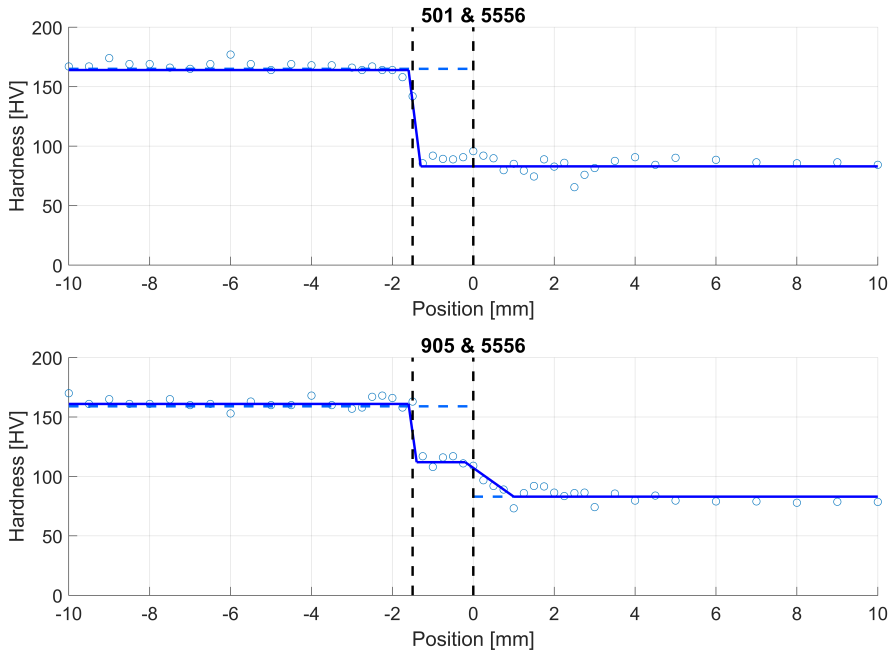


Figure 6.22: Vertical hardness profile of as-deposited interface between 501 & 5556 and 905 & 5556

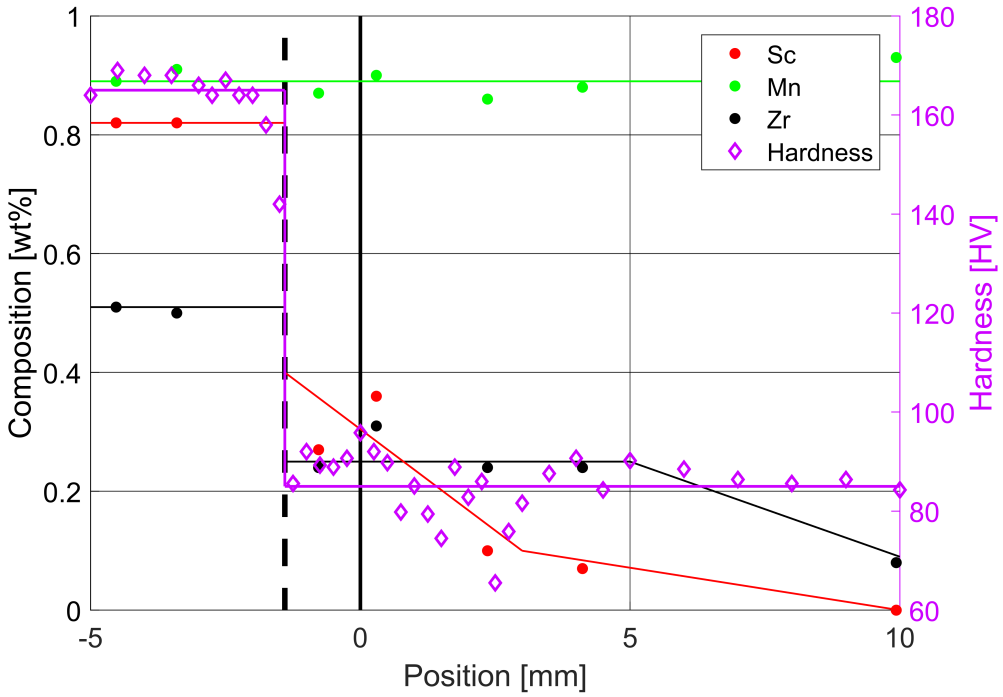


Figure 6.23: Chemical composition profile across the 501 & 5556 interface

6.3.4.3 Tensile test

Table 6.3 provides the tensile tests for both combinations. Both YS values are close, but the 501 & 5556 combination achieves a much higher UTS and elongation than the 905 & 5556 combination. In both cases, the elongation obtained is much lower than the 27% achieved by as-deposited 5556. The UTS reached by the 501 & 5556 is equivalent to UTS of as-deposited 5556 whereas the 905 & 5556 combination UTS is lower than this value.

Table 6.3: Mechanical properties of the as-deposited interface between various alloy combination

Alloy combination	YS [MPa]	UTS [MPa]	Elongation [%]
5556 deposited on			
-501	167 ± 22	298 ± 11	5.8 ± 2.2
-905	169 ± 18	244 ± 37	2.2 ± 1.4
5556 as deposited [78]	129	300	27
905 [148]	480	600	5
501 [148]	525	575	12

6.3.4.4 DIC

Figure 6.24 shows the results of the DIC test for the 501 & 5556 combination. Picture (b) shows the strain distribution just before rupture: the part of the specimen made of 5556 deposit is strained, and there is no clear evidence of strain concentration at the rupture area. The microstructure in picture (a) shows that the rupture occurred in the first layer of deposit, near the boundary between the first and second layer, where the porosity level is higher than in the rest of the deposit. The YS map in (c) shows that the YS is homogeneous in the deposit.

It is worth mentioning here that all specimens from the 501 & 5556 combination did not break in the same area: two specimens broke in the deposit away from the interface, and three broke near the interface. Figure 6.25 provides the average tensile properties measured in these two different cases, along with a photograph of two specimens showing the two different rupture area. The two samples which broke in the deposit reached a lower average YS and a higher average elongation than the other three coupons which broke at the interface. When the rupture occurred in the deposit, the properties were closer to the as-deposited 5556 properties than in the case of a rupture near the interface.

Figure 6.26 and 6.27 give the results of the DIC trials for two specimens of the 905 & 5556 combination. Two specimens are shown here to illustrate the difference

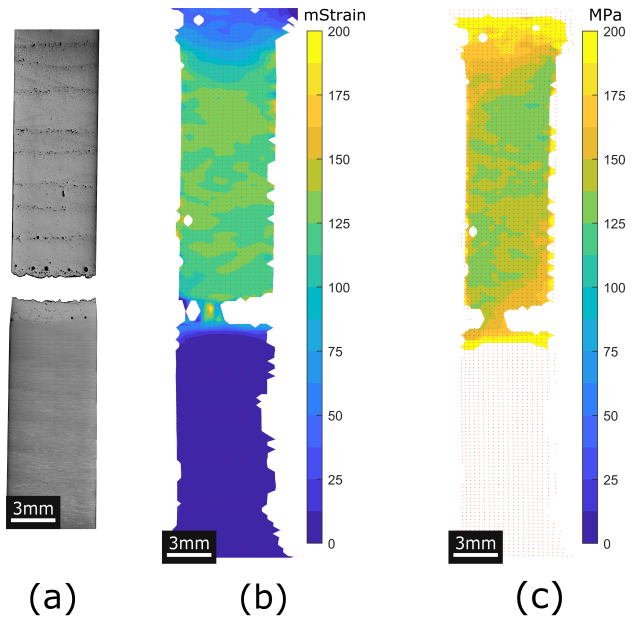


Figure 6.24: Interface 501 & 5556 :(a) tensile specimen microstructure after rupture, (b) maximum strain map, and (c) yield strength map

of behaviour of two specimens of the same combination. The sample provided in Figure 6.26 broke in the first layer of deposit, while the one shown in Figure 6.27 broke at the boundary between the substrate and deposit. However, in both cases, it is possible to see strain concentration at the boundary between the substrate and deposit, and the strain in the deposit is much lower than for the 501 & 5556 combination. Regarding the YS, the values in the deposit are very similar for the two specimens.

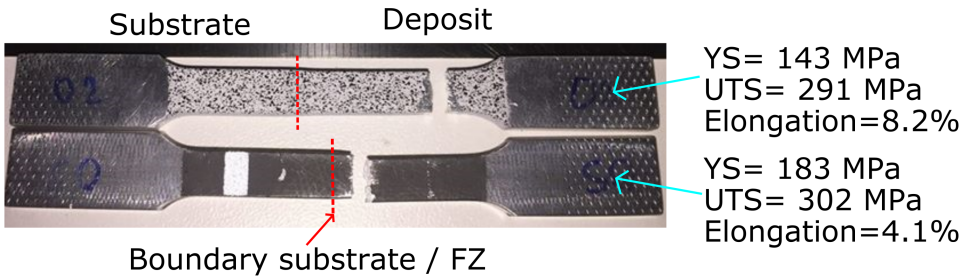


Figure 6.25: Ruptured tensile specimen illustrating the two different tensile properties measured during the test of the 501 & 5556 combination

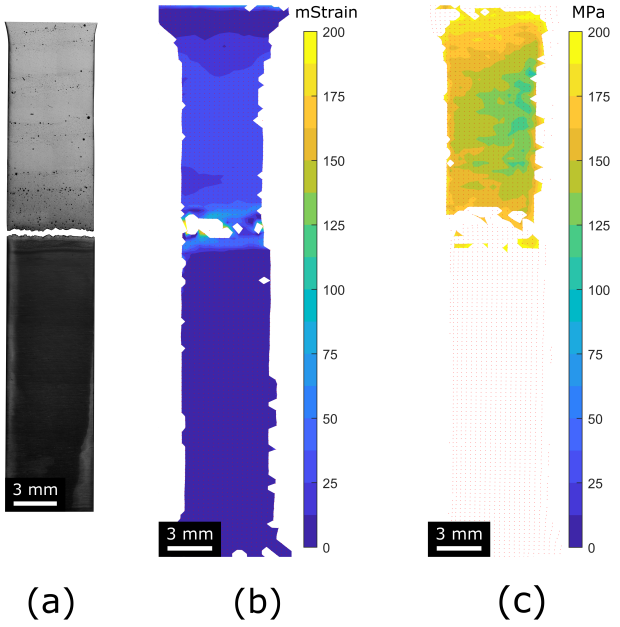


Figure 6.26: (a) Tensile specimen microstructure after rupture at the boundary between the substrate and the FZ, (b) maximum strain map , and (c) yield strength map of the interface 905 & 5556

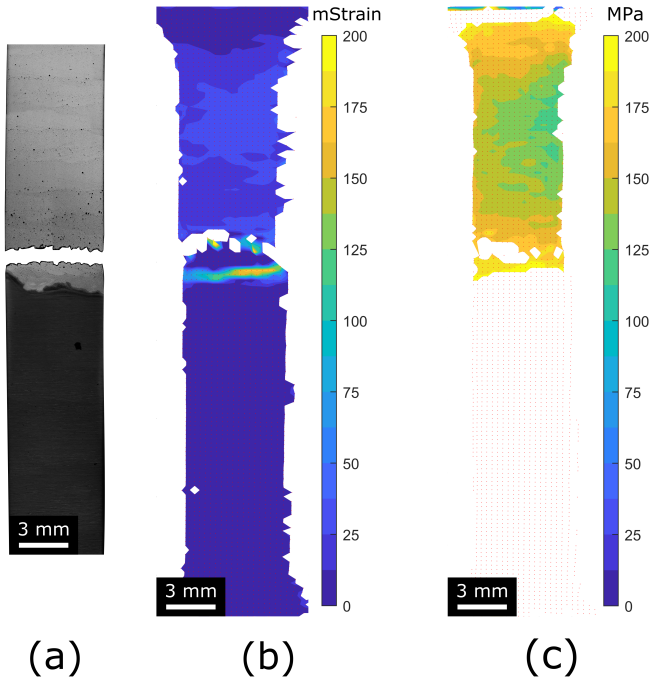


Figure 6.27: (a) Tensile specimen microstructure after rupture in the first deposited layer, (b) maximum strain map, and (c) yield strength map of the interface 905 & 5556

Figure 6.28 provides SEM images of the rupture surfaces for both (a) 501 & 5556 and (b) 905 & 5556 combinations. In both cases, a large number of second phases can be seen in the middle of numerous small dimples, as shown in pictures (c) and (e), as well as pores. In some areas of the rupture surface between 501 substrate and 5556 deposit, features typical from transgranular rupture can be seen, as shown in picture (d). In the case of the 905 & 5556 combination, some large (above 50 μm) broken second phases were observed, as shown in picture (f).

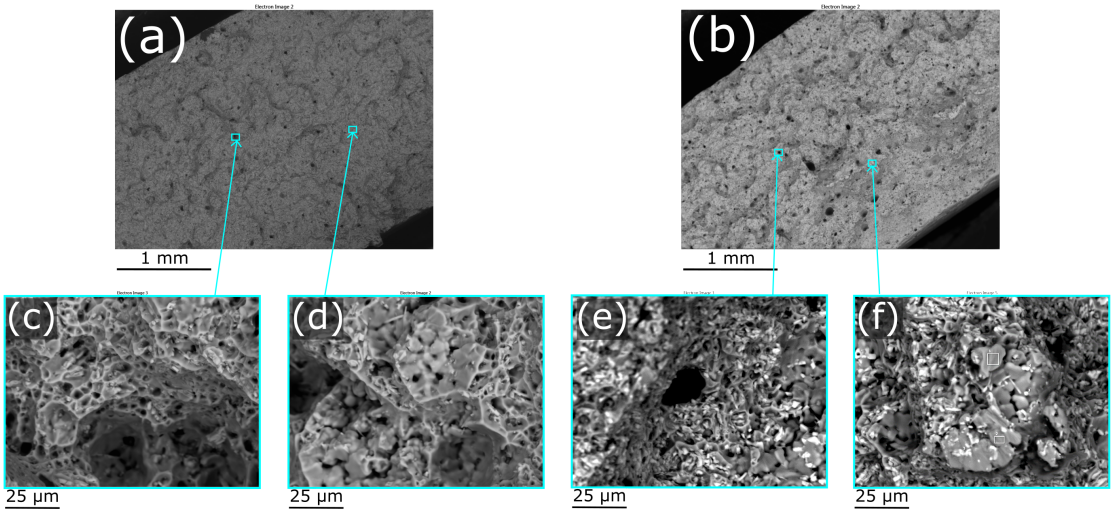


Figure 6.28: Fracture surface of representative specimen of the 501 & 5556 (a) and 905 & 5556 (b) combination

6.4 Discussion

6.4.1 Use of aluminium zinc and aluminium lithium substrate

Porosity is an issue when using 7449 or 2050 substrate. This is due to the content in respectively zinc and lithium of these two alloys: these elements have a low vaporisation point, 907 °C and 1330 °C respectively, generating deposition instabilities and a high porosity level when fusion welded [26, 94]. Micro-cracks can be observed in 7449 substrate, due to the high sensitivity toward hot cracking of this alloy. As illustrated in the literature, cracks are a common issue during the fusion welding of aluminium zinc alloy [104, 115].

As shown in Chapter 4 and the Gu et al. [5] inter-pass rolling can drastically reduce the porosity level in WAAM material. Therefore, inter-pass rolling could be a solution to reduce the porosity level at the interface between the substrate and WAAM material.

6.4.2 Use of aluminium copper as-deposited material and substrate

6.4.2.1 Effect of substrate temper

As shown in Figure 6.8, the HAZ in the 2024 substrate is different from the HAZ in the 2219 substrate. This can be explained by the diffident temper of these two substrates. The 2219 substrate was used in T8 condition (solution treated, cold worked and over-aged), which means the alloy was over-aged before deposition. The 2024 substrate was used in T3 condition (solution treated, cold work and naturally aged): the alloy was therefore under aged. Dumolt et al. conducted a study on the effect of the parent material temper on the HAZ properties after welding [27]. The authors showed that the HAZ microstructure depends on the microstructure before welding (presence of respectively GP zones and θ' phase for the under and over aged conditions). The different HAZ observed in the 2219 and 2024 substrate in Figure 6.8 is coherent with Dumolt's observation.

6.4.2.2 Micro cracks

Micro-cracks were observed in 2139 substrate, but not in 2024 substrate. It is believed to be due to a higher sensitivity toward of cracking of 2139 compared with 2024: Pickin et al. used modelling to show that the solidification path of 2024 is less likely to lead to solidification cracking [149]. Similar results were shown by Fixter et. al [92].

Also, compositions might not be the only factor causing hot cracking in the 2139 substrate. The 2139 substrate grain size, larger than in the 2024 substrate, could enhance a higher sensitivity toward liquation, and liquation cracking [102]. This can be corroborated with the larger PMZ in the 2139 substrate compared with the other substrates used in this study. Therefore, the substrate grain size could be an essential criterion regarding the formation of cracks at the interface between the substrate and WAAM material.

6.4.2.3 Mechanical properties

The hardness of the deposited material is always lower than the substrate hardness: it is therefore expected that all tensile specimens break in the deposit.

Results from the 2219 & 2319 and 2139 & 2319 suggest that the interface does not reduce the properties of the specimen, as the UTS and YS achieved are equivalent to these of 2319 deposit [11]. The DIC measurements show that the substrate is not strained in the case of the 2139 & 2319 combination: this explained the much lower elongation measured for the interface specimen (2219 & 2319 and 2139 & 2319 combination) compared to the elongation at rupture measured for as-deposited 2319 [11].

The tensile tests results of the 2024 & 2319 (tensile properties, fractographs and tensile specimen cross-section) are different from the results obtained for the combination 2219 & 2319. There are micro-cracks between the first and second layer of deposit, and these drastically reduce the sample ductility. This result is in agreement with the results published by Pickin et all in multi-pass welding of 2024 alloy with 2319 wire [149]. It is interesting to notice here that the potential issues at the interface between the substrate and deposition are not restricted to the substrate or first deposited layer : alloying element dilution generate a graded composition across the first deposited layers, and in this case, it is the second layer of material which has a composition sensitive toward hot cracking.

The tensile properties of the interfaces were much lower than the properties of the substrates: the WAAM material properties will need to be increased in order to produce integral parts with homogeneous mechanical properties.

6.4.3 Use of aluminium magnesium and silicon alloy as substrate

The use of a very fine grain substrate reduces the risk of liquation in the PMZ. This is coherent with the literature on fusion welding [102] and with what was observed in the previous section with the 2139 substrate.

The hardness in the HAZ is as low as the hardness of the deposited material. A low hardness in the HAZ of 6061 substrates was observed as well during fusion welding [115, 116]. The YS map in Figures 6.17 (c) and 6.18 (c) shows that the YS drops in the HAZ: this drop of YS in a welded 6061 substrate was shown, using DIC, by Bai et al. [116]. Although the YS is slightly higher in the HAZ than in the as-deposited material, the rupture occurred in the HAZ. This is due to the strain concentration, shown in Figures 6.17 (b) and 6.18 (b), in the HAZ.

Solution treatment followed with artificial or natural ageing could significantly recover the properties of the HAZ, and therefore improve drastically the properties of the 6061 & 2319 interfaces.

6.4.4 Use of aluminium magnesium as deposit material

The hardness profile of the 501 & 5556 combination shows that the deposit is weaker than the substrate, and the deposit seems to have a homogeneous hardness. The two 501 and 5556 alloys are very similar but 501 contains scandium, which can drastically reduce the grain size of the material. Norman et al. showed that, in order to have a significant effect on the grin size, a critical level of scandium is required. Figure 6.29 shows a plot extracted form the authors' paper: the critical scandium level is about 0.4 wt% [15]

Regarding the 501 & 5556 combination, the concentration of scandium in the 501 plate is about 0.8%: this is enough to drastically reduce the grain size. However, in the fusion zone and deposited material the scandium concentration is lower than 0.1%. This

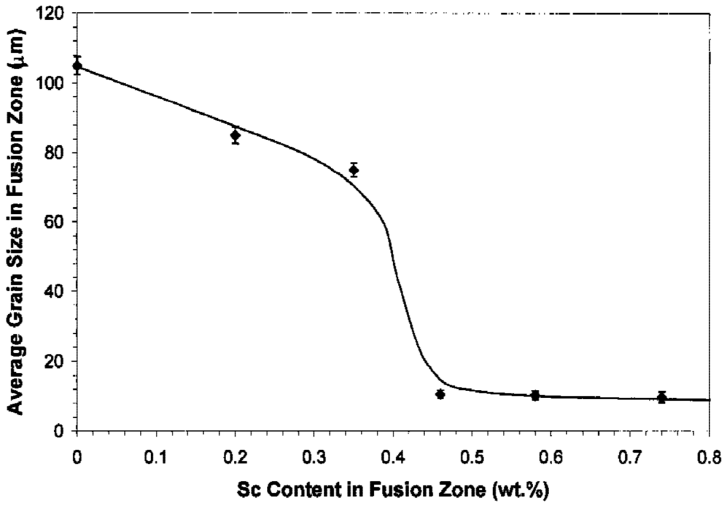


Figure 6.29: Effect of scandium content on grain size in the fusion zone of a 7000 series welded join [15]

phenomenon, along with the different microstructure, is why the drop of hardness is very steep for this combination.

The tensile properties of this combination depend on where the rupture occurred. As shown by the tensile specimen cross-section in Figure 6.24 (a) and the sample cross-section in Figure 6.20 (b), the large amount of pores in the first layer is probably the origin of the rupture near the interface. Also, in the cases where the ruptured occurred near the interface, the ductility is reduced by the proximity of the substrate, generating stress concentration point as it is not strained during the test. In the case where the rupture occurred in the deposit, the properties are similar to 5556 deposition with a much lower elongation, which is partially due to the fact that only part of the specimen stretches during the test. The issue at the interface is not systematic and it might be possible to reduce the interface effect by using different deposition parameters to diminish the porosity level in the first deposited layer.

Regarding the 905 & 5556 combination, the hardness shows that there is a mixed composition in the first deposited layer: it is in this area that the rupture occurred, or at the

boundary between the substrate and FZ. The presence of large second phases in this area seems to behave as stress concentration points under load resulting in a premature rupture of the specimen and leading to a lower UTS and elongation than the one achieved by as-deposited 5556. 5556 alloy is therefore not suitable to be deposited on a 905 substrate.

6.5 Conclusions

None of the combinations investigated in this chapter leads to homogeneous mechanical properties because the WAAM material in the as-deposited condition was much weaker than the substrate. Nevertheless, it was possible to produce graded properties parts with no specific issues at the interface.

Other conclusion which can be drawn from the combinations studied are gathered below:

- Aluminium zinc and aluminium lithium substrates lead to a high porosity level in the first deposited layer. Micro-cracks were also observed in the aluminium zinc substrate used.

- For the combination of aluminium copper alloys, some alloys suffered from hardness drop in the heat affected zone and liquations were found in all PMZ, regardless of the alloy used. Micro-cracks were found only at the edge of the deposit in 2139 substrate and both 2219 and 2024 were crack free. Despite this crack, tensile tests showed that the interface between the substrate and deposit was not detrimental to the specimen mechanical properties when 2139 and 2219 substrate were used. However, the interface drastically reduces the properties of the combination 2024 & 2319 because of the micro-cracks in the deposit, between the first and second layer. When the interface is not an issue, the elongation obtained remained

relatively low compared with both WAAM and wrought product elongation: this is because only the weaker part of the coupon was stretched during the test as the maximum stress reached during the test was lower than the YS of the substrate.

- In the case of 6061 substrates, the drastic and very localised drop of hardness in the HAZ considerably reduces the mechanical properties of the combination. The use of very fine grain substrate leads to no liquation in the PMZ. Unfortunately, the HAZ was so weak it was not possible to evaluate the effect of having no liquation on the mechanical properties.

- Regarding the combination including rapidly solidified 905 and 501 substrates, the interfaces drastically impact on both elongation and UTS. In the case of the 905 & 5556 combination, the two alloys should not be joined, as microstructural features seem to generate stress concentration points, leading to low tensile properties. For the combination 501 & 5556, which are similar alloys, the interface can affect the part performance, but better deposition parameter, or inter-pass rolling, could probably solve this issue.

In order to be able to produce a part with homogeneous mechanical properties, it is essential to increase the properties of the WAAM material. Two strategies could be used: heat treatment and inter-pass rolling. Heat treatment could be carried out to improve the mechanical properties of both WAAM material and HAZ, as well as to reduce detrimental features at the interface, such as large second phases and liquation. Inter-pass rolling could reduce the porosity level in the first layer and limit crack sensitivity in the deposited material while increasing drastically the YS and UTS of the WAAM material. These two strategies are explored in the next chapter.

Chapter 7

Effect of inter-pass rolling and heat treatment on the interface between the substrate and WAAM deposited material

7.1 Introduction

The previous Chapter introduced the issues which can occur at the interface between the substrate and WAAM material. Some local characteristics such as change in grain size and orientation, liquation in the partially melted zone, loss of hardness in the heat affected zone led to a sharp hardness drop at the interface between the substrate and fusion zone, and micro-cracks in the substrate or in the deposited material have been identified as potential property-diminishing interface features. However, in many cases, the as-deposited material mechanical properties were also too low to make those features relevant during tensile tests: no strain was applied to these features because of premature

rupture of the deposit.

Also, to reach the objective of producing an integral part of homogeneous mechanical properties, the deposit needs to achieve the same properties as the substrate. To increase the deposit properties, two strategies were used in this chapter: inter-pass rolling and heat treatment. The effect of these two manufacturing steps has been proven effective to improve deposit quality and tensile properties of both 2319 and 2024 alloys. Therefore, these two alloys were used as wire in this part of the work.

The aim of this chapter was to investigate the effect of inter-pass rolling and heat treatment on the interface between the substrate and deposited material. The two objectives of this study were the same as the previous chapter's: firstly, assess the possibility of producing a part integrating WAAM material and wrought product and achieve homogeneous properties; secondly assess the possibility of producing this type of part, but with graded mechanical properties.

This chapter is organised in a similar manner to Chapter 6 both results and discussion sections are divided into the three following parts: the use of aluminium lithium and aluminium zinc substrates, combinations of 2000 series alloys, and the use of aluminium silicon magnesium substrates.

In the previous chapter, no tensile tests were carried out on as-deposited interfaces when aluminium lithium and aluminium zinc alloy substrates were used. This was due to a high porosity density in the first deposited layer. In this chapter, inter-pass rolling was used to reduce this porosity level, to then be able to conduct tensile tests and evaluate the properties of these interfaces.

Regarding aluminium copper alloys, both heat treatment and inter-pass rolling have the potential of improving the interface properties. According to the literature, heat treatment can drastically improve the properties of WAAM material, but also recover the HAZ and PMZ properties. Inter-pass rolling may also contribute to porosity and micro-cracks

reduction.

For the aluminium magnesium-silicon substrate, the main issue in the as-deposited condition was the low properties of the HAZ. Heat treatment was therefore carried out to attempt to recover the properties in this area and improve the overall properties of the interface.

7.2 Methodology

The deposition parameters, material composition and the experimental procedures used to conduct microstructural study and tensile test, with and without DIC, are described in Chapter 3. The alloys used are detailed further in Chapter 6, section 6.2

In this chapter, two steps heat treatments were carried out. For the combinations including 2319 WAAM material, the solution treatment was done at 535°C for 90 minutes, and the ageing at 171°C for 14 hours. For the combinations 2024 & 2024, the solution treatment was carried out at 498°C for 90 minutes and the ageing at 171°C for 14 hours.

7.3 Results

7.3.1 Aluminium zinc and aluminium lithium substrates

7.3.1.1 7449 substrate

Micro hardness

Figure 7.1 shows the hardness profile of the inter-pass rolled 7449 & 2319 combination.

Below -5 mm there is a difference in hardness. This is not due to inter-pass rolling but caused by the difference of geometry of the deposition: the inter-pass rolled sample was deposited on the substrate edge while the as-deposited sample was deposited on the

substrate surface. As indicated in Chapter 3 section 3.2.3, this affects the HAZ size and properties.

As in the as-deposited condition, there is a hardness plateau in the fusion zone, but this plateau is higher in the inter-pass rolled condition. After this plateau, the properties of the inter-pass rolled material hardness matches with the hardness measured on inter-pass rolled 2319 by Gu et al. [11]. Inter-pass rolling reduces the gap between the substrate and WAAM material hardness.

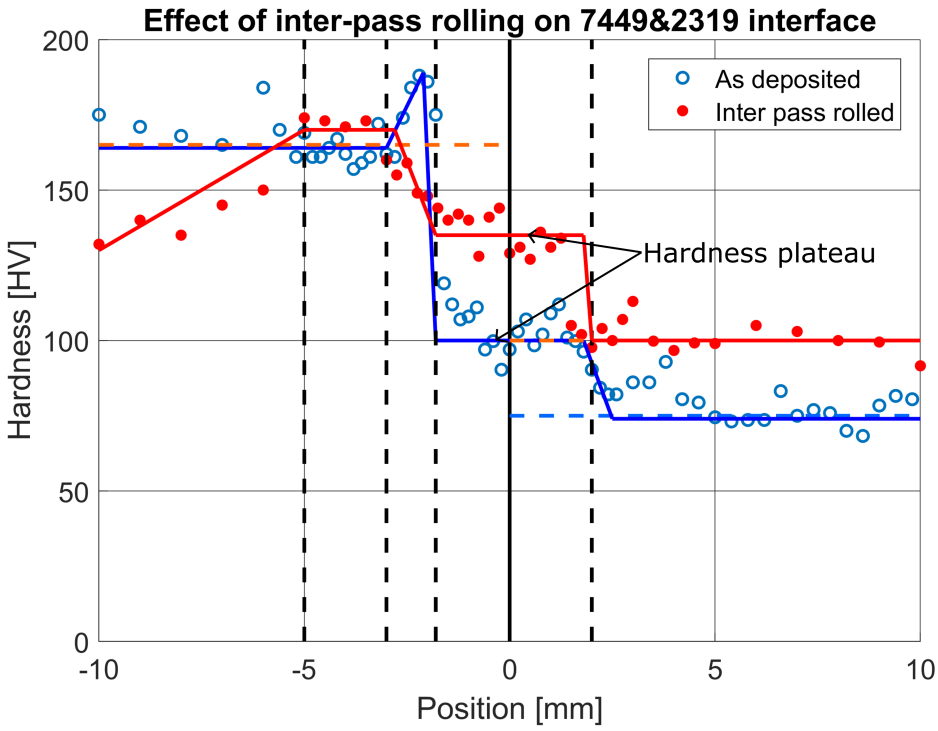


Figure 7.1: Micro hardness profile across the inter-pass rolled 7449 &2319 interface

Tensile test

The tensile test results are given in Table 7.1. All YS, UTS and elongation values are lower than the properties of the 7449 substrate and inter-pass rolled 2319. Therefore, the interface has a large negative effect on the potential performances of this combination.

Table 7.1: Mechanical properties of the inter-pass rolled interfaces integrating 7449 substrates

Alloy combination	Condition	YS [MPa]	UTS [MPa]	Elongation [%]
2319 deposited on - 7449	IR[1]	259 ± 7	270 ± 12	0.8 ± 0.2
As rolled 2319 [11]	IR	244	311	8.6
7449	T7	557	588	11

[1] Inter-pass rolled

Figure 7.2 show optical images of ruptured tensile specimens made of 7449 substrate and 2319 WAAM deposit. Depending on the specimen, the rupture occurred at the interface between the first layer and the substrate (see picture (a)), or in the WAAM material (see picture (b)). No high level of porosity can be seen, which shows that inter-pass rolling can reduce the porosity level, even in the first layer. However, inter-pass rolling does not affect the micro-cracks observed in the PMZ of as-deposited 7449 & 2319 combination in Chapter 6. These micro-cracks caused the rupture of the tensile specimen shown in Figure 7.2 (a).

Figure 7.3 shows the rupture surface on a specimen which broke at the boundary between the substrate and deposit, where micro-cracks can be seen. The rest of the rupture surface is typical of a transgranular rupture.

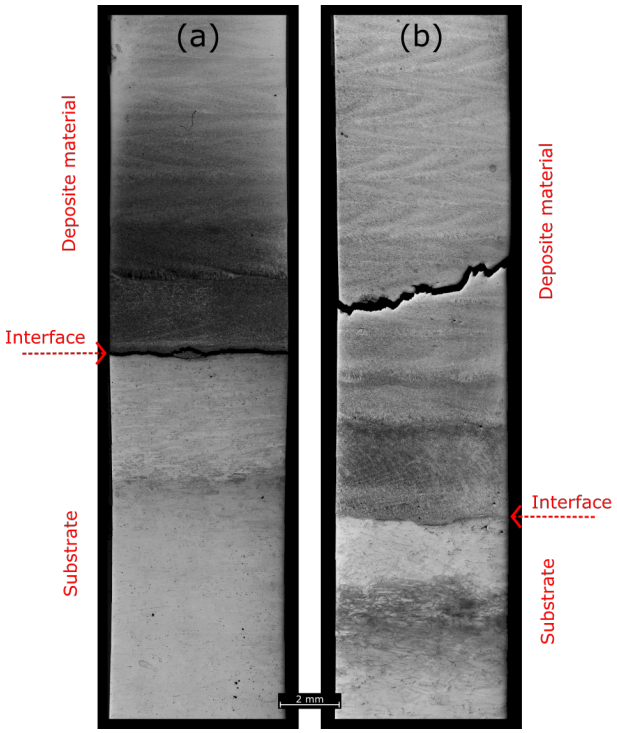


Figure 7.2: Optical images of ruptured tensile specimen of the inter-pass rolled 7449 & 2319 combination

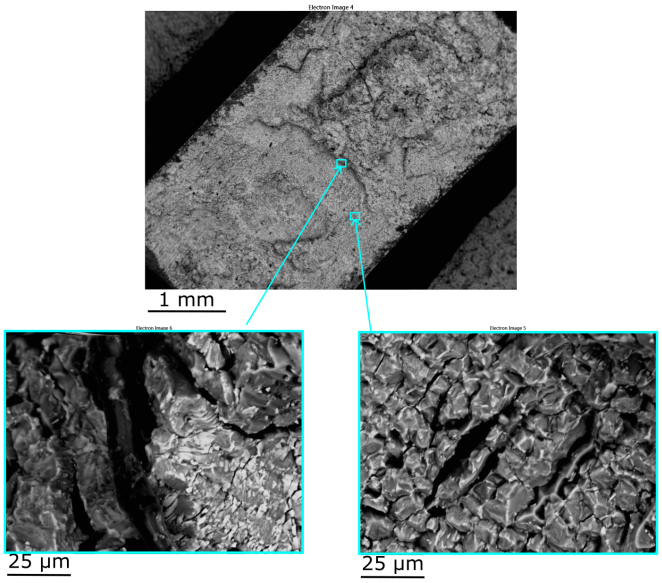


Figure 7.3: SEM image of the rupture surface of the inter-pass rolled 7449 & 2319 combination

7.3.1.2 2050 substrate

Micro hardness

Figure 7.4 (a) shows the hardness profile of the 2050 & 2319 interface, in as deposited and as inter-pass rolled condition. The hardness of the as-deposited sample is higher in the substrate (below -2mm). This is due to a change in geometry, as the as-deposited sample was deposited on the side of the substrate, and the inter-pass rolled was deposited on the edge of the substrate. In the FZ, the hardness is not affected by inter-pass rolling. The deposited material hardness is stable and increased by inter-pass rolling.

If heat treatment is carried out on the 2050 & 2319 interface, the hardness is globally increased, as shown in Figure 7.4 (b). The hardness of the heat treated sample is irregular compared with the as-deposited hardness. Heat treatment reduces the gap between the hardness values of the substrate and WAAM material. This value of 150 HV is coherent with published results on heat treated 2319 deposit [11].

Figure 7.4 (c) shows that inter-pass rolling does not affect the substrate hardness of the 2024 & 2024 interfaces. The FZ and first layer seems to have a slightly higher hardness when inter-pass rolled is carried out. The hardness value reached a stable value above the second layer of deposited material, higher than in as-deposited condition.

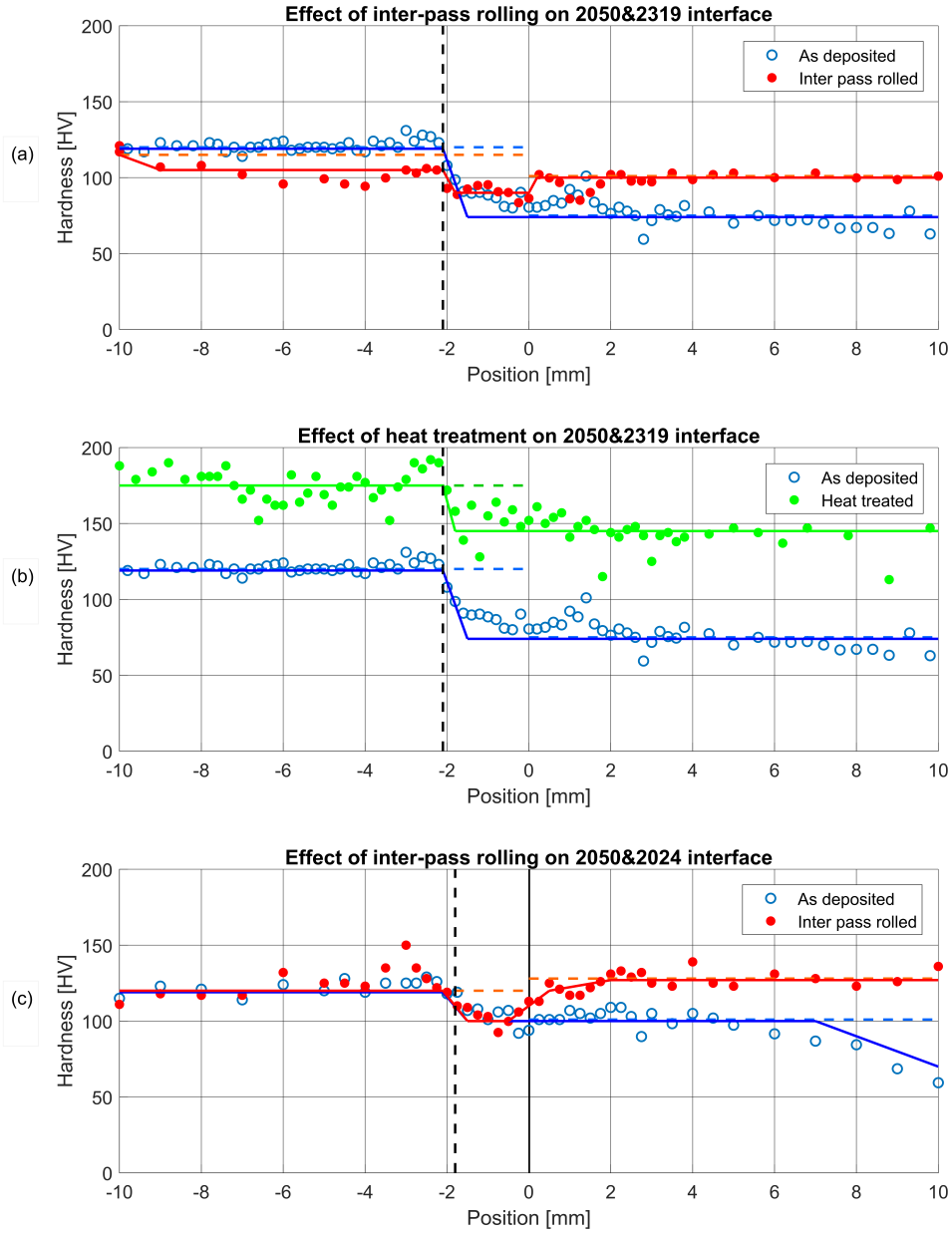


Figure 7.4: Hardness profile of interface using 2050 alloy substrate

Tensile test

The tensile properties can be found in Table 7.2. The tensile properties of the 2050 & 2319 and 2050 & 2024 combination are lower than 2050 substrate properties. The 2050 & 2319 combination also reached lower properties than inter-pass rolled 2319, showing that defects at the interface affect these specimen properties. Regarding the 2050 & 2024 combination, the gap between the interface and rolled 2024 properties is not significant. The large range of UTS and the low elongation measured show that defects largely affect the specimens integrity, making hazardous any analysis of their measured mechanical properties.

Table 7.2: Mechanical properties of the inter-pass rolled interfaces integrating 7449 and 2050 substrates

Alloy combination	Condition	YS [MPa]	UTS [MPa]	Elongation [%]
2319 deposited on -2050	IR	228 ± 9	264 ± 20	1.4 ± 0.8
2024 deposited on -2050	IR	249 ± 8	269 ± 57	1.7 ± 0.9
As rolled 2319 [11]	IR	244	311	8.6
As rolled 2024 [Chapter 4]	IR	273	280	0.5
2050	T3	344	436	21

Figure 7.5 shows an optical image of the cross-section of the interface between 2050 substrate and 2024 deposited material. On this cross-section, it can be seen the effect of rolling on the substrate: it becomes wider near its edge where the material was deposited and rolled, and it is even possible to see a vertical crack propagating along the substrate grain boundary below the FZ. There are not many pores in the sample, apart from at the edge of the deposit, and at the boundary between the FZ and the substrate.



Figure 7.5: Optical image of a cross-section taken from inter-pass rolled 2050 & 2024 combination

Figure 7.6 provides optical images of the ruptured tensile specimens taken from inter-pass rolled 2050 & 2319 and 2050 & 2024 combinations. For the 2050 & 2319 combination, the rupture occurred in the second layer of deposited material. It is possible to see pores in the bottom of the first and second deposited layer, and a large pore can also be seen on the rupture line. The rupture occurred in the first deposited layer for the 2050 & 2024 combination. As shown in Figure 7.5, the first deposited layer has a larger layer height than the subsequent layers. This, added to the fact that the substrate is deformed by inter-pass rolling, suggests that the first deposited layer is not strained as much as the next ones. This could also explain the drop of hardness shown in Figure 7.4 plot (c): inter-pass rolling lead to a same hardness value in the substrate and WAAM material. Unfortunately, the lower hardness in the first layer could be very detrimental to the overall mechanical properties.

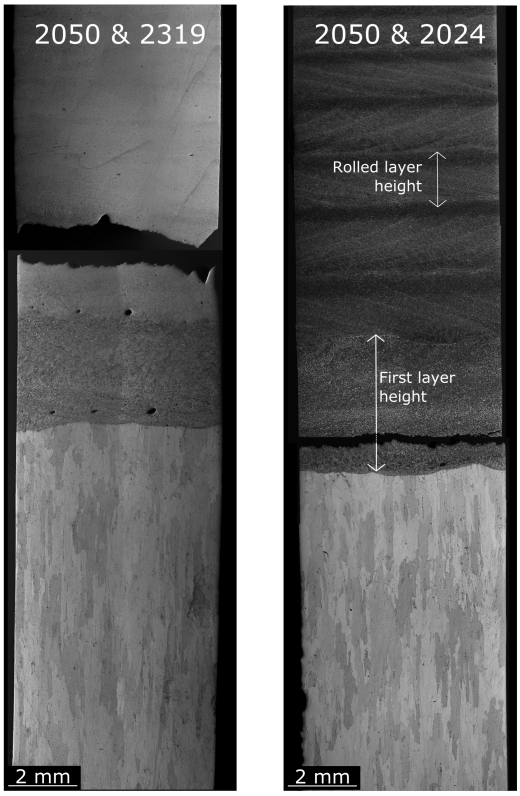


Figure 7.6: Optical images of ruptured tensile specimen cross-section of the 2050 & 2319 and 2050 & 2024 inter-pass rolled combination

Figure 7.7 provides SEM images of the rupture surface of two specimens representing the 2050 & 2319 (a) and 2050 & 2024 (b) combinations. The photograph of the ruptured coupons illustrated the two different rupture mode occurring for these two interfaces. In both case, numerous pores can be observed. In the higher magnification images of the 2050 & 2319 combination, it is possible to see some dimples and transgranular fracture area in the rupture surface. The 2050 & 2024 rupture surface is typical of inter-granular fracture.

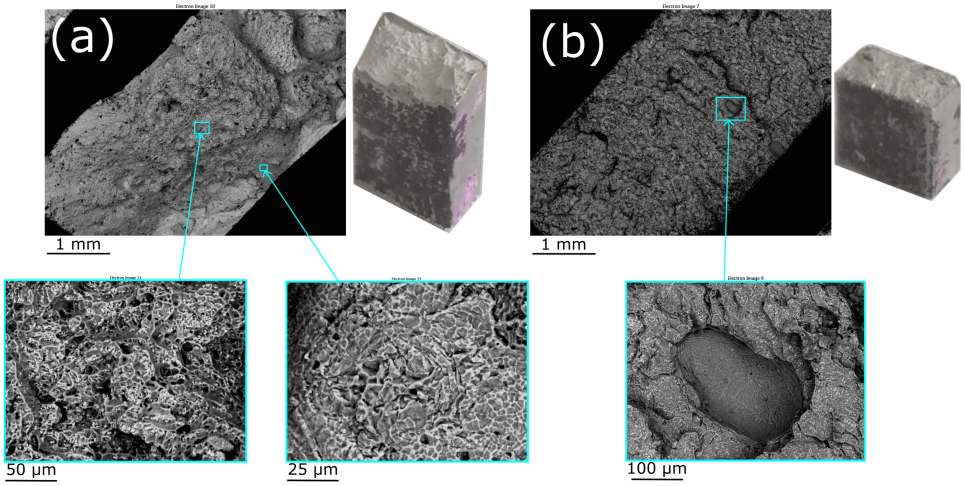


Figure 7.7: Photograph and SEM images of the rupture surface of the (a) 2050 & 2319 and (b) 2050 & 2024 combination

7.3.2 Aluminium copper wire and substrates

7.3.2.1 Effect of heat treatment on microstructure

Figure 7.8 shows the effect of heat treatment on the PMZ. Liquations are largely reduced by heat treatment in the case of the 2219 substrate, shown in pictures (a) and (b). However, images (d) and (h) show that the PMZ is severely affected by grain boundary cracks at the grain boundary in 2024 and 2139 substrates.

During solution treatment, the eutectic compound is solutionised and forms a unique phase with the aluminium matrix. This phenomenon occurred in 2219 substrate: the composition becomes more homogeneous and grain boundary segregation is highly reduced. In the case of the 2024 and 2139 substrate, cracks are generated in the PMZ during solution treatment (Figure 7.8 (d) and (f)). The origin of those cracks is not the same for both cases. For 2024 substrate, the solution treatment temperature, adapted to the deposited 2319 alloy, was too high for 2024 alloy: its melting point is 504°C, and the temperature reached during the heat treatment is 535°C. This means the eutectic compound is melted during the soaking. The molten grain boundary cannot sustain the stress generated by

the surrounding solid during the quench: this leads to solidification cracking. For 2139 substrate, the solution treatment temperature is not higher than the eutectic melting point, but the fast cooling occurring during the quench probably generates stresses helping the propagation of cracks along grain boundary, weakened by micro-cracks generated during deposition.

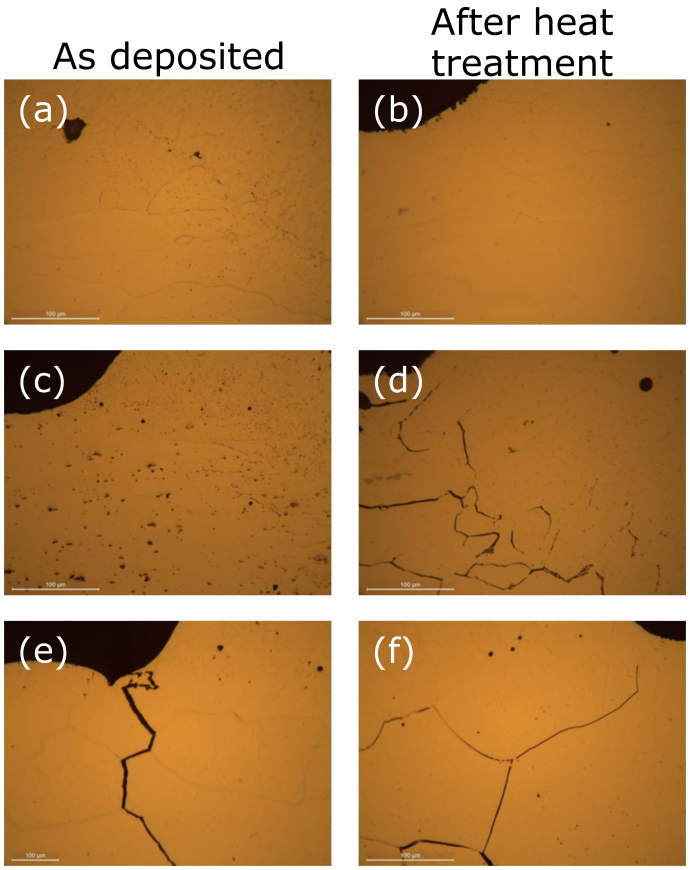


Figure 7.8: optical images of the PMZs before and after heat treatment of the combination 2219 & 2319 in pictures (a) and (b), 2024 & 2319 in pictures (c) and (d), and 2139 & 2319 in pictures (e) and (f)

7.3.2.2 Effect of heat treatment and inter-pass rolling on interface hardness profiles

2219 & 2319

Figure 7.9 provides the hardness profile across the interface between 2219 substrate and 2319 deposit.

Regarding the hardness profile of the inter-pass rolled interface, irregularities can be seen in the FZ and first layers. Inter-pass rolling increases the deposited material hardness, from 65 to about 100 HV, but does not have a clear effect on the FZ hardness.

Heat treatment drastically improves the hardness in the HAZ, FZ, and deposited material, whether it is carried out on as-deposited or inter-pass rolled interface. After heat treatment, the hardness profile is relatively flat across the interface, and the hardness is the same in the substrate and WAAM material.

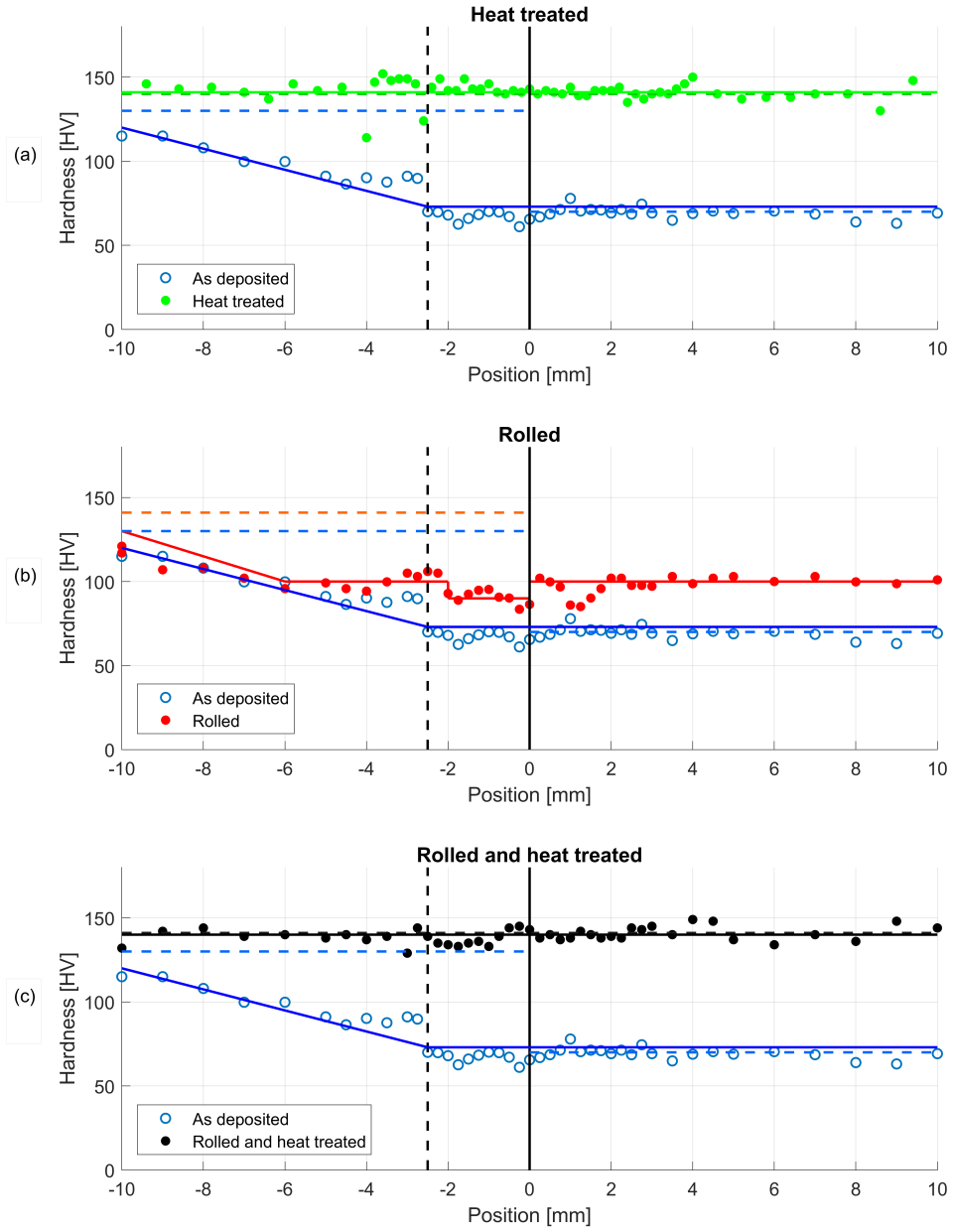


Figure 7.9: Effect of heat treatment and inter-pass rolling on the hardness profile of the combination 2219 & 2319

2024 & 2024

Figure 7.10 provides the hardness profile across the interface between 2024 substrate and 2024 deposit.

As mentioned before, inter-pass rolling does not affect the substrate. The FZ hardness is not significantly affected by inter-pass rolling, but the WAAM material hardness is improved by inter-pass rolling.

Heat treatment seems to have very little effect on the material, and the hardness drop in the HAZ is not recovered. Heat treatment lead to a flat hardness profile across the interface, with the same hardness value in the substrate and WAAM material.

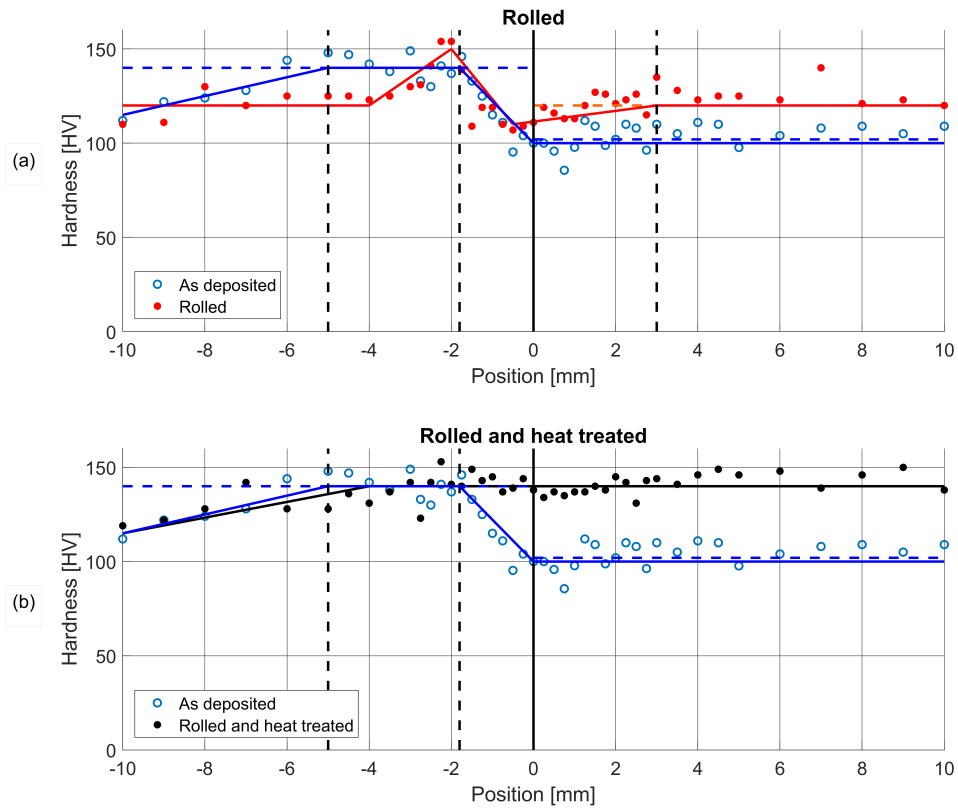


Figure 7.10: Effect of heat treatment and inter-pass rolling on the hardness profile of the combination 2024 & 2024

Graded interfaces

Figure 7.11 provide the hardness profile of various graded interfaces.

- Effect of inter-pass rolling on the 2024 & 2319 combination: Inter-pass rolling does not affect the substrate or the FZ hardness. The WAAM material hardness is increased by inter-pass rolling.

- Effect of heat treatment on 2024 & 2319 combination: The substrate hardness is not affected by heat treatment. The FZ hardness is increased by HT, as well as the WAAM material.

- Effect of Heat treatment on the 2139 & 2319 combination: The hardness is overall improved in all zones of the interface. The hardness gap between the substrate and WAAM material is drastically reduced by heat treatment. The transition between the substrate, FZ and WAAM material is smoother than in as-deposited condition.

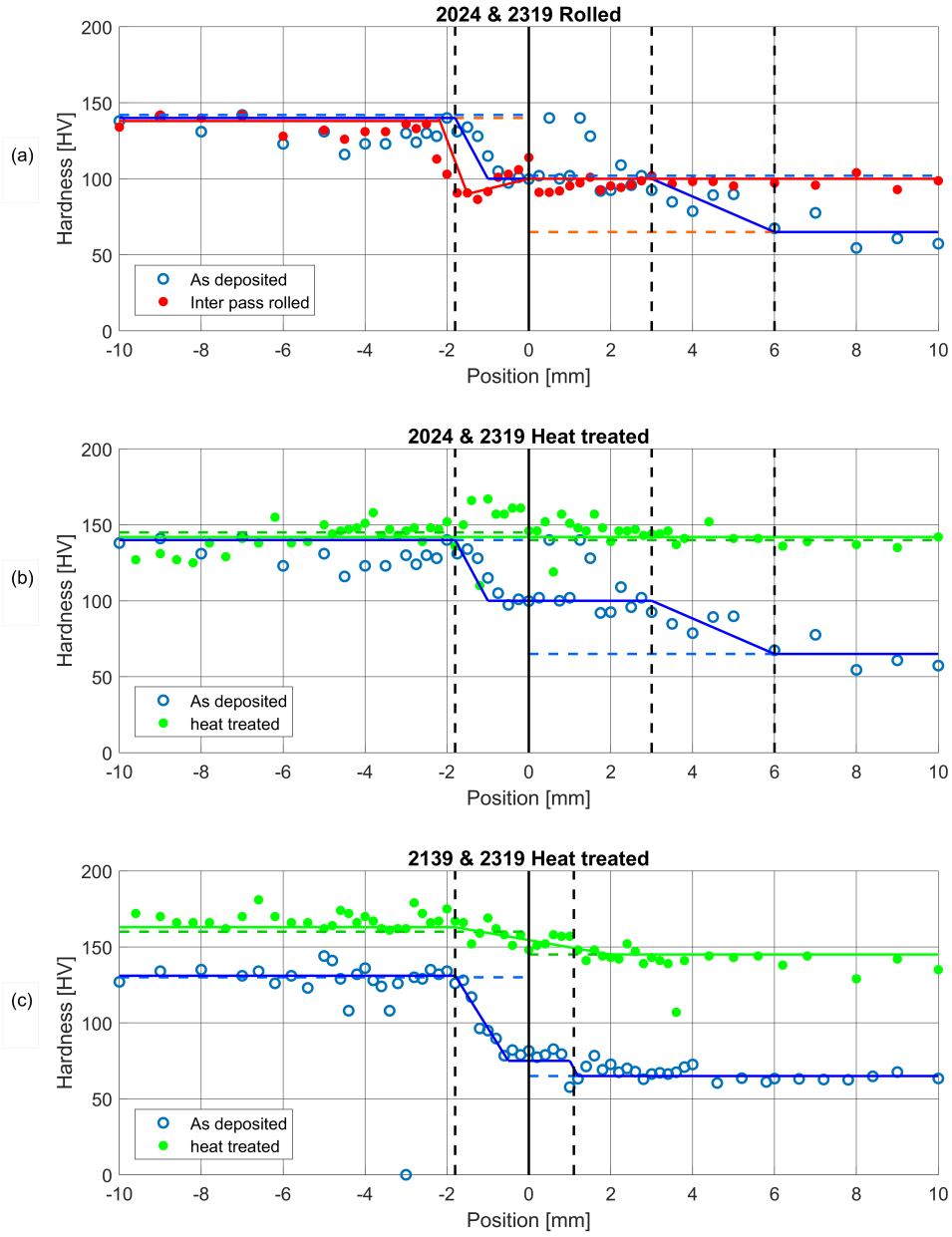


Figure 7.11: Effect of heat treatment and inter-pass rolling on the hardness profile of graded interfaces.

7.3.2.3 Effect of heat treatment and inter-pass rolling on mono-alloy interface mechanical properties

2219 & 2319 combination

Table 7.3 gives the tensile properties achieved by 2219 & 2319 and 2024 & 2024 in different conditions as well as the properties of the substrates and WAAM material.

- Inter-pass rolling drastically improves the YS, slightly increases the UTS, and highly reduces the elongation. This is the same trend observed by Gu et al. [11] for inter-pass rolled 2319 compared to as-deposited 2319.

- The YS obtained for the interface is comparable to the YS of inter-pass rolled 2319, but the UTS and elongation of the interface are lower than these of inter-pass 2319 WAAM material.

- The maximum stress measured during the test was 270 MPa, a value lower than the substrate YS (350 MPa). This partially explains the low elongation of the as-rolled combination compared with the as-rolled 2319 WAAM material.

- Heat treatment increases both YS and UTS compared to as-deposited properties. After heat treatment, the YS of the interface is very similar to the YS of 2319 WAAM material and 2219 substrate after being heat treated with the same heat treatment. The interface UTS is similar to this of WAAM material and the elongation is not significantly lower than the elongation reached by heat treated 2319.

- The average properties of inter-pass rolled then heat treated interface are very similar to those of heat treated interface. A wider range of properties was obtained compared to the heat treated interface, especially for the UTS and elongation.

Table 7.3: Mechanical properties of the interface between various alloy combination, with inter-pass rolling or/and heat treatment

Alloy combination	Condition	YS [MPa]	UTS [MPa]	Elongation [%]
2319 deposited on				
- 2219	AD	118 ± 8	257 ± 13	8.5 ± 1.5
	IR	224 ± 21	270 ± 18	2.2 ± 0.7
	HT[1]	270 ± 18	355 ± 12	3.5 ± 0.7
	IR+HT	272 ± 22	362 ± 26	4 ± 2
2219 substrate	T8	350 ± 5	450 ± 5	10 ± 1
2219 substrate	T6	245 ± 10	423 ± 5	23 ± 2
2319 WAAM material	T6	266 ± 16	370 ± 13	5.3 ± 1.0
2319 WAAM material [11]	R	244	311	8.6

[1] Heat Treated

Figure 7.12 shows the tensile specimen cross-section observed with an optical microscope, and Figure 7.13 provides SEM images of the rupture surface of the heat treated (a), inter-pass rolled (b) and inter-pass rolled then heat treated 2219 & 2319 (c) combinations.

The heat treated specimen broke at the interface between the substrate and deposit. The crack propagated mainly in the deposit, but also in the substrate where the cracks followed the substrate grain boundary. In the rupture surface, Figure 7.13 (a), these two areas can also be observed. Numerous pores and dimples can be seen in the deposit, and some features, typical of inter-granular rupture, show where the rupture occurred in the substrate

The inter-pass rolled samples broke in the deposit. In the top deposited layers no pores can be seen; however, some elongated pores can be observed in the first and second layers. In Figure 7.13 (b), some pores can also be seen on the rupture surface and the rest of the surface is covered with dimples. The rupture profile is irregular.

The rupture surface of the inter-pass rolled then heat treated specimen is much more regular than the other two, and takes place in the deposit, far away from the interface

(for the displayed specimen). Few elongated pores can be observed, but none of them is situated near the rupture area. The rupture surface in 7.13 (c) is mostly covered with small dimples but also with smoother areas. These areas could be generated by pores partially closed during inter-pass rolling, which re-opened under the load.

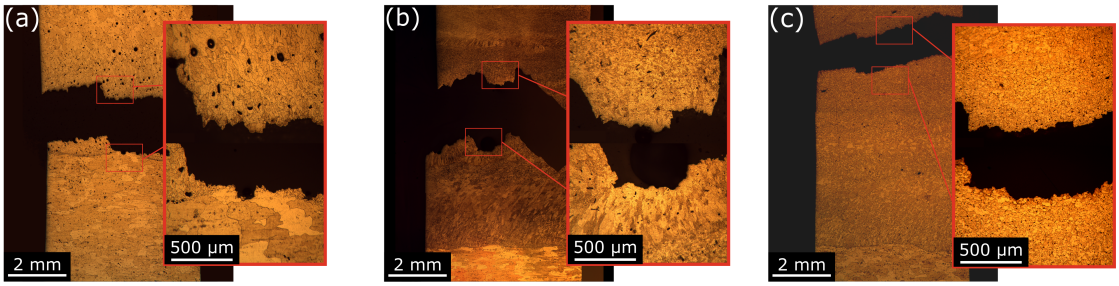


Figure 7.12: Effect of heat treatment (a), inter-pass rolling (b) and heat treatment on inter-pass rolled material (c) on the rupture area of the interface 2219 & 2319

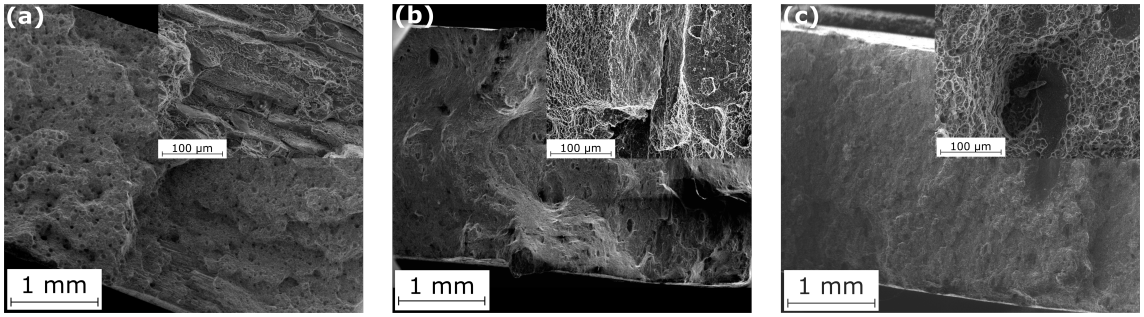


Figure 7.13: Effect of (a) heat treatment, (b) inter-pass rolling, and (c) heat treatment on inter-pass rolled material on the rupture surface of the interface 2219 & 2319

2024 & 2024 combination

The tensile properties are given in Table 7.4 In both cases, the elongation is very low. The 2024 & 2024 interface achieve a similar YS and a higher UTS than that of inter-pass rolled 2024. It is not possible to draw any conclusion on this results, because during both 2024 WAAM material and 2024 & 2024 interface test numerous defects were at the origin of premature ruptures.

Table 7.4: Mechanical properties of the interface between various alloy combination, with inter-pass rolling or/and heat treatment

Alloy combination	Condition	YS [MPa]	UTS [MPa]	Elongation [%]
2024 deposited on - 2024	R	284 ± 28	315 ± 17	1 ± 1
	R+HT	320 ± 9	363 ± 20	1.8 ± 1.0
2024 substrate	T3	364	500	19
2024 WAAM material [Chapter 4]	R	273 ± 16	280 ± 22	0.5 ± 0.2
2024 WAAM material [Chapter 4]	R+HT	284 ± 2	411 ± 35	6.0 ± 2.2

Heat treatment drastically improves the mechanical properties of the inter-pass rolled 2024 & 2024 interfaces, especially the YS and UTS. This same effect has been seen on the properties of WAAM deposit 2024.

The elongation achieved by the inter-pass rolled and heat treated 2024 & 2024 interface is much lower than that of WAAM material, but it reached a higher YS. Figure 7.14 gives stress-strain curve measured for the inter-pass rolled then heat treated 2024 & 2024 interface and 2024 WAAM material. The heat treated interface follows the beginning of the WAAM material but breaks much earlier. This means that the WAAM material behaves the same way regardless of if it is tested on its own or as part of an interface specimen for small elongation. However, the interface seems to drastically reduce the ductility of the samples when it comes to high elongation.

Figure 7.15 shows the cross-section of tensile specimens after rupture for both inter-pass rolled (a) and inter-pass rolled then heat treated (b) 2024 & 2024 combinations, and Figure 7.16 shows the rupture surfaces observed with SEM for these two combinations.

- For the inter-pass rolled specimen, the rupture occurred at the boundary between the second and third layers. The rupture surface is typical of trans-granular rupture.

- For the inter-pass rolled heat treated specimen, the rupture also occurred at the

boundary between two layers. The rupture surface is mainly covered by dimples and macro-voids.

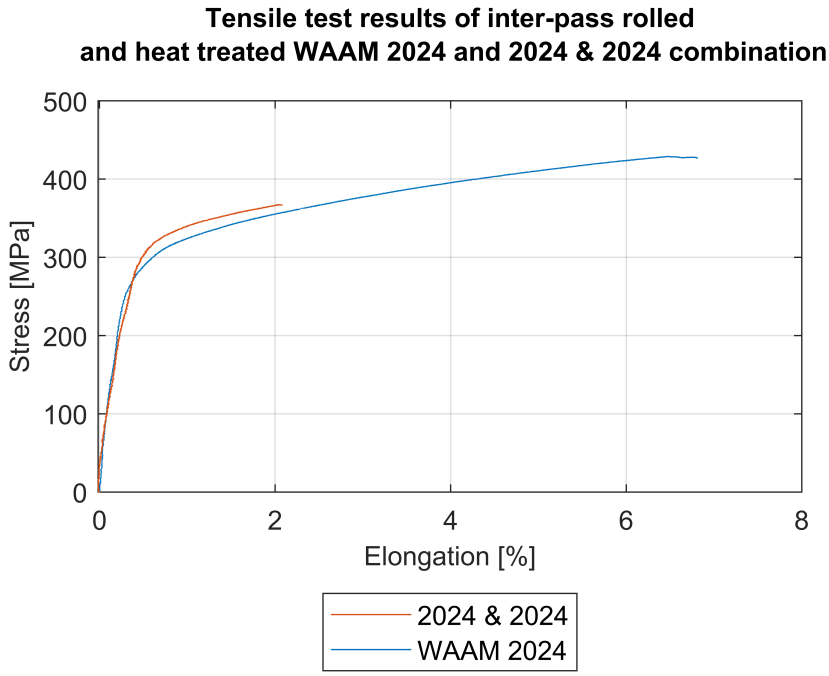


Figure 7.14: Effect of heat treatment and inter-pass rolling on the rupture surface of the interface 2024&2024

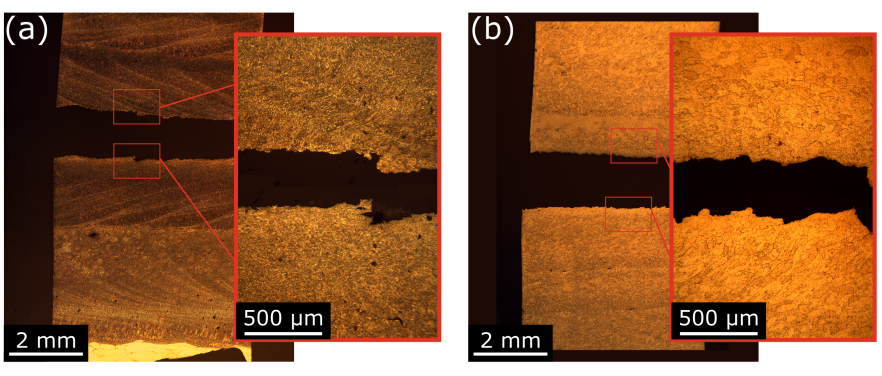


Figure 7.15: Optical images of ruptured tensile specimen of the 2024 & 2024 combination in (a) inter-pass rolled and (b) inter-pass rolled and heat treated conditions

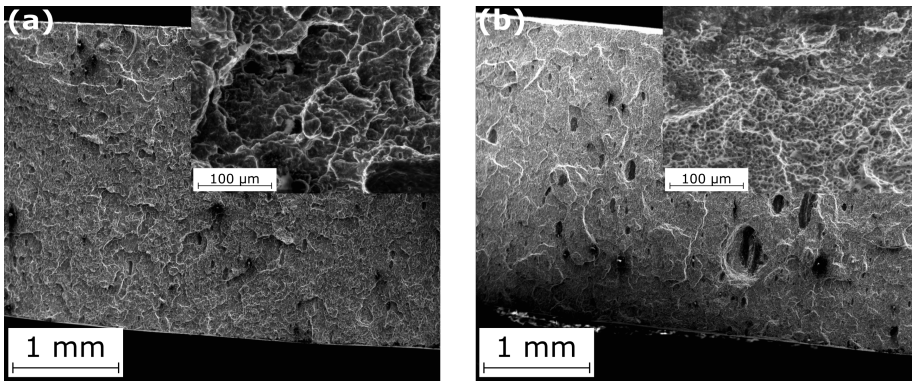


Figure 7.16: SEM images of the rupture surface of 2024 & 2024 combination in (a) inter-pass rolled and (b) inter-pass rolled and heat treated conditions

7.3.2.4 Effect of inter-pass rolling on 2024 & 2319 interface mechanical properties

The tensile properties obtained for this combination are given in Table 7.5. The properties of inter-pass rolled 2024 & 2319 are not significantly different from the inter-pass rolled 2219 & 2319 properties.

Figures 7.18 and 7.17 show a micrograph of a tensile specimen cross-section and an SEM image of its rupture surface. Contrary to what was observed during the analysis of the as-deposited 2024 &2319 interface in Chapter 6, neither the tensile cross-section nor the rupture surface show intra-granular cracks. These micro-cracks have been erased by

Table 7.5: Mechanical properties of the interface between various alloy combination, with inter-pass rolling or/and heat treatment

Alloy combination	Condition	YS [MPa]	UTS [MPa]	Elongation [%]
2319 deposited on				
-2024	AD	147 ± 14	232 ± 12	2.8 ± 0.9
-2024	R	248 ± 17	275 ± 11	1.2 ± 0.7
-2219	AD	118 ± 8	257 ± 13	8.5 ± 1.5
-2219	R	224 ± 21	270 ± 18	2.2 ± 0.7
2024 substrate	T3	364	500	19
2319 WAAM material [11]	R	244	311	8.6

inter-pass rolling.

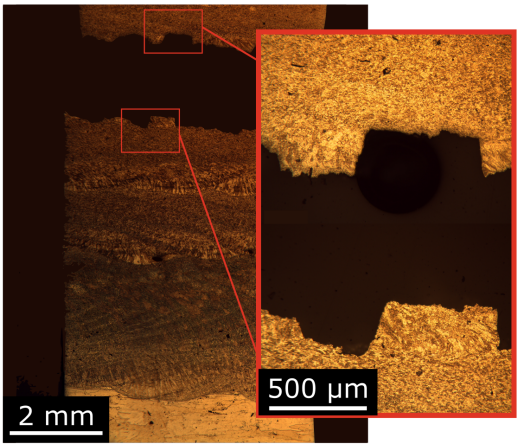


Figure 7.17: Optical image the cross-section of an inter-pass rolled 2024 & 2319 ruptured tensile specimen

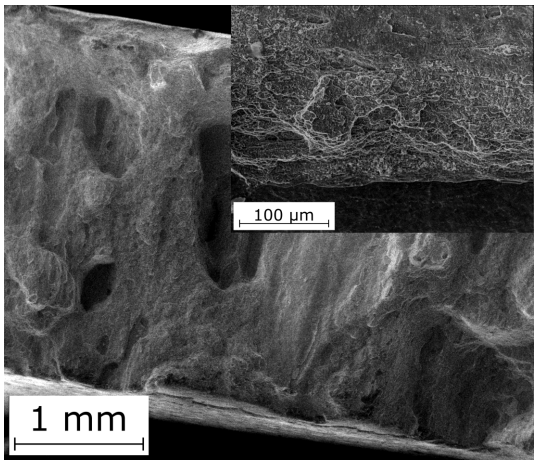


Figure 7.18: SEM image of the rupture surface of a tensile coupon representative of the inter-pass rolled 2024 & 2319 combination

7.3.3 Aluminium-magnesium-silicon substrates

2319 and 6061 alloys have the same solution treatment temperature. Therefore, It was possible to carry out heat treatment on both 6061_{RSP} & 2319 and 6061_{Rolled} & 2319 combinations.

7.3.3.1 Microstructures and micro hardness

Figure 7.19 gives the optical images of the cross-section used for micro hardness measurement, provided in Figure 7.20. The two profiles are very similar, regardless of what type of substrate was used, however, the hardness of the 6061_{Rolled} substrate is slightly lower than the hardness of the 6061_{RSP} substrate. The drop of hardness in the HAZ is partially recovered, but the substrate hardness is not significantly improved by the heat treatment. However, the hardness of the deposited material is drastically increased by the heat treatment. Contrary to all cases presented before, the hardness of the WAAM material is higher than the hardness of the substrate.

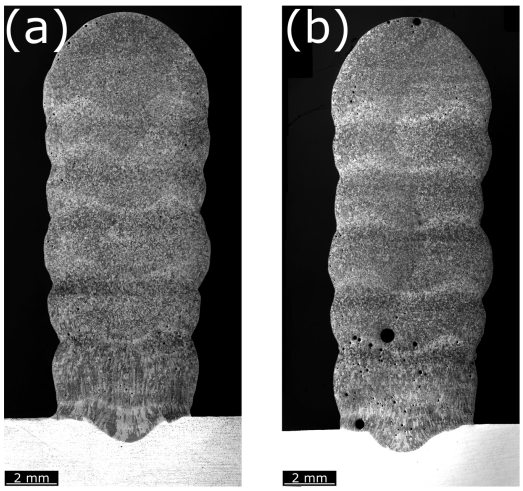


Figure 7.19: cross-section of the interfaces between (a) 6061_{Rolled} & 2319 and (b) 6061_{RSP} & 2319 after heat treatment

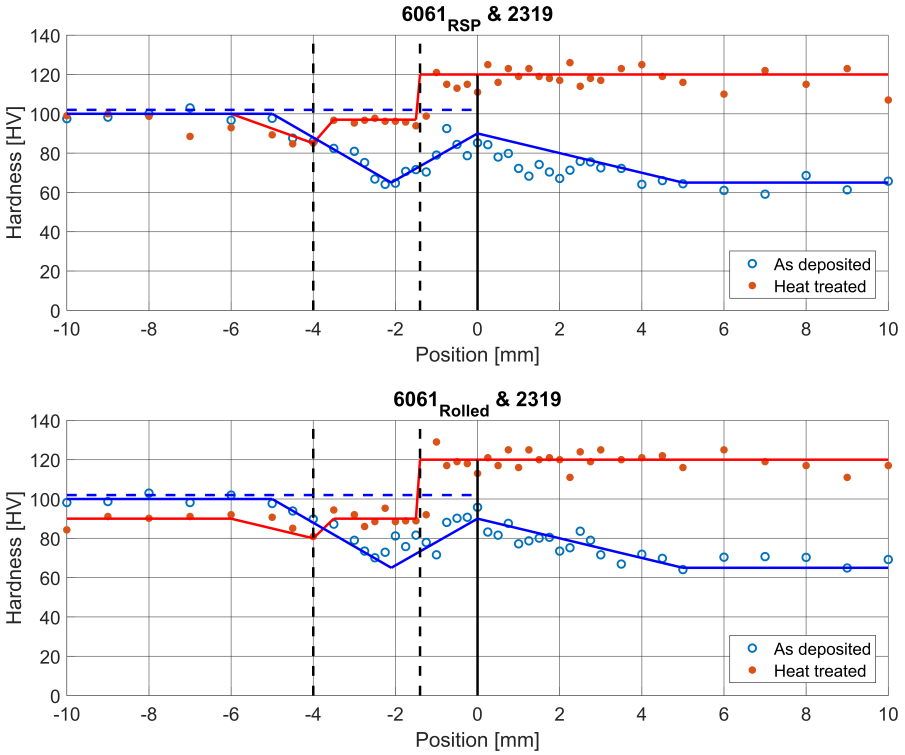


Figure 7.20: Vertical hardness profile of the as-deposited interface between 6061_{RSP} & 2319 and 6061 & 2319

7.3.3.2 Tensile test

Table 7.6 gives the tensile test results of the 6061_{RSP} & 2319 and 6061_{Rolled} & 2319 before and after heat treatment. For both combinations, heat treatment increases drastically YS, UTS, and elongation at rupture. The YS and UTS achieved by the 6061_{RSP} & 2319 combination are higher than those of the 6061_{Rolled} & 2319 combination, but the elongation of the 6061_{RSP} & 2319 is lower than this of the 6061_{Rolled} & 2319 combination. The elongation measured in these both cases is very high compared with all other combinations tested.

Table 7.6: Mechanical properties of the interface between various alloy combination, with inter-pass rolling or/and heat treatment

Alloy combination	Condition	YS [MPa]	UTS [MPa]	Elongation [%]
2319 deposited on				
-6061_{RSP}	HT	209 ± 12	328 ± 7	16.6 ± 1.1
-6061_{RSP}	AD	148 ± 18	225 ± 10	6.9 ± 0.2
-6061_{Rolled}	HT	168 ± 7	280 ± 2	20.0 ± 0.2
-6061_{Rolled}	AD	124 ± 21	208 ± 18	5.9 ± 2.6
2319 [11]	AD	131	259	15.5
6061_{RSP} [148]	T6	315	340	16
6061_{Rolled} [145]	T6	276	310	14

7.3.3.3 DIC

Figure 7.21 and 7.22 provides the DIC results for the 6061_{Rolled} & 2319 and 6061_{RSP} & 2319 combination respectively. In both cases, the micrograph in pictures (a) show that the ruptured occurred in the substrate, away from the interface. A strain concentration in the strain map in pictures (b) can be observed at the rupture areas. For the 6061_{Rolled} & 2319 interface, the deposited material is not strained, which results in no YS data in this area. But, for the 6061_{RSP} & 2319 interface, the whole specimen is strained, deposited material included. This is because the stress reached during the test of the 6061_{RSP} & 2319 specimens (328 MPa) was higher than this reached during the test of the 6061_{Rolled} & 2319 combination (280 MPa). On the YS map, in pictures (c) it is possible to see that the YS of the substrate depends on the substrate nature: between 150 to 175 MPa for the 6061_{Rolled} substrate, and between 200 and 225 MPa for the 6061_{RSP} substrate. This can be correlated with the lower hardness value in the $6061Rolled$ substrate than in the 6061_{RSP} substrate.

Regarding the YS map in Figure 7.22, it is possible to see an area of lower YS between the rupture area and the deposit. This area coincides with the drop of hardness observed in the micro hardness profile in Figure 7.20.

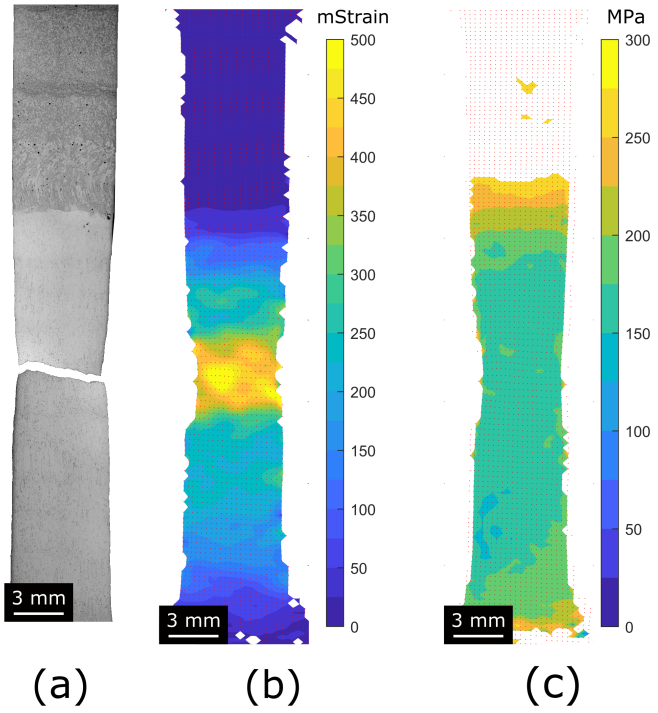


Figure 7.21: (a) Microstructure of a ruptured tensile specimen of the heat treated 6061_{rolled} & 2319 combination along with (b) the map of the maximum strain obtained during the tensile test, and (c) the evaluated yield stress map

Figure 7.23 provides SEM images of the ruptures surfaces of specimens from the 6061_{Rolled} & 2319 and 6061_{RSP} & 2319 combinations in picture (a) and (b) respectively. Dimples can be seen in both rupture surface in pictures (b) and (e), but the dimples in the 6061_{Rolled} substrate (b) are larger than in 6061_{RSP} substrate (e). Also, in the 6061_{Rolled} were found large inclusions, high in titanium and iron content, as shown in picture (c). These must have generated high stress concentration and determine where the sample ruptured. On the other hand, no inclusions were found in the 6061_{RSP} substrate. Picture (f) shows some features observed in the 6061_{RSP} substrate, very different from all other observed rupture surfaces. These rectilinear features are believed to be generated by the very fine grain structure of the 6061_{RSP} material, and the sheared dimples.

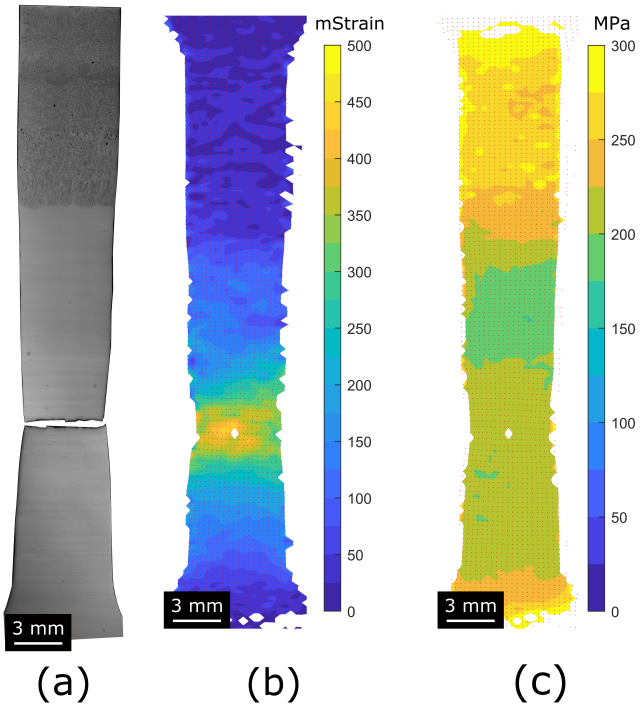


Figure 7.22: (a) Microstructure of a ruptured tensile specimen of the heat treated 6061_{rolled} & 2319 combination along with (b) the map of the maximum strain obtained during the tensile test, and (c) the evaluated yield stress map

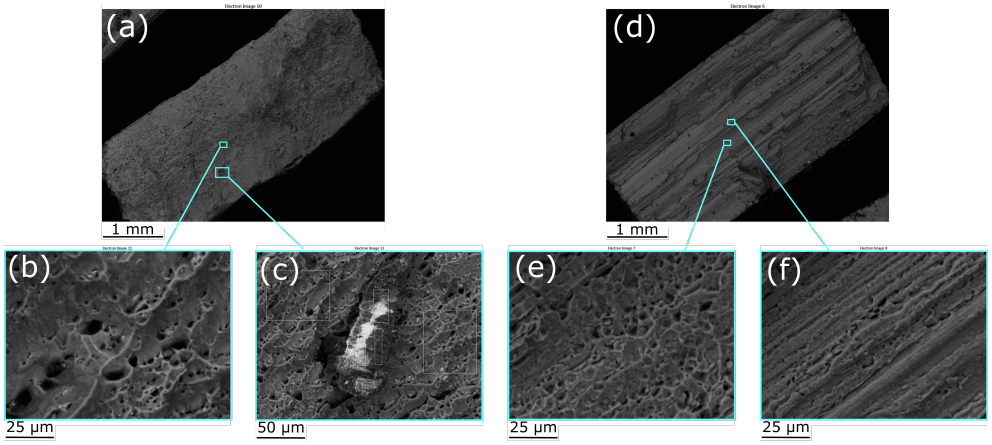


Figure 7.23: Fractopgraphs of (a) 6061_{rolled} & 2319 at low and (c) (d) at higher magnification, and (b) 6061_{RSP} & 2319 at low and (e) (f) at higher magnification

7.4 Discussion

7.4.1 Use of aluminium zinc and aluminium lithium substrate

It was not possible to achieve homogeneous mechanical properties with any of the combinations including 7449 and 2050 substrates.

Inter-pass rolling does not affect the first deposited layer as much as the rest of the deposition. This is due to the geometry of the first bead (deposited using different deposition parameters), and because part of the deformation happens in the substrate especially in the case of 2050 substrate. This is because pores are situated in the bottom of the first deposited bead when 2050 substrate was used. In this area, the strain generated by the rolling load was not high enough to affect the pores. Therefore, porosity was eliminated in the case of 7449 & 2319 but not in the cases 2050 & 2319 or 2050 & 2024 combination, where pores could still be seen in the tensile specimen cross-section.

The interface mechanical properties of the 7449 & 2319 and 2050 & 2319 combinations were much lower than the substrate or 2319 rolled properties due to defect at the interface. These substrates cannot be used with 2319 deposited material, with the deposition process used in this study.

7.4.2 Use of aluminium copper as-deposited material and substrate

7.4.2.1 Effect of heat treatment on graded structure microstructure

As explained in the literature review chapter, aluminium copper alloys require heat treatment to achieve their highest property potential. If the two alloys used as substrate and wire have compatible heat treatment, then it is possible to heat treat the whole part made from wrought product and WAAM material. This is the case when the two alloys are the same (here 2219 and 2024), but it is also theoretically possible if the solution treat-

ment temperature of both alloys is similar. If the solution treatment temperatures are not compatible, then cracks can form and damage the component integrity.

7.4.2.2 Effect of heat treatment and inter-pass rolling on the mechanical properties of the 2219 & 2319 combination

Effect of inter-pass rolling

Inter-pass rolled 2219 & 2319 combination reaches slightly lower properties than inter-pass rolled 2319 (244MPa, 311MPa and 8.6%) [11]. However, the rupture is in the 2^{nd} or 3^{rd} layer, so it seems that the interface does not play a role in the rupture behaviour of the samples. The image of tensile coupon in Figure 7.12 and the rupture surface in Figure 7.13 shows that some pores seem to reopen during the tensile test, which has not been reported by Gu et al. [11]. All layers were rolled using the same load but were deposited with different deposition parameters in order to compensate the heat accumulation during the deposition of the first layers. Also, the first layer geometry is different from the others because of the substrate proximity. Therefore, the rolling efficiency of the first layer is in all likelihood lower than for the rest of the layers. This explains why pores are not fully closed, why the hardness is slightly lower in this area and why the mechanical properties of the inter-pass rolled 2219 & 2319 interface are lower than these of inter-pass rolled 2319 WAAM material.

Effect of heat treatment

Heat treatment is leading to a stable hardness profile across the interface, as both substrate and deposited material reach the same hardness. But when tested separately using tensile tests, heat treated 2219 substrate and WAAM material do not have the same mechanical properties as the substrate has a much higher UTS and elongation. Therefore, the properties are not homogeneous across the interface. This is because despite having very

similar compositions, the two materials have different microstructure. Therefore, they need different solution treatment duration to generate a solid solution of aluminium and copper. Also, when inter-pass rolling is not carried out, heat treatment tends to increase the porosity level in the WAAM material which reduces its mechanical performances. Similar observations were made on heat treated WAAM material [11]

However, for the 2219 & 2319 combination heat treatment increases both YS and UTS compared with as-deposited condition but also reduces the elongation. The rupture profile of heat treated interface shows that the change in microstructure at the interface can facilitate the crack propagation along large grains in the substrate or columnar grain in the deposit.

The properties of the inter-pass rolled then heat treated interface are slightly higher than the properties of the heat treated interface, but because of the large properties scatter, it is difficult to conclude on the benefit of inter-pass rolling in this case. No data has been generated for inter-pass rolled heat treated 2319 using this heat treatment. However, Gu et al. [11] show that the properties of heat treated and inter-pass rolled then heat treated 2319 are similar apart from a higher elongation of the inter-pass rolled then heat treated material. In this case, the elongation of inter-pass rolled then heat treated 2219 & 2319 combination is probably affected by pores not fully closed by rolling because of the issues explained above for the inter-pass rolled 2219 & 2319 combination. These elongated pores can be seen in the tensile test cross-sections and can clearly be detrimental to the mechanical properties by generating stress concentration points.

7.4.2.3 Effect of heat treatment and inter-pass rolling on the mechanical properties of the 2024 & 2024 combination

The hardness profile of inter-pass rolled 2024 & 2024 shows that there is a hardness drop near the interface between the substrate and the deposit. In a similar manner than for the inter-pass rolled 2219 & 2319 combination, this is in all likelihood due to the lack of rolling efficiency during the rolling of the first layers. However, the rupture did not systematically occur at this lowest hardness point: some samples broke in the inter-pass rolled material. This can be explained by the very low ductility of as-rolled 2024 detailed in Chapter 4. It is difficult to analyse the properties of the as-rolled 2024 & 2024 combination since the properties of as-rolled 2024 material are very poor in the vertical direction.

After heat treatment, the hardness profile shows that the HAZ is not affected. This shows that the heat treatment used was not appropriate to the substrate and to its microstructural stage especially in the HAZ. However, the heat treatment drastically improved the hardness of the deposited material and reduced the micro hardness drop near the interface between the substrate and the deposit. The YS measured for these combinations was the YS of the WAAM material: the interface does not affect the sample at low elongation. However, both UTS and elongation of the interface were lower than these of 2024 WAAM material showing the effect of the interface on the specimen ductility.

7.4.2.4 Effect of inter-pass rolling on the mechanical properties of 2024 & 2319 combination

In the as-deposited condition, it has been shown in Chapter 6 that some micro-cracks were generated at the boundary between the first and second deposited layer of 2319 when 2024 substrate was used. These micro-cracks drastically reduced the mechanical properties of

this interface. The results on inter-pass rolled 2024 & 2319 showed that inter-pass rolling can have a large impact on these micro-cracks: no micro-cracks were observed on inter-pass rolled 2024 & 2319 samples. Rolling impacts the material in different ways: first, it greatly deforms the material; secondly it reduces the grain size; and finally, it affects the residual stresses distribution [73]. All these three phenomena drastically reduce the formation and propagation in the further layers of micro-cracks. This micro-crack issue being resolved, the mechanical properties of inter-pass rolled 2024 & 2319 combination were very similar to these of inter-pass rolled 2219 & 2319. Inter-pass rolling can be a solution to reduce the effect of solidification cracking sensitivity if the sensitive area can be rolled properly, meaning if this area is not in the fusion zone or in the first deposited layer.

7.4.3 Aluminium-magnesium-silicon substrates

The 6061_{RSP} & 2319 and 6061_{Rolled} & 2319 combinations are a good example of heat treatable graded interface. Heat treatment recovers the heat affected zone properties, and drastically improves the mechanical performance of the interface.

Despite the fact that no homogeneous mechanical properties were achieved across these interfaces, these samples reached a very large elongation compared to all other combination tested in this study. Also, these interfaces were the only one breaking in the substrate and not in the WAAM material, because the substrate was weaker than the deposit. This is why such high elongations were obtained compared with all other samples which broke before necking because of defects in the WAAM material. The DIC results of the combination 6061_{RSP} & 2319 show that if the properties of the substrate and WAAM material are similar enough, it is possible to strain the whole specimen under load rather than only deforming the weakest part of the component, and this without any detrimental

effect of the interface.

7.5 Conclusion

It was not possible to achieve homogeneous mechanical properties across the interface between the substrate and WAAM material by applying inter-pass rolling or heat treatment. The heat treatment of a mono-alloy component can generate a homogeneous micro hardness, but this is not enough to generate homogeneous mechanical properties as the substrate and WAAM material have different microstructures and behave differently under load. Inter-pass rolling can have a great effect on porosity and can increase drastically the mechanical properties of the WAAM material. It can also reduce the formation of micro-cracks when the composition of the deposited material is sensitive to solidification cracking. However, to have a beneficial effect on the interface properties, inter-pass rolling would need to generate homogeneous mechanical properties. Unfortunately, in this study the rolling load was kept constant while the deposition parameters were changed during the deposition of the first layers. This resulted in slightly inhomogeneous microstructure and mechanical properties across the interface. This had a dramatic effect on the measured tensile properties, especially on the ductility.

The best way of producing graded mechanical properties parts without any detrimental effect of the interface, is to heat treat a graded alloy part, where the substrate has lower mechanical properties than the WAAM material. This can be done only if the temperature of solution treatment is similar for both used alloys; if it is not the case, cracks can appear in the part of the sample where the eutectic temperature is the lowest.

Further studies need to be carried out in order to conclude on the effect of heat treatment and inter-pass rolling on the properties of the interface between the substrate and WAAM material. Firstly, various heat treatments could be applied in order to find the

best compromise between the substrate and WAAM material properties. Secondly, the substrates used for this work were commercial plates, meaning each of them was heat treated in a specific way. To be used as substrate for WAAM deposition, especially if the whole part is then heat treated, the substrate pre-deposition temper might play a key role in the interface microstructure and substrate mechanical properties, which both have an effect on the interface performances. And finally, the issue generated by inter-pass rolling is due to the lack of control of the bead shape when CMT-P-Adv is used, especially near the substrate, where the heat sink effect impacts on the bead profile. In order to uniformly roll the material, a strategy of depositing low layer height bead near the substrate along with adapted rolling load could lead to a more homogeneous interface microstructure and properties.

Chapter 8

Discussion

8.1 Findings summary, future work and literature review connections

8.1.1 Chapter 4

Chapter 4 focuses on the mechanical properties of WAAM 2024 and how these are affected by the deposition process, heat treatment, and inter-pass rolling. The following points are the main findings:

- The deposition process affects the deposited material quality, microstructure, and properties. This is coherent with what was highlighted in the section 2.2.3.4 of the literature review. Both bead shape and re-melting depth are process dependent and play a crucial role when inter-pass rolling is carried out.
- As shown by Gu et al. [11, 14], inter-pass rolling drastically reduces the porosity level of aluminium WAAM material. Two main explanations for the drastic pore reduction are suggested by the authors. Firstly the hydrogen is dissolved in the

dislocations, well known trapping site for hydrogen. Secondly, the formation of high dislocation-pipe diffusion paths could enable the hydrogen to diffuse to the sample surface and eventually escape the material. The result of Chapter 4 seem to indicate that the second phenomena plays a key role in porosity reduction as a drastic pores reduction is observed even when the material is remelted after rolling and do not contains a high dislocation density. Further analysis, including porosity analysis at high resolution and gas chemical analysis, will need to be carried out to fully understand how porosity is affected by inter-pass rolling.

- Heat treatment after deposition drastically increases YS, UTS and elongation at rupture

- It is possible to reduce the anisotropy between the vertical and horizontal directions using inter-pass rolling and heat treatment. Few papers have been published on the deposition of Al-Cu-Mg alloy by WAAM during this research project [8, 58, 92, 93]. Unfortunately, none of them provides data about the mechanical proprieties of the material in the vertical direction. This suggests that the authors faced similar issues of ductility loss during their experiment or they may not have looked at the properties in the vertical direction yet. Regardless, an in-depth study of the material, including Electron Backscatter Diffraction, Transmission Electron Microscope, and X-ray scanning, could help understand why the ductility remains low in the vertical direction, even when the material is inter-pas rolled and heat treated.

- The properties achieved by inter-pass rolled and heat treated material in the horizontal direction are similar to those of wrought material.

8.1.2 Chapter 5

Chapter 5 deals with the deposition of aluminium zinc alloy using laser-assisted WAAM. Its two objectives were to determine if this deposition process could be used in order to generate an elongated melt pool compared with conventional deposition processes, and if it was possible to use this process to deposit an aluminium zinc alloy. The following conclusions were drawn :

- It is possible to use laser-assisted WAAM to deposit aluminium and to elongate the melt pool. The use of a second heat source also has potential in term of bead geometry control.

- The elongated melt pool enables the feeding of a cold wire directly in the melt pool without disturbing the electric arc. Numerous issues observed during the feeding of aluminium zinc or aluminium magnesium wire directly in the arc have been reported in the literature [94, 100, 101]: these phenomena, due to the low vaporisation temperature of these elements were avoided with this set-up and a stable deposition process was obtained.

- The WFS were selected to achieve a stable deposition more than to target specific composition: unfortunately, the compositions deposited were limited due to the wire composition and diameter. However, the laser-assisted WAAM process has the potential of depositing a wide range of composition provided that suitable wire compositions are used. The following research step would be to use adapted wire compositions with a much lower zinc content in the cold wire and an aluminium copper magnesium GMA wire to deposit a high strength aluminium zinc copper magnesium alloy. Further investigation of the effect of process parameters and composition on element segregation, porosity and cracking will then be required.

- Two papers were published by Martin et al. and Aversa et al. on the additive manufacture of aluminium zinc alloys during the course of this research project [6, 7]: the authors focused on the effect of powder composition on the manufacture of 7075 alloy using LPBF. This recent interest and successful results show the potential future of the AM of aluminium zinc alloys: the work presented in Chapter 5 demonstrates the great potential of laser-assisted WAAM to deposit such alloys.

8.1.3 Chapters 6 and 7

Chapters 6 and 7 had the same objectives: the first one was to investigate the possibility of producing integral parts, made of a combination of a wrought substrate and WAAM material having homogeneous mechanical properties. The second objective was to investigate the possibility of manufacturing integral components achieving different properties in different areas of the part. Chapter 6 focused on as-deposited integral component properties while Chapter 7 investigated how these can be affected by inter-pass rolling and heat treatment.

8.1.3.1 Chapter 6

- During the course of this research project, the properties of as-deposited aluminium WAAM material was unable to compete with high strength wrought material properties. Therefore, it was not possible to achieve homogeneous mechanical properties across the interface between the substrate and deposited material with the investigated alloy combinations.

- However, it was possible to produce parts without specific integrity issues at the interface between the substrate and deposited material with different mechanical properties in different areas of the component. This was possible by combining a

unique alloy, for instance 2219 substrate with 2319 WAAM material, or two different alloys, for instance 2139 substrate and 2319 WAAM material.

- The heat affected zone in the substrate can generate a high strain concentration in this region of the substrate : this can drastically reduce the properties of the interface between the substrate and deposited material. This was observed in the case of the combination between 6061 substrates and 2319 WAAM material.

- Using the same alloy for the substrate and wire achieve a smooth transition of properties across the interface between the substrate and deposited material. The pre-deposition temper of the substrate also impacts on the microstructure of the HAZ and affects the transition between the substrate and deposited material.

- When using different alloy for the substrate and wire, different issues were observed and would need to be well considered before building a component:

  - Numerous aluminium alloys are sensitive toward hot cracking because of their composition. During WAAM deposition, the composition of the melt-pool gradually changes during the deposition of the first beads. The risk of hot cracking during the deposition of the first bead is therefore not the only one to consider: the composition of the second or third deposited bead could also be sensitive to hot cracking. However, the stress applied on the solidifying metal during the deposition of the first bead is much higher than during the deposition of the subsequent layers: this is due to the change in geometry. Therefore, the likelihood of hot cracking generation is higher during the deposition of the first layer.

  - The composition mixing at the first deposited bead can induce a two-step sharp change in micro hardness at the interface between the substrate and deposited

material.

- As in fusion welding, alloying elements such as lithium and zinc in the substrate can generate a high porosity level in the first deposited bead.
- Using very different alloys for the substrate and wire can generate a very sharp change in mechanical properties, resulting in high strain concentration at the interface between the substrate and deposited material.

8.1.3.2 Chapter 7

- Heat treatment and inter-pass rolling did not enable the manufacture of samples made of wrought and WAAM material with homogeneous mechanical properties
  - Heat treatment can drastically increase the mechanical properties of the interface between the substrate and WAAM material, as it increases the properties of the WAAM material [11]. However, the heat treatments used in this study were not adapted to both wrought and WAAM material: even after heat treatment the properties were not homogeneous across the interface.
  - Inter-pass rolling increases both YS and UTS of the interface, as it does on WAAM material [11]. However, inter-pass rolling was not efficient during the rolling of the first layer and tended to generate a localised zone with lower mechanical properties and higher porosity level. This reduced the ductility of the interface between the substrate and inter-pass rolled material.
- Heat treatment can be carried out on component made of the same alloy, but it is also possible to heat treatment component made of different alloyed substrate and wire, as long as their solution treatment temperatures are close. Specific substrate tempers could be used to enable the optimised heat treatment of integral parts. In

depth study of specific compositions and precipitation systems using Transmission Electron Microscopy would be required to determined optimised pre-deposition substrate temper.

- Heat treatment can be carried out to recover the properties in the heat affected zone and drastically improve the properties of the interface between the substrate and WAAM material.

8.2 Discussion and future work

8.2.1 Effect of bead geometry and inter-pass rolled material properties

8.2.1.1 Inter-pass rolling studies

A recurrent issue faced during this project was the effect of the bead geometry on the properties of the inter-pass rolled material. In Chapter 4 the effect of the process deposition on the bead shape had a considerable impact on the effect of inter-pass rolling on the material and its properties. In Chapter 7, the different process parameters used to deposit the first layers and the different thermal behaviour induced by the proximity of the substrate, cold before deposition, also changes the bead geometry of the first layers. This made the inter-pass rolling not as effective for the first deposited bead, with a lower strengthening and a lower porosity reduction compared with the rest of the wall.

Previous studies of inter-pass rolling on aluminium WAAM have focused on the effect of rolling load on the porosity density [5] and tensile properties [11, 14]. Colegrove et al. [72] showed the potential of profiled rollers to reduce the lateral deformation induced by inter-pass rolling on steel, and Honnige et al. [71] used another type of profile roller

for their study on the effect of rolling on titanium intersection features. However, in these studies, the effect of the bead geometry on the rolled material properties was not investigated. Most high strength aluminium alloys are heat treatable: therefore, their properties are significantly affected by the thermal history. Not only the pre-rolled bead geometry will have an impact on the strain and deformation generated by inter-pass rolling, but the width and layer height of the inter-pass rolled material will change the thermal history. The reduction in layer height will multiply the number of reheating cycles and the increase in layer width will change the cooling rate.

To conduct a systematic study on the effect of as-deposited the bead shape on the properties of inter-pass rolled material, it would be required to vary the layer height, re-melting depth and heat input independently.

8.2.1.2 Bead geometry

Unfortunately, as shown by Ayarkwa et al. [50], the geometry of a bead deposited with a synergic GMA process can only be partially controlled. When using a power source such as a CMT machine, the waveforms are determined by the WFS, chosen by the operator and only the TS can be changed in order to change the bead shape. However, it is impossible to control the bead width, layer height, and re-melted area independently despite a stable heat input at constant WFS to travel speed ratio [150]. The use of a non-synergic machine is required to have more control on the bead geometry: for aluminium deposition, AC PTA power sources, as used by Pinter [64], or GTA systems, as used by Ayarkwa [68] have great potential regarding bead shape control. In addition, Chapter 5 shows that the use of a second heat source could also be beneficial for bead shape control.

8.2.2 Interface between the substrate and deposited material and component design strategies

As detailed in the literature review in Chapter 2, Lockett et al. gave examples of building strategies which could be used to manufacture components by WAAM [3]. Many of these strategies incorporate the substrate in the final design, meaning that part of the substrate is kept in the component after machining.

These design possibilities and the fact that the properties of the interface between the substrate and deposited material were broadly unknown lead the aim of this research project: investigating the possibility of producing integral high strength aluminium alloy components, integrating wrought material, using Wire + Arc Additive Manufacture. Two possible types of component could be built using this strategy: component with homogeneous mechanical properties and components with different mechanical properties in targeted areas.

As shown in Chapters 4 and 5, many challenges will need to be tackled to enable the deposition of very high strength aluminium alloys in as-deposited condition. Until then, it will not be possible to achieve the same high mechanical properties in the WAAM material as in high strength wrought alloy in as-deposited condition. However, it is possible to reach similar mechanical properties in T6 condition (solution treated + ageing at peak age).

However, Chapters 6 and 7 demonstrated the potential of joining WAAM material and wrought product into a component with different mechanical properties in different areas. Regardless of what part of the component is the weakest, substrate or WAAM material, the dissimilar properties need to be taken into account during the design of the part. The local properties required by the working load and the global behaviour of the component need to be well thought out.

Figure 8.1 (a) shows an example of a component which could greatly benefit from the use of WAAM and the integration of the substrate in the final component. In images (b) and (d), two building strategies are illustrated: in image (b) the WAAM material (in grey) is deposited on the surface and both side of the substrate (in blue); in image (d), the WAAM material is deposited on the edge of the substrate. Images (c) and (e) show a cut of the component build with both strategies. The first strategy generates an intersection which could be problematic under load, with a strain concentration either in the substrate if it is weaker than the WAAM material, or in the WAAM sections if the WAAM material is weaker than the substrate. The second strategy results in a T intersection shown in image (e): this strategy could be used to avoid strain concentration and produce a high strength integral component with mixed materials.

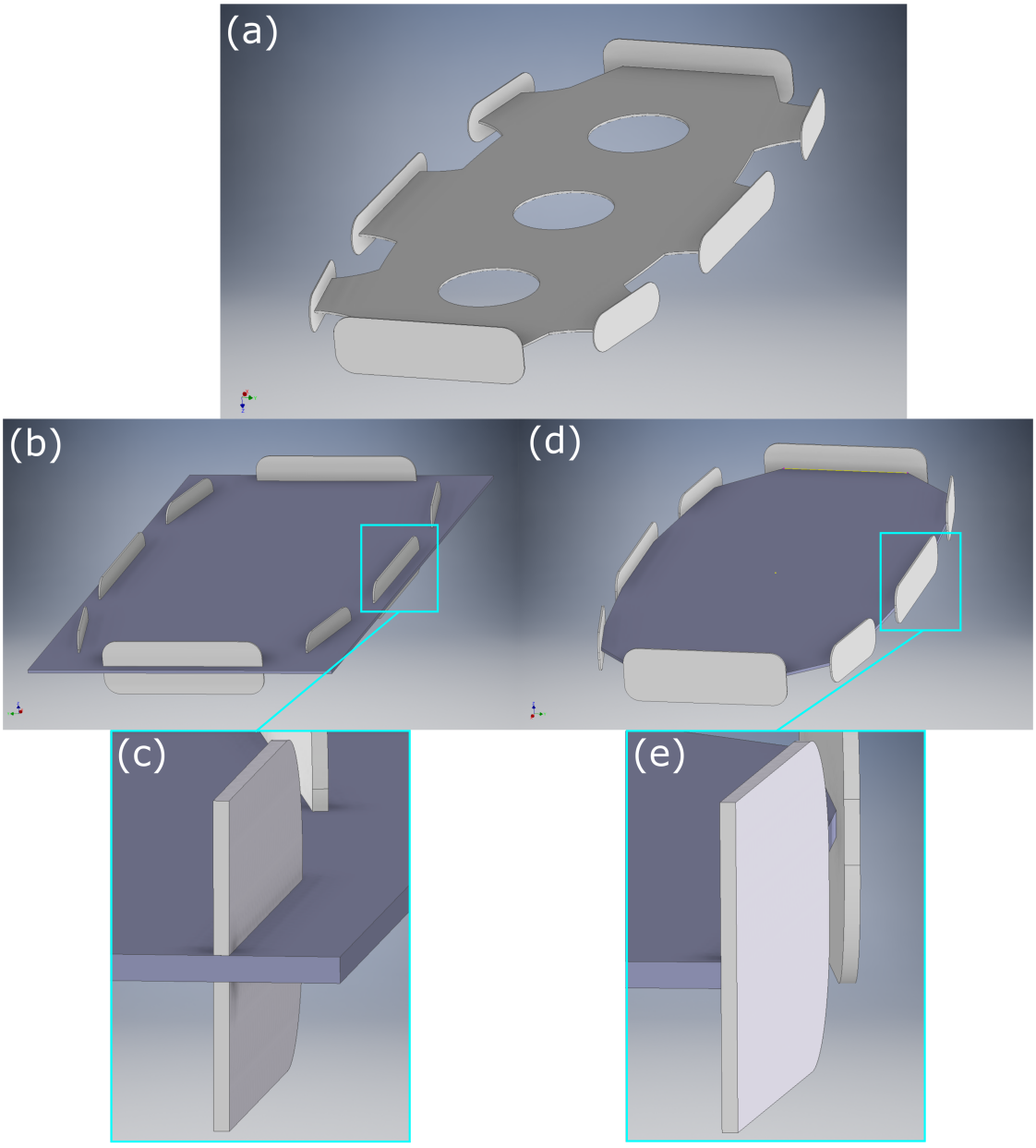


Figure 8.1: Example of potential building strategies to manufacture the part shown in (a): (b) and (c) for the deposition on the substrate surface, and (d) and (e) for the deposition on the edge of the substrate.

Chapter 9

Conclusions

It is possible to produce integral high strength aluminium components with wrought alloy substrates, but it is not possible to get homogeneous properties at this stage. The weakest part, therefore, limits the component performances: components made of very high strength substrates fail in the AM part while failures occur in the substrate if a lower strength substrate is used. To achieve high mechanical properties with a heat treatable integral component, the wrought substrate should be optimised regarding its composition and heat treatment parameters to match the deposited material so that the whole structure can be heat treated.

Aluminium copper magnesium alloys achieve best strength properties as aluminium zinc alloys are difficult to deposit. However, anisotropy issues limit the performance of Al-Cu-Mg alloys and further investigation is needed on this matter. Nonetheless, the properties of Al-Cu-Mg AM material after rolling and heat treatment are similar to those of the wrought material.

The deposition of aluminium zinc alloys is possible using a sophisticated deposition process, laser-assisted WAAM and a cold wire to avoid zinc vaporisation. However, much more work is needed to enable the deposition of large samples of appropriate composition.

Regarding the properties of the interface between the WAAM material and wrought substrate, very inhomogeneous properties are obtained with most alloy combinations, leading to issues of stress concentration and inhomogeneous straining behaviour under load. The best performances are reached when the same alloy is used for both substrate and AM material. Other combinations can also be used: for instance combination of high strength substrate with lower strength AM material could be used with adapted design strategy to take advantage of dissimilar alloy component with different performances in different areas.

Bibliography

[1] M. K. Thompson, G. Moroni, T. Vaneker, G. Fadel, R. I. Campbell, I. Gibson, A. Bernard, J. Schulz, P. Graf, B. Ahuja, F. Martina, Design for Additive Manufacturing : Trends , opportunities , considerations , and constraints, CIRP Ann. - Manuf. Technol. 65 (2) (2016) 737–760. doi:10.1016/j.cirp.2016.05.004.

[2] Welding Engineering and Laser Processing Center, Application and buisness. URL https://waammat.com/about/business-drivers

[3] H. Lockett, J. Ding, S. Williams, F. Martina, Design for Wire + Arc Additive Manufacture: design rules and build orientation selection, J. Eng. Des. 4828 (2017) 1–31. doi:10.1080/09544828.2017.1365826.

[4] N. T. Aboulkhair, N. M. Everitt, I. Ashcroft, C. Tuck, Reducing porosity in AlSi10Mg parts processed by selective laser melting, Addit. Manuf. 1-4 (2014) 77–86. doi:10.1016/j.addma.2014.08.001.

[5] J. Gu, J. Ding, S. W. Williams, H. Gu, P. Ma, Y. Zhai, The effect of inter-layer cold working and post-deposition heat treatment on porosity in additively manufactured aluminum alloys, J. Mater. Process. Technol. 230 (2016) 26–34. doi:10.1016/j.jmatprotec.2015.11.006.

[6] A. Aversa, G. Marchese, D. Manfredi, M. Lorusso, F. Calignano, S. Biamino, M. Lombardi, P. Fino, M. Pavese, Laser Powder Bed Fusion of a High Strength Al-Si-Zn-Cu Alloy, Metals (Basel). (2018) 1–12doi:10.3390/met8050300.

[7] J. H. Martin, B. D. Yahata, J. M. Hundley, J. A. Mayer, T. A. Schaedler, T. M. Pollock, 3D printing of high-strength aluminium alloys, Nature 549 (7672) (2017) 365–369. doi:10.1038/nature23894.

[8] Z. Qi, B. Cong, B. Qi, H. Sun, G. Zhao, J. Ding, Microstructure and mechanical properties of double wire + arc additively manufactured Al Cu Mg alloys, J. Mater. Process. Technol. 255 (August 2017) (2018) 347–353. doi:10.1016/j.jmatprotec.2017.12.019.

[9] B. Acherjee, Hybrid laser arc welding: State-of-art review, Opt. Laser Technol. 99 (2018) 60–71. arXiv:arXiv:1011.1669v3, doi:10.1016/j.optlastec.2017.09.038.

[10] E. Assuncao, S. Williams, Effect of Material Properties on the Stability of Solid, J. Laser Appl. 26 (1). doi:10.2351/1.4826153.

[11] J. Gu, J. Ding, S. W. Williams, H. Gu, J. Bai, Y. Zhai, P. Ma, The strengthening effect of inter-layer cold working and post-deposition heat treatment on the additively manufactured Al– 6.3Cu alloy, J. Mater. Process. Technol. 230 (2016) 26–34. doi:10.1016/j.jmatprotec.2015.11.006.

[12] B. Cong, J. Ding, S. W. Williams, Effect of arc mode in cold metal transfer process on porosity of additively manufactured Al-6.3%Cu alloy, Int. J. Adv. Manuf. Technol. 76 (9-12) (2014) 1593–1606. doi:10.1007/s00170-014-6346-x.

[13] Dynamics Dantec GMbH, Istra 4D Software Manual Q-400 system, Tech. rep., Nova instrument (2012).

[14] J. Gu, X. Wang, J. Bai, J. Ding, S. Williams, Y. Zhai, K. Liu, Deformation microstructures and strengthening mechanisms for the wire+arc additively manufactured Al-Mg4.5Mn alloy with inter-layer rolling, Mater. Sci. Eng. A 712 (November 2017) (2018) 292–301. doi:10.1016/j.msea.2017.11.113.

[15] A. F. Norman, S. S. Birley, P. B. Prangnell, Development of new high strength Al-Sc filler wires for fusion welding 7000 series aluminium aerospace alloys, Sci. Technol. Weld. Join. 8 (4) (2003) 235–245. doi:10.1179/136217103225010989.

[16] The Aluminum Association Inc., International Alloy Designations and Chemical Composition Limits for Wrought Aluminum and Wrought Aluminum Alloys, Tech. Rep. February 2009, The Aluminum Association, Arlington (2009).

[17] E. A. Starke, J. T. Staleyt, Application of modern aluminum alloys to aircraft, Prog. Aerosp. Sci. 32 (95) (1996) 131–172. doi:0376--0421(95)00004-6.

[18] A. Heinz, A. Haszler, C. Keidel, S. Moldenhauer, R. Benedictus, W. S. Miller, Recent development in aluminium alloys for aerospace applications, Mater. Sci. Eng. A 280 (2000) 102–107.

[19] R. J. Rioja, J. Liu, The evolution of Al-Li base products for aerospace and space applications, Metall. Mater. Trans. A Phys. Metall. Mater. Sci. 43 (9) (2012) 3325–3337. doi:10.1007/s11661-012-1155-z.

[20] T. Dursun, C. Soutis, Recent devlopment in advanced aircraft aluminium alloys, Mater. Des. 56 (2008) 862–871. doi:10.1016/j.matdes.2008.06.063.

[21] D. McLellan, Understanding casting factors in aircraft, Mod. Cast. 84 (10) (1994) 21–24.
URL http://www.thefreelibrary.com/{_}/print/PrintArticle.aspx?id=16383186

[22] Y. Liu, R. Zhang, J. Zhang, An Introduction of Aluminum Alloy Casting in Aircraft Structure, Appl. Mech. Mater. 529 (2014) 79–83. doi:10.4028/www.scientific.net/AMM.529.79.

[23] Constellium, Aluminium Aerospace products by Constelium.
URL http://aerospace.products.constellium.com/

[24] L. Katgerman, D. Eskin, Hardening, Annealing, and Ahging, in: G. E. Totten, D. S. MacKenzie (Eds.), Handb. Alum. Vol. 1 Phys. Metall. Process., CRC Press, 2003, Ch. 3, pp. 259–304.

[25] ASTM International, Standard Specification for Aluminum and Aluminum-Alloy Sheet and Plate. doi:10.1520/B0209M-14.

[26] S. Kou, Precipitation-Hardening Materials I: Aluminium Alloys, in: Weld. Metall. Second Ed., second edi Edition, John Wiley & Sons, Inc., Hoboken, NJ, USA, 2003, Ch. 15, pp. 353–374. doi:10.1002/0471434027.

[27] S. Dumolt, D. E. Laughlin, J. C. Williams, The effect of welding on the microstructure of the age hardening Al alloy 2219, in: First Int. Alum. Weld. Conf., Cleveland, Ohio, 1981, pp. 115–135.

[28] Y. L. Zhao, Z. Q. Yang, Z. Zhang, G. Y. Su, X. L. Ma, Double-peak age strengthening of cold-worked 2024 aluminum alloy, Acta Mater. 61 (5) (2013) 1624–1638. doi:10.1016/j.actamat.2012.11.039.

[29] J. Allen, An Investigation into the Comparative Costs of Additive Manufacture vs . Machine from Solid for Aero Engine Parts, in: Cost Eff. Manuf. via Net Shape Process., 2006, pp. 1–10. doi:10.14339/RTO-MP-AVT-139.

[30] F. Martina, S. W. Williams, Wire + arc additive vs . traditional machining from solid: a cost comparison, Tech. rep., Welding Engineering and Laser Processing Centre, Cranfield (2015).
URL http://waammat.com/documents/waam-vs-machining-from-solid-a-cost-comparis

[31] A. Fernando Padilha, R. Lesley Plaut, Work Hardening, Recovery, Recrystallization, and Grain Growth, in: G. E. Totten, D. S. MacKenzie (Eds.), Handb. Alum. Vol. 2, CRC Press, 2003, Ch. 6, pp. 193–220.

[32] M. Weimin, Recrystalisation and grain growth, in: G. E. Totten, D. S. MacKenzie (Eds.), Handb. Alum. Vol. 1 Phys. Metall. Process., CRC Press, 2003, Ch. 4, pp. 211–258.

[33] S. W. Williams, F. Martina, A. C. Addison, J. Ding, G. Pardal, P. Colegrove, Wire+Arc Additive Manufacturing, Mater. Sci. Technol. 32 (7) (2016) 641–647. doi:10.1179/1743284715Y.0000000073.

[34] J. Coykendall, M. Cotteleer, L. Holdowsky, M. Mahto, 3D opportunity in Aerospace and Defense, Deloitte Univ. Press (2014) 1–28.
URL https://www2.deloitte.com/insights/us/en/focus/3d-opportunity/additive-manufacturing-3d-opportunity-in-aerospace.html

[35] Advanced Manufacturing Research Centre, Rapid Production of Large Aersospace components, Tech. rep., FP6-AEROSPACE (2006).

[36] M. Revaud, A. Lagardere, A. Thou-kin, N. Ravier, ALM process for rocket engine - application to prometheus, in: 2nd Ed. Met. Mater. Process. Ind. challenges, Vol. 1, 2017, pp. 1–7.

[37] J. Van Doeselaar, Introduction of Additive Manufacturing for Airbus Products, in: 2nd Ed. Met. Mater. Process. Ind. challenges, 2017.

[38] J. ROMERO, The Dawn of AM in the Railway Industry, in: Met. Mater. Process. indistrual challenges, Deauville, 2017.

[39] A. Queguineur, G. Rückert, F. Cortial, J. Y. Hascoët, Evaluation of wire arc additive manufacturing for large-sized components in naval applications, Weld. World 62 (2) (2018) 259–266. doi:10.1007/s40194-017-0536-8.

[40] P. Gerhard, K. Ferdinand, C. Harald, Manufacturing of turbine blades by shape giving CMT Welding, in: Met. Addit. Manuf. Conf., Vienna, 2014.

[41] ISO/ASTM International, 52900:2015 (E) Standard Terminology for Additive Manufacturing – General Principles – Terminology (2015). arXiv:arXiv:1011.1669v3, doi:10.1520/F2792-12A.2.

[42] W. E. Frazier, Metal Additive Manufacturing : A Review, J. Mater. Eng. Perform. 23 (June) (2014) 1917–1928. doi:10.1007/s11665-014-0958-z.

[43] D. Herzog, V. Seyda, E. Wycisk, C. Emmelmann, Additive manufacturing of metals, Acta Mater. 117 (2016) 371–392. doi:10.1016/j.actamat.2016.07.019.

[44] R. plc., RenAM 500 series additive manufacturing system - Data Sheet (2018). URL https://www.renishaw.com/en/renam-500q--42781

[45] Sciaky INC., ELECTRON BEAM ADDITIVE MANUFACTURING (EBAM®) (2018).
URL http://www.sciaky.com/additive-manufacturing/electron-beam-additive-manufacturing-technology

[46] F. Martina, J. Mehnen, S. W. Williams, P. Colegrove, F. Wang, Investigation of the benefits of plasma deposition for the additive layer manufacture of Ti-6Al-4V, J. Mater. Process. Technol. 212 (6) (2012) 1377–1386. doi:10.1016/j.jmatprotec.2012.02.002.

[47] R. R. Unocic, J. N. DuPont, Process Efficiency Measurements in the Laser Engineered Net Shaping Process, Metall. Mater. Trans. B Process Metall. Mater. Process. Sci. 35 (1) (2004) 143–152. doi:10.1007/s11663-004-0104-7.

[48] Sciaky INC., Advantages of Wire AM vs. Powder AM (2018).
URL http://www.sciaky.com/additive-manufacturing/wire-am-vs-powder-am

[49] R. Baker, Method of making decorative articles, Tech. rep., United states patent office (1925).

[50] K. F. Ayarkwa, S. Williams, J. Ding, Investigation of pulse advance cold metal transfer on aluminium wire arc additive manufacturing, Int. J. Rapid Manuf. 5 (1) (2015) 44–57.

[51] J. Ding, P. Colegrove, F. Martina, S. Williams, R. Wiktorowicz, M. Palt, Development of a laminar flow local shielding device for wire+arc additive manufacture, J. Mater. Process. Technol. 226 (2015) 99–105. doi:10.1016/j.jmatprotec.2015.07.005.

[52] F. Wang, S. Williams, P. Colegrove, A. A. Antonysamy, Microstructure and Mechanical Properties of Wire and Arc Additive Manufactured Ti-6Al-4V, Metall. Mater. Trans. A 44 (2) (2013) 968–977. doi:10.1007/s11661-012-1444-6.

[53] E. Brandl, F. Palm, V. Michailov, B. Viehweger, C. Leyens, Mechanical properties of additive manufactured titanium (Ti-6Al-4V) blocks deposited by a solid-state laser and wire, Mater. Des. 32 (10) (2011) 4665–4675. doi:10.1016/j.matdes.2011.06.062.

[54] B. Baufeld, Mechanical Properties of INCONEL 718 Parts Manufactured by Shaped Metal Deposition (SMD), J. Mater. engin 21 (July) (2012) 1416–1421. doi:10.1007/s11665-011-0009-y.

[55] X. Xu, S. Ganguly, J. Ding, S. Guo, S. Williams, F. Martina, Microstructural evolution and mechanical properties of maraging steel produced by wire + arc additive manufacture process, Mater. Charact. 143 (September) (2018) 152–162. doi:10.1016/j.matchar.2017.12.002.

[56] B. Dong, Z. Pan, C. Shen, Y. Ma, H. Li, Fabrication of Copper-Rich Cu-Al Alloy Using the Wire-Arc Additive Manufacturing Process, Metall. Mater. Trans. B Process Metall. Mater. Process. Sci. 48 (6) (2017) 3143–3151. doi:10.1007/s11663-017-1071-0.

[57] J. Guo, Y. Zhou, C. Liu, Q. Wu, X. Chen, J. Lu, Wire arc additive manufacturing of AZ31 magnesium alloy: Grain refinement by adjusting pulse frequency, Materials (Basel). 9 (10). doi:10.3390/ma9100823.

[58] J. Gu, J. Bai, J. Ding, S. Williams, L. Wang, K. Liu, Design and cracking susceptibility of additively manufactured Al-Cu-Mg alloys with tandem wires and pulsed

arc, J. Mater. Process. Technol. 262 (May) (2018) 210–220. doi:10.1016/j.jmatprotec.2018.06.030.

[59] H. Wang, W. Jiang, J. Ouyang, R. Kovacevic, Rapid prototyping of 4043 Al-alloy parts by VP-GTAW, J. Mater. Process. Technol. 148 (1) (2004) 93–102. doi:10.1016/j.jmatprotec.2004.01.058.

[60] A. Gomez Ortega, L. Corona Galvan, F. Deschaux-Beaume, B. Mezrag, S. Rouquette, Effect of process parameters on the quality of aluminium alloy Al5Si deposits in wire and arc additive manufacturing using a cold metal transfer process, Sci. Technol. Weld. Join. 23 (4) (2018) 316–332. doi:10.1080/13621718.2017.1388995.

[61] D. Ding, Z. Pan, D. Cuiuri, H. Li, A multi-bead overlapping model for robotic wire and arc additive manufacturing (WAAM), Robot. Comput. Integr. Manuf. 31 (2015) 101–110. doi:10.1016/j.rcim.2014.08.008.

[62] C. Zhang, Y. Li, M. Gao, X. Zeng, Wire arc additive manufacturing of Al-6Mg alloy using variable polarity cold metal transfer arc as power source, Mater. Sci. Eng. A 711 (August 2017) (2018) 415–423. doi:10.1016/j.msea.2017.11.084.

[63] B. Cong, Z. Qi, B. Qi, H. Sun, G. Zhao, J. Ding, A Comparative Study of Additively Manufactured Thin Wall and Block Structure with Al-6.3%Cu Alloy Using Cold Metal Transfer Process Baoqiang, Appl. Sci. 7 (2017) 1–11. doi:10.3390/app7030275.

[64] Z. Pinter, Study of wire +arc additive manufacturing, Msc thesis, Cranfield University (2017).

[65] E. M. Ryan, T. J. Sabin, J. F. Watts, M. J. Whiting, The influence of build parameters and wire batch on porosity of wire and arc additive manufactured aluminium alloy 2319, J. Mater. Process. Tech. 262 (July) (2018) 577–584. doi:10.1016/j.jmatprotec.2018.07.030.

[66] A. S. Haselhuhn, M. W. Buhr, B. Wijnen, P. G. Sanders, J. M. Pearce, Structure-property relationships of common aluminum weld alloys utilized as feedstock for GMAW-based 3-D metal printing, Mater. Sci. Eng. A 673 (2016) 511–523. doi:10.1016/j.msea.2016.07.099.

[67] J. Y. Bai, C. L. Yang, S. B. Lin, B. L. Dong, C. L. Fan, Mechanical properties of 2219-Al components produced by additive manufacturing with TIG, Int. J. Adv. Manuf. Technol. 86 (1-4) (2015) 479–485. doi:10.1007/s00170-015-8168-x.

[68] K. F. Ayarkwa, S. W. Williams, J. Ding, Assessing the effect of TIG alternating current time cycle on aluminium wire + arc additive manufacture, Addit. Manuf. 18 (2017) 186–193. doi:10.1016/j.addma.2017.10.005.

[69] P. Wang, S. Hu, J. Shen, Y. Liang, Characterization the contribution and limitation of the characteristic processing parameters in cold metal transfer deposition of an Al alloy, J. Mater. Process. Technol. 245 (2017) 122–133.

[70] F. Martina, M. J. Roy, B. A. Szost, S. Terzi, P. A. Colegrove, S. W. Williams, P. J. Withers, J. Meyer, M. Hofmann, Residual stress of as-deposited and rolled wire+arc additive manufacturing Ti–6Al–4V components, Mater. Sci. Technol. (United Kingdom) 32 (14) (2016) 1439–1448. doi:10.1080/02670836.2016.1142704.

[71] J. R. Honnige, P. A. Colegrove, B. Ahmad, M. E. Fitzpatrick, S. Ganguly, T. L. Lee, S. W. Williams, Residual stress and texture control in Ti6Al4V wire + arc

additively manufactured intersections by stress relief and rolling, Mater. Des. 150 (2018) 193–205. doi:10.1016/j.matdes.2018.03.065.

[72] P. a. Colegrove, H. E. Coules, J. Fairman, F. Martina, T. Kashoob, H. Mamash, L. D. Cozzolino, Microstructure and residual stress improvement in wire and arc additively manufactured parts through high-pressure rolling, J. Mater. Process. Technol. 213 (10) (2013) 1782–1791. doi:10.1016/j.jmatprotec.2013.04.012.

[73] J. R. Honnige, P. A. Colegrove, S. Ganguly, E. Eimer, S. Kabra, S. Williams, Control of residual stress and distortion in aluminium wire + arc additive manufactured with rolling, Addit. Manuf. 22 (2018) 775–783.

[74] F. Martina, S. W. Williams, P. Colegrove, Improved microstructure and increased mechanical properties of additive manufacture produced Ti-6Al-4V by interpass cold rolling, SFF Symp. (2013) 490–496arXiv:9809069v1, doi:10.1007/s13398-014-0173-7.2.

[75] J. Ding, P. Colegrove, J. Mehnen, S. Ganguly, P. Sequeira Almeida, F. Wang, S. Williams, Thermo-mechanical analysis of Wire and Arc Additive Layer Manufacturing process on large multi-layer parts, Comput. Mater. Sci. 50 (12) (2011) 3315–3322. doi:10.1016/j.commatsci.2011.06.023.

[76] D. Ding, Z. Pan, D. Cuiuri, H. Li, A practical path planning methodology for wire and arc additive manufacturing of thin-walled structures, Robot. Comput. Integr. Manuf. 34 (2015) 8–19. doi:10.1016/j.rcim.2015.01.003.

[77] J. Zhang, X. Zhang, X. Wang, J. Ding, Y. Traoré, S. Paddea, S. Williams, Crack path selection at the interface of wrought and wire + arc additive manufactured

Ti–6Al–4V, Mater. Des. 104 (2016) 365–375. doi:10.1016/j.matdes.2016.05.027.

[78] M. P. Akuno, Characterisation of wire + arc additively manufactured high strength aluminium alloy components, Msc thesis, Cranfield University (2017).

[79] M. Courbiere, Welding Aluminum Alloys, in: R. Blondeau (Ed.), Metall. Mech. Weld. Process. Ind. Appl., ISTE, London, 2008, Ch. Ch 13: Wel, pp. 433–471. doi:10.1002/9780470611272.ch13.

[80] N. E. Prasad, A. A. Gokhale, R. J. H. Wanhill, Aluminum-Lithium Alloys : Processing, Properties, and Applications, Elsevier, 2014.

[81] E. Louvis, P. Fox, C. J. Sutcliffe, Selective laser melting of aluminium components, J. Mater. Process. Technol. 211 (2) (2011) 275–284. doi:10.1016/j.jmatprotec.2010.09.019.

[82] E. O. Olakanmi, Selective laser sintering / melting (SLS / SLM) of pure Al , Al – Mg , and Al – Si powders : Effect of processing conditions and powder properties, J. Mater. Process. Tech. 213 (8) (2013) 1387–1405. doi:10.1016/j.jmatprotec.2013.03.009.

[83] J. Gu, J. Ding, B. Cong, J. Bai, H. Gu, S. W. Williams, Y. Zhai, The Influence of Wire Properties on the Quality and Performance of Wire+Arc Additive Manufactured Aluminium Parts, Adv. Mater. Res. 1081 (2014) 210–214. doi:10.4028/www.scientific.net/AMR.1081.210.

[84] H. Toda, T. Hidaka, M. Kobayashi, K. Uesugi, A. Takeuchi, K. Horikawa, Growth behavior of hydrogen micropores in aluminum alloys during high-temperature ex-

posure, Acta Mater. 57 (2009) 2277–2290. doi:10.1016/j.actamat.2009.01.026.

[85] J. Bai, H. L. Ding, J. L. Gu, X. S. Wang, H. Qiu, Porosity evolution in additively manufactured aluminium alloy during high temperature exposure, in: 1st Int. Conf. New Mater. Chem. Ind., Vol. 365, 2017, pp. 1–4. doi:10.1088/1742-6596/365/1/011001.

[86] S. Kou, Weld Metal Solidification Cracking, in: Weld. Metall. Second Ed., John Wiley & Sons, 2003, Ch. 11, pp. 263–300.

[87] E. Brandl, U. Heckenberger, V. Holzinger, D. Buchbinder, Additive manufactured AlSi10Mg samples using Selective Laser Melting (SLM): Microstructure, high cycle fatigue, and fracture behavior, Mater. Des. 34 (2012) 159–169. doi:10.1016/j.matdes.2011.07.067.

[88] K. Kempen, L. Thijs, J. Van Humbeeck, J.-P. Kruth, Mechanical Properties of AlSi10Mg Produced by Selective Laser Melting, Phys. Procedia 39 (2012) 439–446. doi:10.1016/j.phpro.2012.10.059.

[89] A. Mauduit, S. Pillot, H. Gransac, Study of the suitability of aluminum alloys for additive manufacturing by laser powder bed fusion, UPB Sci. Bull. Ser. B Chem. Mater. Sci. 79 (4) (2017) 219–238.

[90] N. Kaufmann, M. Imran, T. M. Wischeropp, C. Emmelmann, S. Siddique, F. Walther, Influence of process parameters on the quality of aluminium alloy EN AW 7075 using selective laser melting (SLM), Phys. Procedia 83 (2016) 918–926. doi:10.1016/j.phpro.2016.08.096.

[91] H. Zhang, H. Zhu, X. Nie, J. Yin, Z. Hu, X. Zeng, Effect of Zirconium addition on crack, microstructure and mechanical behavior of selective laser melted Al-Cu-Mg alloy, Scr. Mater. 134 (2017) 6–10. doi:10.1016/j.scriptamat.2017.02.036.

[92] J. Fixter, J. Gu, J. Ding, S. W. Williams, P. B. Prangnell, Preliminary Investigation into the Suitability of 2xxx Alloys for Wire-Arc Additive Manufacturing, in: Mater. Sci. Forum, Vol. 877, Scientifis.net, 2017, pp. 611–616. doi:10.4028/www.scientific.net/MSF.877.611.

[93] Z. Qi, B. Cong, B. Qi, J. Ding, Properties of wire + arc additively manufactured 2024 aluminum alloy with different solution treatment temperature, Mater. Lett. 230 (2018) 275–278. doi:10.1016/j.matlet.2018.07.144.

[94] R. A. Woods, Metal Transfer in Aluminum Alloys, Weld. Res. Suppl. February (1979) 59–66.

[95] C. Brice, R. Shenoy, M. Kral, K. Buchannan, Precipitation behavior of aluminum alloy 2139 fabricated using additive manufacturing, Mater. Sci. Eng. A 648 (2015) 9–14. doi:10.1016/j.msea.2015.08.088.

[96] H. Geng, J. Li, J. Xiong, X. Lin, F. Zhang, Geometric Limitation and Tensile Properties of Wire and Arc Additive Manufacturing 5A06 Aluminum Alloy Parts, J. Mater. Eng. Perform. 26 (2) (2016) 621–629. doi:10.1007/s11665-016-2480-y.

[97] H. Zuo, H. Li, L. Qi, S. Zhong, Influence of Interfacial Bonding between Metal Droplets on Tensile Properties of 7075 Aluminum Billets by Additive Manufacturing Technique, J. Mater. Sci. Technol. 32 (2015) 485–488. doi:10.1016/j.jmst.2016.03.004.

[98] C. E. Roberts, D. Bourell, T. Watt, J. Cohen, A novel processing approach for additive manufacturing of commercial aluminium alloys, Phys. Procedia 83 (2016) 909–917. doi:10.1016/j.phpro.2016.08.095.

[99] K. Bartkowiak, S. Ullrich, T. Frick, M. Schmidt, New Developments of Laser Processing Aluminium alloys via additive manufacturing technique.pdf, Phys. Procedia 12 (2011) 393–401.

[100] C. G. Pickin, S. W. Williams, P. B. Prangnell, J. Robson, M. Lunt, Control of weld composition when welding high strength aluminium alloy using the tandem process, Sci. Technol. Weld. Join. 14 (8) (2009) 734–739. doi:10.1179/136217109X12505932584817.

[101] C. G. Pickin, S. W. Williams, P. Prangnell, C. Derry, M. Lunt, Control of weld composition when arc welding high strength aluminium alloys using multiple filler wires, Sci. Technol. Weld. Join. 15 (6) (2010) 491–496. doi:10.1179/136217110X12785889549660.

[102] K. S. Rao, G. M. Reddy, K. P. Rao, Studies on partially melted zone in aluminium-copper alloy welds - Effect of techniques and prior thermal temper, Mater. Sci. Eng. A 403 (1-2) (2005) 69–76. doi:10.1016/j.msea.2005.04.041.

[103] S. Malarvizhi, V. Balasubramanian, Effect of welding processes on AA2219 aluminium alloy joint properties, Trans. Nonferrous Met. Soc. China 21 (5) (2011) 962–973. doi:10.1016/S1003-6326(11)60808-X.

[104] S. Kou, A Simple Index for Predicting the Susceptibility to Solidification Cracking, Weld. J. 94 (December) (2015) 374–388.

[105] W. Liu, X. Tian, X. Zhang, Preventing Weld Hot Cracking by Synchronous Rolling during Welding, Weld. Res. Suppl. 75 (September) (1996) 197–304.

[106] S. Sasabe, Weld cracking and joint strength of 2219 by MIG welding, Keikinzoku Yosetsu/Journal Light Met. Weld. Constr. 48 (8) (2010) 23–32. doi:10.1080/09507116.2011.590684.

[107] G. Cao, S. Kou, Predicting and Reducing Liquation-Cracking Susceptibility Based on Temperature vs. Fraction Solid, Weld. J. 85 (Jan) (2006) 9–18.

[108] S. Kou, Difficulties Associated with the Partially Melted Zone, in: Weld. Met. Second Ed., no. Chapter 11, John Wiley & Sons, Inc, 2003, Ch. 13, pp. 321–340.

[109] C. Huang, S. Kou, Partially Melted Zone in Aluminum Welds — Liquation Mechanism and Directional Solidification, Weld. Res. 79 (May) (2000) 113–120.

[110] C. Huang, S. Kou, Liquation mechanisms in multicomponent aluminum alloys during welding, Weld. Res. (2002) 211–222.

[111] R. Xiao, X. Zhang, Problems and issues in laser beam welding of aluminum–lithium alloys, J. Manuf. Process. 16 (2) (2014) 166–175. doi:10.1016/j.jmapro.2013.10.005.

[112] T. S. Srivatsan, T. S. Sudarshan, Welding of Lightweight Aluminum-Lithium Alloys, Weld. J. 70 (7) (1991) S173–S185.

[113] S. Kou, PART IV The Heat-Affected Zone, in: Weld. Metall., 2003, pp. 343–352.

[114] J. G. Yang, S. H. Sung, C. S. Chen, a. H. Tan, Study of microstructural and mechanical properties of weld heat affected zones of 2024-T3 aluminium using Gleeble simulation, Mater. Sci. Technol. 27 (1) (2011) 357–365.

doi:10.1179/026708310X12668415533964.
URL http://openurl.ingenta.com/content/xref?genre=article{&}issn=0267-0836{&}volume=27{&}issue=1{&}spage=357

[115] S. Kou, Precipitation hardening materials I: Aluminum alloys, in: Weld. Metall. Second Ed., Wiley-Blackwell, 2003, pp. 353–375.

[116] R. Bai, Y. Wei, Z. Lei, H. Jiang, W. Tao, C. Yan, X. Li, Local zone-wise elastic-plastic constitutive parameters of Laser-welded aluminium alloy 6061 using digital image correlation, Opt. Lasers Eng. 101 (May 2017) (2018) 28–34. doi:10.1016/j.optlaseng.2017.09.023.

[117] A. T. Kermanidis, A. D. Zervaki, G. N. Haidemenopoulos, S. G. Pantelakis, Effects of temper condition and corrosion on the fatigue performance of a laser-welded Al–Cu–Mg–Ag (2139) alloy, Mater. Des. 31 (1) (2010) 42–49. doi:10.1016/j.matdes.2009.07.020.
URL http://search.ebscohost.com/login.aspx?direct=true{&}db=a9h{&}AN=44172733{&}site=ehost-live

[118] M. O. Acar, S. Gungor, S. Ganguly, P. J. Bouchard, M. E. Fitzpatrick, Variation of Mechanical Properties in a Multi-pass Weld Measured Using Digital Image Correlation, Proc. SEM Annu. Conf. (2009) .

[119] C. Huang, S. Kou, Partially Melted Zone in Aluminum Welds : Solute Segregation and Mechanical Behavior, Weld. Res. Suppl. 80 (Jan) (2001) 9–17.

[120] A. Mahrle, S. Rose, M. Schnick, E. Beyer, U. Füssel, Laser-assisted plasma arc welding of stainless steel, J. Laser Appl. 25 (3) (2013) 032006. doi:10.2351/1.4798338.

[121] C. Cai, J. Feng, L. Li, Y. Chen, Influence of laser on the droplet behavior in short-circuiting, globular, and spray modes of hybrid fiber laser-MIG welding, Opt. Laser Technol. 83 (2016) 108–118. doi:10.1016/j.optlastec.2016.03.029.

[122] Y. B. Chen, Z. L. Lei, L. Q. Li, L. Wu, Experimental study on welding characteristics of CO2 laser TIG hybrid welding process, Sci. Technol. Weld. Join. 11 (4) (2006) 403–411. doi:10.1179/174329306X129535.

[123] S. Liu, F. Liu, C. Xu, H. Zhang, Experimental investigation on arc characteristic and droplet transfer in CO2laser-metal arc gas (MAG) hybrid welding, Int. J. Heat Mass Transf. 62 (1) (2013) 604–611. doi:10.1016/j.ijheatmasstransfer.2013.03.051.

[124] E. Assuncao, S. Williams, D. Yapp, Interaction time and beam diameter effects on the conduction mode limit (2012). doi:10.1016/j.optlaseng.2012.02.001.

[125] W. A. Ayoola, W. J. Suder, S. W. Williams, Parameters controlling weld bead profile in conduction laser welding, J. Mater. Process. Technol. 249 (June) (2017) 522–530. doi:10.1016/j.jmatprotec.2017.06.026.

[126] J. Gu, B. Cong, J. Ding, S. W. Williams, Y. Zhai, Wire+Arc Additive Manufacturing of Aluminium, SFF Symp. Austin Texas (2014) 451–458.

[127] J. N. Dupont, A. R. Marder, Thermal Efficiency of Arc Welding Processes, Weld. Res. Suppl. 74 (December) (1995) 406–416. doi:10.1016/j.jmatprotec.2014.12.002.

[128] F. Martina, Investigation of methods to manipulate geometry , microstructure and mechanical properties in titanium large scale Wire + Arc Additive Manufacturing, Phd thesis, Cranfield University (2014).

[129] H. Toda, K. Minami, K. Koyama, K. Ichitani, M. Kobayashi, K. Uesugi, Y. Suzuki, Healing behavior of preexisting hydrogen micropores in aluminum alloys during plastic deformation, Acta Mater. 57 (15) (2009) 4391–4403. doi:10.1016/j.actamat.2009.06.012.

[130] H. Toda, H. Oogo, K. Uesugi, M. Kobayashi, Roles of Pre-Existing Hydrogen Micropores on Ductile Fracture, Mater. Trans. 50 (9) (2009) 2285–2290. doi:10.2320/matertrans.M2009123.

[131] ASTM International, Standard Specification for Aluminum and Aluminum-Alloy Extruded Bars, Rods, Wire, Profiles, and Tubes. doi:10.1520/B0221M-13.

[132] L. Liu, R. Huang, G. Song, X. Hao, Behavior and spectrum analysis of welding arc in low-power YAG-laser-MAG hybrid-welding process, IEEE Trans. Plasma Sci. 36 (4 PART 5) (2008) 1937–1943. doi:10.1109/TPS.2008.927138.

[133] X. Gu, H. Li, L. Yang, Y. Gao, Coupling mechanism of laser and arcs of laser-twin-arc hybrid welding and its effect on welding process, Opt. Laser Technol. 48 (2013) 246–253. doi:10.1016/j.optlastec.2012.10.025.

[134] C. G. Pickin, Arc Welding of High Strength Aluminium Alloys for Armour System Applications, Ph.D. thesis, Cranfield University (2011).

[135] S. Kou, Fluid Flow and Metal Evaporation in welding, in: Weld. Metall. Second Ed., John Wiley & Sons, 2003, Ch. Chapter 4, pp. 97–121.

[136] S. Kou, Y. H. Wang, Weld Pool Convection and Its Effect, Weld. J. 65 (3) (1986) 63–70.

[137] A. development association, Al-Cu-Zn, in: Equilib. diagrams Alum. Alloy Syst., Aluminium development association information bulletin, 1961.

[138] Q. Li, A. Wu, Y. Li, G. Wang, D. Yan, J. Liu, Influence of temperature cycles on the microstructures and mechanical properties of the partially melted zone in the fusion welded joints of 2219 aluminum alloy, Mater. Sci. Eng. A 623 (2015) 38–48. doi:10.1016/j.msea.2014.11.047.

[139] J.-k. Ding, D.-p. Wang, Y. Wang, H. Du, Effect of post weld heat treatment on properties of variable polarity TIG welded AA2219 aluminium alloy joints, Trans. Nonferrous Met. Soc. China 24 (5) (2014) 1307–1316. doi:10.1016/S1003-6326(14)63193-9.

[140] Pecchiney Rhenalu, Aluminium semi-finished products, Pechiney rhenalu, Courbevois, 1997.

[141] C. Huang, G. Cao, S. Kou, Liquation cracking in partial penetration aluminium welds: assessing tendencies to liquate, crack and backfill, Sci. Technol. Weld. Join. 9 (2) (2004) 149–156. doi:10.1179/136217104225017071.

[142] P. Lequeu, K. P. Smith, A. Daniélou, Aluminum-Copper-Lithium Alloy 2050 Developed for Medium to Thick Plate, J. Mater. Eng. Perform. 19 (6) (2010) 841–847. doi:10.1007/s11665-009-9554-z.

[143] B. M. Gable, A. W. Zhu, A. A. Csontos, E. A. Starke, The role of plastic deformation on the competitive microstructural evolution and mechanical properties of a novel Al-Li-Cu-X alloy, J. Light Met. 1 (1) (2001) 1–14. doi:10.1016/S1471-5317(00)00002-X.

[144] T. Kozmel, M. Vural, S. Tin, EBSD analysis of high strain rate application Al–Cu based alloys, Mater. Sci. Eng. A 630 (2015) 99–106. doi:10.1016/j.msea.2015.02.024.

[145] D. Ortiz, M. Abdelshehid, R. Dalton, J. Soltero, R. Clark, M. Hahn, E. Lee, W. Lightell, B. Pregger, J. Ogren, P. Stoyanov, O. S. Es-Said, Effect of cold work on the tensile properties of 6061, 2024, and 7075 Al alloys, J. Mater. Eng. Perform. 16 (5) (2007) 515–520. doi:10.1007/s11665-007-9074-7.

[146] G. Gubbels, L. Tegelaers, R. Senden, Melt spun aluminium alloys for moulding optics, in: Proc. SPIE, no. 8884, 2013, pp. 1–8. doi:10.1117/12.2030181.

[147] D. Broek, The role of inclusions in ductile fracture and fracture toughness, Eng. Fract. Mech. 5 (1) (1973) 55–66. doi:10.1016/0013-7944(73)90007-6.

[148] RSP Technology, RS Alloys Overview.
URL http://www.rsp-technology.com/site-media/user-uploads/rsp{_}alloys{_}overview{_}2018lr.pdf

[149] C. G. Pickin, S. W. Williams, P. B. Prangnell, J. Robson, M. Lunt, Control of weld composition when welding high strength aluminium alloy using the tandem process, Sci. Technol. Weld. Join. 14 (8) (2009) 734–739. doi:10.1179/136217109X12505932584817.

[150] P. Miguel Sequeira Almeida, Process control and developement in wire and arc additive manufacturing, Ph.D. thesis, Cranfield University (2012).

Appendix A

Matlab code for the post treatment of tensile tests

```
%% Tensile properties
%% Data extraction
clear UTS YS Rupture_Elongation Sample_Name % clear previous ...
    calculation
% set the number of tensile tests
prompt='how many samples do you have for this trial ?';
nbsamples=input(prompt);
for s = 1 : nbsamples

% Initialize variables, looking for the tensile test text file
[Filename,PathName]= uigetfile;
filename=[PathName,'',Filename];
delimiter = '\t';

% Read columns of data as text (for more information, see the TEXTSCAN
```

```
% documentation)
formatSpec = '%*s%*s%*s%s%s%[^\n\r]';
fileID = fopen(filename,'r');

% Read columns of data according to the format.
% This call is based on the structure of the file used to generate this
% code. If an error occurs for a different file, try regenerating ...
    the code
% from the Import Tool.
dataArray = textscan(fileID, formatSpec, 'Delimiter', delimiter,...
'ReturnOnError', false);

%% Close the text file.
fclose(fileID);

% Convert the contents of columns containing numeric text to numbers.
% Replace non-numeric text with NaN.
raw = repmat({''},length(dataArray{1}),length(dataArray)-1);
for col=1:length(dataArray)-1
raw(1:length(dataArray{col}),col) = dataArray{col};
end
numericData = NaN(size(dataArray{1},1),size(dataArray,2));

for col=[1,2]
% Converts text in the input cell array to numbers. Replaced ...
    non-numeric
% text with NaN.
rawData = dataArray{col};
for row=1:size(rawData, 1)
% Create a regular expression to detect and remove non-numeric ...
    prefixes and
```

```
% suffixes.
regexstr = '(?<prefix>.*?)(?<numbers>([-]*(\d+[\,]*)+[\.]{0,1...'
%TO UNCOMENT and join together:
%regexstr = ...
    '(?<prefix>.*?)(?<numbers>([-]*(\d+[\,]*)+[\.]{0,1}\d*[eEdD]{0,1}
%[-+]*\d*[i]{0,1})|([-]*(\d+[\,]*)*[\.]{1,1}\d+[eEdD]{0,1}
%[-+]*\d*[i]{0,1}))(?<suffix>.*)';
try
result = regexp(rawData{row}, regexstr, 'names');
numbers = result.numbers;

% Detected commas in non-thousand locations.
invalidThousandsSeparator = false;
if any(numbers==',')
thousandsRegExp = '^\d+?(\,\d{3})*\.{0,1}\d*$';
if isempty(regexp(numbers, thousandsRegExp, 'once'))
numbers = NaN;
invalidThousandsSeparator = true;
end
end
% Convert numeric text to numbers.
if ¬invalidThousandsSeparator
numbers = textscan(strrep(numbers, ',', ''), '%f');
numericData(row, col) = numbers{1};
raw{row, col} = numbers{1};
end
catch me
end
end
end

```

```
73
74 % Replace non-numeric cells with NaN
75 R = cellfun(@(x) ¬isnumeric(x) && ¬islogical(x),raw); % Find ...
       non-numeric cells
76 raw(R) = {NaN}; % Replace non-numeric cells
77
78 % Allocate imported array to column variable names
79 LoadN = cell2mat(raw(:,1)); % Load provided by the tensile test machine
80 LaserDispmm = cell2mat(raw(:,2)); % Gauge length provided by the ...
       laser extensometer
81 % Clear temporary variables
82 clearvars filename delimiter formatSpec fileID dataArray ans raw ...
       col numericData rawData row regexstr result numbers ...
       invalidThousandsSeparator thousandsRegExp me R;
83 % Clear the first three values from the .txt files (no numerical ...
       values)
84 LoadN=LoadN(4:end,:);
85 LaserDispmm=LaserDispmm(4:end,:);
86 %% Data analysis
87 % Detection begining of the test by selecting only positive load
88 a=LoadN(1);
89 beg=1;
90 while a<0
91 a=LoadN(beg);
92 beg=beg+1;
93 end
94 LoadN=LoadN(beg:end,:);
95 LaserDispmm=LaserDispmm(beg:end,:);
96 % Detection of the specimen rupture. The rupture is considered when the
97 % load is divided by more than 10 from one step to the other
98 i=200;
```

```
99  [m,n]=size(LoadN);
100 while i<m
101 if LoadN(i+1)<LoadN(i)/10
102 n=i;
103 break
104 else
105 i=i+1;
106 end
107 end
108 LoadN=LoadN(1:n,:);
109 LaserDispmm=LaserDispmm(1:n,:);
110 % Stress calculation
111 Sample_Name(s) = inputdlg({'Sample name'},...
112 'Customer', [1 50]); % request the sample name from the user
113 prompt = 'What is the thickness of the sample in mm ';
114 thickness = input(prompt); % request the sample thickness from the user
115 prompt = 'What is the width of the sample in mm'; % request the ...
        sample width from the user
116 width = input(prompt);
117 Stress = LoadN/(thickness * width); % calculation of the stress
118 Elongation = 100* (-LaserDispmm(1)+ LaserDispmm) / LaserDispmm(1); ...
        %calculation of the elongation
119 % plot the curve stress elongation
120 subplot (1,nbsamples ,s)
121 plot( Elongation, Stress)
122 %% Youg's modulus determination
123 prompt = 'Between which stress value do you want to evaluate the ...
        Young modulus of this sample [min,max] ? '; % request to the user
124 YSestimation = input(prompt);
125 A=Stress<YSestimation(1,1);
126 B=Stress<YSestimation(1,2);
```

```
127 C=B-A;
128 y=zeros([1,n]);
129 x=zeros([1,n]);
130 W=zeros([1,n]);
131 for i= 1:n
132 y(i)= Stress(i)*C(i);
133 x(i)= Elongation(i)*C(i);
134 end
135 E=y/x %Youg's Modulus
136 for i= 1:n
137 W(i)=E*Elongation(i)-E*0.2;
138 end
139 %% Plot of the curves, figures features
140 plot( Elongation, Stress,Elongation,W )
141 title([Sample_Name(s)])
142 ylim([0 300]);
143 xlim([0 20]);
144 %% Yield Stress calculation
145 for i= 1:n
146 if Stress(i) < W(i)
147 F(i)= 0;
148 else F(i)= Stress (i);
149 end
150 end
151 YieldStress=max(F);
152 RuptureElongation = max(Elongation);
153 UltimateTensileStress = max(Stress);
154 grid on
155 clear A B C F i m n thickness width x y YSestimation W a beg
156 %% Matrix of results
157 YS(s)=YieldStress;
```

```
158 UTS(s)=UltimateTensileStress;
159 Rupture_Elongation(s)=RuptureElongation;
160 end
161 YS=YS';
162 UTS=UTS';
163 Rupture_Elongation=Rupture_Elongation';
164 Results=table(YS,UTS,Rupture_Elongation,'Rowname',Sample_Name')
```

Appendix B

Matlab code for the post treatment of DIC test

```
%Clear previous data
clear A B Cor H i I k n numfiles numpoint p q P PP Q QQ r R Rot RR ...
    s SStrain Strain x X X_a X_b Xr XX XXr XY y Y Y_a Y_b Yr ys YS ...
    yy YY YYr total_length UTS YS gauge_length Gauge_length ...
    Elongation elongation_rupture Data F step W YieldStress
%Start new analyisis
numfiles =746; % Number of steps
numpoint =3000; % number of point extrated for the DIC data
% Extraction of data from the step files
mydata = cell(1, numfiles);
for k = 1:numfiles
myfilename = sprintf('Step_%d.txt', k);
mydata{k} = importdata(myfilename);
end
% Stress values
```

```
13 Stress=stress_M8(1:numfiles); % To be filed manually using the load ...
       provided by the Istra software
14 E=72; % Young's modulous to be given by the user
15 %% Open the text file.
16 % fileID = fopen(myfilename,'r');
17 X=zeros(numpoint,numfiles); % X coordinate of all points, for all steps
18 XX=zeros(1,1,numfiles); % X cordinate of all points, distributed in ...
       one matrix for each step
19 x=zeros(numpoint,numfiles); % pointer provided by Istra indicating ...
       the relative position of each point in the x direction for each ...
       step
20 xx=zeros(numpoint,1); % x pointer for one step
21 Y=zeros(numpoint,numfiles);
22 YY=zeros(1,1,numfiles);
23 y=zeros(numpoint,1);
24 yy=zeros(numpoint,1);
25
26 % Data extraction
27 for H=1:numfiles
28 Data=mydata{1,H}.data;
29 Strain(:,H)=Data(1:numpoint,38); % Strain for all points and all ...
       steps in one D matrix
30 X(:,H)=Data(1:numpoint,3);
31 xx(:,H)=Data(1:numpoint,1);
32 Y(:,H)=Data(1:numpoint,4);
33 yy(:,H)=Data(1:numpoint,2);
34 end
35
36 % Distribution of point in multi dimentional matrix (required to ...
       use contourf function
37 for H=1:numfiles
```

```
for i=1:numpoint
XX(xx(i,H),yy(i,H),H)=X(i,H);
YY(xx(i,H),yy(i,H),H)=Y(i,H);
SStrain(xx(i,H),yy(i,H),H)=Strain(i,H);
end
end

% Determination of matrix characteristics
numlines=max(xx);
numlines=numlines(numfiles);
numcolumn=max(yy);
numcolumn=numcolumn(numfiles);
clear F W
figure
g=1;
j=1;

%% Calculation of the YS for each point
for p=1:numlines
for q=1:numcolumn
A=mean(SStrain(p,q,1:10));
clear F plot_strain
for t=1:numfiles
W(t)=E*SStrain(p,q,t)-E*(A+2);
plot_strain(t)=SStrain(p,q,t);
if Stress(t) < W(t)
F(t)= 0;
else
F(t)= Stress (t);
end
end
```

```
YS(p,q)=max(F);

if YS(p,q)≥ (0.9*max(Stress))% YS above 90% of the UTS measured ...
    during this test will be removed to
% avoid numerical issues. The limit of 90% can be modified by the user
YS(p,q)=NaN;
end

%% Results ploting
% Especially when using the code for a new specimen, it is ...
    important to
% check the aspect of the stress strain surve obtained. figures of ...
    4 x 4
% plots will be provided by the code, the value of g indicates the
% ploting frequency

if g==10000
if j≤16
subplot(4,4,j)
plot(plot_strain,Stress,plot_strain,W)
ylim([0 400]) % range of load obtained during the test
title(['Position x=' num2str(XX(p,q,1)) ' y=' num2str(YY(p,q,1))])
g=0;
j=j+1;
else
j=1;
figure('PaperPosition',[.2 .2 15 15])
subplot(4,4,j)
plot(plot_strain,Stress,plot_strain,W)
ylim([0 400])  % range of load obtained during the test
g=0;
```

```
97  j=j+1;
98  end
99  else g=g+1;
100 end
101 end
102 end
103
104 %% Remove non physical data
105 % Remove X and Y equal to 0
106 [R,P,Q]=size(XX);
107 for r=1:R
108 for p=1:P
109 for q=1:Q
110 XXX(r,p,q)=XX(r,p,q);
111 YYY(r,p,q)=YY(r,p,q);
112 if XXX(r,p,q)==0
113 if YYY(r,p,q)==0
114 XXX(r,p,q)=NaN;
115 YYY(r,p,q)=NaN;
116 end
117
118 end
119 end
120 end
121 end
122
123 [R,P]=size(YS);
124 for r=1:R
125 for p=1:P
126 if YS(r,p)==0
127 YS(r,p)=NaN;
```

```
128 end
129 if SStrain(r,p,numfiles)==0
130 SStrain(r,p,numfiles)=NaN;
131 end
132 end
133 end
134
135 %% Rotation and translation of the coordinate
136 % This is to obtain straight specimen in the map
137 [R,P,Q]=size(XX);
138 p=floor(P/2); % this centering is based on the centre line of the ...
       sample disganted by the absciss p
139 % calculation of the rational matrix
140 X_a=min(YYY(:,p,1));
141 X_b=max(YYY(:,p,1));
142 Y_a=min(XXX(:,p,1));
143 Y_b=max(XXX(:,p,1));
144 A=(Y_b-Y_a)/sqrt((Y_b-Y_a)^2+(X_b-X_a)^2);
145 B=(X_b-X_a)/sqrt((Y_b-Y_a)^2+(X_b-X_a)^2);
146 Rot=[B,-A;A,B];
147 % Rot=[1,0;0,1]; % To be used if no rotation is wanted
148 %% Calculation of the new coordinates
149 for i=1:numfiles
150 Cor=[X(:,i)';Y(:,i)'];
151 XY=Rot*Cor;
152 Xr(:,i)=XY(1,:); % new X as 1D matrix (all points, all steps)
153 Yr(:,i)=XY(2,:); % new Y  as 1D matrix (all points, all steps)
154 end
155
156 XXr=zeros(R,P,Q); % reorganisation of the Xr with 1 dimention for ...
       each step
```

```
157 YYr=zeros(R,P,Q); % reorganisation of the Xr with 1 dimention for ...
       each step
158 for H=1:numfiles
159 for i=1:numpoint
160 XXr(xx(i,H),yy(i,H),H) = Xr(i,H);
161 YYr(xx(i,H),yy(i,H),H) = Yr(i,H);
162 end
163 end
164
165 % Remove points for wich XXr=0 and YYr=0 at the final iteration
166 [R,P,Q]=size(XX);
167 for r=1:R
168 for p=1:P
169 if XXr(r,p,numfiles)==0;
170 XXr(r,p,numfiles)=NaN;
171 YYr(r,p,numfiles)=NaN;
172 end
173 if YYr(r,p,numfiles)==0;
174 XXr(r,p,numfiles)=NaN;
175 YYr(r,p,numfiles)=NaN;
176 end
177 end
178 end
179
180
181 %% Figure plotting
182 % The figures are ploted for the step final. to plot the figures at ...
       another
183 % time step, numfiles needs to changed in all contourf ans scatter
184 % functions
185 %% Yield strength
```

```
figure('PaperPosition',[.2 .2 10 30])
[C,h]=contourf(XXr(:,:,numfiles),YYr(:,:,numfiles),YS(:,:),'LineColor','none')
hold on
scatter(Xr(:,numfiles),Yr(:,numfiles),5,'r.')
colorbar
h.LevelStep=1
a=300; % maximum YS
caxis([0 a])
A=a/8; % 8 = number of  color marker (8x2=16 number of color in the ...
    map)
colormap(parula(4*a/A))
YS_ticks=0;
for i=1:A+1
YS_ticks(i)=A*(i-1);
end
YS_ticks(1)=0
colorbar('Ticks',YS_ticks)
title('YS')
%% Maximum strain
figure('PaperPosition',[.2 .2 10 30])
[Q,p]=contourf(XXr(:,:,numfiles),YYr(:,:,numfiles),SStrain(:,:,numfiles),...
'LineColor','none');
colorbar
hold on
scatter(Xr(:,numfiles),Yr(:,numfiles),5,'r.')
p.LevelStep=1
b=800; % maximum strain
caxis([0 b]);
B=b/8; % 8 = number of  color marker (8x2=16 number of color in the ...
    map)
colormap(parula(2*b/B))
```

```
Strain_ticks=0
for i=1:B+1
Strain_ticks(i)=B*(i-1);
end
colorbar('Ticks',Strain_ticks)
title('Strain')
```